Two Birds with One Stone:
Theranostic Applications of Nanobodies

Dissertation

der Mathematisch-Naturwissenschaftlichen Fakultät
der Eberhard Karls Universität Tübingen
zur Erlangung des Grades eines
Doktors der Naturwissenschaften
(Dr. rer. nat.)

vorgelegt von
Teresa Raphaela Wagner
Nürtingen

Tübingen
2023

Gedruckt mit Genehmigung der Mathematisch-Naturwissenschaftlichen Fakultät der Eberhard Karls Universität Tübingen.

Tag der mündlichen Qualifikation:	12.12.2023
Dekan:	Prof. Dr. Thilo Stehle
1. Berichterstatter:	Prof. Dr. Ulrich Rothbauer
2. Berichterstatter:	Prof. Dr. Bernd Pichler
3. Berichterstatter:	Prof. Dr. Markus Seeger

Table of Contents

Abstract

As precision medicine advances, the term "theranostics" is becoming increasingly established and refers to the growing interlinking of diagnostics and therapeutics. Nanobodies (Nbs) derived from heavy-chain-only antibodies (HCAbs), exhibit as small and stable binding molecules unique properties such as good solubility, high tissue penetration, low immunogenicity and inexpensive production. Therefore, Nbs have ideal characteristics for diagnostic and therapeutic purposes.

In this work, novel Nbs from immune libraries against two divergent target structures (receptor binding domain, RBD, of SARS-CoV-2; human signal-regulating protein α, hSIRPα, on myeloid cells) for theranostic applications were generated. Through in-depth *in vitro* characterization, including binding affinity, stability analysis and detailed epitope mapping, we identified potent candidates and demonstrated their suitability as diagnostic and therapeutic tools in detail.

For SARS-CoV-2, we developed neutralizing Nbs that functionally inhibit the interaction between RBD and angiotensin-converting enzyme (ACE) 2 as the viral entry site exposed on human cells. To enhance their neutralizing potency, biparatopic (bip) Nb formats capable of binding multiple variants of concern (VOCs) were generated. By using these bipNbs as antibody (Ab) surrogates in a high-throughput assay, termed NeutrobodyPlex, we were able to determine the neutralizing capacity of anti-SARS-CoV-2 Abs in serum samples of patients. In addition, in a murine disease model, intranasal administration of our bipNbs resulted in a significantly reduced disease progression and increased survival rates at lethal doses of SARS-CoV-2 B.1, Beta, and Delta.

To further demonstrate the suitability of Nbs as theranostics in the context of novel immunotherapies, we developed Nbs against hSIRPα expressed by myeloid cells. Applying a binary screening campaign, we identified modulatory and inert binding molecules. Three Nbs targeting the domain 1 (D1) of hSIRPα functionally block the hSIRPα/hCD47 interaction and thus effectively enhance Ab-dependent cellular phagocytosis (ADCP) *in vitro*. For imaging purposes, the inert hSIRPα Nb S36 was sequence optimized to enable site-directed radiolabeling. High-resolution positron emission tomography (PET) imaging allowed us to visualize hSIRPα^{+} myeloid cells in tumor lesions of mice. Given the dual applications of the selected hSIRPα Nbs, there is substantial potential to further develop these biologicals into myeloid-specific checkpoint inhibitors for combination therapies or for diagnostic imaging to monitor individual response to immunotherapy. In conclusion, this work shows the great potential of Nbs as

theranostics that will assume increasing importance in the field of personalized medicine in the future.

Zusammenfassung

Im Zuge der Präzisionsmedizin etabliert sich zunehmend der Begriff "Theranostik", welcher die verstärkte Verzahnung von Diagnostik und Therapie bezeichnet. Nanobodies (Nbs), die sich von Schwere-Ketten-Antikörpern (HCAb) ableiten, besitzen als kleine und stabile Bindungsmoleküle einzigartige Eigenschaften wie z.B. gute Löslichkeit, hohe Gewebepenetration, geringe Immunogenität und kostengünstige Herstellung, was Nbs zu attraktiven Reagenzien für diagnostische und therapeutische Zwecke macht.

In dieser Arbeit wurden aus Immunbibliotheken Nbs gegen zwei unterschiedliche Zielstrukturen (Rezeptorbindungsdomäne, RBD, von SARS-CoV-2; humanes signalregulierendes Protein α, hSIRPα, auf myeloischen Zellen) selektiert und für theranostische Anwendungen weiterentwickelt. Auf Basis eingehender In-vitro-Charakterisierung, einschließlich Bestimmung der Bindungsaffinität, Stabilitätsanalyse und detaillierter Epitopkartierung, haben wir potente Nb-Kandidaten identifiziert und ihre Eignung als diagnostische und therapeutische Hilfsmittel im Detail untersucht.

Für SARS-CoV-2 wurden neutralisierende Nbs entwickelt, die funktionell die Interaktion zwischen RBD und dem Angiotensin Converting Enzyme (ACE) 2, als viraler Rezeptor auf menschlichen Zellen, inhibieren. Zur Verstärkung ihrer neutralisierenden Wirkung wurden biparatopische (bip) Nb-Formate gegen mehrere Variants of Concern (VOCs) generiert. Eingesetzt als Antikörper- (Ab-) Surrogate in einem Hochdurchsatz-Assay, dem sogenannten NeutrobodyPlex, konnten wir mit den bipNbs die Neutralisationskapazität von anti-SARS-CoV-2-Abs in Serumproben von PatientInnen bestimmen.

Vor dem Hintergrund neuer Immuntherapien wurden Nbs gegen hSIRPα als Oberflächenrezeptor myeloischer Zellen generiert. Mittels einer binären Screeningstrategie identifizierten wir modulierende und inerte Nbs. Drei Nbs, die auf die D1-Domäne (D1) von hSIRPα gerichtet sind, blockieren die Interaktion zwischen hSIRPα und hCD47 und verstärken so die Ab-abhängige zelluläre Phagozytose (ADCP). Für den Einsatz in der diagnostischen Bildgebung wurde der nicht-modulierende hSIRPα Nb S36 für eine ortsgerichtete Radiomarkierung sequenzoptimiert. In Kombination mit hochauflösender Positronen-Emissions-Tomographie (PET) wurden hSIRPα^{+} myeloische Zellen in Tumorläsionen von Mäusen gezielt sichtbar gemacht. In Anbetracht der dualen Einsatzmöglichkeiten der selektierten hSIRPα-Nbs besteht ein substanzielles Potential zur Weiterentwicklung dieser Biologicals z.B. zu myeloidspezifischen Checkpoint-Inhibitoren für Kombinationstherapien oder für die diagnostische Bildgebung zur Überwachung des individuellen Ansprechens auf eine Immuntherapie. Zusammenfassend zeigt diese Arbeit

das große Potenzial von Nbs als Theranostika, die in Zukunft im Bereich der personalisierten Medizin an Bedeutung gewinnen werden.

Abbreviations

aa	amino acid
Ab	antibody
ACE2	angiotensin-converting enzyme 2
ADCP	Ab-dependent cellular phagocytosis
ALX-0081	caplazizumab
bip	biparatopic
BLI	biolayer interferometry
BSL3	biosafety level 3
CAR	chimeric antigen receptor
CDR	complementarity-determining region
CFSE	carboxyfluorescein diacetate succinimidyl ester
CH	heavy chain domain
CL	constant light chain
CLIA	chemiluminescence immunoassay
CRIg	complement receptor of the Ig superfamily
CT	computed tomography
DAA	direct acting antiviral
E	SARS-CoV-2 envelope protein
E. coli	escherichia coli
ELISA	enzyme-linked immunosorbent assay
Fc	fragment crystallizable
FcR	Fc receptor
FDA	food and drug administration
FR	framework region
GFP	green fluorescent protein
GM-CSF	granulocyte macrophage colony stimulating factor
GPCR	G-protein coupled receptor
H&E	hematoxylin and eosin
HCAb	heavy-chain-only antibody
HCV	hepatitis C virus
HDX-MS	hydrogen-deuterium exchange mass spectrometry
HIV	human immunodeficiency virus-1
HTA	host-targeting agent
i.v.	intravenous
IgG	immunoglobulin G
IL	interleukin
IMAC	immobilized metal affinity chromatography
ISH	in situ hybridization
ITIM	immunoreceptor tyrosine-based inhibitory motif
JAK	janus kinase
LFIA	lateral flow immunoassay
M	SARS-CoV-2 membrane
mAb	monoclonal Ab
MDM	monocyte-derived macrophages
MERS-CoV	middle east respiratory syndrome-related coronavirus
MFI	mean fluorescence intensity

MHC	major histocompatibility complex
MMR	macrophage mannose receptor
MRI	magnetic resonance imaging
N	SARS-CoV-2 nucleocapsid protein
NAb	neutralizing Ab
NTD	N-terminal domain
ORF	open reading frame
PBMC	peripheral blood mononuclear cell
PE	phycoerythrin
PET	positron emission tomography
QPCTL	glutaminyl peptide cyclotransferase-like protein
RBD	SARS-CoV-2 receptor-binding domain
RSV	respiratory syncytial virus
RT-PCR	reverse-transcription polymerase chain reaction
S	SARS-CoV-2 spike protein
SARS-CoV	acute respiratory syndrome coronavirus
scFv	single chain variable fragment
SEC	size exclusion chromatography
SHP	small heterodimer partner
hSIRP	human signal-regulating protein
hSIRPαD	hSIRPα domain
SPECT	single-photon emission computed tomography
TAM	tumor-associated macrophage
TLR	toll like receptor
TMD	transmembrane domain
TME	tumor microenvironment
TMPRSS2	TM protease serine 2
TNF	tumor necrosis factor
TSPO	mitochondrial translocator protein
VH	variable heavy chain
VHH/Nb	nanobody
VL	variable light chain
VNT	virus neutralization test
VOC	variants of concern
VOI	variants of interest

List of Figures

List of Publications

§ authors contributed equally

Accepted Manuscripts

1. **Wagner TR**, Rothbauer U (2020) **Nanobodies right in the middle: intrabodies as toolbox to visualize and modulate antigens in the living cell**. Biomolecules 10: 1701.

2. Becker M, Dulovic A, Junker D, Ruetalo N, Kaiser PD, Pinilla YT, Heinzel C, Haering J, Traenkle B, **Wagner TR**, Layer M, Mehrlaender M, Mirakaj V, Held J, Planatscher H, Schenke-Layland K, Krause G, Strengert M, Bakchoul T, Althaus K, Fendel R, Kreidenweiss A, Koeppen M, Rothbauer U, Schindler M, Schneiderhan-Marra N (2021) **Immune response to SARS-CoV-2 variants of concern in vaccinated individuals**. Nature Communications 12: 3109.

3. Kratzer U, Sommersdorf C, Maier S, **Wagner TR**, Templin M, Joos TO, Rothbauer U, Zeck A, Poetz O (2021) **Tris (hydroxymethyl) aminomethane Compatibility with N-Hydroxysuccinimide Ester Chemistry: Biotinylation of Peptides and Proteins in TRIS Buffer**. Bioconjugate Chemistry 32: 1960-1965.

4. Traenkle B, Kaiser PD, Pezzana S, Richardson J, Gramlich M, **Wagner TR**, Seyfried D, Weldle M, Holz S, Parfyonova Y, Nueske S, Scholz AM, Zeck A, Jakobi M, Schneiderhan-Marra N, Schaller M, Maurer A, Gouttefangeas C, Kneilling M, Pichler BJ, Sonanini D, Rothbauer U (2021) **Single-Domain Antibodies for Targeting, Detection, and In Vivo Imaging of Human CD4$^+$ Cells**. Front Immunol 12: 799910.

5. **Wagner TR**[§], Ostertag E[§], Kaiser PD, Gramlich M, Ruetalo N, Junker D, Haering J, Traenkle B, Becker M, Dulovic A, Schweizer H, Nueske S, Scholz A, Zeck A, Schenke-Layland K, Nelde A, Strengert M, Walz JS, Zocher G, Stehle T, Schindler M, Schneiderhan-Marra N, Rothbauer U (2021) **NeutrobodyPlex-monitoring SARS-CoV-2 neutralizing immune responses using nanobodies**. EMBO Rep 22: e52325.

6. **Wagner TR**, Rothbauer U (2021) **Nanobodies – Little helpers unravelling intracellular signaling**. Free Radical Biology and Medicine 176: 46-61.

7. Burgstaller S, **Wagner TR**, Bischof H, Bueckle S, Padamsey A, Frecot D, Kaiser PD, Skrabak D, Malli R, Lukowski R, Rothbauer U (2022) **Monitoring extracellular ion and metabolite dynamics with recombinant nanobody-fused biosensors**. iScience 25: 104907.

8. Fagbadebo FO, Kaiser PD, Zittlau K, Bartlick N, **Wagner TR**, Froehlich T, Jarjour G, Nueske S, Scholz A, Traenkle B, Macek B, Rothbauer U (2022) **A Nanobody-Based Toolset to Monitor and Modify the Mitochondrial GTPase Miro1**. Front Mol Biosci 9: 835302.

9. Gramlich M, Maier S, Kaiser PD, Traenkle B, **Wagner TR**, Voglmeir J, Stoll D, Rothbauer U, Zeck A (2022) **A Novel PNGase Rc for Improved Protein N-Deglycosylation in Bioanalytics and Hydrogen-Deuterium Exchange Coupled with Mass Spectrometry Epitope Mapping under Challenging Conditions**. Anal Chem 94: 9863-9871.

10. Junker D[§], Becker M[§], **Wagner TR[§]**, Kaiser PD, Maier S, Grimm TM, Griesbaum J, Marsall P, Gruber J, Traenkle B, Heinzel C, Pinilla YT, Held J, Fendel R, Kreidenweiss A, Nelde A, Maringer Y, Schroeder S, Walz JS, Althaus K, Uzun G, Mikus M, Bakchoul T, Schenke-Layland K, Bunk S, Haeberle H, Göpel S, Bitzer M, Renk H, Remppis J, Engel C, Franz AR, Harries M, Kessel B, Lange B, Strengert M, Krause G, Zeck A, Rothbauer U, Dulovic A, Schneiderhan-Marra N (2022a) **Antibody binding and ACE2 binding inhibition is significantly reduced for both the BA1 and BA2 omicron variants**. Clin Infect Dis 76: e240–e249.

11. Junker D, Dulovic A, Becker M, **Wagner TR**, Kaiser PD, Traenkle B, Kienzle K, Bunk S, Struemper C, Haeberle H, Schmauder K, Ruetalo N, Malek N, Althaus K, Koeppen M, Rothbauer U, Walz JS, Schindler M, Bitzer M, Göpel S, Schneiderhan-Marra N (2022b) **COVID-19 patient serum less potently inhibits ACE2-RBD binding for various SARS-CoV-2 RBD mutants**. Scientific Reports 12: 7168.

12. Singh A, Toma F, Uzun G, **Wagner TR**, Pelzl L, Zlamal J, Freytag V, Weich K, Nowak-Harnau S, Rothbauer U, Althaus K, Bakchoul T (2022) **The interaction between anti-PF4 antibodies and anticoagulants in vaccine-induced thrombotic thrombocytopenia**. Blood 139: 3430-3438.

13. **Wagner TR[§]**, Schnepf D[§], Beer J[§], Ruetalo N[§], Klingel K, Kaiser PD, Junker D, Sauter M, Traenkle B, Frecot DI, Becker M, Schneiderhan-Marra N, Ohnemus A, Schwemmle M, Schindler M, Rothbauer U (2022) **Biparatopic nanobodies protect mice from lethal challenge with SARS-CoV-2 variants of concern**. EMBO Rep 23: e53865.

14. **Wagner TR**, Blaess S, Leske IB, Frecot DI, Gramlich M, Traenkle B, Kaiser PD, Seyfried D, Maier S, Rezza A, Sonego F, Thiam K, Pezzana S, Zeck A, Gouttefangeas C, Scholz A, Nueske S, Maurer A, Kneilling M, Pichler BJ, Sonanini D, Rothbauer U (2023) **Two birds with one stone: human SIRPα nanobodies for functional modulation and in vivo imaging of myeloid cells**. Front Immunol 14: 1264179.

Publications referred to in this doctoral thesis.

CHAPTER 1

INTRODUCTION

1. Introduction

1.1. Nanobodies: Single-domain antibodies

1.1.1. Structural features & biochemical properties

The serendipitous discovery of heavy-chain-only antibodies (HCAbs) more than thirty years ago has ushered in a new era of binding molecules for biomedical research, diagnostics and therapeutics[1]. Originally identified in camels, further species like new world camelids including llamas, alpacas, guanacos, and vicunas were discovered to carry this type of antibody (Ab)[2]. In comparison to conventional Abs (IgGs), HCAbs consist of only two heavy chains, lacking light chains (VLs, CLs) and constant heavy chain domains 1 (CH1s). Antigen binding is thereby conferred exclusively via the variable heavy chain of HCAbs (VHH). Due to the nanometer scale (2.5 nm diameter, 4 nm length) of the VHH, the name "nanobody (Nb)" was coined, originally trademarked by the company Ablynx. To date, Nbs are the smallest naturally derived intact antigen binding fragments with a molecular weight between 13-15 kDa[3-5].

The sequences of Nbs are highly homologous to those of the VH domains of conventional IgGs comprising three hypervariable domains called CDR1-3 (complementarity-determining region) surrounded by four conserved framework regions (FR1-4) (**Figure 1A & B**)[3; 6; 7]. Structurally, Nbs consist of nine β-strands divided into a five-stranded and a four-stranded β-fold and connected by loops, thus showing a classical IgV folding which is further stabilized by at least one conserved disulfide bond bridging FR1 and FR3 (**Figure 1B & C**). The paratope is formed by the CDRs typically exposed on the surface on the N-terminal site of the molecule[8]. To achieve high affinity interaction a para-/epitope surface area of 600-800 Å^2 is required[9-11]. Due to the lack of the VL, the lengths of the CDR loops evolved and especially the CDR3 is extended by several amino acids in comparison to conventional Abs. The finger-like projection of the CDR3 loop can enable the recognition of cavity-like binding epitopes, which are typically not addressable by IgGs[12-14]. Moreover, hydrophobic amino acids in conventional VHs are replaced by smaller/hydrophilic residues in FR2[15; 16]. These so-called "hallmark" residues are responsible for the increased solubility and lower aggregation tendency of Nbs[3; 7].

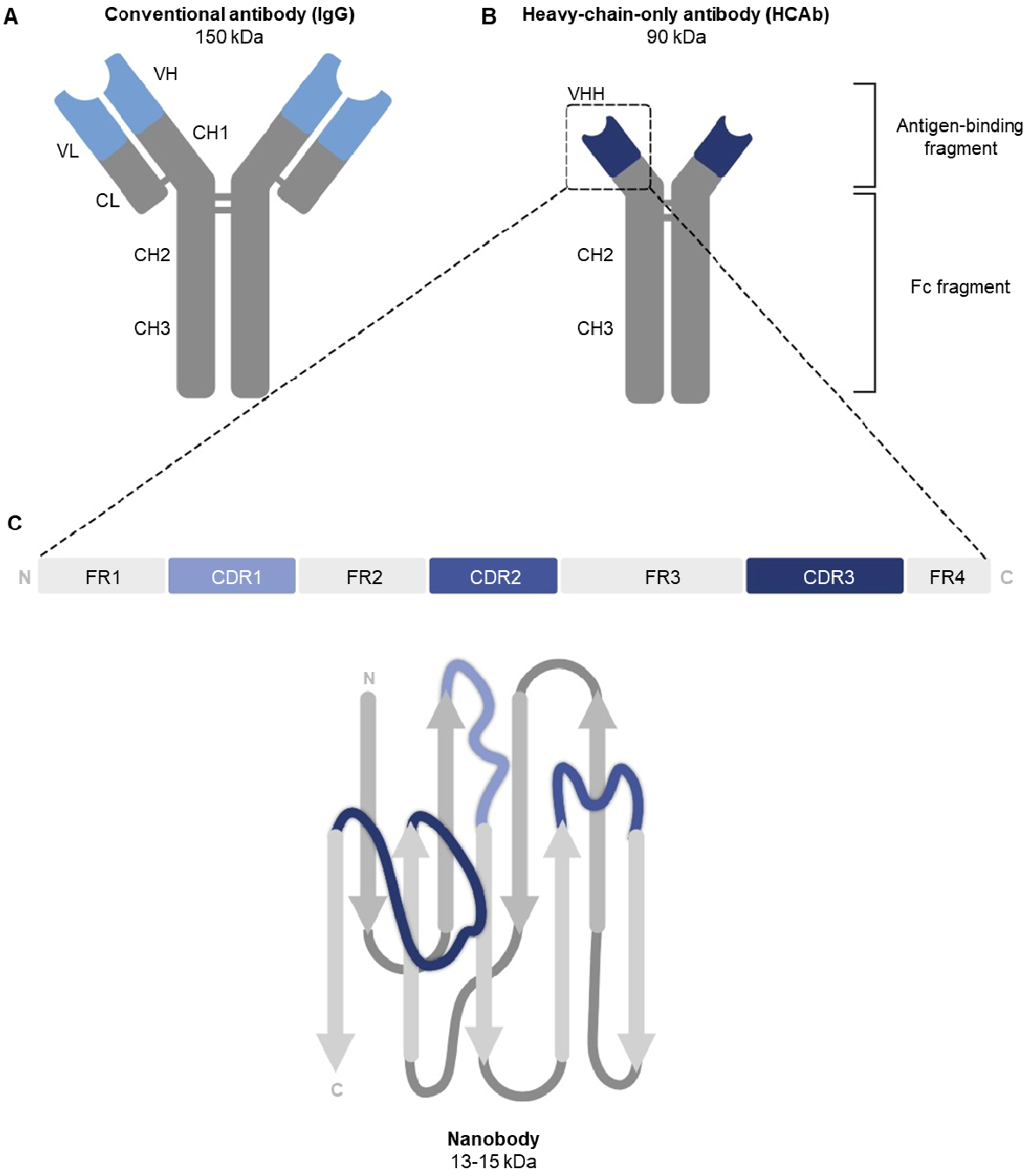

Figure 1: Comparison of conventional Abs and Nbs derived from HCAbs.
A) Conventional Abs (IgGs) consist of two identical heavy (H) and light (L) chains, with paired variable domains (VH and VL) mediating antigen recognition. **B)** HCAbs are lacking the light chain and the CH1 domain, therefore the paratope is formed by the VHH fragment. **C)** The VHH, termed Nb, comprises four framework regions (FR) 1–4 and three hypervariable domains (CDR1-3) mediating antigen recognition. Structurally Nbs consist of nine β-strands, which are connected by CDR1-3 as hypervariable loops (illustration adapted by[17]).

These inherent properties make Nbs unique binding molecules with various advantages compared to conventional Abs. Due to their robust structure Nbs can tolerate high

temperatures (~60–80°C, several weeks at 37°C), elevated pressures (500–750 MPa), non-physiological pHs (3.0–9.0), and strong chemical denaturants (2.3–3.3 M guanidinium chloride, 6–8 M urea)[5; 18-20]. Their nanoscale size allows rapid and deep penetration into tissues, and certain Nbs are even able to cross the blood-brain barrier[21; 22]. In addition, Nbs have low immunogenicity due to their high homology to human IGHV3-derived domains[23]. Lacking post-translational modifications, Nbs can be cost-effectively produced in microbial systems yielding homogeneous products[24]. Moreover, the modular nature of Nbs enables the generation of multi-valent/-paratopic Nb-constructs and Nb-fusion molecules, exhibiting higher avidity as well as multi-specificity/-functionality[25-27].

1.1.2. Overview of generation and application

The starting point for generating target-specific Nbs are Nb libraries, of which three types are available: immune[28-30], naïve[31; 32] and synthetic[33; 34]. Classically, Nb libraries are generated from blood samples of immunized camelids or, more recently, transgenic mice[35; 36]. The main advantages of this approach are that the Nbs are affinity matured *in vivo* and relatively high titers of target-specific binders are usually obtained. Therefore, relatively small library sizes (10^6-10^8) are sufficient to select potent Nb candidates. On contrary, a time-consuming immunization has to be performed for each project and the generation of Nbs against toxic or non-immunogenic proteins is not possible[37]. Naïve libraries consist of a genetic Nb pool from several non-immunized animals[37]. The generation of a synthetic library involves the randomization of CDRs with compatible amino acids on the basis of a stable scaffold[38; 39]. The ability to use one library for multiple projects and to generate Nbs against any target structure are the advantages of both techniques. However, a very large library size (10^9-10^{15}) is typically requested and Nbs may need to be optimized for both stability and affinity[37]. Following library generation, specific Nb candidates are selected. A variety of selection systems have been established, including phage, yeast or ribosome display as well as phenotypic selection strategies to directly select for modulating Nbs[37; 40-42]. Recently, deep sequencing approaches have revolutionized Nb selection campaigns as a complementary tool to conventional selection strategies by enabling the identification of a larger number of high-affinity binders within a much broader sequence space[43].

Following generation, identification and characterization of most potent Nb candidates, their unique features resulted in a wide range of applications, e.g. as research or diagnostic tools or therapeutics, where conventional Abs either failed or were difficult to apply. In the following an overview of Nb applications providing a special advantage over other binding molecules or technologies is presented.

As a research tool, Nbs initially revolutionized the field of live-cell imaging (**Figure 2**). The reducing environment in the cytosol severely impairs disulfide bond formation, making intracellular expression of conventional Abs per se impossible[44]. In contrast, many Nbs retain antigen specificity despite lacking functional disulfide bonds and are therefore ideal for intracellular expression as intrabodies[17; 45-50]. By using Nbs fused with fluorescent proteins, *Rothbauer et al.* provided the first proof of principle to recognize target structures in subcellular compartments in living cells[47]. Moreover, intrabodies were used for targeted protein removal. In contrast to knockdown at DNA or RNA level, target depletion at protein level can be achieved via the ubiquitin/proteasome pathway. Fusion of Nbs with F-box proteins resulted in the first proof of concept study in *Drosophila melanogaster* and *Danio rerio*, showing immediate protein depletion[51]. Nbs as intracellular research tools advanced further with the development of conformational sensitive Nbs. For G-protein coupled receptors (GPCRs) precise monitoring of rapid state transformation was demonstrated, proving the application of Nbs as biosensors to elucidate intracellular signaling cascades[52]. In addition, precise intracellular spatial and temporal control was achieved by the intelligent design of light- or ligand-switchable Nb systems, e.g. by splitting Nb sequences and inserting light/ligand-sensitive protein domains or photocaged tyrosine residues[53-56].

With super-resolution imaging techniques offering resolution down to ~20 nm, the sheer size of conventional Abs has been a barrier to progress in this field due to linkage error (**Figure 2**). The application of nanoscale binders coupled to organic dyes enabled visualization of fine cytoskeletal structures, including microtubules, at nanometer resolution for the first time[57; 58]. Nbs are now an established tool for super-resolution imaging, especially Nbs recognizing small peptide-derived epitope tags are manifoldly applicable, e.g. to visualize tagged vimentin, lamin, tubulin and actin[59].

The development of a nanotrap system by covalent linkage of Nbs to solid and inert materials, e.g. magnetic beads, served both as research tool and prototype for diagnostic application. Initially shown with the GFP-Nb as binding molecule of the GFP-Trap various applications are conceivable to capture and enrich analytes at low concentrations in complex solutions like serum (**Figure 2**)[60; 61].

Structural analysis of dynamic and membranous proteins is highly challenging, therefore fixability reagents stabilizing flexible protein loops, shielding hydrophobic surface structures, or capturing proteins in certain conformation states were urgently required. Nbs with high production yield, small size, robust structure, and target-specific antigen binding emerged as ideal chaperones for crystallization and cryoelectron microscopy analysis, enabling structural determination of proteins like GPCRs or membranous transporter complexes (**Figure 2**)[62-64].

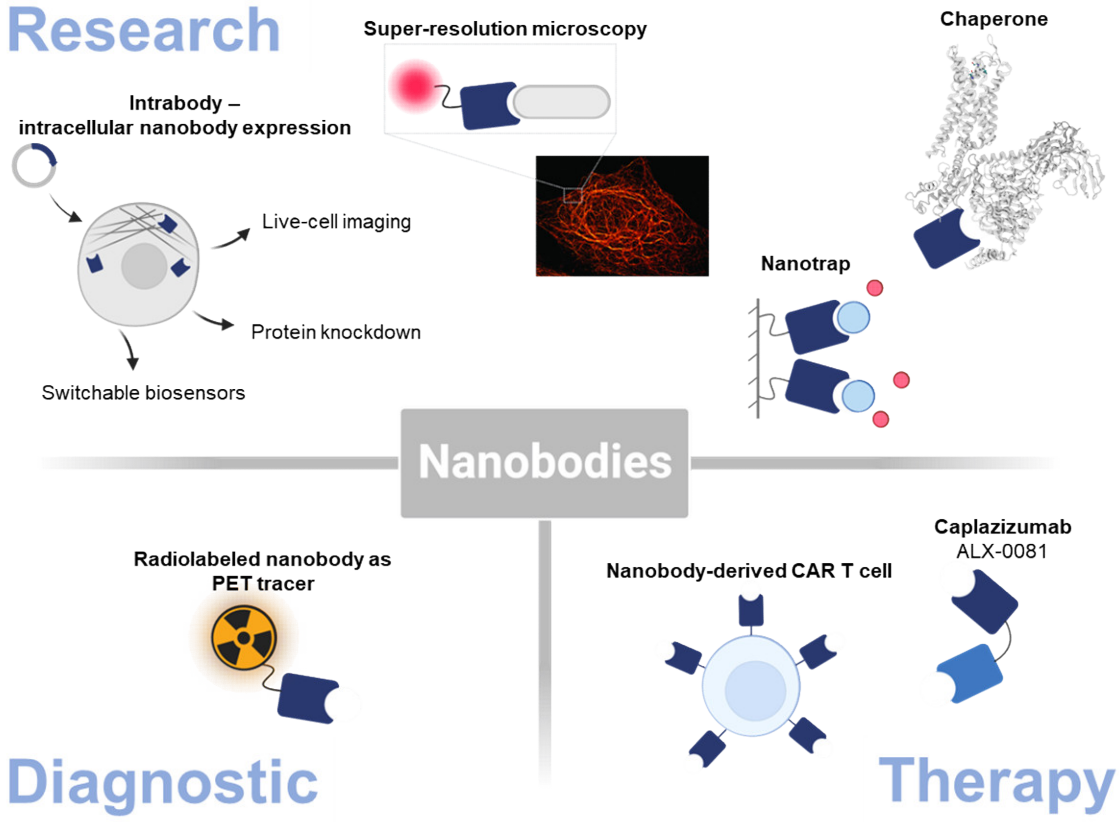

Figure 2: Applications of Nbs as research tools and for diagnostic and therapeutic purposes. Various research applications of Nbs are based on intrabodies by genetic linkage to fusion partners and intracellular expression. Nbs linked to fluorophores enable the visualization of structures up to nanometer resolution using super-resolution microscopy techniques. By immobilizing Nbs to inert matrixes, affinity capturing tools so-called nanotraps e.g. for immunoprecipitation analysis were generated. Nbs as chaperones enabled the structural analysis of dynamic proteins. Radiolabeled Nbs have emerged as advanced tracer molecules for diagnostic PET imaging. Caplazizumab (ALX-0081) is the first approved therapeutic Nb. Nb-derived chimeric antigen receptor (CAR) T cells are promising personalized cell-based therapy approaches.

The development of theranostics is an emerging field in precision medicine. Theranostics enables patient selection, treatment, and monitoring. Owing to their small size, fast tissue penetration, strong target specificity and ease of modification, Nbs gained great interest in the field of theranostics[65]. For diagnostic purposes Nbs coupled with short-lived nuclides (^{68}Ga, ^{18}F, ^{64}Cu, ^{99m}Tc) were developed as advanced tracer molecules for positron emission tomography (PET) or single photon emission computed tomography (SPECT) (**Figure 2**). Due to the fast renal excretion, Nbs are rapidly eliminated whereby a beneficial signal-to-noise ratio is achieved[66; 67]. Moreover, only minimal doses must be applied, resulting in low radiation burden for patients. In comparison to currently used Abs and small molecules, Nbs exhibit superior properties for diagnostic imaging and several candidates already entered early clinical testing including the Her2-Nb in breast cancer patients (NCT03924466), the MMR-Nb to trace pro-tumorigenic macrophages

(NCT04168528) and the PD-L1-Nb to recognize solid tumors (NCT05156515)[68; 69]. The showcase example for Nbs as therapeutics is Caplacizumab (ALX-0081), which is the first therapeutic Nb approved in the U.S. and Europe in 2019 for treatment of acquired thrombotic thrombocytopenic purpura. The humanized bivalent Nb targeting the A1 domain of von Willebrand factor prevents the interaction with the platelet glycoprotein Ib-IX-V receptor and thus the development of microvascular thrombosis (**Figure 2**)[70; 71]. Currently, the focus of clinical investigation of Nbs is the application of different formats such as bivalent monospecific, bivalent bispecific, bivalent bispecific albumin-conjugated, and trivalent bispecific Nbs e.g., to link tumor and immune cells[72]. In addition, Nbs can be applied as nanocarriers for the directed delivery of drugs or targeted application of gene therapy[73; 74]. Novel adoptive cell-based cancer immunotherapies using chimeric antigen receptor (CAR) T cells have been developed by engineering autologous T cells with single chain variable fragments (scFvs). Experimental studies showed that the correct assembly of scFvs remains challenging, so Nbs may be a superior choice as tumor recognition modules[75]. Preclinical proof of principle was achieved early and through continued development, the first clinical candidate using CD19/20 bispecific Nb-derived CAR T cells for B-cell lymphoma was launched in 2019 (**Figure 2**) (NCT03881761)[76 77]. Currently, Nbs are typically developed as either diagnostic tools or therapeutic agents, but Nbs also hold promising potential for combined application as true theranostics. To date, a variety of Nbs (Her2, EGFR, M-protein, CD20, CD38, MHC II) have been used for non-invasive diagnostic imaging such SPECT, PET and optical imaging, and for therapeutic applications such as tumor targeted therapy, cytolytic cell therapy and CAR T-cell therapy, providing initial evidence for the successful application of Nbs as theranostics[65].

The diverse applications underline the great potential of Nbs, which outperform conventional Abs in numerous research, diagnostic and therapeutic areas due to their inherent properties. The increasing number of listed clinical trials in the diagnostic and therapeutic field points to a promising future for versatile applications of Nbs.

1.2. SARS-CoV-2 and COVID-19

1.2.1. Emergence & characteristics

Severe Acute Respiratory Syndrome Coronavirus 2 (SARS-CoV-2), a highly transmissible novel virus in the *Coronaviridae* family, emerged in late 2019 and has triggered a pandemic of acute respiratory disease, known as COVID-19[78]. With the origin in Wuhan, China; SARS-CoV-2 emerged as major global public health concern with around 7 million COVID-19-related deaths in June 2023[79]. The enveloped single-stranded RNA virus with a

genome of 29.8 kb and a virion size of 50 to 140 nm belongs to one of the largest RNA viruses[78; 80].

The genome of SARS-CoV-2 encodes for functional and non-functional open reading frames (ORFs) resulting in six structural proteins: RNA-dependent RNA polymerase (ORF1a/ORF1b), spike (S), envelope (E), membrane (M) and nucleocapsid (N) (**Figure 3A**)[81]. The S, a transmembrane glycoprotein, forms a homotrimer on the virion surface. Each of the three domains consists of two subdomains S1 and S2, from which the S1 subunit contains a region with 223 amino acids called the receptor-binding domain (RBD) (**Figure 3B**)[82]. Via the RBD, SARS-CoV-2 mediates cellular entry into epithelial cells in the respiratory tract by interaction with the angiotensin-converting enzyme (ACE) 2. Upon binding the fusogen activity of the S protein is triggered by the transmembrane protease serine 2 (TMPRSS2) located on the host cell surface. Once the virus has entered the target cell, RNA-dependent RNA polymerase coordinates with other viral and host factors to produce both viral mRNAs and new genomes. Translation by the host cell's translational machinery follows, ultimately resulting in the assembly and exocytosis of new virions[83; 84].

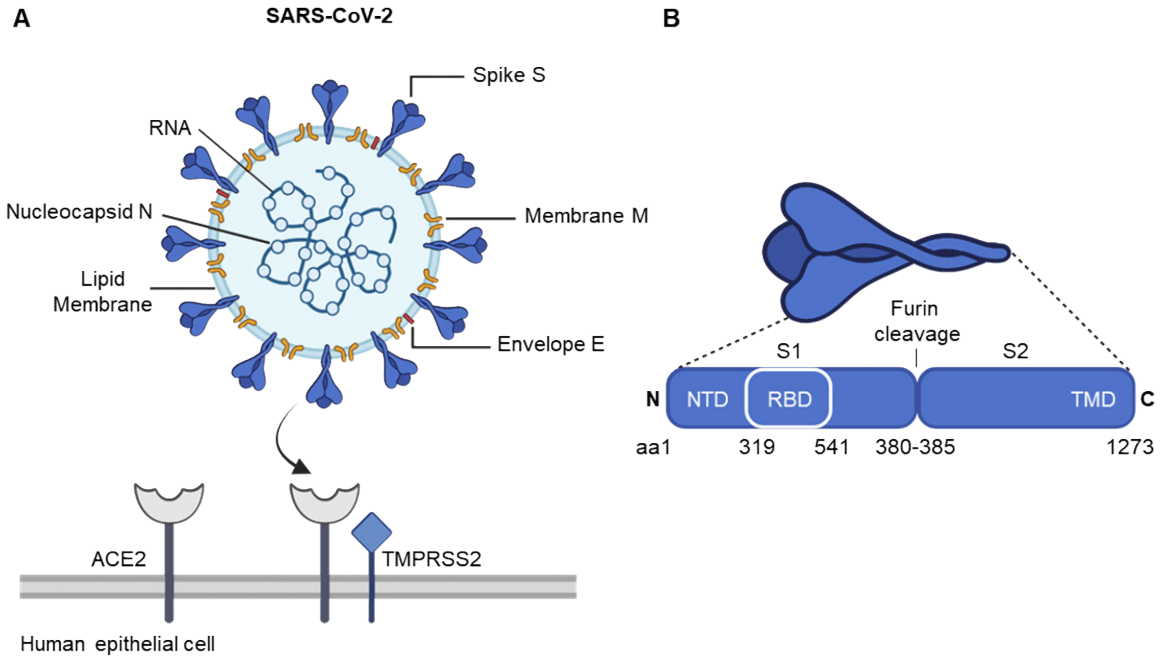

Figure 3: Schematic structure of SARS-CoV-2.
A) SARS-CoV-2 is an enveloped RNA virus with four structural proteins including Spike (S), envelope (E), membrane (M) and nucleocapsid (N). SARS-CoV-2 mediates entry into human epithelial cells by interaction of the S protein and ACE2, followed by the activation of TMPRSS2 for membrane fusion. **B)** SARS-CoV-2 S is a homotrimer, with each domain consisting of two subdomains S1 and S2. The receptor-binding domain (RBD) is part of S1 and mediates interaction with ACE2 (N-terminal domain, NTD; transmembrane domain, TMD).

Rapid replication of SARS-CoV-2 in lung tissue triggers a strong immune response. Whereas the majority of infections are asymptomatic or cause only mild symptoms, severe pathogenesis with cytokine storm followed by acute respiratory distress syndrome and respiratory failure is the main cause of death, observed mainly in patients over 60 years of age with severe preexisting conditions, accounting for ~1% of all confirmed cases[85; 86]. Long-term effects, including impairment of physical, mental, and psychological health that persist months after SARS-CoV-2 infection, also known as long COVID, are observed with a variable prevalence of 5-20% even after asymptomatic infection[87; 88].

Since late 2020, the first mutations of SARS-CoV-2 impacting transmissibility and antigenicity were described. Due to the reason, that 90% of the plasma or serum Abs with neutralizing activity target the RBD and thereby inhibit viral entry, increased selective pressure caused a multitude of immune escape mutations within this protein domain[89; 90]. To prioritize global monitoring and research, the World Health Organization (WHO) has defined variants of concern (VOCs) and interest (VOIs) that pose an increased risk to global public health. Previously circulating VOCs include Alpha, Beta, Gamma and Delta. By the end of 2022, Omicron with a double-digit number of mutations within the RBD is the only circulating VOC, which was rapidly splintered into several sublines[91-93].

1.2.2. Diagnostic detection methods

Early diagnosis of COVID-19 was crucial to avoid uncontrollable viral spread. As a gold standard, detection of SARS-CoV-2 nucleic acid by reverse transcription-polymerase chain reaction (RT-PCR) was performed using primer pairs targeting ORF1b, N, E, or S genes with a detection limit of 100 copies/mL or less (**Figure 4**)[94; 95]. Detection of viral antigens represents an alternative and especially point-of-care lateral flow immunoassays (LFIA), which combine several advantages such as low cost, easy end-user handling and rapid test result, have reached wide application, however lacking sensitivity compared to the gold standard method using RT-PCR (**Figure 4**)[96]. Lung tissue damage concomitant with acute COVID-19 infection, enables diagnostic detection using clinical imaging techniques, however due to comparatively low sensitivity and specificity and increased costs, broad applicability was never reached (**Figure 4**)[97-101].

In contrast to the detection of viral parts, diagnostic approaches detecting SARS-CoV-2-specific Abs provide information about developed immunity upon infection or vaccination (**Figure 4**). Serological tests including ELISA (enzyme-linked immunosorbent assay), CLIA (chemiluminescence immunoassay), LFIA and bead-based multiplex immunoassays are valid methodologies to investigate seroprevalence within the population and monitor

vaccination trials[102; 103]. Depending on the applied method, Ab type, amount and specificity can be determined, and a multitude of commercially available immunoassay tests were government-approved[100]. However, most of these assays measure total Ab response against SARS-CoV-2 without distinguishing between neutralizing and non-neutralizing Abs[100; 101; 104-106]. The gold standard method to determine neutralizing capacity of serum samples is the virus neutralization test (VNT), in which serum and virus are inoculated into cell culture and incubated for a certain time frame. In case neutralizing antibodies (NAbs) are present virus replication will be inhibited. However, besides requiring biosafety level 3 (BSL3) facilities, several days are needed until test results are available[107-110]. In the course of the pandemic, a variety of specialized biochemical assays to detect NAbs were developed, which are majorly based on ACE2-mediated blockage of the RBD/ACE2 interaction[111-115].

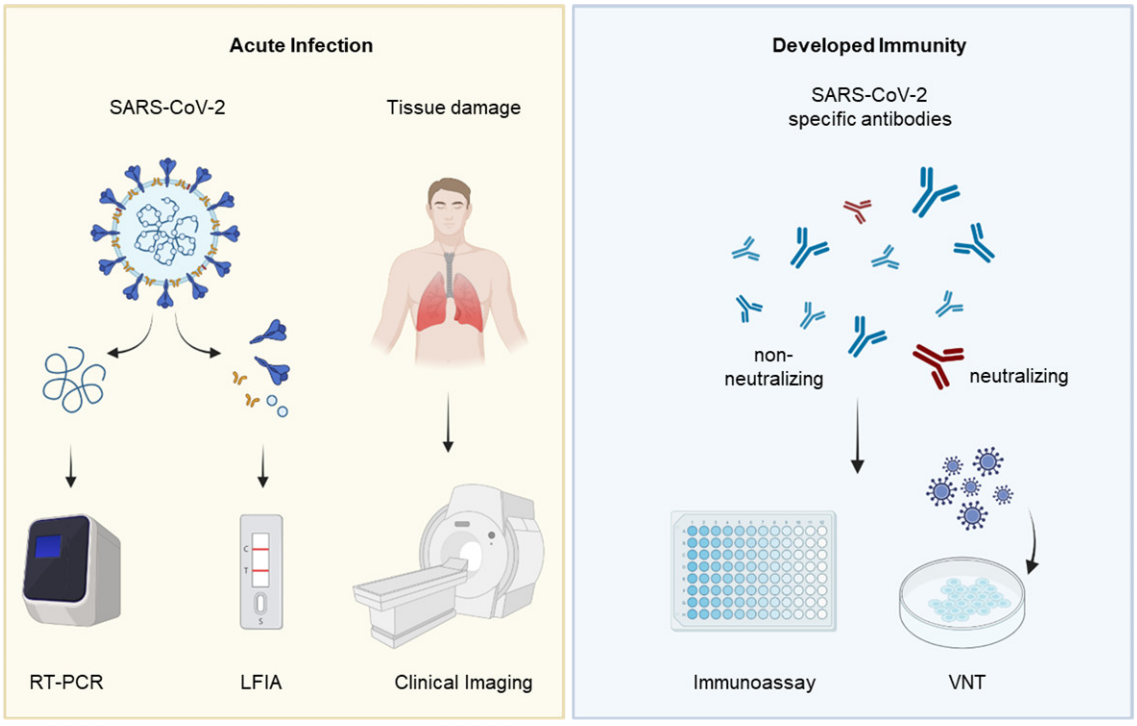

Figure 4: Diagnostic methods to determine acute SARS-CoV-2 infection and developed immunity.
Detection of viral constituents including RNA and protein using RT-PCR or LFIA respectively are standard diagnostic methods to determine acute infection of SARS-CoV-2. Lung tissue damage caused by acute SARS-CoV-2 infection can be determined by clinical imaging. Developed immunity following infection or vaccination can be detected by serological immunoassays. To determine neutralizing activity standardly the VNT is applied.

1.2.3. Vaccines & therapeutics

With the start of the COVID-19 pandemic also the race for efficient vaccines and therapeutics took its course. Currently 11 vaccines are granted emergency use listing by WHO and more than 350 are currently in preclinical or clinical development (*COVID19 vaccine tracker*). Four vaccine platforms of approved vaccines can be distinguished: messenger RNA (mRNA) vaccines (Comirnaty *Pfizer-BioNTech*, Spikevax *Moderna*), inactivated virus vaccines (Covaxin *Bharat Biotech*, Covilo *Sinopharm*, CoronaVac *Sinovac*), non-replicating vector-based vaccines (Vaxzevria *AstraZeneca,* Jcovden *Janssen*, Covishield *Serum Institute of India*, Convidecia *CanSino*), and protein subunit vaccines (Nuvaxovid *Novavax*, Covovax *Serum Institute of India*). To date close to 70% of the global population received at least one dose of a COVID-19 vaccine[116]. Due to rapid acquisition of mutations and the concomitant breakthrough infection, Omicron-adapted mRNA vaccines are available. Overall vaccines induce high short-term NAb responses, which however wane after several months[117-119]. In parallel also cellular immune responses with greater durability are induced, including persisting germinal center B-cells and $CD8^+$ T cell responses, providing protection against severe disease[120-122].

In contrast to the preventive strategies pursued with vaccination campaigns, COVID-19 therapies to treat acute infections are relevant for those who are awaiting vaccination or who do not respond robustly to vaccination. The COVID-19 therapeutic landscape can be divided into different classes applicable for different disease stages.

For small molecule inhibitors two main approaches can be distinguished: direct acting antivirals (DAA) targeting viral components and host-targeting agents (HTA) inhibiting host elements to prevent viral replication and spread[123]. Remdesivir, originally developed against hepatitis C inhibiting the viral RNA polymerase, Nirmatrelvir/Ritonavir a co-medication of 3CL protease and CYP3A inhibitor and Molnupiravir a prodrug inhibiting the viral replication are available DAAs for COVID-19 treatment[124-126]. However, the clinical utility of DAAs is controversial in practice because of the small window of application of <5-7 days after symptom onset[123; 127]. HTA, as broad-spectrum therapeutics, are generally more robust against escape variants, but safety concerns due to their mechanism of action inhibiting host proteins limit their development[128; 129].

Alternatives to antiviral small molecule therapies are SARS-CoV-2-targeting neutralizing monoclonal antibodies (mAbs). Several candidates including bamlanivimab-etesevimab, casirivimab-imdevimab, tixagevimab-cilgavimab, sotrovimab and bebtelovimab achieved FDA emergency use authorization for mild-to-moderate COVID-19[130-135]. All approved mAbs target epitopes on S to block virus entry. However, the increasing prevalence of

Omicron subvariants accompanied by treatment failure resulted in revoke of recommendation for all candidates[135]. Despite the high efficacy of mAbs before the onset of the Omicron variants in high-risk patients in preventing progression of serious disease, high cost, limited availability, and logistical problems limited their wide applicability[123].

1.3. SIRPα as promising target on tumor-associated macrophages

1.3.1. Role of tumor-associated macrophages in the tumor microenvironment

Increasing evidence suggests that the tumor microenvironment (TME), providing an essential pro-tumorigenic milieu for cancer cells, plays a critical role for maximizing anti-cancer treatment response in solid tumors[136; 137]. The TME including blood vessels, immune cells, stromal cells, fibroblasts, adipocytes, soluble signaling molecules and extracellular matrix, orchestrates angiogenesis, proliferation, invasion and metastasis[138; 139]. Within the TME myeloid cells are the most frequent cell type[140] and are comprised of tumor-associated macrophages (TAM), dendritic cells, myeloid-derived suppressor cells and neutrophils. Especially, TAMs are highly abundant and form between 30-50% of the tumor mass[141]. In the context of cancer a dual nature of TAMs with partially opposite effects for cancer progression can be observed[142; 143] and historically two main directions of polarization, including M1-and M2-like TAMs, were distinguished within this highly heterogenous cell population[144]. The pro-inflammatory M1 type is activated by interferon-γ, toll like receptors (TLRs), lipopolysaccharide and granulocyte macrophage colony stimulating factor and expresses molecules including nitric oxide synthase and IL-12. M1-TAMs not only engulf and kill target cells, but also enhance the T helper 1 response and secrete proinflammatory cytokines such as TNF-α, IL-1, IL-6, IL-12, and IL-23[145-147]. M2-TAMs expressing IL-10, IL-1β, VEGF and matrix metalloprotein are known as alternative macrophages and are activated by IL-4 and IL-13. By strengthening the T helper 2 response, promoting angiogenesis, rebuilding tissue, and repairing injury, M2-TAMs are known as anti-inflammatory macrophages that secrete IL-10 and TGF-β[145; 148]. Overall, macrophages are highly plastic cells that undergo constant state transitions, which also result in mixed phenotypes. Therefore, the classical M1/M2 differentiation represents an oversimplification of reality[149; 150].

In most established solid tumors, a pro-tumor function of TAMs predominates, driving tumor progression[149]. During carcinogenesis, TAMs release nitric oxide and reactive oxygen intermediates that lead to genetic instability. Moreover, the production of various growth factors leads to proliferation of cancer stem cells[151; 152]. In advanced tumor stages, TAMs are the main drivers of angiogenesis and metastatic spread by producing pro-

angiogenic factors and remodeling the extracellular matrix[153; 154]. Through increased expression of immune checkpoint molecules and secretion of anti-inflammatory cytokines, TAMs additionally induce an immunosuppressive milieu within the TME[149; 155; 156]. For these reasons, poor clinical prognosis e.g. in breast, ovarian and prostate cancer correlates with high TAM infiltration in the TME[157-159].

In contrast, TAMs can also exert potent antitumor activity through macrophage-mediated killing of cancer cells, Ab-dependent cellular cytotoxicity, and activation of innate and adaptive immune responses[156; 160]. Several conventional antitumor therapies, e.g. the chemotherapeutic drug doxorubicin, are highly dependent on the phagocytic activity of TAMs to eliminate cancer cells[161]. Similarly, the efficacy of classical immune checkpoint blockade, which elicits T cell-mediated immune responses, depends on the immunosuppressive circuits of the myeloid cell population through the expression of checkpoint ligands such as PD-L1/2 and B7-1/2[149]. Targeted recruitment, activation, and reprogramming to anti-tumor TAMs can occur via cytokines, TLRs, stimulator of interferon genes agonists, mAbs, and microRNAs[149; 162-164]. Novel antitumor strategies are built on CAR macrophages equipped with tumor antigen receptors. Macrophage-based cell therapy is highly interesting due to their specific recognition of tumor cells, their persistent proinflammatory M1 phenotype, and their ability to invade the tumor and therefore may overcome current limitations for CAR T cells especially for solid tumors[165; 166]. In addition, several myeloid checkpoints, including sialic acid-binding immunoglobulin-like lectin, leukocyte immunoglobulin-like receptor B, and signal-regulating protein α (SIRPα), were found to negatively regulate macrophage effector function[167-169]. In particular, the SIRPα/CD47 axis was identified as a promising target for future myeloid-specific checkpoint inhibition to induce macrophage-mediated anti-cancer activity[169; 170].

1.3.2. The SIRPα/CD47 axis

SIRPα, also known as CD172a or SHPS-1, is an innate immune checkpoint inhibitor predominantly expressed on myeloid cells like monocytes, macrophages, dendritic cells and neutrophils as well as neurons and stem cells[171-173]. Structurally SIRPα consists of three Ig-like domains, a transmembrane domain and a cytoplasmic domain containing two immunoreceptor tyrosine-based inhibitory motifs (ITIMs) with four tyrosine residues that are potential sites for phosphorylation[171]. This surface receptor belongs to the SIRP paired receptor family, which consists of the inhibitory receptor SIRPα, an activating receptor SIRPβ1 (CD172b), a non-signaling receptor SIRPγ (CD172g), and SIRPδ and SIRPβ2, whose functions have not yet been characterized[174; 175]. There is also the presence of two

isoforms of SIRPα with SIRPαV1 and SIRPαV2 described that are homozygously (v1/v1 or v2/v2) or heterozygously (v1/v2) distributed in the human population[176].

The ligand for SIRPα and SIRPγ is CD47. CD47 is ubiquitously expressed on most cell types and mediates a "don't eat me" signal to inhibit phagocytosis and prevent subsequent autoimmune responses (**Figure 5**)[177; 178]. The SIRPα/CD47 axis is primarily responsible for myeloid cell-mediated clearance of altered cells, erythrocytes, hematopoietic stem cells, and neuronal synapses. This homeostatic regulatory process was first discovered in an *in vivo* experiment demonstrating the rapid elimination of erythrocytes lacking CD47 by splenic macrophages[179]. CD47 is a highly glycosylated protein and is predicted to have five transmembrane regions with one single Ig-like domain, which interacts with the N-terminal domain (domain 1, SIRPαD1) of SIRPα[180; 181]. For the low affinity interaction of human SIRPα and CD47 a K_D of 2 µM was determined and a distance of 14 nm between both opposing cells was estimated, which is in line to distances found in immunological synapses (**Figure 5**)[181; 182].

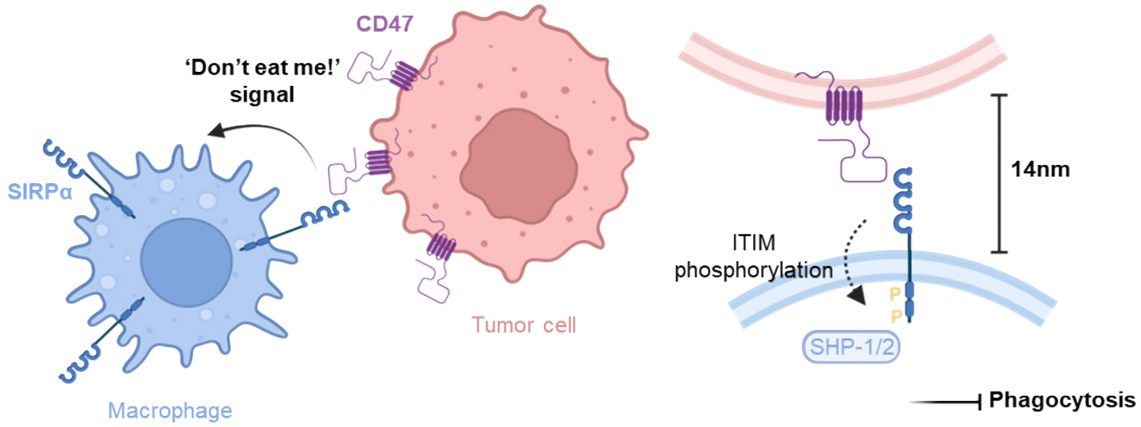

Figure 5: SIRPα/CD47 interaction causes the repression of macrophage-mediated phagocytosis.
SIRPα contains three extracellular domains, one transmembrane region, and an intracellular domain with ITIM motifs. Interaction of CD47 and SIRPα mediates a "don't eat me" signal by causing ITIM phosphorylation and recruitment of phosphatases including SHP-1 and SHP-2. Eventually, SIRPα/CD47 binding inhibits phagocytosis of host cells or CD47-expressing tumor cells.

Interaction of SIRPα and CD47 promotes cytosolic ITIM phosphorylation of SIRPα, most likely through the activity of Src family kinases[171; 183]. After phosphorylation, the cytosolic tyrosine phosphatases SHP-1 or SHP-2 are recruited and initiate dephosphorylation of a variety of downstream substrates in an inhibitory manner[184]. As a downstream

consequence, SIRPα activity in the phagocytic synapse is inhibited e.g. by deactivation of the motor protein myosin IIA[185].

Exploiting this physiological checkpoint mechanisms, tumor cells upregulate CD47 and thereby escape macrophage recognition and programmed cell removal[186-188]. Based on its importance for cancer immune evasion, the SIRPα/CD47 axis constitutes a promising theranostic target.

1.3.3. Theranostic approaches targeting the SIRPα/CD47 axis

The prognostic significance and clinical relevance of the two cellular surface markers SIRPα and CD47 in human malignancies are under intense investigation[187; 189-195]. CD47 overexpression was observed in various hematological and solid cancer types including non-Hodgkin lymphoma, acute myeloid leukemia, glioblastoma, ovarian, breast, colon, bladder, hepatocellular, and prostate cancer[187; 189; 190]. Therefore, CD47 is a widely recognized tumor immune evasion marker, and its upregulation correlates with shorter overall survival[196]. In contrast, data characterizing SIRPα expression of monocytes and macrophages in the context of malignancies are fragmentary, which is likely due to the low numbers and diverse phenotypes of TAMs within tumor tissue samples[195]. However, strong expression levels of SIRPα were found to be associated with inferior survival in follicular lymphoma, colorectal cancer, intrahepatic cholangiocarcinoma and esophageal carcinoma[192-195]. Therefore, the SIRPα/CD47 axis appears to be a promising target for diagnostic and therapeutic applications.

The therapeutic potential of the SIRPα/CD47 axis has been extensively explored, and currently three different strategies are available for therapeutic manipulation: i) blocking CD47 on target cells, ii) blocking SIRPα on myeloid cells, or iii) inhibiting the glutaminyl peptide cyclotransferase-like protein (QPCTL) required for CD47 maturation (**Figure 6**)[190]. For the first class, treatment with CD47-specific Abs and Nbs blocking the SIRPα/CD47 interaction, as well as SIRPα-Fc fusions, have been shown to result in increased levels of phagocytosis, inhibition of cancer transplantation, and elimination of pre-existing leukemia *in vivo*[187; 189; 197-200]. However, due to the endogenous expression of CD47 on non-malignant cells, a considerable off-tumor antigen sink limits the efficacy of CD47-targeting therapies, while hematological toxicities such as anemia and thrombocytopenia have been observed by the depletion of erythrocytes and platelets upon CD47-binding molecules retaining FcR binding[201; 202]. Furthermore, the requirement of large initiation doses and/or manifold administrations limit clinical translatability. Nevertheless, several CD47-targeting agents including the anti-CD47 Ab magrolimab (Hu5F9-G4) and SIRPα fusion protein

ALX148 are currently tested in various clinical trials in combination with a diverse set of tumor-targeting agents[170; 203-205].

SIRPα is only expressed on a limited number of cell types and therefore SIRPα-blocking agents including SIRPα-specific Abs and high affinity CD47 variants are considered to have an improved efficacy. Especially in combination with tumor-opsonizing Abs *in vivo* data showed a strong synergistic anti-tumor effect[176; 206-208]. To date two anti-SIRPα mAbs, BI765063 and GS-0189 (FIS-189), have entered clinical testing for mono- and combination treatment regimens[201]. Additionally, several bispecific Abs targeting CD47 or SIRPα in addition to tumor antigens e.g. CD19, CD20 and PD-1 or molecules expressed by T cells like CD40L are also in clinical testing (NCT04886271, NCT04406623).

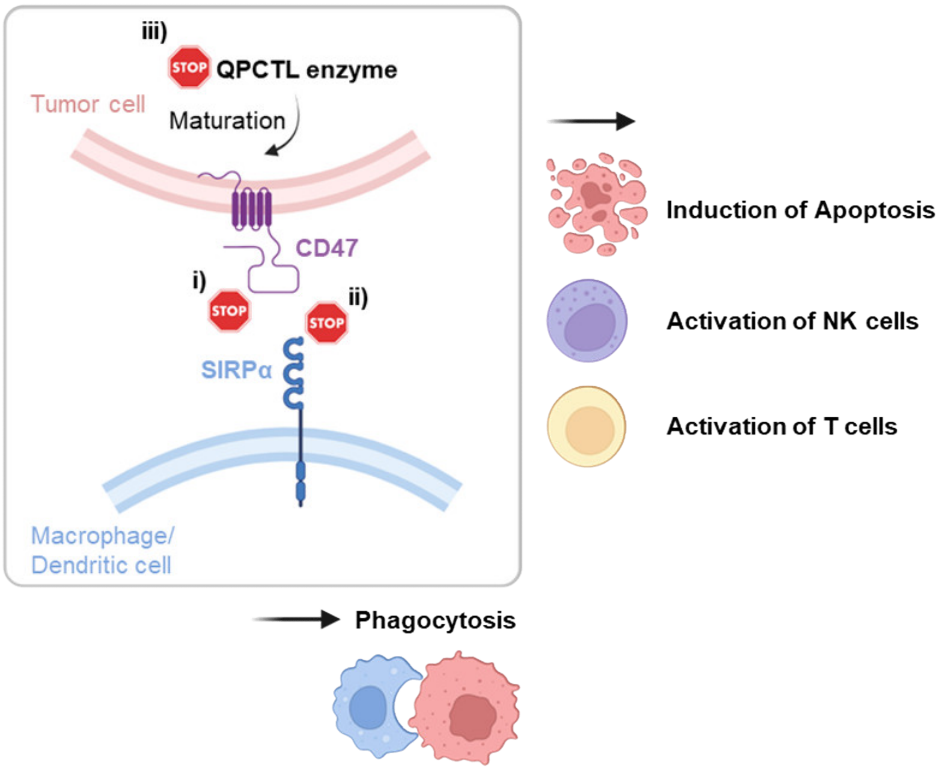

Figure 6: Different therapeutic strategies for manipulation of the SIRPα/CD47 axis.
i) Blocking CD47 on target cells, ii) blocking SIRPα on myeloid cells, or iii) inhibiting the QPCTL required for CD47 maturation are currently available possibilities to target the SIRPα/CD47 pathway. Besides induction of phagocytic activity of macrophages and dendritic cells, initiation of apoptosis of tumor cells and activation of NK and $CD4^+/CD8^+$ T cells were observed as consequence of SIRPα/CD47 targeting.

In contrast to CD47 or SIRPα blocking agents, which require the application of biologicals, inhibition of the QPCTL enzyme can be achieved by small molecule inhibitors. Experimental data suggest that QPCTL deficiency, which prevents the formation of

pyroglutamate residues at the NH_2 terminus of CD47, places the TME in a pro-inflammatory state. However, clinical transition of a lead candidate has not yet been successful[209].

Besides the activation of phagocytosis of macrophages, further mechanism involving innate and adaptive immune responses were elucidated how therapeutic targeting of the SIRPα/CD47 axis are causing the elimination of tumor cells[210]. For example, increased phagocytic activity of dendritic cells and subsequent activation of $CD4^+$ and $CD8^+$ T cells were observed using anti-CD47 Abs[211]. In addition, anti-CD47 Abs can cause enhancement of natural killer (NK) cell-mediated cytotoxicity and apoptosis of tumor cells through a caspase-independent mechanism (**Figure 6**)[210-212].

CHAPTER 2

OBJECTIVE OF THE THESIS

2. Objective of the Thesis

Due to their small size, high target specificity and flexible modifiability, Nbs hold great potential for theranostic applications. This thesis aims to investigate the theranostic potential of Nbs based on two diverse application areas (viral and immune cell targets) and to develop novel diagnostic and therapeutic agents for future clinical translation.

With the outbreak of the COVID-19 pandemic in March 2020, rapid and widely available high-throughput diagnostic methods to estimate the extent of endemic infection in the population on the one hand, and effective therapeutics to bridge the time until effective vaccines are available and severe disease symptoms can be alleviated on the other hand, were urgently needed. Therefore, in a first step we developed Nbs against RBD with neutralizing activity. To overcome the limitations of available SARS-CoV-2 serological tests, we assessed the applicability of RBD-specific biparatopic (bip) Nbs as Ab surrogate in a competitive high-throughput multiplex binding assay to measure NAbs in serum samples. In addition to investigate the therapeutic potential of selected RBD-specific bipNbs, we evaluated their protective activity against immune-evading VOCs in a murine disease model.

For a second example to demonstrate the applicability of Nbs as theranostics, we focused on immune cell targets. Cancer immunotherapies have significantly improved therapeutic options, however varying response rates remain unsatisfactory. Thus, new diagnostic and therapeutic approaches are needed to increase treatment success. Due to its importance as an innate immune checkpoint and its predominant expression on TAMs, SIRPα represents a promising theranostic target. Thus, we developed hSIRPα-specific Nbs by applying a binary selection strategy. We identified hSIRPα/CD47-blocking Nbs and assessed their applicability as novel immunotherapeutics *in vitro*. Additionally, we selected inert Nbs and evaluated their use as PET tracers for patient stratification and therapy monitoring *in vivo*.

CHAPTER 3

RESULTS & DISCUSSION I

NANOBODIES AGAINST SARS-COV-2

3. Results & Discussion I: Nanobodies against SARS-CoV-2

The content of this chapter is based on:

Wagner TR§, Ostertag E§, Kaiser PD, Gramlich M, Ruetalo N, Junker D, Haering J, Traenkle B, Becker M, Dulovic A, Schweizer H, Nueske S, Scholz A, Zeck A, Schenke-Layland K, Nelde A, Strengert M, Walz JS, Zocher G, Stehle T, Schindler M, Schneiderhan-Marra N, Rothbauer U (2021) **NeutrobodyPlex-monitoring SARS-CoV-2 neutralizing immune responses using nanobodies**. EMBO Rep 22: e52325.

Wagner TR§, Schnepf D§, Beer J§, Ruetalo N§, Klingel K, Kaiser PD, Junker D, Sauter M, Traenkle B, Frecot DI, Becker M, Schneiderhan-Marra N, Ohnemus A, Schwemmle M, Schindler M, Rothbauer U (2022) **Biparatopic nanobodies protect mice from lethal challenge with SARS-CoV-2 variants of concern**. EMBO Rep 23: e53865.

3.1. Generation and characterization of RBD-specific nanobodies

At the start of the study in early 2020, neither prophylactic vaccines protecting against SARS-CoV-2 nor effective therapeutics for infected high-risk patients were available. NAbs offer great potential as immediate antiviral agents, but shortcomings such as high production costs, limited long-term stability, high efforts to produce multi-specific molecules, and the risk of causing Ab-dependent enhancement of infection limit their widespread use[213; 214]. Therefore Nbs, providing favorable biochemical characteristics, appeared to be a promising alternative to conventional Abs for various applications related to the emerging SARS-CoV-2 pandemic[215].

For the generation of Nbs an alpaca (*Vicugna pacos*) was immunized with the recombinant RBD-derived from SARS-CoV-2 B.1 ($RBD_{B.1}$) (**Figure 7A**), followed by the generation of a Nb phagemid library with a size of ~4 × 10^7 clones. After two consecutive rounds of phage display on RBD, we achieved a positive selection rate of ~66% with 325 positive binders from 492 individually analyzed clones. Finally, 11 unique Nb sequences were identified and purified (**Figure 7B & C**). Affinity measurements revealed 10 high-affinity binders with K_D values ranging from ~1.4 to ~53 nM (Wagner & Ostertag et al., **Appendix I**, Figure 2A-C, Figure S1).

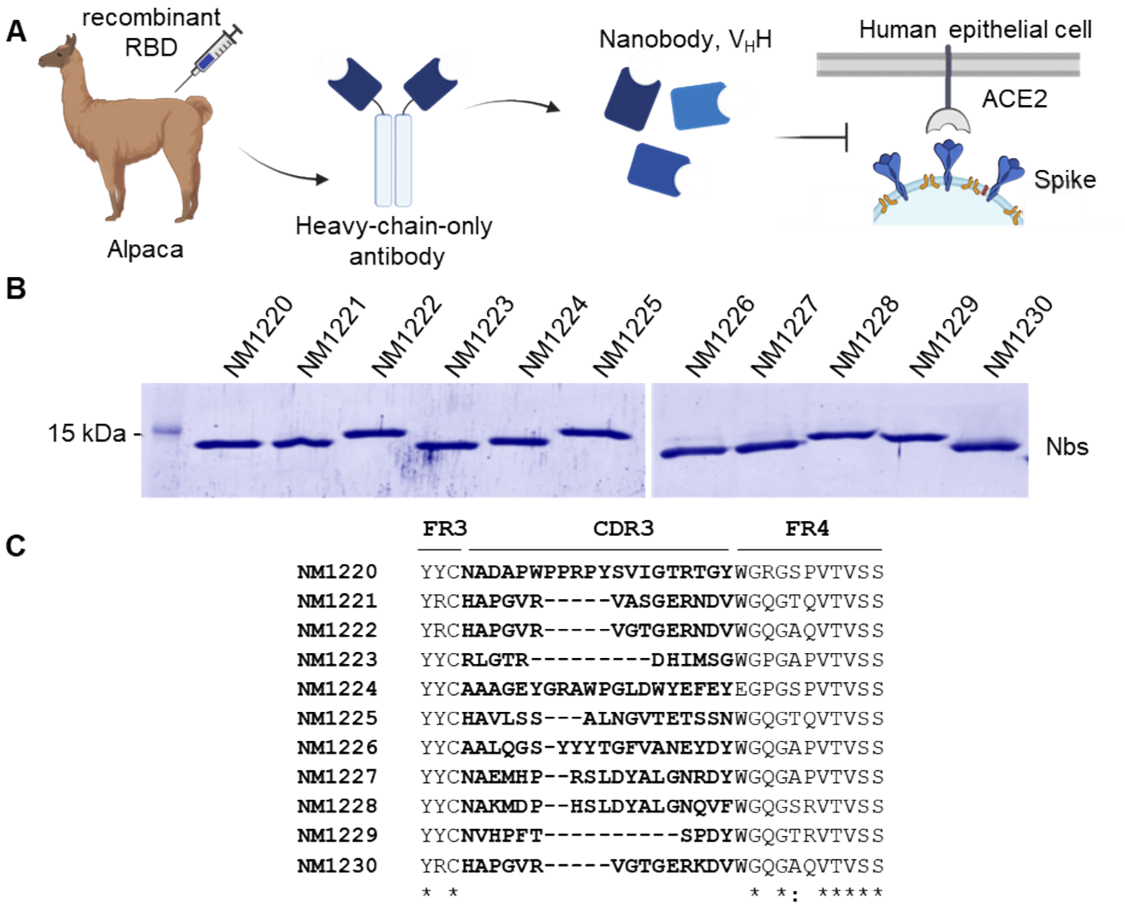

Figure 7: Generation of Nbs targeting the SARS-CoV-2 RBD/ACE2 interface.
A) RBD-specific Nbs were identified from a Nb phage library upon immunization of an alpaca with recombinant RBD. **B)** 11 Nbs were produced by recombinant expression and **C)** revealing highly heterogenous CDR3s.

For targeted selection of Nbs blocking the interaction between RBD and human ACE2, we first performed a biochemical multiplex ACE2 competition assay on paramagnetic beads coupled with SARS-CoV-2 antigens (RBD, S1, S)[101] and determined IC_{50} values reflecting neutralization potential of tested Nbs. Notably, 8 out of 10 tested candidates were inhibiting ACE2 binding to all tested SARS-CoV-2 antigens (Wagner & Ostertag et al., **Appendix I**, Figure EV1).

To confirm neutralization potency, we performed a VNT, using serial dilutions of NM1223, NM1224, NM1226, NM1228, NM1230. In line with the data obtained from the multiplex ACE2 competition assay, NM1223 was found to be non-neutralizing, whereas NM1226 and NM1228 revealed strongest neutralization with IC_{50} values of ~15 and ~7 nM, respectively, followed by NM1230 (~37 nM) and NM1224 (~256 nM) (Wagner & Ostertag et al., **Appendix I**, Figure S2).

As the observed neutralization effects are mediated either by direct blockade of RBD residues essential for ACE2 binding or by steric hindrance of the RBD/ACE2 interaction, we next performed epitope binning to group the Nbs according to their relative positions to each other. In total, five different Nb-Sets were identified, revealing high epitope diversity of selected candidates (Wagner & Ostertag et al., **Appendix I**, Figure S3). Analysis showed that despite their highly diverse CDR3 regions, both Nbs NM1226 and NM1228 with the strongest neutralization potency share binding epitopes on RBD (**Figure 8A**). In contrast, NM1230 was assigned to a different Nb-Set with NM1221 and NM1222 (Nb-Set 2). The neutralizing Nb NM1224 (Nb-Set 4) as well as the non-neutralizing Nbs NM1223 (Nb-Set 3) and NM1220 (Nb-Set 5) each bound a separate epitope class.

While epitope binning only provides information on relative binding behavior, we additionally performed hydrogen deuterium exchange mass spectrometry (HDX-MS) to identify detailed RBD epitopes that are protected upon Nb binding. HDX protection of NM1226 was highest between aa (amino acid) $N_{RBD}370$–$L_{RBD}387$, which are not part of the RBD/ACE2 interface (Wagner & Ostertag et al., **Appendix I**, Figure EV2A and B). In contrast, NM1228 binding an overlapping epitope as NM1226, displayed additional protection of $Y_{RBD}489$-$S_{RBD}514$ involved in ACE2 interaction (**Figure 8B**) (Wagner & Ostertag et al., **Appendix I**, Figure EV2C). Set-2 Nbs including NM1230, bound to the top of the RBD and thereby covering multiple residues directly involved in ACE2 binding ($G_{RBD}446$, $Y_{RBD}449$, $N_{RBD}487$-$G_{RBD}496$) (Wagner & Ostertag et al., **Appendix I**, Figure EV2D, E, F). As proposed by epitope binning results NM1224 (Nb-Set4) and the non-inhibitory NM1223 showed interaction sites distinct from all other Nbs, whereas the latter one contacted majorly residues at the front/lower left with large spatial distance to the RBD/ACE2 interaction site (Wagner & Ostertag et al., **Appendix I**, Figure EV2G and H).

These analyses indicated that we discovered both directly and indirectly neutralizing Nbs. For a more detailed understanding of their neutralization mechanism, we elucidated the binding mode of NM1226 and NM1230 by crystal structure analysis. RBD:NM1226 complex structure was solved at a resolution of 2.3 Å and an interface of 698 $Å^2$ was determined (Wagner & Ostertag et al., **Appendix I**, Figure 3A and B, Table S2). Crystal structure analysis confirmed that the RBD regions (aa 369-384 and aa 504-508), which are not part of the ACE2 binding site, are involved in the interaction, where mainly residues of the CDR3 of NM1226 mediate RBD binding (**Figure 8B**). Furthermore, these structural data suggest that the neutralizing effect of NM1226 is mainly achieved by steric collision (Wagner & Ostertag et al., **Appendix I**, Figure EV3). For NM1230 a resolution of 2.9 Å in complex with RBD was determined. (Wagner & Ostertag et al., **Appendix I**, Figure 3A and B, Table S2). Data revealed that specific binding of NM1230 is accomplished by a

combination of residues from the CDR3 and framework regions, burying a surface area of ~830 Å^2 (**Figure 8B**) (Wagner & Ostertag et al., **Appendix I**, Figure 3A and C, Table S2). Interaction sites on RBD involved $Y_{RBD}351$ and the loop region ranging from aa 437–503, forming polar contacts, one salt bridge ($R_{NM1230}98$ to $E_{RBD}484$) and π-π stackings. Interestingly, the binding of NM1230 partially overlaps with the ACE2 interface but also impairment of ACE2 binding through steric collision on the neighboring RBD was observed, consequently NM1230 mediates simultaneous blocking of two RBDs of the trimeric S protein (Wagner & Ostertag et al., **Appendix I**, Figure EV3, Figure S5).

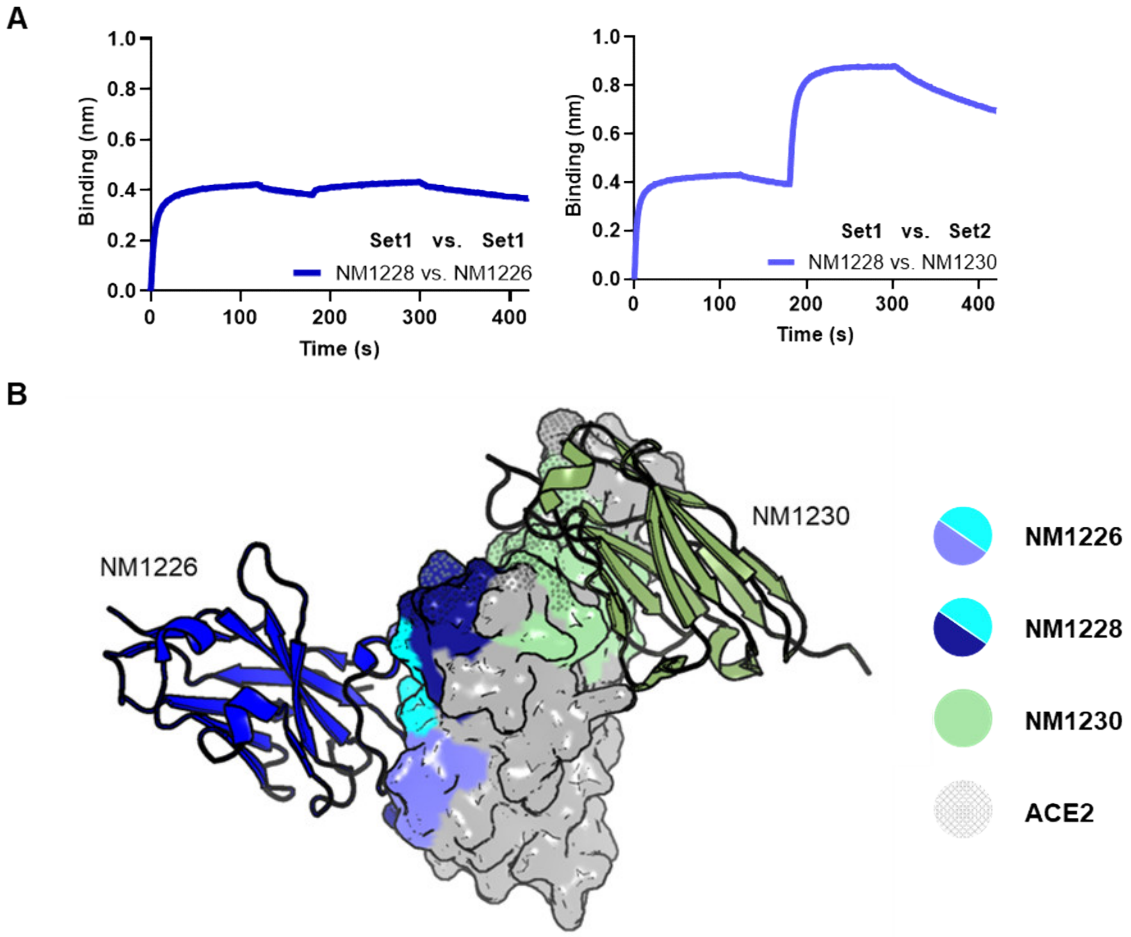

Figure 8: Epitope mapping of lead candidates NM1226, NM1228 and NM1230.
A) Representative BLI-based sensograms of NM1228 and NM1226 targeting an overlapping epitope and NM1228 and NM1230 targeting different epitopes on RBD. **B)** Summary of binding epitopes on RBD derived from crystal structure of RBD:Nb complexes NM1226 (blue, PDB 7NKT) and NM1230 (green, PDB 7B27) and derived from HDX-MS analysis for NM1228 (dark blue). Overlapping binding epitopes of NM1226 and NM1228 are illustrated in cyan and ACE2 interaction site on RBD is illustrated as dotted surface.

Previous to the COVID-19 pandemic, antiviral Nbs against human immunodeficiency virus-1 (HIV-1), influenza viruses, hepatitis C virus (HCV), respiratory syncytial virus (RSV) and enteric viruses were developed[216-220]. Even several SARS-CoV-1- or MERS-CoV-specific Nbs have been described with neutralizing effect[221; 222]. However, the start of the pandemic has boosted an ever-growing list of SARS-CoV-2 specific Nbs (reviewed in[223-225]). The high success rate in identifying RBD-specific Nbs is consistent with other studies, suggesting that SARS-CoV-2 derived proteins including the RBD are highly immunogenic antigens for generation of HCAbs in alpacas, llamas and camels[226-230]. In addition, several high-affinity RBD-specific Nbs were successfully selected from naïve or synthetic libraries[231-234].

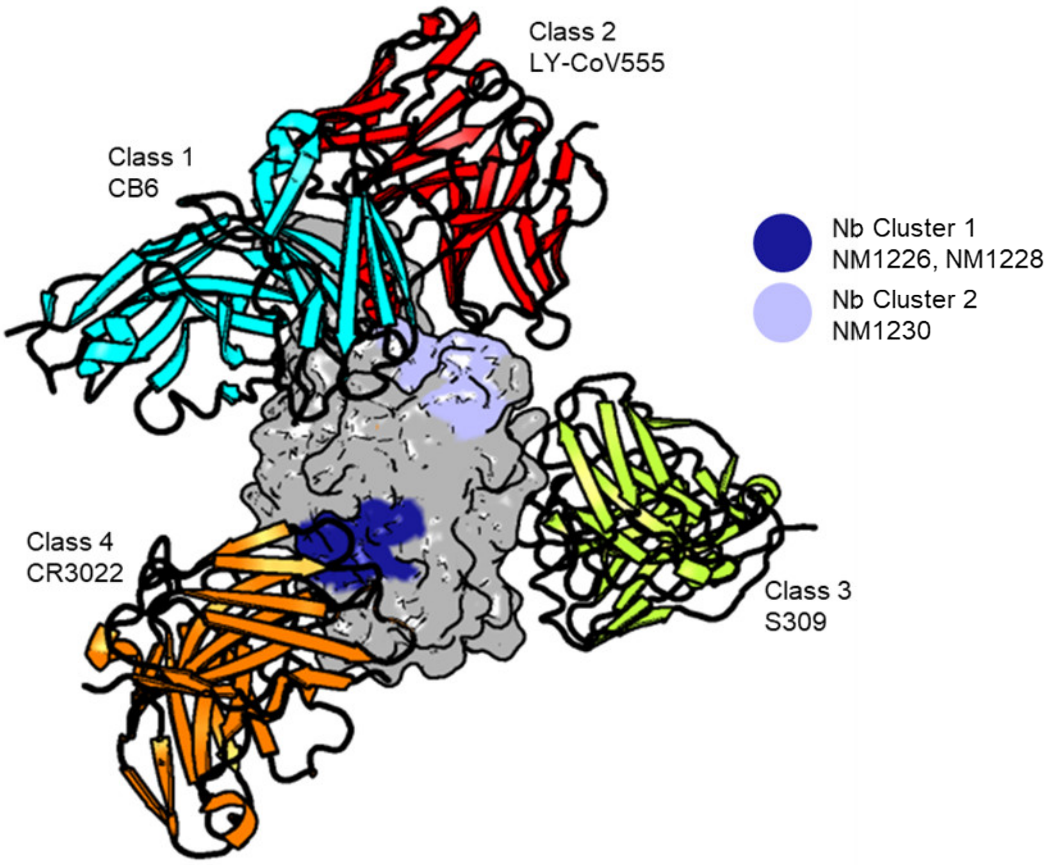

Figure 9: Comparison of classified binding epitopes on RBD of neutralizing Nbs and Abs. RBD-directed Nbs and NAbs are classified into different categories depending on which epitopes of RBD are recognized. Two clusters were identified for Nbs and six classes were defined for NAbs, of which the four main classes are illustrated. Core aa residues of Nb cluster 1 (dark blue) represented by NM1226 and NM1228 and cluster 2 (blue) represented by NM1230 on RBD are highlighted. For each main NAb class, a representative binder to RBD is shown: class 1, CB6; class 2, LY-CoV555; class 3, S309; class 4, CR3022.

According to binding affinity, we selected several Nb candidates with K_D values in the nanomolar range, which are in line with the high-affinity candidates identified in other

selection campaigns[223-225]. Remarkably, we identified highly diverse Nb sets with in total five distinct epitopes. Moreover, directly and indirectly neutralizing mechanisms were elucidated. Crystal structure analysis revealed that NM1226 targets a similar epitope as the first structurally characterized Nb V_HH72[215], the so-called cluster 1, which is conserved between SARS-CoV-1 and -2 (**Figure 9**). Further cluster 1 Nbs include C1, F2[235] or the synthetic Sb68[236]. NM1230 belongs to cluster 2 Nbs as well as H11-H4[232], C5[235] or Sb23[233]. In comparison, six different epitope classes have been identified for NAbs, while class 5 and 6 are only rarely found[237-239]. NAb classes 1 and 2, which include CB6[240] and LY-CoV555[241] bind the RBD/ACE2 interface corresponding to cluster 2 Nbs (**Figure 9**). Class 3 NAbs include S309[242] targeting the outer face of RBD, but no Nb resembling this cluster has yet been crystallized[243]. According to the HDX-MS data, NM1224 could probably be assigned to this class. Class 4 NAbs targeting the inner face of RBD typically exhibit less potent neutralization activity such as CR3022[244] since they are not competing with the ACE2 interface. Cluster 1 Nbs correspond to this class but, as shown for NM1226 and NM1228, have a strong neutralization potential[243].

3.2. Potent biparatopic nanobodies against variants of concern

Viral infections lead to the formation of polyclonal Abs that bind to different epitopes and thus provide a better protection. We therefore hypothesized that targeting multiple epitopes may further increase the neutralizing effect and additionally ensure binding to escape mutations of SARS-CoV-2. Based on detailed epitope mapping and potent neutralization, we decided to fuse NM1230 or NM1228 to NM1226 via a flexible glycine-serine-linker ($(G_4S)_4$), resulting in the bipNbs NM1267 (NM1230-NM1226) and NM1268 (NM1228-NM1226), respectively. Both bipNbs were designed to target two distinct epitopes one inside and one outside the RBD/ACE2 interface (Wagner & Schnepf et al., **Appendix II**, Figure EV1). Both bipNbs were efficiently produced in mammalian cells, showed affinities to $RBD_{B.1}$ in the picomolar range (**Figure 10**) (Wagner & Ostertag et al., **Appendix I**, Figure 4, S7C; Wagner & Schnepf et al., **Appendix II**, Figure 1A) and picomolar IC_{50} values for RBD, S1 and S determined in the multiplex ACE2 competition assay (Wagner & Ostertag et al., **Appendix I**, Figure 4; Wagner & Schnepf et al., **Appendix II**, Figure EV2). In addition, evaluation of thermal unfolding and aggregation with nano differential scanning fluorimetry (nanoDSF) as well as accelerated aging, showed good biophysical properties and thus applicability for *in vivo* experiments (Wagner & Schnepf et al., **Appendix II**, Figure 1B).

Knowing the exact epitopes of individual Nbs, we proposed that both bipNbs are highly effective against several described variants of SARS-CoV-2 at this time, including Alpha

(B.1.1.7), Beta (B.1.351), Gamma (P1), Delta (B.1.617.2), Epsilon (B.1.429), Theta (P3), Kappa (B.1.617.1), and A.23.1 (**Figure 10**) (Wagner & Schnepf et al., **Appendix II**, Figure EV1). Therefore, we analyzed binding affinities against purified RBDs of listed variants (Wagner & Schnepf et al., **Appendix II**, Figure 2). Robust binding of both bipNbs to all tested variants was observed, in some cases even with significantly increased affinities. An exception was the binding of NM1267 to RBDs with exchange of leucine to arginine at position 452 (L452R) such as Delta, Epsilon and Kappa, where slightly decreased K_D values were determined.

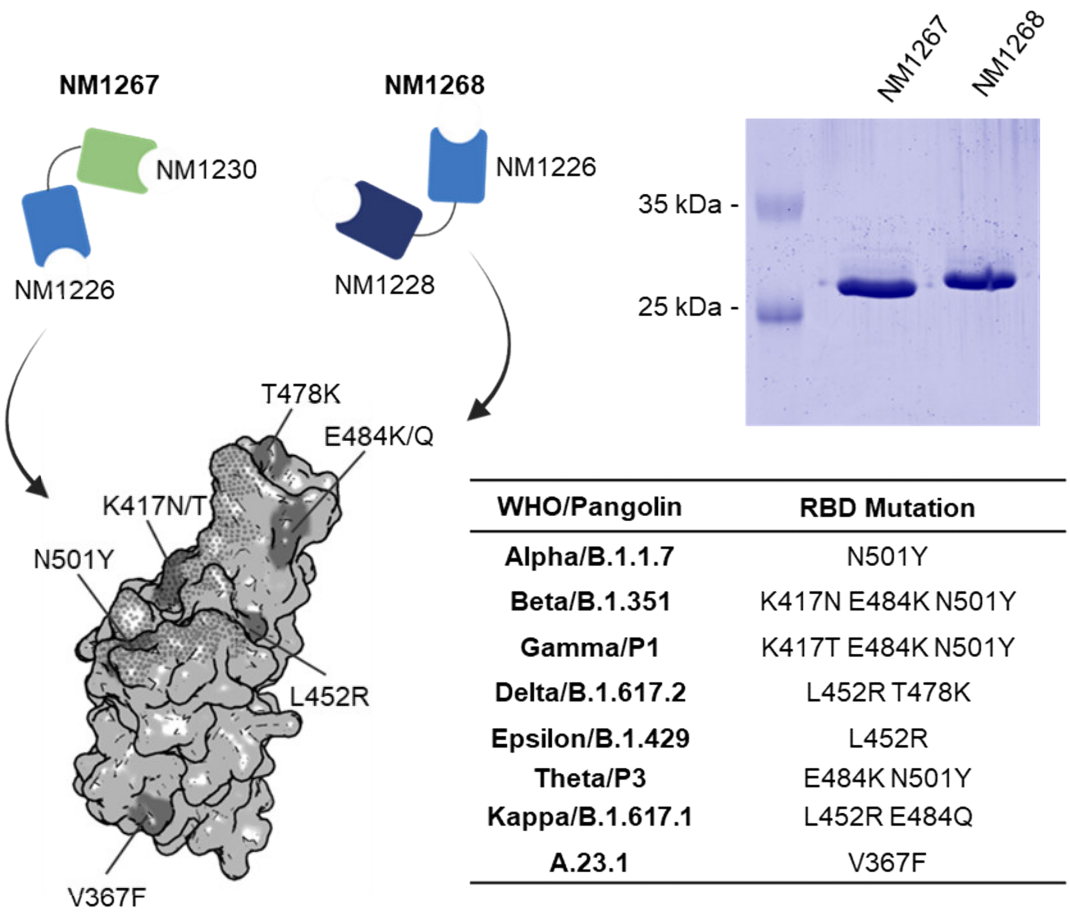

WHO/Pangolin	RBD Mutation
Alpha/B.1.1.7	N501Y
Beta/B.1.351	K417N E484K N501Y
Gamma/P1	K417T E484K N501Y
Delta/B.1.617.2	L452R T478K
Epsilon/B.1.429	L452R
Theta/P3	E484K N501Y
Kappa/B.1.617.1	L452R E484Q
A.23.1	V367F

Figure 10: BipNbs NM1267 and NM1268 target several SARS-CoV-2 variants.
BipNbs NM1267 and NM1268 consisting of single Nbs NM1230-NM1226 and NM1228-NM1226, respectively were produced in high yields and were able to bind several SARS-CoV-2 RBD variants including Alpha, Beta, Gamma, Delta, Epsilon, Theta, Kappa, and A.23.1.

Escape variants of SARS-CoV-2 that evade established immune responses are of great concern. At the time of the study, especially VOCs Beta and Delta posed a major thread since reduced neutralization was determined in postvaccination serum[245-247]. Knowing that NM1267 and NM1268 bipNbs are effective against both VOCs, next we tested their

neutralization potency using VNTs. Consistent with affinity measurements, NM1267 showed profound efficacy against SARS-CoV-2 B.1 and Beta with IC_{50} values of 0.33 and 0.78 nM, respectively (Wagner & Schnepf et al., **Appendix II**, Figure 3). However, as expected decreased neutralization potential for Delta with an IC_{50} value of 52.55 nM was determined. In contrast, we observed strong inhibition of viral infection using NM1268 with IC_{50} values of 2.37 nM for SARS-CoV-2 B.1, 6.06 nM for Beta and 0.67 nM for Delta.

To achieve enhanced neutralization effect, several studies focused on the preparation of multi-valent constructs in the form of homodi-/-trimeric Nbs or Nb-Fc fusions[248-250]. Although avidity can be significantly increased, these molecules are highly susceptible to escape mutations. An early study by *Koenig et al.* showed that targeting two independent epitopes on RBD can prevent viral escape[228]. Consequently, bipNbs have increased resistance to circulating and emerging VOCs[228; 251; 252]. By combining NM1226, which binds to a conserved epitope outside the RBD/ACE2 interaction site, and two different Nbs with epitopes within this interface, we ensured a robust binding mode. Affinity and neutralization efficacy in the multiplex ACE2 competition assay and VNT against SARS-CoV-2 B.1 were significantly enhanced by both bipNbs, and as suggested, strong binding to most circulating VOCs was detected. In summary, based on rational design we developed two promising candidates with increased neutralizing activity and built-in protection against escape variants for further applications.

3.3. Monitoring of SARS-CoV-2 neutralizing immune responses via NeutrobodyPlex

Since the pandemic outbreak, identification of immune correlates for protection against SARS-CoV-2 infection and prediction of clinical outcomes has been one of the major challenges. Due to their important role in host protection and ease of sampling, the determination of Ab titers lends itself as a defined correlate of protection. In severely ill and hospitalized patients, however, high production of Abs was observed; yet, these Abs exhibited low binding affinity due to impaired Ab maturation[253; 254]. Therefore, total Ab titers are not a reliable prognostic marker of immune protection in symptomatic COVID-19[255]. NAbs, which are part of the Ab response, play a critical role to prevent SARS-CoV-2 infection and support rapid virus clearance due to interference with receptor binding, blockade of virus uptake into host cells as well as prevention of uncoating of viral genomes into endosomes[256]. In contrast to the full Ab response, studies showed that the neutralization level is highly correlating with immune protection and models based on neutralizing titers are robust predictors for waning immunity and the requirement for the

next boosting vaccination[255; 257]. Since the onset of the pandemic, numerous SARS-CoV-2 serologic tests have been developed to monitor seroconversion of individuals but not to determine their neutralizing effect. At the same time, the gold standard method to measure NAb titers the VNT has numerous disadvantages, such as an elaborate protocol, long incubation times, and the need for a BSL3 laboratory[107-110]. To overcome listed limitations, we investigated the application of Nbs as Ab surrogate in a competitive binding assay to detect NAbs within serum samples (Wagner & Ostertag et al., **Appendix I**).

To develop an antigen-resolved serological assay capable of determining neutralizing immune responses against SARS-CoV-2, we investigated whether NM1267 could be used as a suitable Ab surrogate to monitor NAbs in serum samples. Based on its binding mode, we hypothesized that NM1267 robustly displaces serum Abs from the RBD/ACE2 interface (**Figure 11A**). To test this hypothesis, we first used the well-characterized NAb (clone REGN10933) in the competitive multiplex binding assay[101] and observed increasing displacement of NAbs in the presence of rising concentrations of NM1267 (Wagner & Ostertag et al., **Appendix I**, Figure S8). Next, we examined five SARS-CoV-2 patient samples in a similar experimental setup (**Figure 11B**). We observed that ~63 nM of NM1267 was sufficient to displace bound IgGs on RBD and S1. A minor signal decrease was observed on S, suggesting that most S-binding Abs do not target the RBD/ACE2 interface. Notably, already in this small sample set distinct differences within the neutralizing capacity of tested serum samples could be resolved by using NM1267 as Ab surrogate (Wagner & Ostertag et al., **Appendix I**, Figure 5, Table S3). Based on the application of bipNb NM1267 to determine neutralizing capacities, the novel multiplex serological assay was named NeutrobodyPlex.

For further validation a set of 18 serum samples collected from PCR-positive SARS-CoV-2 patients and four control samples from healthy donors were analyzed in parallel by the NeutrobodyPlex on RBD and the gold standard method VNT. In calculating the mean percent infection (% infection) of all individual serum dilutions for the VNT plotted against the corresponding MFI (% control) from the NeutrobodyPlex with 1 nM NM1267, a negative correlation was observed (**Figure 11C**) (Wagner & Ostertag et al., **Appendix I,** Figure 6C). These findings suggest that the NeutrobodyPlex is a valid serological high-through put assay allowing both the detection of individual neutralizing immune responses and the assessment of their neutralizing potency.

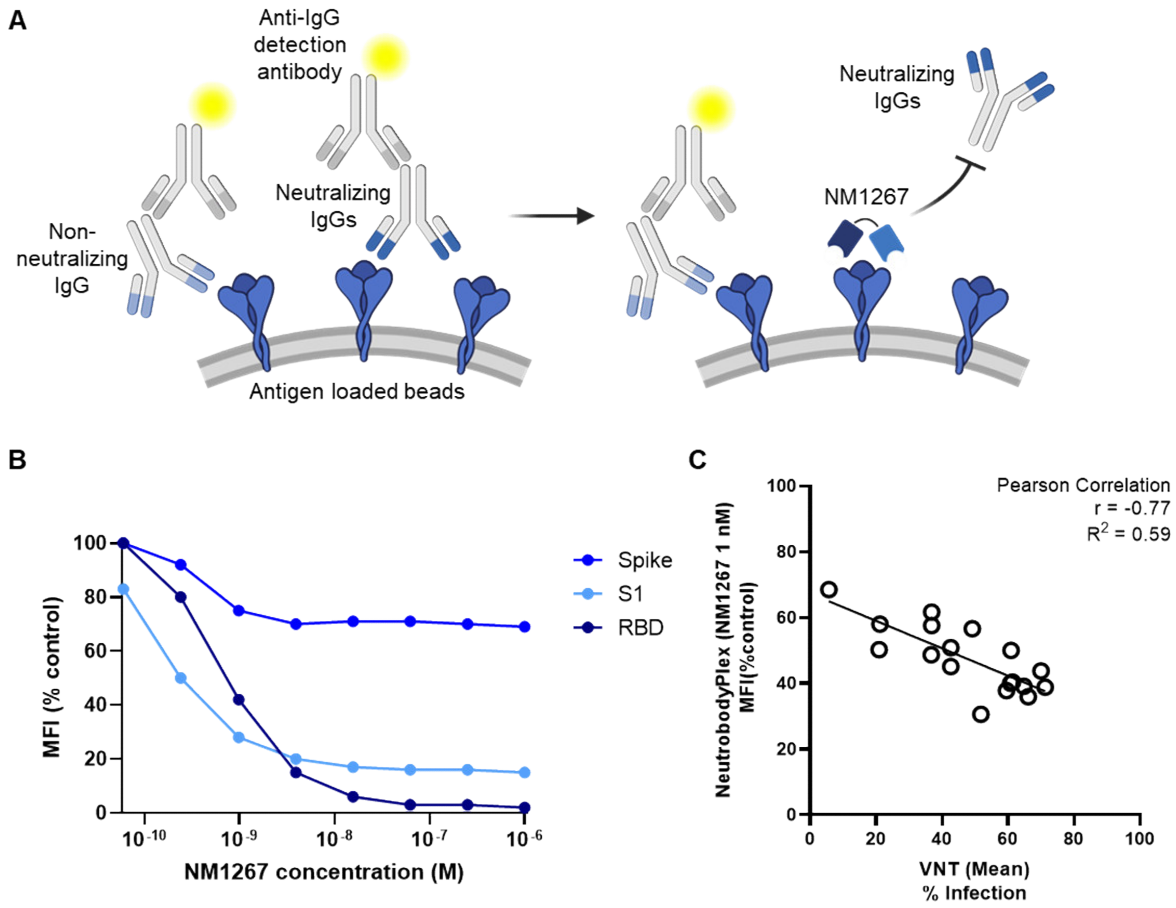

Figure 11: NeutrobodyPlex: multiplex competitive binding assay to monitor neutralizing immune responses.
A) Serum-derived neutralizing IgGs are displaced by the addition of the bipNb NM1267. The resulting signal decline represents the neutralizing capacity of the individual serum sample. **B)** Antigen-coated beads comprising RBD, S1, or S were co-incubated with serum samples and a dilution series of NM1267 (1 µM to 6 pM). The mean fluorescent intensities (MFI) derived from antigen-bound IgGs in the presence of bipNb were normalized to the MFI values of IgG binding without bipNb, which are exemplary illustrated for one serum sample as MFI (% control). **C)** For comparison to the gold standard method to determine NAbs, the mean percent of infection (% Infection) derived from all individual serum dilutions obtained by the VNT was plotted against the respective MFI (% control) obtained from the NeutrobodyPlex on RBD in the presence of NM1267 (1 nM).

Finally, the NeutrobodyPlex was validated with a larger sample set of 112 convalescent SARS-CoV-2-infected and eight uninfected individuals and included in total five SARS-CoV-2 antigens (RBD, S1, S2, S, and N). To examine the extent to which total immune response and neutralizing capacity are related, S-binding or N-binding IgGs as measure for the complete Ab response were plotted against normalized MFI values from IgGs binding to RBD in the presence of two concentrations of NM1267 (1 µM, 1 nM (MFI RBD (% control)) (Wagner & Ostertag et al., **Appendix I**, Figure 7). Total immune responses for both antigens were highly variable with MFI values ranging from ~3,500–~50,000 within the tested sample group. In particular, analysis of 1 nM NM1267 allowed conclusions

about the relationship between neutralizing capacity and the overall immune response in SARS-CoV-2 (Wagner & Ostertag et al., **Appendix I**, Figure 7B and D). Within this sample set, we identified several individuals with low SARS-CoV-2-specific Ab levels but who exhibited a strong neutralizing immune response. Therefore, our data suggest that high SARS-CoV-2-specific Ab titers do not directly correlate with the presence of strong neutralizing IgGs after infection with SARS-CoV-2. In summary, the NeutrobodyPlex provides a qualitative and quantitative assessment of the presence of neutralizing SARS-CoV-2 Abs in serum samples.

The NeutrobodyPlex was the first antigen-resolved multiplex assay to determine a SARS-CoV-2-specific neutralizing IgG response in serum samples. Compared to other assays such as VNT, the NeutrobodyPlex represents a fully automated, high-throughput test system suitable for screening of large cohorts by requiring non-living and non-infectious viral material and reducing costs and safety conditions[108; 111; 258]. In addition, minimal sample volumes are required due to the high sensitivity of the assay. In parallel to the development of the NeutrobodyPlex, competition assays with ACE2 were performed to determine neutralizing serum Abs[111; 112; 259]. The use of the human entry receptor ACE2 offers the advantage that the interaction between RBD, ACE2 and neutralizing serum Abs is based on the natural setup. However, compared to ACE2, the bipNb NM1267 exhibits an increased binding affinity to RBD[260], which leads to a higher resolution of strong neutralizing immune responses. With the NeutrobodyPlex, we have developed a rapid and cost-effective method to classify individual neutralizing immune responses against SARS-CoV-2 in detail, which can provide information about protection against re-infection and the need for the next booster vaccination.

3.4. Prophylactic application of biparatopic nanobodies against SARS-CoV-2 variants of concern

In light of the increasing emergence of SARS-CoV-2 VOCs that evade established immune responses and lead to loss of efficacy of therapeutic NAbs, vaccine adaptation and development of novel therapeutic agents were urgently needed at the time of the study[245-247]. It was shown, that by single mutations within the RBD including E484K, K417N/T and L452R present in the Beta and/or Delta VOC the binding of a majority of NAbs was impaired[261-263]. Therefore, major efforts to develop VOC cross-reactive neutralizing agents have been undertaken. Given the strong ACE2 displacement, high thermal stability, robust binding to SARS-CoV-2 RBD variants, and strong *in vitro* neutralization against VOCs Beta

and Delta, we decided to investigate the protective activity of NM1267 and NM1268 *in vivo*.

As an infection model, we used K18-hACE2 transgenic mice expressing human ACE2 that have been shown to be highly susceptible to SARS-CoV-2 infection[264]. The therapeutic regimen consisted of intranasal administration of 20 µg bipNb followed by SARS-CoV-2 infection 7 h after treatment. A control group of mice was treated with a non-specific bivalent Nb (NM1251). During all studies, weight loss and survival of infected mice were monitored for 14 days (Wagner & Schnepf et al., **Appendix II**, Figure 4A, 6A, EV3A).

To investigate *in vivo* treatment conditions, NM1267 was administered first, followed by infection with SARS-CoV-2 B.1 or Beta. All control-treated animals became severely ill and showed obvious clinical signs of disease, including significant weight loss, and therefore had to be euthanized (Wagner & Schnepf et al., **Appendix II**, Figure 4B-D, EV3B). Prophylactic treatment with NM1267 was highly effective in preventing disease progression in both SARS-CoV-2 lineages. Nine of 12 mice infected with B.1 and five of six mice infected with Beta survived infection, and significantly reduced signs of disease were observed. In addition, histopathological analyses of lung tissue using hematoxylin and eosin (H&E) staining and *in situ* hybridization (ISH) to assess the extent of tissue damage and localization of viral RNA confirmed *in vivo* outcomes. Marked inflammation and loss of functional lung epithelia with widespread presence of viral RNA were examined in all treated control mice (Wagner & Schnepf et al., **Appendix II,** Figure 5, EV3C). In contrast, minimal SARS-CoV-2 RNA-positive areas and only mild virus- and inflammation-related tissue damage were detected in lung tissue of NM1267-treated mice.

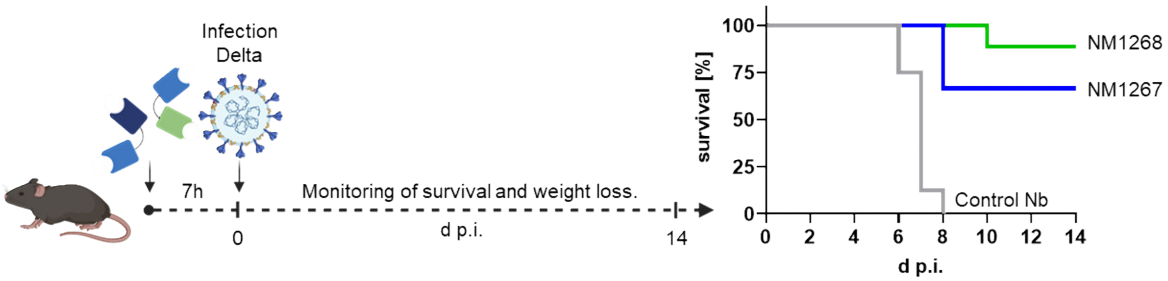

Figure 12: Comparison of the protective effect of bipNbs against SARS-CoV-2 Delta.
Intranasal prophylactic application of NM1267, NM1268 and one control Nb followed by infection with SARS-CoV-2 Delta in K18-hACE2 transgenic mice. To determine the protective effect, survival and weight loss were monitored for 14 days.

For the final comparison of *in vivo* efficacy between bipNbs NM1267 and NM1268, the predominant circulating VOC Delta at this time was selected for infection (**Figure 12**). Consistent with SARS-CoV-2 B.1 and Beta, severe disease progression was observed in Delta-infected animals receiving control treatment, whereas most mice survived on treatment with NM1267 or NM1268 (Wagner & Schnepf et al., **Appendix II**, Figure 6B & C). When comparing the two bipNbs, NM1268 showed stronger protection against SARS-CoV-2 Delta infection compared to NM1267, as suggested by the previous *in vitro* characterization. In summary, both bipNbs are highly effective in protecting against disease progression and mortality caused by SARS-CoV-2 B.1, Beta, and Delta following prophylactic intranasal administration.

Multiple studies were performed using neutralizing Nbs in various formats e.g. Fc-fusion, multi-valent/-paratopic constructs to test their efficacy *in vivo*[34; 235; 248-250; 265; 266]. Both prophylactic and therapeutic settings were investigated in animal models including transgenic mice and Syrian hamster. Due to the unique characteristics of Nbs intranasal application, aerosol delivery as well as intraperitoneal injection could successfully protect animals against SARS-CoV-2 B.1 and VOCs challenge. In this study rational design, enabled by in depths *in vitro* characterization and detailed epitope analysis lead to the generation of two bipNbs, both showing strong short-term efficacy against SARS-CoV-2 Delta infection. Remarkably, in retrospect, it can be shown that *in vitro* data clearly predict *in vivo* results. For example, affinity measurements on isolated RBD already indicated that NM1268 has a higher protective potential against SARS-CoV-2 Delta compared to NM1267. To convert bipNbs into therapeutic agents, modifications that extend the duration of efficacy, such as fusion with the Fc moiety, addition of an albumin-binding motif, or binding to carrier proteins such as albumin, are likely to be required[248-250]. In addition, therapeutic treatment regimens, as well as non-transgenic animal models such as hamsters or non-human primates, must be chosen to demonstrate efficacy.

CHAPTER 4

RESULTS & DISCUSSION II

NANOBODIES AGAINST HSIRPα

4. Results & Discussion II: Nanobodies against hSIRPα

The content of this chapter is based on:

Wagner TR, Blaess S, Leske IB, Frecot DI, Gramlich M, Traenkle B, Kaiser PD, Seyfried D, Maier S, Rezza A, Sonego F, Thiam K, Pezzana S, Zeck A, Gouttefangeas C, Scholz A, Nueske S, Maurer A, Kneilling M, Pichler BJ, Sonanini D, Rothbauer U (2023) **Two birds with one stone: human SIRPα nanobodies for functional modulation and in vivo imaging of myeloid cells**. bioRxiv 2023.06.27.546763.

4.1. Generation and characterization of hSIRPα-specific nanobodies

The unequivocal evidence that TAMs in the TME play a key role in cancer therapy response makes the search for meaningful TAM-specific markers an important challenge[149; 156]. SIRPα as myeloid specific marker and innate immune checkpoint inhibitor represents a highly interesting surface receptor to track and modulate the function of TAMs[173; 183]. To elucidate the theranostic potential of SIRPα, we decided to develop SIRPα-specific Nbs for diagnostic and therapeutic applications.

For the generation of Nbs against human SIRPα (hSIRPα), two alpacas (*Vicugna pacos*) were immunized with the recombinant extracellular portion of hSIRPα followed by the establishment of a comprehensive Nb phage library. For targeted enrichment of Nbs, we performed a binary selection campaign using either the entire extracellular portion or exclusively domain 1 of hSIRPα (hSIRPαD1) (**Figure 13A**). In total we identified 14 highly diverse hSIRPα Nbs named with S7-S45 (Wagner et al., **Appendix III**, Figure 1A). Bacterial production and purification, followed by stability and affinity analysis revealed 11 Nbs with melting temperatures ranging between ~55°C to ~75°C and K_D values in the range of ~0.12 nM and ~27 nM (**Figure 13B**) (Wagner et al., **Appendix III**, Figure 1B-C, Supplementary Figure 1). Specific binding of selected candidates to cellularly exposed hSIRPα was confirmed by live-cell staining of U2OS cells stably expressing full-length hSIRPα (**Figure 13B**) (Wagner et al., **Appendix III**, Figure 1E, Supplementary Figure 2A).

To explore the theranostic potential of Nbs, the aim of this study was to select both (i) modulatory Nbs targeting hSIRPαD1 blocking hSIRPα/hCD47 interaction as potential therapeutic binding molecules and (ii) inert Nbs binding hSIRPαD2 or D3 to be used for diagnostic purposes. Therefore, we performed domain mapping on U2OS cells expressing the individual domains of hSIRPα (Wagner et al., **Appendix III**, Figure 2E, Supplementary Figure 2B). In the screening we identified eight Nbs (S12, S14, S17, S41, S42, S43, S44,

and S45) with predominant hSIRPαD1 specificity, five Nbs (S8, S21, S29, S33 and S36) binding to hSIRPαD2 and one Nb (S7) recognizing hSIRPαD3. For further characterization, we limited ourselves to the most promising Nbs (S7, S8, S12, S33, S36, S41, S44 and S45) in terms of production yield, stability, affinity, domain specificity and developability. To further elucidate binding characteristics, epitope binning experiments were performed (Wagner et al., **Appendix III**, Supplementary Figure 2B, 3). A common binding epitope was identified for each of the hSIRPαD1 Nbs S12 & S41 and S44 & S45, and two sets consisting of S8 and S33 & S36 were found for the hSIRPαD2 Nbs.

The high homology of hSIRPα to members of the SIRP family and the presence of hSIRPα allelic variants make it necessary to investigate the cross-specificity of selected Nbs[174-176]. Thus, the two best described hSIRP family members hSIRPβ1 and hSIRPγ as well as hSIRPα variants V1 and V2 were transiently expressed on U2OS cells, followed by immunofluorescence staining using hSIRPα Nbs (**Figure 13B**) (Wagner et al., **Appendix III**, Figure 3A, Supplementary Figure 2C). All Nbs recognized SIRPβ1 in addition to hSIRPα, whereas only S12 and S44 (both hSIRPαD1 Nbs) and S8 and S36 (both hSIRPαD2 Nbs) showed additional binding of hSIRPγ. Moreover, all hSIRPαD2/D3 and hSIRPαD1 Nb S45 were able to detect both polymorphisms. Notably, for none of the Nbs, cross-reactive binding to murine SIRPα was detected.

We next examined hSIRPα binding on peripheral blood mononuclear cells (PBMCs) from three different donors. In a flow cytometric analysis, the monocyte/macrophage marker CD14 and the T cell-specific CD3 marker were included to additionally investigate the influence of SIRPγ binding in the PBMC pool (**Figure 13B**) (Wagner et al., **Appendix III**, Supplementary Figure 3B). All Nbs, except S7, revealed strong recognition of endogenously expressed hSIRPα on $CD14^+$ PBMCs of all tested donors. Concomitantly, binding of hSIRPγ on $CD3^+$ T cells was negligible. According to their domain specificity, we classified the identified Nbs into two subgroups for further characterization: (i) as modulatory binders blocking the hSIRPα/hCD47 interaction and (ii) as probes for PET-based *in vivo* imaging of myeloid cells.

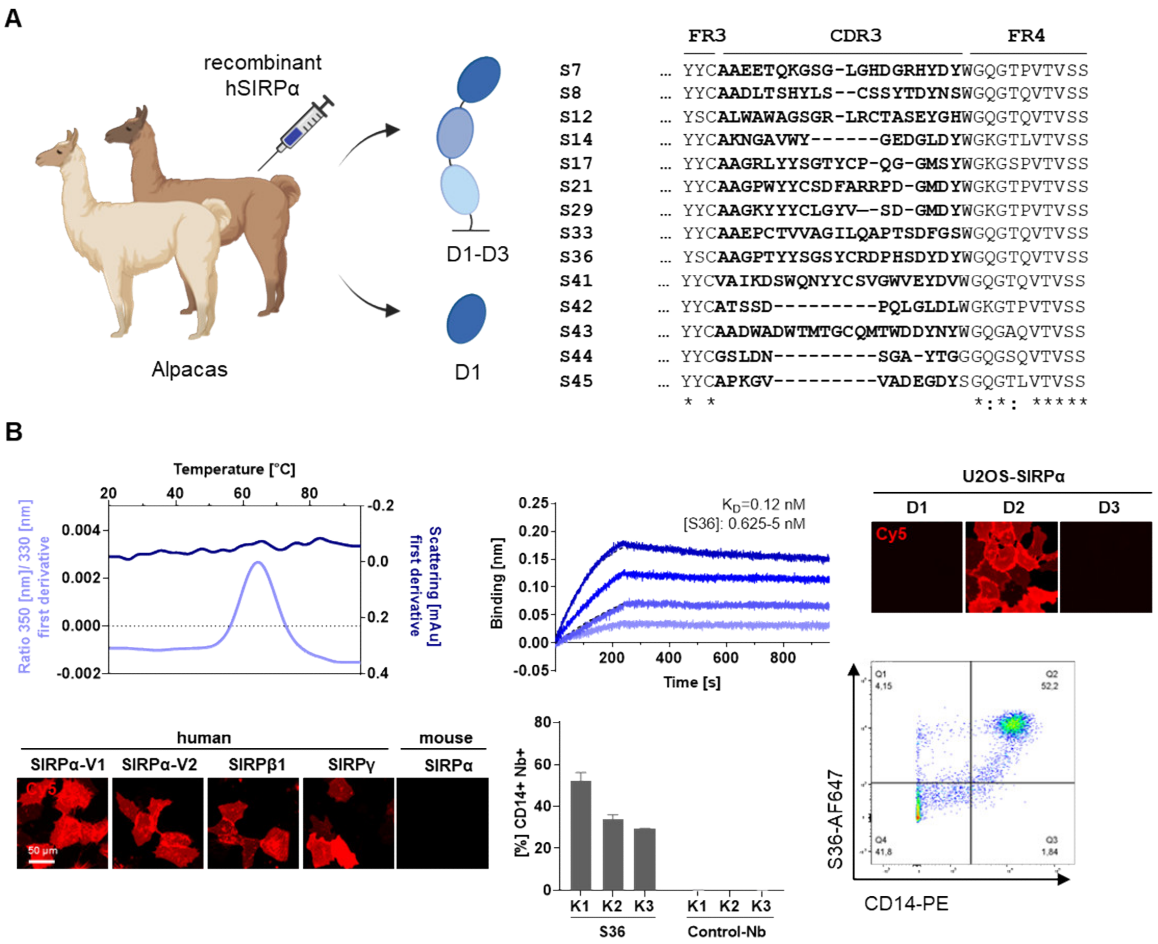

Figure 13: Generation and characterization of hSIRPα Nbs.
A) hSIRPα Nbs were generated by immunization of two alpacas, followed by a binary selection strategy on the complete extracellular portion (hSIRPαD1-D3) or hSIRPαD1, resulting in 14 diverse Nbs according to their CDR3 sequences. **B)** Exemplary shown for hSIRPα Nb S36 detailed *in vitro* characterization, including thermal stability and aggregation, binding affinity, epitope mapping, cross-reactivity, and binding to the endogenous antigen on PBMCs, was assessed.

Previously, a number of macrophage-specific surface receptors including macrophage mannose receptor (MMR, CD206), CD11b, major histocompatibility complex (MHC) class II, complement receptor of the Ig superfamily (CRIg) and V-set immunoglobulin domain-containing 4 (Vsig4) have been targeted by Nb selection campaigns[267-270]. More recently, also Nbs against murine SIRPα have been identified for SPECT imaging of glioblastoma tumor-associated myeloid cells, which demonstrates the value of hSIRPα-specific Nbs[271]. However, all those Nbs were selected against murine receptors and are therefore solely applicable as research tools in artificial mouse models. Merely the MMR-Nb targeting the endocytic carbohydrate-binding receptor MMR, showed cross-reactivity to the human receptor. However, MMR is only expressed on M2-like/hypoxic MHC II^{low} TAMs and therefore only a TAM subpopulation can be visualized[267]. Thus, the diverse set of human hSIRPα-specific Nbs identified within this study, targeting different domains and epitopes

within the extracellular domain of hSIRPα, opens various possibilities to track and modulate the entire human myeloid cell population and expands the portfolio of currently available macrophage specific Nbs.

4.2. hSIRPαD1 nanobodies potentiate macrophage phagocytosis

Within the evolving field of cancer immunotherapy, novel strategies increasingly focus on unleashing innate immune responses. The SIRPα/CD47 axis represents one key innate immune checkpoint highly attractive as potential target[169; 170]. Numerous agents directed to SIRPα/CD47 are currently under preclinical and clinical development, and already revealed pronounced therapeutic anti-cancer activities[201]. Due to the specific expression of SIRPα on the myeloid cell population, SIRPα-targeting agents seemed to be the preferred approach avoiding undesirable on-target and off-tumor function, which are observed for CD47 blocking therapeutics. To date, the majority of SIRPα-specific modulators are Ab-based[176; 206-208]. Properties such as stability, lack of post-translational modifications resulting in homogeneous products, and ease of formatting into multivalent binding molecules also make Nbs highly attractive for clinical application[37; 272]. Therefore, the previously identified hSIRPαD1-specific Nbs were investigated for their functional properties to potentiate phagocytosis.

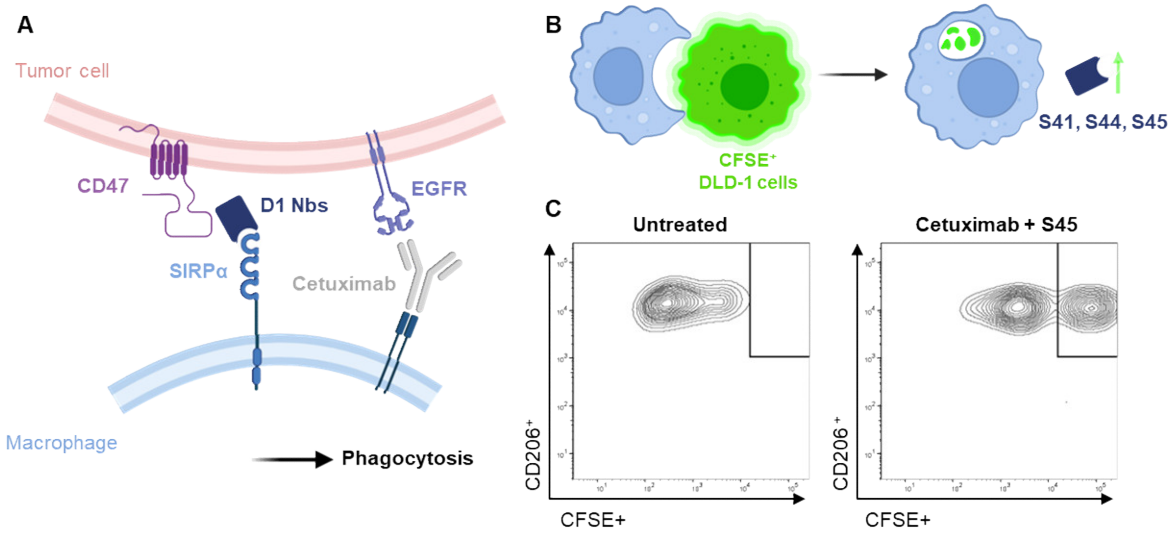

Figure 14: Potential of hSIRPαD1 Nbs to augment phagocytosis of tumor cells.
A) Mechanism by which hSIRPαD1 Nbs in combination with tumor-opsonizing Abs (e.g. the anti-EGFR Ab cetuximab) enhance macrophage-mediated phagocytosis of tumor cells. **B)** Upon combination treatment with cetuximab plus S41, S44 and S45 macrophages increasingly engulfed CFSE-labelled DLD-1 cells. **C)** Representative flow cytometry plots show $CD206^{+}CFSE^{+}$ macrophages of untreated and cetuximab plus hSIRPαD1 Nb S45 in the phagocytosis assay.

First, we investigated the potential of hSIRPαD1 Nbs to inhibit the interaction between hSIRPα and hCD47 (Wagner et al., **Appendix III**, Figure 4A). To this end, we performed a competitive hSIRPα/hCD47 binding assay using the hSIRPαD1 Nbs (Wagner et al., **Appendix III**, Figure 4B). Nbs S44 and S45 blocked hSIRPα binding to hCD47 to a similar extent as the proven therapeutically active Ab KWAR23[206]. While only partial inhibition of the hSIRPα/hCD47 interaction was observed for Nb S41, S12 had no effect on hSIRPα binding. For functional testing, we next analyzed the ability of these Nbs to enhance macrophage-mediated Ab-dependent cellular phagocytosis (ADCP) (**Figure 14A**) (Wagner et al., **Appendix III**, Figure 4C). Therefore, carboxyfluorescein diacetate succinimidyl ester- (CFSE-) pre-stained $EGFR^+$ DLD-1 tumor cells and incubated with human monocyte-derived macrophages (MDMs). To induce ADCP, the tumor-opsonizing EGFR-specific Ab cetuximab and hSIRPαD1 Nbs were added, followed by analysis of the $CD206^+CFSE^+$ cell population reflecting DLD-1 cells engulfed by MDMs through phagocytosis (**Figure 14B & C**) (Wagner et al., **Appendix III**, Figure 4D). Both hSIRPα-blocking Nbs S44 and S45 and the partial blocking Nb S41 were able to enhance macrophage-mediated phagocytosis in comparison to cetuximab single treatment. In contrast, Nb S12 did not influence phagocytic activity (Wagner et al., **Appendix III**, Figure 4E).

Considering that approximately 43.6% of cancer patients in the U.S. are eligible for therapy with immune checkpoint inhibitors but only 12.5% respond to it, it becomes obvious that new classes and combinations of specific immunotherapeutics that achieve synergistic treatment effects are urgently needed[273]. In particular, the regulatory pathways coordinating the interplay between innate and adaptive immune responses - the TME and cancer cells - offer new opportunities for targeted intervention to induce a rapid and durable antitumor response and prevent therapy-induced resistance[274-276]. To date, little attention has been paid to the innate immune response in the development of immunotherapies. However, it is becoming increasingly apparent that especially TAMs in the myeloid cell population, frequently infiltrating tumors and modulating tumor angiogenesis are key drivers for therapy response[149; 277; 278]. The hSIRPα/hCD47 axis thus represents a promising target for the development of next-generation immunotherapeutics. In this study, we have developed the first Nb-based human hSIRPα blockers capable of selectively inhibiting the interaction between hSIRPα and hCD47. Candidates S41, S44, and S45 showed strong ADCP enhancement in combination with tumor-opsonizing Abs to a similar extent as the previously described Ab KWAR23[206]. With S45 we identified a highly potent hSIRPα-blocking Nb with strong affinity and stability as well as specificity to both isoforms of hSIRPα, thereby ensuring wide applicability. In addition, S45's selective

hSIRPα blockade and lack of hSIRPγ specificity makes it an ideal candidate for therapeutic applications, as it has been shown that nonselective hSIRPα/hSIRPγ blockade can impair T cell activation, proliferation, and endothelial transmigration[279]. In particular, by establishing bivalent or biparatopic formats the blocking efficacy of selected inhibitory hSIRPα-specific candidates can be increased. Alternatively, a single therapeutic agent with dual efficacy can be established by fusing selected hSIRPα-blocking Nbs with a tumor-opsonizing Nb and Fc moiety[280; 281] or by linking to CD40L present on activated T cells bridging innate and adaptive immune responses[282]. In addition, for therapeutic applications further modifications as mentioned above have to be implemented to increase serum half-life of the Nb. Interestingly, a recent study found that hSIRPα is expressed on various cancers, particularly melanoma cells, and that hSIRPα-overexpressing cells are more efficiently killed by cytotoxic $CD8^+$ T cells. The authors suggest that the hSIRPα/hCD47 interaction causes enhanced cell-cell adhesion between tumor cells and $CD8^+$ T cells. Therefore, blocking such an interaction using Abs or Nbs could significantly reduce tumor killing. For this reason, the authors proposed to use bispecific molecules targeting hSIRPα and another macrophage-specific antigen to specifically target TAMs[283]. As depicted, the studies considering the human hSIRPα blocking Nbs were limited to *in vitro* analysis. Consequently, the next step is to investigate their *in vivo* efficacy in suitable humanized animal models e.g. including combinatory treatment approaches targeting the PD-1/PDL-1 axis.

4.3. hSIRPα nanobodies for non-invasive *in vivo* imaging

Inter-individual variability in response to immunotherapies, combined with the risk of immune-related side effects and high costs, make patient stratification to predict response rate imperative[273; 284]. Current diagnostic methods to predict responsiveness are based on biopsies to assess the expression of biomarkers. However, due to the dynamic and inhomogeneous nature of malignancies, non-repeatable single-site tumor biopsies fail to represent the complex composition of the TME[285; 286]. At the same time, experimental blood biomarkers used to assess response to therapy do not provide spatial resolution[287]. Non-invasive imaging modalities such as magnetic resonance imaging (MRI), CT, PET and SPECT provide repeatable assessment of tumor size during therapy application. However, the classical imaging methodologies cannot provide information on the composition of the tumor environment and immune cell activity, which are important for early estimation of therapy response[288]. Recently, increasing efforts have been made to develop novel radiolabeled probes for PET imaging to assess the presence, infiltration, and activation of single immune cell populations within the TME[289]. To date, various Abs,

their derivatives including minibodies, diabodies, Fabs, scFv and Nbs as well as Ab mimetics e.g. affibodies have been generated to specifically track immune cells *in vivo*[290; 291]. Properties such as small size and the absence of an Fc moiety are highly desirable for PET tracer development since high tissue penetration, low serum half-life, and rapid renal excretion provide improved signal-to-noise ratios[65; 292; 293]. Thus, Nbs have great potential as novel probes for non-invasive, whole body, serial imaging of immune cell populations to predict immunotherapy responsiveness[69; 294; 295].

Given its high prognostic significance[192-195] and its expression on the entire myeloid cell population, we hypothesized that hSIRPα is a highly interesting biomarker of responsiveness to therapy and thus investigated the potential of hSIRPαD2 Nbs for their application as PET tracers. Nbs as diagnostic tracer molecules are ideally not interfering with the inherent function of the target receptor. To ensure inert properties we performed detailed epitope analysis of S8, S33 and S36. All three Nbs target overlapping three-dimensional epitopes on hSIRPαD2 with large spatial distance to the hSIRPα/hCD47 interaction site (Wagner et al., **Appendix III**, Supplementary Table 1, Supplementary Figure 4). In line with the affinity measurements, S36 displayed the strongest deuteration protection of all three Nbs (< -15%) covering the regions aa D163 - L187, aa H202 - G207 and aa C140 - K153 of hSIRPα. Due to the desirable characteristics of S36 including high affinity, good thermostability and non-modulating epitope binding, we decided to continue our tracer development with this lead candidate.

A major challenge in the development of biologically based tracers is the covalent binding of chelator molecules for the complexation of radionuclides. Conventional strategies are based on non-selective bioconjugation, which result in heterogeneous tracer pools[296]. Therefore, recent advances have focused on site-directed labeling approaches to obtain homogeneous and well-defined tracer molecules. These include e.g. the conjugation of one solvent exposed cysteine inserted into the sequence[296-298] or enzyme-mediated conjugation, e.g. using sortase A[30; 294; 299]. Due to various drawbacks of these methods, we decided for a novel site-directed labeling strategy based on conventional isothiocyanate conjugation. Therefore, all four lysine residues in the original S36 sequence were first replaced by arginines (hSIRPα-S36$_{K>R}$ Nb) (**Figure 15**) (Wagner et al., **Appendix III**, Figure S5A). This left only one solvent-accessible primary amine at the N terminus, resulting in the exclusive covalent conjugation of the chelator to the Nb. The modified Nb yielded comparable amounts and characteristics to the original S36, and site-specific chelator conjugation was confirmed (Wagner et al., **Appendix III**, Figure S5B-E). Next, hSIRPα-S36$_{K>R}$ Nb and the non-specific GFP Nb were labeled with the positron emitter ^{64}Cu. For ^{64}Cu-hSIRPα-S36$_{K>R}$ Nb a high radiochemical purity of ≥95% and an

immunoreactivity to hSIRPα⁺ cells of ~82% were determined (Wagner et al., **Appendix III**, Figure 5A & B).

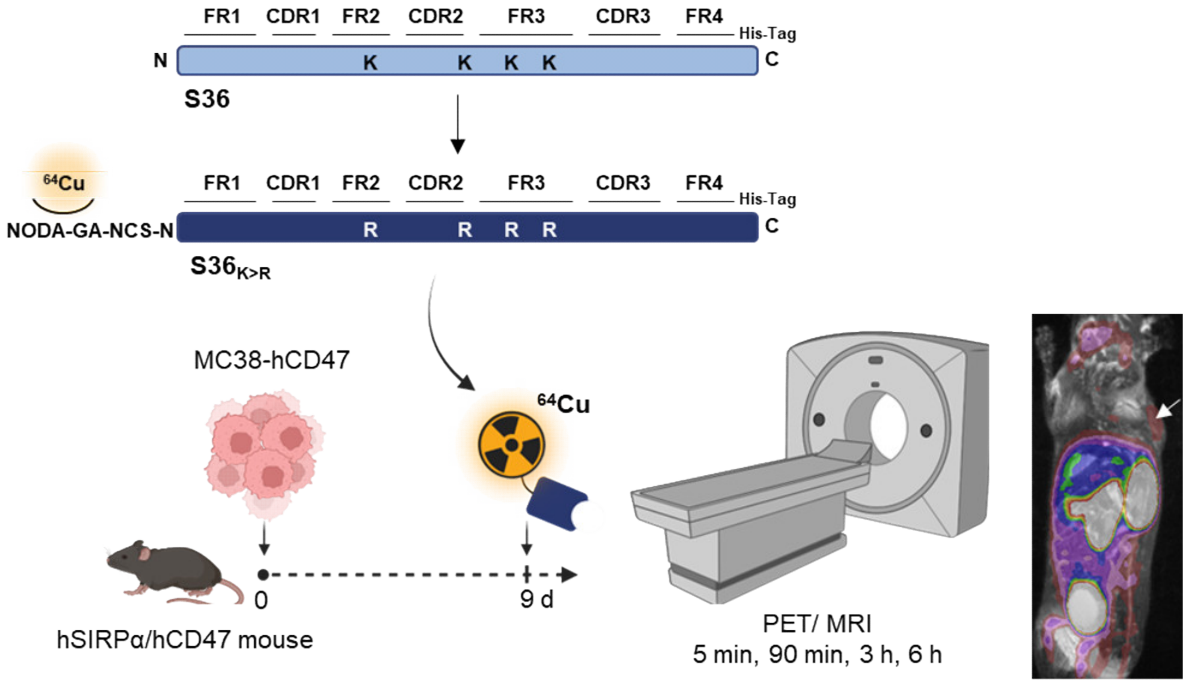

Figure 15: Application of ^{64}Cu-hSIRPα-S36$_{K>R}$ Nb for PET imaging.
Sequence optimization of hSIRPα Nb S36 (S36$_{K>R}$) by changing lysin (K) to arginine (R) residues for site-specific chelator (p-NCS-benzyl-NODA-GA) conjugation and radiolabeling (^{64}Cu). PET/MR scans of tumor bearing mice expressing humanized hSIRPα show specific enrichment in the tumor (white arrow) and tissues with high hSIRPα⁺ myeloid cells.

For *in vivo* validation of ^{64}Cu-hSIRPα-S36$_{K>R}$ Nb, we used a novel human hSIRPα/hCD47 mouse model (hSIRPα/hCD47). To non-invasively visualize the distribution of hSIRPα⁺ cells in a tumor-relevant model, CD47-overexpresssing MC38 (MC38-hCD47) adenocarcinoma bearing hSIRPα/hCD47 or C57BL/6 wildtype (wt) mice were injected with the ^{64}Cu-hSIRPα-S36$_{K>R}$ Nb or the control tracer (**Figure 15**). *In vivo* PET/MR imaging revealed a strong accumulation of the ^{64}Cu-hSIRPα-S36$_{K>R}$ Nb in the tumors of hSIRPα/hCD47 mice up to 6 h, which was not visible in the control ^{64}Cu-GFP$_{K>R}$ Nb injected hSIRPα/hCD47 mice and ^{64}Cu-hSIRPα-S36$_{K>R}$ Nb injected wt mice (Wagner et al., **Appendix III**, Figure 5C). Quantification of the PET images 3 h after injection furthermore revealed, significantly increased tracer accumulation in organs which are known to harbor high numbers of hSIRPα expressing myeloid cells including spleen, salivary gland, liver, bone and blood (Wagner et al., **Appendix III**, Figure 5C-E). In contrast, in myeloid-poor tissues including kidney and muscle no significant differences between the ^{64}Cu-hSIRPα-S36$_{K>R}$ Nb injected hSIRPα/hCD47 mice and the two described control groups were

identified. In conclusion, these results demonstrate the applicability of the novel ^{64}Cu-hSIRPα-S36$_{K>R}$ Nb-based PET tracer for visualization and monitoring of hSIRPα^{+} cell distribution by non-invasive *in vivo* PET.

Given the important role of TAMs in response to therapy and development of resistance, major efforts have been made to identify molecular markers with prognostic value. Several promising targeting strategies such as radiolabeled macrophage-targeted nanoparticles engulfed by endocytosis and small molecule-, Ab-, or Nb-based radiotracers targeting surface receptors such as MMR, macrophage scavenger receptor CD163, folate receptor beta (FR-β), MHC-II or CD11b, and mitochondrial translocator protein (TSPO) localized on the outer membrane of mitochondria, have been developed to selectively visualize TAMs by *in vivo* PET imaging[294; 300-304]. Clinically available detection methods for TAMs include ferumoxytol-enhanced MRI and TSPO radioligands for PET imaging. In addition, ^{68}Ga anti-MMR Nb for PET imaging is currently tested in early clinical trials in malignant solid tumors (NCT04168528, NCT04758650). In comparison to established strategies typically targeting TAM subpopulations, the ^{64}Cu-hSIRPα-S36$_{K>R}$ Nb enables the monitoring of the complete myeloid cell population. Particularly, with regard to future therapies, including the hSIRPα/hCD47 blocking strategies currently being clinically tested, the ^{64}Cu-hSIRPα-S36$_{K>R}$ Nb can be used to directly determine the presence of the hSIRPα^{+} target population in the TME. This allows not only the identification of suitable patients, but also early visualization of the response to therapy. With our lead candidate S36, we have developed a radiotracer that specifically targets hSIRPα^{+} cells. Uniquely, we have succeeded in achieving highly efficient site-directed radiolabeling by exchanging lysine for arginine throughout the Nb sequence. Remarkably, this extensive engineering approach did not affect protein properties. Compared to other elaborate site-directed labeling strategies requiring enzymes or terminal cysteines, we have managed to overcome the disadvantages of conventional labeling strategies[296]. Moreover, due to the strong binding affinity of S36, the probability of detecting even low numbers of hSIRPα^{+} cells or low hSIRPα^{+} expression levels are greatly increased. In addition, S36 recognizes both allelic variants present in the human population, which is critical for clinical translation. Although cross-reactivity for SIRPγ was observed, recognition by T cells within the PBMC pool was negligible. Of note, S36 has been shown to have no modulatory function on phagocytosis activity, thus representing an ideal candidate for diagnostic PET imaging. The radionuclide ^{64}Cu was selected due to its half-life of 12.7 hours, matching to the short biological half-life of Nbs[305]. Consequently, future patients are earlier free of radioactivity and exposed to even lower doses of radiation. Likewise, the selected p-NCS-benzyl-NODA-GA chelator also enables the flexibility of ^{68}Ga (half-life 68 min) radiolabeling.

In summary, the ^{64}Cu-hSIRPα-S36$_{K>R}$ Nb developed here complements the currently available portfolio of PET tracer molecules for non-invasive imaging of tumor associated immune cells[30; 267; 294]. and could serve as valuable probe for monitoring individual therapy responses during cancer immunotherapy.

CHAPTER 5

CONCLUSION & OUTLOOK

5. Conclusion & Outlook

The aim of this thesis was to investigate and demonstrate the potential of Nbs as biologicals applicable for theranostic approaches. Thus, Nbs were developed against two highly divergent targets for use as advanced diagnostic and therapeutic tools.

For SARS-CoV-2, the main focus was to generate neutralizing Nbs that inhibit the interaction between RBD and ACE2. To improve their neutralizing potency, bipNb constructs were generated by genetic fusion of two Nbs binding different epitopes within the RBD. Applied as Ab surrogates in a high-throughput assay termed NeutrobodyPlex, we were able to simultaneously determine NAbs in serum samples from a large number of individuals. At the time published, the NeutrobodyPlex demonstrated the first antigen resolved assay to determine a neutralizing response against SARS-CoV-2. Recently, it has been used to monitor long-term immunity to SARS-CoV-2 in clinical professionals at the University Hospital of Tübingen as part of the TüSeRe:exact trial and in turn, can contribute valuable information for future SARS-CoV-2 vaccination guidelines. In a therapeutic setting, intranasal prophylactic treatment with our bipNbs further showed significantly reduced disease progression and increased survival rates upon lethal dose of SARS-CoV-2 B.1, Beta and Delta in a murine model.

With regard to viruses, this work confirmed the fundamental applicability to generate Nbs for neutralizing viral infectivity and their applicability as diagnostic tools was comprehensively demonstrated using SARS-CoV-2 as an example. Thus, Nbs represent a cost-effective alternative to conventional NAbs. In particular, for viruses such as flaviviruses like dengue, yellow fever, and Zika; orthomyxoviruses like influenza; retroviruses like HIV; and orthopneumoviruses like RSV as well as alpha- and betacoronaviruses, the use of Nbs lacking the Fc domain holds an advantage over mAbs due to the phenomenon of Ab-dependent enhancement, whereby suboptimal Abs enhance viral entry into immune cells via the Fc gamma receptor[306; 307].

Due to selective choice of Nbs with different epitopes, the developed anti-RBD bipNbs potently neutralized most nascent VOCs up to Omicron. However, the appearance of the Omicron variant with multiple sub lineages and an unprecedented number of mutations (e.g. 44 mutations in S for XBB.1.16) presented a major change in the SARS-CoV-2 pandemic[93], which also implicated binding behavior of developed anti-RBD bipNbs. We as well as others developing neutralizing RBD-specific Abs or Nbs, observed a significant reduction in binding affinity to Omicron, finally leading to the revocation of emergency approval for all SARS-CoV-2 Abs[308-310]. Currently only a limited number of Nbs to efficiently

neutralize SARS-CoV-2 Omicron are described, targeting hidden clefts or highly conserved epitopes on RBD[251; 311; 312]. Remarkably, although there was a dramatic increase in the number of infections with the emergence of the Omicron variant due to immune escape, the severity of the disease course was reduced at the same time[313; 314]. In this context, the cost and risk of renewed loss of function no longer justify the development of new therapeutic biologicals targeting the Omicron variant. Nevertheless, for infectious agents with a high mutation rate, such as RNA viruses, future selection strategies would need to be designed to ensure Nb binding even after mutational events[239]. In those cases, a technically complex solution would be to generate a synthetic library of the target antigen with variable residues at positions which are not relevant for receptor binding or structural integrity. Using such a variable library e.g. expressed on cells for immunization and selection, mutational robust binders might be identified.

As a second example to investigate the theranostic potential of Nbs, hSIRPα as a cell surface receptor on human myeloid cells was chosen as antigen. Thereby, we aimed to identify modulating and inert candidates using a binary selection strategy. For therapeutic applications, we generated the first hSIRPα blocking Nbs with comparable efficiency as a previously described hSIRPα blocking mAb. The inert binder S36 represents the first PET tracer to non-invasively visualize hSIRPα^{+} myeloid cells within tumor lesions *in vivo*. Additionally, we developed a highly efficient site-directed labeling strategy by protein engineering of the original S36 Nb sequence, overcoming several limitations of previously described site-directed targeting strategies[296].

Future focus of selected hSIRPα-Nbs will be on further development for clinical translation. In regard of therapeutic application, the here developed hSIRPα-blocking Nbs represent interesting binding molecules to be combined with tumor targeting binders such as the Her2- or EGFR-specific Nbs[28; 315], T cell markers like PD1-, CD4- or CD8- specific Nbs[30; 316; 317], further macrophage specific Nbs such as MMR[267] and/or immune stimulators like cytokines[318]. However, due to the interplay between cancer cells, adaptive and innate immunity, fully humanized rodent models are essential for preclinical *in vivo* testing. Alternatively further therapeutic options such as controlled TAM depletion is currently considered to create a favorable milieu e.g. of PD1 Ab therapy[319; 320]. Therefore, besides blocking the hSIRPα/hCD47 interaction, radiotherapeutic approaches by conjugating selected Nbs with therapeutic radionuclides to deplete TAMs within the TME are considerable possibilities for the application of hSIRPα-specific Nbs.

For clinical translation of the hSIRPα-specific PET tracer for diagnostic non-invasive *in vivo* imaging, further improvement of the molecule is thought of including removal of non-functional sequence motifs such as the His-tag, humanization of the Nb sequence and

employing current clinical state-of the art radiolabeling using ^{18}F. Following design freeze, tracer production under GMP conditions and approval relevant safety and toxicities studies have to be initiated. With the hSIRPα-PET tracer, we predict to non-invasively monitor subtle changes in the distribution of the myeloid cell population. However, given the highly heterogeneous and complex nature of this cell population, further tracer molecules targeting subpopulations and activation status will need to be developed for subsequent PET imaging of different markers. Detailed differential analysis as available with *ex vivo* FACS analyses is unlikely using non-invasive PET imaging, for this reason increased efforts need to be made to identify further meaningful surface markers for clinical application. Due to the high prognostic significance of hSIRPα on TAMs in numerous malignancies, we initially tested the novel hSIRPα PET tracer in a colon carcinoma model. Interestingly for melanoma, it was shown that high hSIRPα expression correlates with response to anti-PD-1 treatment. Therefore, the hSIRPα PET tracer may also be highly applicable to stratify patients for PD-1 therapy response[283]. Currently, the hSIRPα lead PET tracer S36 is tested for imaging of inflammation in SARS-CoV-2-infected non-human primates to elucidate the role of macrophages for the development of long-COVID[321]. In addition, there is increasing evidence that presence and activation of monocytes and macrophages also play a critical role in autoimmune diseases and initial studies suggest that especially the hSIRPα/hCD47 signaling pathway is involved in the development of autoimmune encephalomyelitis[322; 323]. In conclusion, site-specifically labeled human hSIRPα Nbs offer great potential for non-invasive *in vivo* PET imaging in diverse applications such as cancer, autoimmunity and infectious diseases.

Exactly 30 years after the discovery of HCAbs in camelids[1], the Nbs described here and their versatile applicability for diagnostic and therapeutic purposes are further evidence of their great potential. The exceptional properties of Nbs - small size, stability, affinity, ease of modification into multifunctional constructs - provide ideal conditions for advanced theranostic applications. In this work, a novel diagnostic test system, novel diagnostic tracer molecules and novel therapeutic agents based on Nbs were developed with the goal of advancing selected candidates into clinical applications for use as next-generation theranostics. Particularly in the emerging field of precision medicine, there are many indications that Nbs will be instrumental in solving current and future healthcare challenges.

References

1 Hamers-Casterman C *et al.* (1993) Naturally occurring antibodies devoid of light chains. *Nature* 363: 446-448.

2 Blanc MR *et al.* (2009) A one-step exclusion-binding procedure for the purification of functional heavy-chain and mammalian-type gamma-globulins from camelid sera. *Biotechnol Appl Biochem* 54: 207-212.

3 Muyldermans S, Atarhouch T, Saldanha J, Barbosa JA & Hamers R (1994) Sequence and structure of VH domain from naturally occurring camel heavy chain immunoglobulins lacking light chains. *Protein Eng* 7: 1129-1135.

4 Muyldermans S *et al.* (2009) Camelid immunoglobulins and nanobody technology. *Vet Immunol Immunopathol* 128: 178-183.

5 van der Linden RH *et al.* (1999) Comparison of physical chemical properties of llama VHH antibody fragments and mouse monoclonal antibodies. *Biochim Biophys Acta* 1431: 37-46.

6 Padlan EA (1994) Anatomy of the antibody molecule. *Mol Immunol* 31: 169-217.

7 Vu KB, Ghahroudi MA, Wyns L & Muyldermans S (1997) Comparison of llama VH sequences from conventional and heavy chain antibodies. *Mol Immunol* 34: 1121-1131.

8 Govaert J *et al.* (2012) Dual beneficial effect of interloop disulfide bond for single domain antibody fragments. *J Biol Chem* 287: 1970-1979.

9 Muyldermans S (2013) Nanobodies: natural single-domain antibodies. *Annu Rev Biochem* 82: 775-797.

10 De Genst E *et al.* (2006) Molecular basis for the preferential cleft recognition by dromedary heavy-chain antibodies. *Proc Natl Acad Sci U S A* 103: 4586-4591.

11 Koide A *et al.* (2007) Exploring the capacity of minimalist protein interfaces: interface energetics and affinity maturation to picomolar KD of a single-domain antibody with a flat paratope. *J Mol Biol* 373: 941-953.

12 Desmyter A, Decanniere K, Muyldermans S & Wyns L (2001) Antigen specificity and high affinity binding provided by one single loop of a camel single-domain antibody. *J Biol Chem* 276: 26285-26290.

13 Mitchell LS & Colwell LJ (2018) Analysis of nanobody paratopes reveals greater diversity than classical antibodies. *Protein Engineering, Design and Selection* 31: 267-275.

14 Zavrtanik U, Lukan J, Loris R, Lah J & Hadži S (2018) Structural Basis of Epitope Recognition by Heavy-Chain Camelid Antibodies. *J Mol Biol* 430: 4369-4386.

15 Chothia C, Novotný J, Bruccoleri R & Karplus M (1985) Domain association in immunoglobulin molecules. The packing of variable domains. *J Mol Biol* 186: 651-663.

16 Harmsen MM *et al.* (2000) Llama heavy-chain V regions consist of at least four distinct subfamilies revealing novel sequence features. *Mol Immunol* 37: 579-590.

17 Wagner TR & Rothbauer U (2021) Nanobodies–Little helpers unravelling intracellular signaling. *Free Radical Biology and Medicine* 176: 46-61.

18 Braun MB *et al.* (2016) Peptides in headlock--a novel high-affinity and versatile peptide-binding nanobody for proteomics and microscopy. *Sci Rep* 6: 19211.

19 Dumoulin M *et al.* (2002) Single-domain antibody fragments with high conformational stability. *Protein Sci* 11: 500-515.

20 De Vos J, Devoogdt N, Lahoutte T & Muyldermans S (2013) Camelid single-domain antibody-fragment engineering for (pre)clinical in vivo molecular imaging applications: adjusting the bullet to its target. *Expert Opin Biol Ther* 13: 1149-1160.

21 Debie P *et al.* (2020) Size and affinity kinetics of nanobodies influence targeting and penetration of solid tumours. *J Control Release* 317: 34-42.

22 Muruganandam A, Tanha J, Narang S & Stanimirovic D (2002) Selection of phage-displayed llama single-domain antibodies that transmigrate across human blood-brain barrier endothelium. *Faseb j* 16: 240-242.

23 Ackaert C *et al.* (2021) Immunogenicity Risk Profile of Nanobodies. *Front Immunol* 12: 632687.

24 Arbabi-Ghahroudi M, Tanha J & MacKenzie R (2005) Prokaryotic expression of antibodies. *Cancer Metastasis Rev* 24: 501-519.

25 Chames P & Baty D (2009) Bispecific antibodies for cancer therapy: the light at the end of the tunnel? *MAbs* 1: 539-547.

26 Emmerson CD *et al.* (2011) Enhancement of polymeric immunoglobulin receptor transcytosis by biparatopic VHH. *PLoS One* 6: e26299.

27 Els Conrath K, Lauwereys M, Wyns L & Muyldermans S (2001) Camel single-domain antibodies as modular building units in bispecific and bivalent antibody constructs. *J Biol Chem* 276: 7346-7350.

28 Vaneycken I *et al.* (2011) Preclinical screening of anti-HER2 nanobodies for molecular imaging of breast cancer. *Faseb j* 25: 2433-2446.

29 Koch-Nolte F *et al.* (2007) Single domain antibodies from llama effectively and specifically block T cell ecto-ADP-ribosyltransferase ART2.2 in vivo. *Faseb j* 21: 3490-3498.

30 Traenkle B *et al.* (2021) Single-Domain Antibodies for Targeting, Detection, and In Vivo Imaging of Human CD4+ Cells. *Frontiers in immunology*: 5206.

31 Yan J *et al.* (2015) Characterization and applications of Nanobodies against human procalcitonin selected from a novel naïve Nanobody phage display library. *J Nanobiotechnology* 13: 33.

32 Yau KY *et al.* (2003) Selection of hapten-specific single-domain antibodies from a non-immunized llama ribosome display library. *J Immunol Methods* 281: 161-175.

33 Zimmermann I *et al.* (2020) Generation of synthetic nanobodies against delicate proteins. *Nat Protoc* 15: 1707-1741.

34 Li T *et al.* (2021) A synthetic nanobody targeting RBD protects hamsters from SARS-CoV-2 infection. *Nature Communications* 12: 4635.

35 Janssens R *et al.* (2006) Generation of heavy-chain-only antibodies in mice. *Proc Natl Acad Sci U S A* 103: 15130-15135.

36 Teng Y *et al.* (2020) Diverse human V(H) antibody fragments with bio-therapeutic properties from the Crescendo Mouse. *N Biotechnol* 55: 65-76.

37 Muyldermans S (2021) A guide to: generation and design of nanobodies. *The FEBS Journal* 288: 2084-2102.

38 Zimmermann I *et al.* (2018) Synthetic single domain antibodies for the conformational trapping of membrane proteins. *Elife* 7

39 McMahon C *et al.* (2018) Yeast surface display platform for rapid discovery of conformationally selective nanobodies. *Nat Struct Mol Biol* 25: 289-296.

40 Smith GP (1985) Filamentous fusion phage: novel expression vectors that display cloned antigens on the virion surface. *Science* 228: 1315-1317.

41 McCafferty J, Griffiths AD, Winter G & Chiswell DJ (1990) Phage antibodies: filamentous phage displaying antibody variable domains. *Nature* 348: 552-554.

42 Hoogenboom HR (2005) Selecting and screening recombinant antibody libraries. *Nat Biotechnol* 23: 1105-1116.

43 Deschaght P *et al.* (2017) Large Diversity of Functional Nanobodies from a Camelid Immune Library Revealed by an Alternative Analysis of Next-Generation Sequencing Data. *Front Immunol* 8: 420.

44 Biocca S, Ruberti F, Tafani M, Pierandrei-Amaldi P & Cattaneo A (1995) Redox state of single chain Fv fragments targeted to the endoplasmic reticulum, cytosol and mitochondria. *Biotechnology (N Y)* 13: 1110-1115.

45 Aires da Silva F *et al.* (2004) Camelized rabbit-derived VH single-domain intrabodies against Vif strongly neutralize HIV-1 infectivity. *J Mol Biol* 340: 525-542.

46 Gueorguieva D *et al.* (2006) Identification of single-domain, Bax-specific intrabodies that confer resistance to mammalian cells against oxidative-stress-induced apoptosis. *Faseb j* 20: 2636-2638.

47 Rothbauer U *et al.* (2006) Targeting and tracing antigens in live cells with fluorescent nanobodies. *Nature Methods* 3: 887-889.

48 Li T *et al.* (2012) Cell-penetrating anti-GFAP VHH and corresponding fluorescent fusion protein VHH-GFP spontaneously cross the blood-brain barrier and specifically recognize astrocytes: application to brain imaging. *Faseb j* 26: 3969-3979.

49 Wagner TR & Rothbauer U (2020) Nanobodies right in the middle: intrabodies as toolbox to visualize and modulate antigens in the living cell. *Biomolecules* 10: 1701.

50 Soetens E, Ballegeer M & Saelens X (2020) An Inside Job: Applications of Intracellular Single Domain Antibodies. *Biomolecules* 10

51 Caussinus E, Kanca O & Affolter M (2011) Fluorescent fusion protein knockout mediated by anti-GFP nanobody. *Nat Struct Mol Biol* 19: 117-121.

52 Irannejad R *et al.* (2013) Conformational biosensors reveal GPCR signalling from endosomes. *Nature* 495: 534-538.

53 Yu D *et al.* (2019) Optogenetic activation of intracellular antibodies for direct modulation of endogenous proteins. *Nat Methods* 16: 1095-1100.

54 Gil AA *et al.* (2020) Optogenetic control of protein binding using light-switchable nanobodies. *Nature Communications* 11: 4044.

55 Jedlitzke B, Yilmaz Z, Dörner W & Mootz HD (2020) Photobodies: Light-Activatable Single-Domain Antibody Fragments. *Angewandte Chemie International Edition* 59: 1506-1510.

56 Farrants H *et al.* (2020) Chemogenetic Control of Nanobodies. *Nat Methods* 17: 279-282.

57 Ries J, Kaplan C, Platonova E, Eghlidi H & Ewers H (2012) A simple, versatile method for GFP-based super-resolution microscopy via nanobodies. *Nat Methods* 9: 582-584.

58 Carrington G, Tomlinson D & Peckham M (2019) Exploiting nanobodies and Affimers for superresolution imaging in light microscopy. *Mol Biol Cell* 30: 2737-2740.

59 Virant D *et al.* (2018) A peptide tag-specific nanobody enables high-quality labeling for dSTORM imaging. *Nat Commun* 9: 930.

60 Rothbauer U *et al.* (2008) A versatile nanotrap for biochemical and functional studies with fluorescent fusion proteins. *Mol Cell Proteomics* 7: 282-289.

61 Klooster R *et al.* (2007) Improved anti-IgG and HSA affinity ligands: clinical application of VHH antibody technology. *J Immunol Methods* 324: 1-12.

62 Rasmussen SG *et al.* (2011) Structure of a nanobody-stabilized active state of the β(2) adrenoceptor. *Nature* 469: 175-180.

63 Steyaert J & Kobilka BK (2011) Nanobody stabilization of G protein-coupled receptor conformational states. *Curr Opin Struct Biol* 21: 567-572.

64 Botte M *et al.* (2022) Cryo-EM structures of a LptDE transporter in complex with Pro-macrobodies offer insight into lipopolysaccharide translocation. *Nat Commun* 13: 1826.

65 Lecocq Q *et al.* (2019) Theranostics in immuno-oncology using nanobody derivatives. *Theranostics* 9: 7772-7791.

66 Vaneycken I *et al.* (2011) Immuno-imaging using nanobodies. *Curr Opin Biotechnol* 22: 877-881.

67 Rashidian M & Ploegh H (2020) Nanobodies as non-invasive imaging tools. *Immuno-Oncology Technology* 7: 2-14.

68 Keyaerts M *et al.* (2016) Phase I Study of 68Ga-HER2-Nanobody for PET/CT Assessment of HER2 Expression in Breast Carcinoma. *J Nucl Med* 57: 27-33.

69 Xavier C *et al.* (2019) Clinical Translation of [(68)Ga]Ga-NOTA-anti-MMR-sdAb for PET/CT Imaging of Protumorigenic Macrophages. *Mol Imaging Biol* 21: 898-906.

70 Callewaert F *et al.* (2012) Evaluation of efficacy and safety of the anti-VWF Nanobody ALX-0681 in a preclinical baboon model of acquired thrombotic thrombocytopenic purpura. *Blood* 120: 3603-3610.

71 Scully M *et al.* (2019) Caplacizumab Treatment for Acquired Thrombotic Thrombocytopenic Purpura. *New England Journal of Medicine* 380: 335-346.

72 Jovčevska I & Muyldermans S (2020) The Therapeutic Potential of Nanobodies. *BioDrugs* 34: 11-26.

73 Panikar SS *et al.* (2021) Nanobodies as efficient drug-carriers: Progress and trends in chemotherapy. *J Control Release* 334: 389-412.

74 Hamann MV *et al.* (2021) Improved targeting of human CD4+ T cells by nanobody-modified AAV2 gene therapy vectors. *PLoS One* 16: e0261269.

75 Ingram JR, Schmidt FI & Ploegh HL (2018) Exploiting Nanobodies' Singular Traits. *Annu Rev Immunol* 36: 695-715.

76 Khaleghi S, Rahbarizadeh F, Ahmadvand D, Rasaee MJ & Pognonec P (2012) A caspase 8-based suicide switch induces apoptosis in nanobody-directed chimeric receptor expressing T cells. *Int J Hematol* 95: 434-444.

77 Wang H *et al.* (2021) Nanobody-armed T cells endow CAR-T cells with cytotoxicity against lymphoma cells. *Cancer Cell International* 21: 450.

78 Wu F *et al.* (2020) A new coronavirus associated with human respiratory disease in China. *Nature* 579: 265-269.

79 Wu JT, Leung K & Leung GM (2020) Nowcasting and forecasting the potential domestic and international spread of the 2019-nCoV outbreak originating in Wuhan, China: a modelling study. *Lancet* 395: 689-697.

80 Laue M *et al.* (2021) Morphometry of SARS-CoV and SARS-CoV-2 particles in ultrathin plastic sections of infected Vero cell cultures. *Scientific Reports* 11: 3515.

81 Gordon DE *et al.* (2020) A SARS-CoV-2 protein interaction map reveals targets for drug repurposing. *Nature* 583: 459-468.

82 Lan J *et al.* (2020) Structure of the SARS-CoV-2 spike receptor-binding domain bound to the ACE2 receptor. *Nature* 581: 215-220.

83 Hu B, Guo H, Zhou P & Shi Z-L (2021) Characteristics of SARS-CoV-2 and COVID-19. *Nature Reviews Microbiology* 19: 141-154.

84 Fehr AR & Perlman S (2015) Coronaviruses: an overview of their replication and pathogenesis. *Methods Mol Biol* 1282: 1-23.

85 Wu C *et al.* (2020) Risk Factors Associated With Acute Respiratory Distress Syndrome and Death in Patients With Coronavirus Disease 2019 Pneumonia in Wuhan, China. *JAMA Intern Med* 180: 934-943.

86 Tian J *et al.* (2020) Clinical characteristics and risk factors associated with COVID-19 disease severity in patients with cancer in Wuhan, China: a multicentre, retrospective, cohort study. *Lancet Oncol* 21: 893-903.

87 Michelen M *et al.* (2021) Characterising long COVID: a living systematic review. *BMJ Global Health* 6: e005427.

88 Organization WH, 2021. A clinical case definition of post COVID-19 condition by a Delphi consensus, 6 October 2021. World Health Organization.

89 Piccoli L *et al.* (2020) Mapping Neutralizing and Immunodominant Sites on the SARS-CoV-2 Spike Receptor-Binding Domain by Structure-Guided High-Resolution Serology. *Cell* 183: 1024-1042.e1021.

90 Harvey WT *et al.* (2021) SARS-CoV-2 variants, spike mutations and immune escape. *Nature Reviews Microbiology* 19: 409-424.

91 Wu L *et al.* (2022) SARS-CoV-2 Omicron RBD shows weaker binding affinity than the currently dominant Delta variant to human ACE2. *Signal Transduction and Targeted Therapy* 7: 8.

92 WHO, 2023. Tracking SARS-CoV-2 variants.

93 Hodcroft EB, 2021. CoVariants: SARS-CoV-2 Mutations and Variants of Interest.

94 Corman VM *et al.* (2020) Detection of 2019 novel coronavirus (2019-nCoV) by real-time RT-PCR. *Euro Surveill* 25

95 Konrad R *et al.* (2020) Rapid establishment of laboratory diagnostics for the novel coronavirus SARS-CoV-2 in Bavaria, Germany, February 2020. *Euro Surveill* 25

96 Perchetti GA, Huang ML, Mills MG, Jerome KR & Greninger AL (2021) Analytical Sensitivity of the Abbott BinaxNOW COVID-19 Ag Card. *J Clin Microbiol* 59

97 Xu Y, Lam HK & Jia G (2021) MANet: A two-stage deep learning method for classification of COVID-19 from Chest X-ray images. *Neurocomputing* 443: 96-105.

98 Bernheim A *et al.* (2020) Chest CT Findings in Coronavirus Disease-19 (COVID-19): Relationship to Duration of Infection. *Radiology* 295: 200463.

99 Bosso G *et al.* (2021) Lung ultrasound as diagnostic tool for SARS-CoV-2 infection. *Intern Emerg Med* 16: 471-476.

100 Filchakova O *et al.* (2022) Review of COVID-19 testing and diagnostic methods. *Talanta* 244: 123409.

101 Becker M *et al.* (2021) Exploring beyond clinical routine SARS-CoV-2 serology using MultiCoV-Ab to evaluate endemic coronavirus cross-reactivity. *Nat Commun* 12: 1152.

102 Robbiani DF *et al.* (2020) Convergent antibody responses to SARS-CoV-2 in convalescent individuals. *Nature* 584: 437-442.

103 Ejazi SA, Ghosh S & Ali N (2021) Antibody detection assays for COVID-19 diagnosis: an early overview. *Immunol Cell Biol* 99: 21-33.

104 Petherick A (2020) Developing antibody tests for SARS-CoV-2. *Lancet* 395: 1101-1102.

105 Amanat F *et al.* (2020) A serological assay to detect SARS-CoV-2 seroconversion in humans. *Nat Med* 26: 1033-1036.

106 Stadlbauer D *et al.* (2020) SARS-CoV-2 Seroconversion in Humans: A Detailed Protocol for a Serological Assay, Antigen Production, and Test Setup. *Curr Protoc Microbiol* 57: e100.

107 Nie J *et al.* (2020) Establishment and validation of a pseudovirus neutralization assay for SARS-CoV-2. *Emerg Microbes Infect* 9: 680-686.

108 Muruato AE *et al.* (2020) A high-throughput neutralizing antibody assay for COVID-19 diagnosis and vaccine evaluation. *Nat Commun* 11: 4059.

109 Matusali G *et al.* (2021) SARS-CoV-2 Serum Neutralization Assay: A Traditional Tool for a Brand-New Virus. *Viruses* 13

110 Ruetalo N *et al.* (2021) Antibody Response against SARS-CoV-2 and Seasonal Coronaviruses in Nonhospitalized COVID-19 Patients. *mSphere* 6

111 Tan CW *et al.* (2020) A SARS-CoV-2 surrogate virus neutralization test based on antibody-mediated blockage of ACE2–spike protein–protein interaction. *Nature Biotechnology* 38: 1073-1078.

112 Junker D *et al.* (2022) COVID-19 patient serum less potently inhibits ACE2-RBD binding for various SARS-CoV-2 RBD mutants. *Scientific Reports* 12: 7168.

113 Lynch KL, Zhou S, Kaul R, Walker R & Wu AH (2022) Evaluation of Neutralizing Antibodies against SARS-CoV-2 Variants after Infection and Vaccination Using a Multiplexed Surrogate Virus Neutralization Test. *Clin Chem* 68: 702-712.

114 Luo YR, Yun C, Chakraborty I, Wu AHB & Lynch KL (2021) A SARS-CoV-2 Label-Free Surrogate Virus Neutralization Test and a Longitudinal Study of Antibody Characteristics in COVID-19 Patients. *J Clin Microbiol* 59: e0019321.

115 Sancilio AE *et al.* (2021) A surrogate virus neutralization test to quantify antibody-mediated inhibition of SARS-CoV-2 in finger stick dried blood spot samples. *Sci Rep* 11: 15321.

116 Mathieu E *et al.* (2021) A global database of COVID-19 vaccinations. *Nature Human Behaviour* 5: 947-953.

117 Falsey AR *et al.* (2021) SARS-CoV-2 Neutralization with BNT162b2 Vaccine Dose 3. *N Engl J Med* 385: 1627-1629.

118 Widge AT *et al.* (2021) Durability of Responses after SARS-CoV-2 mRNA-1273 Vaccination. *N Engl J Med* 384: 80-82.

119 Alter G *et al.* (2021) Immunogenicity of Ad26.COV2.S vaccine against SARS-CoV-2 variants in humans. *Nature* 596: 268-272.

120 Grifoni A *et al.* (2020) Targets of T Cell Responses to SARS-CoV-2 Coronavirus in Humans with COVID-19 Disease and Unexposed Individuals. *Cell* 181: 1489-1501.e1415.

121 Turner JS *et al.* (2021) SARS-CoV-2 mRNA vaccines induce persistent human germinal centre responses. *Nature* 596: 109-113.

122 Dan JM *et al.* (2021) Immunological memory to SARS-CoV-2 assessed for up to 8 months after infection. *Science* 371

123 Robinson PC *et al.* (2022) COVID-19 therapeutics: Challenges and directions for the future. *Proc Natl Acad Sci U S A* 119: e2119893119.

124 Gottlieb RL *et al.* (2021) Early Remdesivir to Prevent Progression to Severe Covid-19 in Outpatients. *New England Journal of Medicine* 386: 305-315.

125 Hammond J *et al.* (2022) Oral Nirmatrelvir for High-Risk, Nonhospitalized Adults with Covid-19. *New England Journal of Medicine* 386: 1397-1408.

126 Jayk Bernal A *et al.* (2021) Molnupiravir for Oral Treatment of Covid-19 in Nonhospitalized Patients. *New England Journal of Medicine* 386: 509-520.

127 Ahmad B, Batool M, Ain QU, Kim MS & Choi S (2021) Exploring the Binding Mechanism of PF-07321332 SARS-CoV-2 Protease Inhibitor through Molecular Dynamics and Binding Free Energy Simulations. *Int J Mol Sci* 22

128 Williams SJ & Goddard-Borger ED (2020) α-glucosidase inhibitors as host-directed antiviral agents with potential for the treatment of COVID-19. *Biochem Soc Trans* 48: 1287-1295.

129 Rajasekharan S *et al.* (2021) Inhibitors of Protein Glycosylation Are Active against the Coronavirus Severe Acute Respiratory Syndrome Coronavirus SARS-CoV-2. *Viruses* 13

130 Dougan M *et al.* (2021) Bamlanivimab plus Etesevimab in Mild or Moderate Covid-19. *N Engl J Med* 385: 1382-1392.

131 Razonable RR *et al.* (2021) Casirivimab-Imdevimab treatment is associated with reduced rates of hospitalization among high-risk patients with mild to moderate coronavirus disease-19. *EClinicalMedicine* 40: 101102.

132 (2022) Tixagevimab-cilgavimab for treatment of patients hospitalised with COVID-19: a randomised, double-blind, phase 3 trial. *Lancet Respir Med* 10: 972-984.

133 Gupta A *et al.* (2021) Early Treatment for Covid-19 with SARS-CoV-2 Neutralizing Antibody Sotrovimab. *N Engl J Med* 385: 1941-1950.

134 Cao Y *et al.* (2022) BA.2.12.1, BA.4 and BA.5 escape antibodies elicited by Omicron infection. *Nature* 608: 593-602.

135 Health NIo, COVID-19 Treatment Guidelines Panel. Coronavirus Disease 2019 (COVID-19) Treatment Guidelines.

136 Jin M-Z & Jin W-L (2020) The updated landscape of tumor microenvironment and drug repurposing. *Signal Transduction and Targeted Therapy* 5: 166.

137 Labani-Motlagh A, Ashja-Mahdavi M & Loskog A (2020) The Tumor Microenvironment: A Milieu Hindering and Obstructing Antitumor Immune Responses. *Front Immunol* 11: 940.

138 Anderson NM & Simon MC (2020) The tumor microenvironment. *Curr Biol* 30: R921-r925.

139 Baghban R *et al.* (2020) Tumor microenvironment complexity and therapeutic implications at a glance. *Cell Communication and Signaling* 18: 59.

140 Schupp J *et al.* (2019) Targeting myeloid cells in the tumor sustaining microenvironment. *Cell Immunol* 343: 103713.

141 Vinogradov S, Warren G & Wei X (2014) Macrophages associated with tumors as potential targets and therapeutic intermediates. *Nanomedicine (Lond)* 9: 695-707.

142 Pathria P, Louis TL & Varner JA (2019) Targeting Tumor-Associated Macrophages in Cancer. *Trends Immunol* 40: 310-327.

143 Murray PJ *et al.* (2014) Macrophage activation and polarization: nomenclature and experimental guidelines. *Immunity* 41: 14-20.

144 Yunna C, Mengru H, Lei W & Weidong C (2020) Macrophage M1/M2 polarization. *Eur J Pharmacol* 877: 173090.

145 Orecchioni M, Ghosheh Y, Pramod AB & Ley K (2019) Macrophage Polarization: Different Gene Signatures in M1(LPS+) vs. Classically and M2(LPS-) vs. Alternatively Activated Macrophages. *Front Immunol* 10: 1084.

146 Liu J, Geng X, Hou J & Wu G (2021) New insights into M1/M2 macrophages: key modulators in cancer progression. *Cancer Cell International* 21: 389.

147 Viola A, Munari F, Sánchez-Rodríguez R, Scolaro T & Castegna A (2019) The Metabolic Signature of Macrophage Responses. *Front Immunol* 10: 1462.

148 Fu LQ *et al.* (2020) The roles of tumor-associated macrophages in tumor angiogenesis and metastasis. *Cell Immunol* 353: 104119.

149 Mantovani A, Allavena P, Marchesi F & Garlanda C (2022) Macrophages as tools and targets in cancer therapy. *Nat Rev Drug Discov* 21: 799-820.

150 Locati M, Curtale G & Mantovani A (2020) Diversity, Mechanisms, and Significance of Macrophage Plasticity. *Annu Rev Pathol* 15: 123-147.

151 Allavena P, Digifico E & Belgiovine C (2021) Macrophages and cancer stem cells: a malevolent alliance. *Molecular Medicine* 27: 121.

152 Radharani NNV *et al.* (2022) Tumor-associated macrophage derived IL-6 enriches cancer stem cell population and promotes breast tumor progression via Stat-3 pathway. *Cancer Cell International* 22: 122.

153 Güç E & Pollard JW (2021) Redefining macrophage and neutrophil biology in the metastatic cascade. *Immunity* 54: 885-902.

154 Lin Y, Xu J & Lan H (2019) Tumor-associated macrophages in tumor metastasis: biological roles and clinical therapeutic applications. *J Hematol Oncol* 12: 76.

155 Cassetta L & Pollard JW (2018) Targeting macrophages: therapeutic approaches in cancer. *Nat Rev Drug Discov* 17: 887-904.

156 Mantovani A, Marchesi F, Malesci A, Laghi L & Allavena P (2017) Tumour-associated macrophages as treatment targets in oncology. *Nat Rev Clin Oncol* 14: 399-416.

157 Tiainen S *et al.* (2015) High numbers of macrophages, especially M2-like (CD163-positive), correlate with hyaluronan accumulation and poor outcome in breast cancer. *Histopathology* 66: 873-883.

158 Zhang QW *et al.* (2012) Prognostic significance of tumor-associated macrophages in solid tumor: a meta-analysis of the literature. *PLoS One* 7: e50946.

159 Larionova I *et al.* (2020) Tumor-Associated Macrophages in Human Breast, Colorectal, Lung, Ovarian and Prostate Cancers. *Front Oncol* 10: 566511.

160 DeNardo DG & Ruffell B (2019) Macrophages as regulators of tumour immunity and immunotherapy. *Nat Rev Immunol* 19: 369-382.

161 Galluzzi L, Humeau J, Buqué A, Zitvogel L & Kroemer G (2020) Immunostimulation with chemotherapy in the era of immune checkpoint inhibitors. *Nat Rev Clin Oncol* 17: 725-741.

162 Fitzgerald KA & Kagan JC (2020) Toll-like Receptors and the Control of Immunity. *Cell* 180: 1044-1066.

163 Ishikawa H & Barber GN (2008) STING is an endoplasmic reticulum adaptor that facilitates innate immune signalling. *Nature* 455: 674-678.

164 Zhang F *et al.* (2019) Genetic programming of macrophages to perform anti-tumor functions using targeted mRNA nanocarriers. *Nat Commun* 10: 3974.

165 Klichinsky M *et al.* (2020) Human chimeric antigen receptor macrophages for cancer immunotherapy. *Nat Biotechnol* 38: 947-953.

166 Zhang W *et al.* (2019) Chimeric antigen receptor macrophage therapy for breast tumours mediated by targeting the tumour extracellular matrix. *Br J Cancer* 121: 837-845.

167 Mantovani A & Longo DL (2018) Macrophage Checkpoint Blockade in Cancer - Back to the Future. *N Engl J Med* 379: 1777-1779.

168 Barkal AA *et al.* (2019) CD24 signalling through macrophage Siglec-10 is a target for cancer immunotherapy. *Nature* 572: 392-396.

169 Feng M *et al.* (2019) Phagocytosis checkpoints as new targets for cancer immunotherapy. *Nat Rev Cancer* 19: 568-586.

170 Advani R *et al.* (2018) CD47 Blockade by Hu5F9-G4 and Rituximab in Non-Hodgkin's Lymphoma. *N Engl J Med* 379: 1711-1721.

171 Fujioka Y *et al.* (1996) A novel membrane glycoprotein, SHPS-1, that binds the SH2-domain-containing protein tyrosine phosphatase SHP-2 in response to mitogens and cell adhesion. *Mol Cell Biol* 16: 6887-6899.

172 Adams S *et al.* (1998) Signal-regulatory protein is selectively expressed by myeloid and neuronal cells. *J Immunol* 161: 1853-1859.

173 Matlung HL, Szilagyi K, Barclay NA & van den Berg TK (2017) The CD47-SIRPα signaling axis as an innate immune checkpoint in cancer. *Immunol Rev* 276: 145-164.

174 Barclay AN & Brown MH (2006) The SIRP family of receptors and immune regulation. *Nat Rev Immunol* 6: 457-464.

175 van den Berg TK *et al.* (2005) A nomenclature for signal regulatory protein family members. *J Immunol* 175: 7788-7789.

176 Sim J *et al.* (2019) Discovery of high affinity, pan-allelic, and pan-mammalian reactive antibodies against the myeloid checkpoint receptor SIRPα. *MAbs* 11: 1036-1052.

177 Seiffert M *et al.* (1999) Human signal-regulatory protein is expressed on normal, but not on subsets of leukemic myeloid cells and mediates cellular adhesion involving its counterreceptor CD47. *Blood* 94: 3633-3643.

178 van den Berg TK & van der Schoot CE (2008) Innate immune 'self' recognition: a role for CD47-SIRPalpha interactions in hematopoietic stem cell transplantation. *Trends Immunol* 29: 203-206.

179 Oldenborg PA *et al.* (2000) Role of CD47 as a marker of self on red blood cells. *Science* 288: 2051-2054.

180 Hatherley D, Harlos K, Dunlop DC, Stuart DI & Barclay AN (2007) The structure of the macrophage signal regulatory protein alpha (SIRPalpha) inhibitory receptor reveals a binding face reminiscent of that used by T cell receptors. *J Biol Chem* 282: 14567-14575.

181 Hatherley D *et al.* (2008) Paired receptor specificity explained by structures of signal regulatory proteins alone and complexed with CD47. *Mol Cell* 31: 266-277.

182 Brooke G, Holbrook JD, Brown MH & Barclay AN (2004) Human lymphocytes interact directly with CD47 through a novel member of the signal regulatory protein (SIRP) family. *J Immunol* 173: 2562-2570.

183 Barclay AN & Van den Berg TK (2014) The interaction between signal regulatory protein alpha (SIRPα) and CD47: structure, function, and therapeutic target. *Annu Rev Immunol* 32: 25-50.

184 Kharitonenkov A *et al.* (1997) A family of proteins that inhibit signalling through tyrosine kinase receptors. *Nature* 386: 181-186.

185 Tsai RK & Discher DE (2008) Inhibition of "self" engulfment through deactivation of myosin-II at the phagocytic synapse between human cells. *J Cell Biol* 180: 989-1003.

186 Campbell IG, Freemont PS, Foulkes W & Trowsdale J (1992) An ovarian tumor marker with homology to vaccinia virus contains an IgV-like region and multiple transmembrane domains. *Cancer Res* 52: 5416-5420.

187 Majeti R *et al.* (2009) CD47 is an adverse prognostic factor and therapeutic antibody target on human acute myeloid leukemia stem cells. *Cell* 138: 286-299.

188 Jaiswal S, Chao MP, Majeti R & Weissman IL (2010) Macrophages as mediators of tumor immunosurveillance. *Trends Immunol* 31: 212-219.

189 Chao MP *et al.* (2010) Anti-CD47 antibody synergizes with rituximab to promote phagocytosis and eradicate non-Hodgkin lymphoma. *Cell* 142: 699-713.

190 Willingham SB *et al.* (2012) The CD47-signal regulatory protein alpha (SIRPa) interaction is a therapeutic target for human solid tumors. *Proc Natl Acad Sci U S A* 109: 6662-6667.

191 Barrera L *et al.* (2017) CD47 overexpression is associated with decreased neutrophil apoptosis/phagocytosis and poor prognosis in non-small-cell lung cancer patients. *Br J Cancer* 117: 385-397.

192 Yang H, Yan M, Li W & Xu L (2022) SIRPα and PD1 expression on tumor-associated macrophage predict prognosis of intrahepatic cholangiocarcinoma. *Journal of Translational Medicine* 20: 140.

193 Sugimura-Nagata A *et al.* (2021) Expression and Prognostic Significance of CD47-SIRPA Macrophage Checkpoint Molecules in Colorectal Cancer. *Int J Mol Sci* 22

194 Tao K, Wei Z, Xia Y, Zhao R & Xu H (2022) High SIRPA Expression Predicts Poor Prognosis and Correlates with Immune Infiltrates in Patients with Esophageal Carcinoma. *Journal of Healthcare Engineering* 2022: 3565676.

195 Chen Y-P *et al.* (2019) SIRPα expression delineates subsets of intratumoral monocyte/macrophages with different functional and prognostic impact in follicular lymphoma. *Blood Cancer Journal* 9: 84.

196 Zhao H-J *et al.* (2018) Prognostic significance of CD47 in human malignancies: a systematic review and meta-analysis. *Translational Cancer Research* 7: 609-621.

197 Chao MP *et al.* (2011) Therapeutic antibody targeting of CD47 eliminates human acute lymphoblastic leukemia. *Cancer Res* 71: 1374-1384.

198 Chao MP *et al.* (2011) Extranodal dissemination of non-Hodgkin lymphoma requires CD47 and is inhibited by anti-CD47 antibody therapy. *Blood* 118: 4890-4901.

199 Ingram JR *et al.* (2017) Localized CD47 blockade enhances immunotherapy for murine melanoma. *Proc Natl Acad Sci U S A* 114: 10184-10189.

200 Zhang X *et al.* (2017) Targeting CD47 and Autophagy Elicited Enhanced Antitumor Effects in Non-Small Cell Lung Cancer. *Cancer Immunol Res* 5: 363-375.

201 Dizman N & Buchbinder EI (2021) Cancer Therapy Targeting CD47/SIRP&alpha. *Cancers* 13: 6229.

202 Jiang Z, Sun H, Yu J, Tian W & Song Y (2021) Targeting CD47 for cancer immunotherapy. *Journal of Hematology & Oncology* 14: 180.

203 Park JC *et al.* (2021) 439 A phase 2 study of evorpacept (ALX148) in combination with pembrolizumab in patients with advanced head and neck squamous cell carcinoma (HNSCC); ASPEN-03. *Journal for ImmunoTherapy of Cancer* 9: A469-A469.

204 Gan HK *et al.*, 2021. Safety of AK117, an anti-CD47 monoclonal antibody, in patients with advanced or metastatic solid tumors in a phase I study. Wolters Kluwer Health.

205 Ansell SM *et al.* (2021) Phase I study of the CD47 blocker TTI-621 in patients with relapsed or refractory hematologic malignancies. *Clinical Cancer Research* 27: 2190-2199.

206 Ring NG *et al.* (2017) Anti-SIRPα antibody immunotherapy enhances neutrophil and macrophage antitumor activity. *Proc Natl Acad Sci U S A* 114: E10578-e10585.

207 Voets E *et al.* (2019) Functional characterization of the selective pan-allele anti-SIRPα antibody ADU-1805 that blocks the SIRPα-CD47 innate immune checkpoint. *J Immunother Cancer* 7: 340.

208 Ho CC *et al.* (2015) "Velcro" engineering of high affinity CD47 ectodomain as signal regulatory protein α (SIRPα) antagonists that enhance antibody-dependent cellular phagocytosis. *J Biol Chem* 290: 12650-12663.

209 Bresser K *et al.* (2022) QPCTL regulates macrophage and monocyte abundance and inflammatory signatures in the tumor microenvironment. *OncoImmunology* 11: 2049486.

210 Zhang W *et al.* (2020) Advances in Anti-Tumor Treatments Targeting the CD47/SIRPα Axis. *Frontiers in Immunology* 11

211 Liu X *et al.* (2015) CD47 blockade triggers T cell-mediated destruction of immunogenic tumors. *Nat Med* 21: 1209-1215.

212 Kim MJ *et al.* (2008) Association of CD47 with natural killer cell-mediated cytotoxicity of head-and-neck squamous cell carcinoma lines. *Tumour Biol* 29: 28-34.

213 Abraham J (2020) Passive antibody therapy in COVID-19. *Nat Rev Immunol* 20: 401-403.

214 Iwasaki A & Yang Y (2020) The potential danger of suboptimal antibody responses in COVID-19. *Nat Rev Immunol* 20: 339-341.

215 Wrapp D *et al.* (2020) Structural Basis for Potent Neutralization of Betacoronaviruses by Single-Domain Camelid Antibodies. *Cell* 181: 1004-1015.e1015.

216 Chen W, Zhu Z, Feng Y & Dimitrov DS (2008) Human domain antibodies to conserved sterically restricted regions on gp120 as exceptionally potent cross-reactive HIV-1 neutralizers. *Proc Natl Acad Sci U S A* 105: 17121-17126.

217 Ashour J *et al.* (2015) Intracellular expression of camelid single-domain antibodies specific for influenza virus nucleoprotein uncovers distinct features of its nuclear localization. *J Virol* 89: 2792-2800.

218 Tarr AW *et al.* (2013) An alpaca nanobody inhibits hepatitis C virus entry and cell-to-cell transmission. *Hepatology* 58: 932-939.

219 Schepens B *et al.* (2011) Nanobodies® specific for respiratory syncytial virus fusion protein protect against infection by inhibition of fusion. *J Infect Dis* 204: 1692-1701.

220 Wu Y, Jiang S & Ying T (2017) Single-Domain Antibodies As Therapeutics against Human Viral Diseases. *Front Immunol* 8: 1802.

221 Zhao G *et al.* (2018) A Novel Nanobody Targeting Middle East Respiratory Syndrome Coronavirus (MERS-CoV) Receptor-Binding Domain Has Potent Cross-Neutralizing Activity and Protective Efficacy against MERS-CoV. *J Virol* 92

222 Stalin Raj V *et al.* (2018) Chimeric camel/human heavy-chain antibodies protect against MERS-CoV infection. *Sci Adv* 4: eaas9667.

223 Aria H *et al.* (2022) Outlook of therapeutic and diagnostic competency of nanobodies against SARS-CoV-2: A systematic review. *Anal Biochem* 640: 114546.

224 Valenzuela-Nieto G *et al.* (2022) Nanobodies: COVID-19 and Future Perspectives. *Frontiers in Drug Discovery* 2

225 Bessalah S *et al.* (2021) Perspective on therapeutic and diagnostic potential of camel nanobodies for coronavirus disease-19 (COVID-19). *3 Biotech* 11: 89.

226 Hanke L *et al.* (2020) An alpaca nanobody neutralizes SARS-CoV-2 by blocking receptor interaction. *Nat Commun* 11: 4420.

227 Xiang Y *et al.* (2020) Versatile and multivalent nanobodies efficiently neutralize SARS-CoV-2. *Science* 370: 1479-1484.

228 Koenig PA *et al.* (2021) Structure-guided multivalent nanobodies block SARS-CoV-2 infection and suppress mutational escape. *Science* 371

229 Güttler T *et al.* (2021) Neutralization of SARS-CoV-2 by highly potent, hyperthermostable, and mutation-tolerant nanobodies. *Embo j* 40: e107985.

230 Favorskaya IA *et al.* (2022) Single-Domain Antibodies Efficiently Neutralize SARS-CoV-2 Variants of Concern. *Frontiers in Immunology* 13

231 Chi X *et al.* (2020) Humanized single domain antibodies neutralize SARS-CoV-2 by targeting the spike receptor binding domain. *Nat Commun* 11: 4528.

232 Huo J *et al.* (2020) Neutralizing nanobodies bind SARS-CoV-2 spike RBD and block interaction with ACE2. *Nature Structural & Molecular Biology* 27: 846-854.

233 Custódio TF *et al.* (2020) Selection, biophysical and structural analysis of synthetic nanobodies that effectively neutralize SARS-CoV-2. *Nat Commun* 11: 5588.

234 Walter JD *et al.* (2022) Biparatopic sybodies neutralize SARS-CoV-2 variants of concern and mitigate drug resistance. *EMBO Rep* 23: e54199.

235 Huo J *et al.* (2021) A potent SARS-CoV-2 neutralising nanobody shows therapeutic efficacy in the Syrian golden hamster model of COVID-19. *Nature Communications* 12: 5469.

236 Ahmad J *et al.* (2021) Structures of synthetic nanobody-SARS-CoV-2 receptor-binding domain complexes reveal distinct sites of interaction. *J Biol Chem* 297: 101202.

237 Barnes CO *et al.* (2020) SARS-CoV-2 neutralizing antibody structures inform therapeutic strategies. *Nature* 588: 682-687.

238 Starr TN *et al.* (2021) SARS-CoV-2 RBD antibodies that maximize breadth and resistance to escape. *Nature* 597: 97-102.

239 Rouet R *et al.* (2023) Broadly neutralizing SARS-CoV-2 antibodies through epitope-based selection from convalescent patients. *Nature Communications* 14: 687.

240 Shi R *et al.* (2020) A human neutralizing antibody targets the receptor-binding site of SARS-CoV-2. *Nature* 584: 120-124.

241 Jones BE *et al.* (2021) The neutralizing antibody, LY-CoV555, protects against SARS-CoV-2 infection in nonhuman primates. *Sci Transl Med* 13

242 Pinto D *et al.* (2020) Cross-neutralization of SARS-CoV-2 by a human monoclonal SARS-CoV antibody. *Nature* 583: 290-295.

243 Tang Q, Owens RJ & Naismith JH (2021) Structural Biology of Nanobodies against the Spike Protein of SARS-CoV-2. *Viruses* 13

244 Yuan M *et al.* (2020) Structural basis of a shared antibody response to SARS-CoV-2. *Science* 369: 1119-1123.

245 Zhou D *et al.* (2021) Evidence of escape of SARS-CoV-2 variant B.1.351 from natural and vaccine-induced sera. *Cell* 184: 2348-2361.e2346.

246 Planas D *et al.* (2021) Reduced sensitivity of SARS-CoV-2 variant Delta to antibody neutralization. *Nature* 596: 276-280.

247 Tian D, Sun Y, Zhou J & Ye Q (2021) The Global Epidemic of the SARS-CoV-2 Delta Variant, Key Spike Mutations and Immune Escape. *Frontiers in Immunology* 12

248 Schepens B *et al.* (2021) An affinity-enhanced, broadly neutralizing heavy chain-only antibody protects against SARS-CoV-2 infection in animal models. *Sci Transl Med* 13: eabi7826.

249 Wu X *et al.* (2021) A potent bispecific nanobody protects hACE2 mice against SARS-CoV-2 infection via intranasal administration. *Cell Rep* 37: 109869.

250 Nambulli S *et al.* (2021) Inhalable Nanobody (PiN-21) prevents and treats SARS-CoV-2 infections in Syrian hamsters at ultra-low doses. *Sci Adv* 7

251 Chi X *et al.* (2022) An ultrapotent RBD-targeted biparatopic nanobody neutralizes broad SARS-CoV-2 variants. *Signal Transduction and Targeted Therapy* 7: 44.

252 Pymm P *et al.* (2022) Biparatopic nanobodies targeting the receptor binding domain efficiently neutralize SARS-CoV-2. *iScience* 25: 105259.

253 Hendriks J *et al.* (2022) High Titers of Low Affinity Antibodies in COVID-19 Patients Are Associated With Disease Severity. *Frontiers in Immunology* 13

254 Uysal BB, Yavuzer S, Islamoglu MS & Cengiz M (2022) Measurement of antibody levels in patients with COVID-19 over time by immunofluorescence assay: a longitudinal observational study. *J Int Med Res* 50: 3000605211069279.

255 Khoury DS *et al.* (2021) Neutralizing antibody levels are highly predictive of immune protection from symptomatic SARS-CoV-2 infection. *Nat Med* 27: 1205-1211.

256 Pang NY-L, Pang AS-R, Chow VT & Wang D-Y (2021) Understanding neutralising antibodies against SARS-CoV-2 and their implications in clinical practice. *Military Medical Research* 8: 47.

257 Cromer D *et al.* (2022) Neutralising antibody titres as predictors of protection against SARS-CoV-2 variants and the impact of boosting: a meta-analysis. *Lancet Microbe* 3: e52-e61.

258 Schöler L *et al.* (2020) A Novel In-Cell ELISA Assay Allows Rapid and Automated Quantification of SARS-CoV-2 to Analyze Neutralizing Antibodies and Antiviral Compounds. *Front Immunol* 11: 573526.

259 Walker SN *et al.* (2020) SARS-CoV-2 Assays To Detect Functional Antibody Responses That Block ACE2 Recognition in Vaccinated Animals and Infected Patients. *J Clin Microbiol* 58

260 Junker D *et al.* (2022) Antibody binding and ACE2 binding inhibition is significantly reduced for both the BA1 and BA2 omicron variants. *Clinical Infectious Diseases* 76: e240–e249.

261 Greaney AJ *et al.* (2021) Mapping mutations to the SARS-CoV-2 RBD that escape binding by different classes of antibodies. *Nature Communications* 12: 4196.

262 Xiong D *et al.* (2022) Immune Escape Mechanisms of SARS-CoV-2 Delta and Omicron Variants against Two Monoclonal Antibodies That Received Emergency Use Authorization. *The Journal of Physical Chemistry Letters* 13: 6064-6073.

263 Wang P *et al.* (2021) Antibody resistance of SARS-CoV-2 variants B.1.351 and B.1.1.7. *Nature* 593: 130-135.

264 Winkler ES *et al.* (2020) SARS-CoV-2 infection of human ACE2-transgenic mice causes severe lung inflammation and impaired function. *Nat Immunol* 21: 1327-1335.

265 Haga K *et al.* (2021) Nasal delivery of single-domain antibody improves symptoms of SARS-CoV-2 infection in an animal model. *PLoS Pathog* 17: e1009542.

266 Pymm P *et al.* (2021) Nanobody cocktails potently neutralize SARS-CoV-2 D614G N501Y variant and protect mice. *Proc Natl Acad Sci U S A* 118

267 Movahedi K *et al.* (2012) Nanobody-Based Targeting of the Macrophage Mannose Receptor for Effective In Vivo Imaging of Tumor-Associated Macrophages. *Cancer Research* 72: 4165-4177.

268 Rashidian M *et al.* (2015) Noninvasive imaging of immune responses. *Proc Natl Acad Sci U S A* 112: 6146-6151.

269 Zheng F *et al.* (2014) Molecular Imaging with Macrophage CRIg-Targeting Nanobodies for Early and Preclinical Diagnosis in a Mouse Model of Rheumatoid Arthritis. *Journal of Nuclear Medicine* 55: 824-829.

270 Zheng F *et al.* (2015) Monitoring liver macrophages using nanobodies targeting Vsig4: Concanavalin A induced acute hepatitis as paradigm. *Immunobiology* 220: 200-209.

271 De Vlaminck K *et al.* (2021) Imaging of Glioblastoma Tumor-Associated Myeloid Cells Using Nanobodies Targeting Signal Regulatory Protein Alpha. *Front Immunol* 12: 777524.

272 Ulrichts H *et al.* (2011) Antithrombotic drug candidate ALX-0081 shows superior preclinical efficacy and safety compared with currently marketed antiplatelet drugs. *Blood* 118: 757-765.

273 Haslam A, Gill J & Prasad V (2020) Estimation of the Percentage of US Patients With Cancer Who Are Eligible for Immune Checkpoint Inhibitor Drugs. *JAMA Netw Open* 3: e200423.

274 Khalil DN, Smith EL, Brentjens RJ & Wolchok JD (2016) The future of cancer treatment: immunomodulation, CARs and combination immunotherapy. *Nat Rev Clin Oncol* 13: 273-290.

275 Marin-Acevedo JA *et al.* (2018) Next generation of immune checkpoint therapy in cancer: new developments and challenges. *Journal of Hematology & Oncology* 11: 39.

276 Yang L, Li A, Lei Q & Zhang Y (2019) Tumor-intrinsic signaling pathways: key roles in the regulation of the immunosuppressive tumor microenvironment. *Journal of Hematology & Oncology* 12: 125.

277 Ugel S, De Sanctis F, Mandruzzato S & Bronte V (2015) Tumor-induced myeloid deviation: when myeloid-derived suppressor cells meet tumor-associated macrophages. *J Clin Invest* 125: 3365-3376.

278 Condamine T, Ramachandran I, Youn JI & Gabrilovich DI (2015) Regulation of tumor metastasis by myeloid-derived suppressor cells. *Annu Rev Med* 66: 97-110.

279 Gauttier V *et al.* (2020) Selective SIRPα blockade reverses tumor T cell exclusion and overcomes cancer immunotherapy resistance. *The Journal of Clinical Investigation* 130: 6109-6123.

280 Ma L *et al.* (2020) Preclinical development of a novel CD47 nanobody with less toxicity and enhanced anti-cancer therapeutic potential. *J Nanobiotechnology* 18: 12.

281 Hatterer E *et al.* (2019) Co-engaging CD47 and CD19 with a bispecific antibody abrogates B-cell receptor/CD19 association leading to impaired B-cell proliferation. *MAbs* 11: 322-334.

282 Lakhani N *et al.* (2021) 429 Phase 1 dose escalation study of the agonist redirected checkpoint, SL-172154 (SIRPα-Fc-CD40L) in subjects with platinum-resistant ovarian cancer. *Journal for ImmunoTherapy of Cancer* 9: A459-A459.

283 Zhou Z *et al.* (2022) Tumor-intrinsic SIRPA promotes sensitivity to checkpoint inhibition immunotherapy in melanoma. *Cancer Cell* 40: 1324-1340.e1328.

284 Postow MA, Sidlow R & Hellmann MD (2018) Immune-Related Adverse Events Associated with Immune Checkpoint Blockade. *N Engl J Med* 378: 158-168.

285 Naimi A *et al.* (2022) Tumor immunotherapies by immune checkpoint inhibitors (ICIs); the pros and cons. *Cell Communication and Signaling* 20: 44.

286 Gilson P, Merlin JL & Harlé A (2022) Deciphering Tumour Heterogeneity: From Tissue to Liquid Biopsy. *Cancers (Basel)* 14

287 Russano M *et al.* (2020) Liquid biopsy and tumor heterogeneity in metastatic solid tumors: the potentiality of blood samples. *J Exp Clin Cancer Res* 39: 95.

288 Abousaway O, Rakhshandehroo T, Van den Abbeele AD, Kircher MF & Rashidian M (2021) Noninvasive Imaging of Cancer Immunotherapy. *Nanotheranostics* 5: 90-112.

289 Schwenck J *et al.* (2023) Advances in PET imaging of cancer. *Nature Reviews Cancer*

290 Wei W *et al.* (2020) ImmunoPET: Concept, Design, and Applications. *Chem Rev* 120: 3787-3851.

291 Dewulf J, Adhikari K, Vangestel C, Wyngaert TVD & Elvas F (2020) Development of Antibody Immuno-PET/SPECT Radiopharmaceuticals for Imaging of Oncological Disorders-An Update. *Cancers (Basel)* 12

292 D'Huyvetter M *et al.* (2014) Radiolabeled nanobodies as theranostic tools in targeted radionuclide therapy of cancer. *Expert Opin Drug Deliv* 11: 1939-1954.

293 Manafi-Farid R *et al.* (2022) ImmunoPET: Antibody-Based PET Imaging in Solid Tumors. *Frontiers in Medicine* 9

294 Rashidian M *et al.* (2017) Predicting the response to CTLA-4 blockade by longitudinal noninvasive monitoring of CD8 T cells. *J Exp Med* 214: 2243-2255.

295 Liu Q *et al.* (2021) Immuno-PET imaging of (68)Ga-labeled nanobody Nb109 for dynamic monitoring the PD-L1 expression in cancers. *Cancer Immunol Immunother* 70: 1721-1733.

296 Morais M & Ma MT (2018) Site-specific chelator-antibody conjugation for PET and SPECT imaging with radiometals. *Drug Discov Today Technol* 30: 91-104.

297 Chigoho DM *et al.* (2021) Site-Specific Radiolabeling of a Human PD-L1 Nanobody via Maleimide-Cysteine Chemistry. *Pharmaceuticals (Basel)* 14

298 Hansen SB & Andersen KR (2022) Introducing Cysteines into Nanobodies for Site-Specific Labeling. *Methods Mol Biol* 2446: 327-343.

299 Massa S *et al.* (2016) Sortase A-mediated site-specific labeling of camelid single-domain antibody-fragments: a versatile strategy for multiple molecular imaging modalities. *Contrast Media Mol Imaging* 11: 328-339.

300 Mukherjee S, Sonanini D, Maurer A & Daldrup-Link HE (2019) The yin and yang of imaging tumor associated macrophages with PET and MRI. *Theranostics* 9: 7730-7748.

301 Blykers A *et al.* (2015) PET Imaging of Macrophage Mannose Receptor-Expressing Macrophages in Tumor Stroma Using 18F-Radiolabeled Camelid Single-Domain Antibody Fragments. *J Nucl Med* 56: 1265-1271.

302 Eichendorff S *et al.* (2015) Biodistribution and PET imaging of a novel [68Ga]-anti-CD163-antibody conjugate in rats with collagen-induced arthritis and in controls. *Mol Imaging Biol* 17: 87-93.

303 Jager NA *et al.* (2014) Folate Receptor-β Imaging Using ^{99m}Tc-Folate to Explore Distribution of Polarized Macrophage Populations in Human Atherosclerotic Plaque. *Journal of Nuclear Medicine* 55: 1945-1951.

304 Hellberg S *et al.* (2018) Positron Emission Tomography Imaging of Macrophages in Atherosclerosis with (18)F-GE-180, a Radiotracer for Translocator Protein (TSPO). *Contrast Media Mol Imaging* 2018: 9186902.

305 Bailly C *et al.* (2019) What is the Best Radionuclide for Immuno-PET of Multiple Myeloma? A Comparison Study Between (89)Zr- and (64)Cu-Labeled Anti-CD138 in a Preclinical Syngeneic Model. *Int J Mol Sci* 20

306 Takada A & Kawaoka Y (2003) Antibody-dependent enhancement of viral infection: molecular mechanisms and in vivo implications. *Reviews in Medical Virology* 13: 387-398.

307 Shimizu J *et al.* (2022) Reevaluation of antibody-dependent enhancement of infection in anti-SARS-CoV-2 therapeutic antibodies and mRNA-vaccine antisera using FcR- and ACE2-positive cells. *Scientific Reports* 12: 15612.

308 VanBlargan LA *et al.* (2022) An infectious SARS-CoV-2 B.1.1.529 Omicron virus escapes neutralization by therapeutic monoclonal antibodies. *Nat Med* 28: 490-495.

309 Liu L *et al.* (2022) Striking antibody evasion manifested by the Omicron variant of SARS-CoV-2. *Nature* 602: 676-681.

310 Planas D *et al.* (2022) Considerable escape of SARS-CoV-2 Omicron to antibody neutralization. *Nature* 602: 671-675.

311 Maeda R *et al.* (2022) A panel of nanobodies recognizing conserved hidden clefts of all SARS-CoV-2 spike variants including Omicron. *Communications Biology* 5: 669.

312 Nagata K *et al.* (2022) Intratracheal trimerized nanobody cocktail administration suppresses weight loss and prolongs survival of SARS-CoV-2 infected mice. *Communications Medicine* 2: 152.

313 Sheikh A *et al.* (2022) Severity of omicron variant of concern and effectiveness of vaccine boosters against symptomatic disease in Scotland (EAVE II): a national cohort study with nested test-negative design. *The Lancet Infectious Diseases* 22: 959-966.

314 Hyams C *et al.* (2023) Severity of Omicron (B.1.1.529) and Delta (B.1.617.2) SARS-CoV-2 infection among hospitalised adults: a prospective cohort study in Bristol, United Kingdom. *The Lancet Regional Health - Europe* 25: 100556.

315 Roovers RC *et al.* (2011) A biparatopic anti-EGFR nanobody efficiently inhibits solid tumour growth. *International Journal of Cancer* 129: 2013-2024.

316 Zhang F *et al.* (2017) Structural basis of a novel PD-L1 nanobody for immune checkpoint blockade. *Cell Discov* 3: 17004.

317 Zhao H *et al.* (2021) ImmunoPET imaging of human CD8(+) T cells with novel (68)Ga-labeled nanobody companion diagnostic agents. *J Nanobiotechnology* 19: 42.

318 Hutmacher C & Neri D (2019) Antibody-cytokine fusion proteins: Biopharmaceuticals with immunomodulatory properties for cancer therapy. *Advanced Drug Delivery Reviews* 141: 67-91.

319 Li Z *et al.* (2022) Depletion of tumor associated macrophages enhances local and systemic platelet-mediated anti-PD-1 delivery for post-surgery tumor recurrence treatment. *Nature Communications* 13: 1845.

320 Chen Y *et al.* (2021) Targeting tumor-associated macrophages: A potential treatment for solid tumors. *J Cell Physiol* 236: 3445-3465.

321 Sefik E *et al.* (2022) Inflammasome activation in infected macrophages drives COVID-19 pathology. *Nature* 606: 585-593.

322 Ma WT, Gao F, Gu K & Chen DK (2019) The Role of Monocytes and Macrophages in Autoimmune Diseases: A Comprehensive Review. *Front Immunol* 10: 1140.

323 Nishimura T *et al.* (2020) SIRPα on CD11c(+) cells induces Th17 cell differentiation and subsequent inflammation in the CNS in experimental autoimmune encephalomyelitis. *Eur J Immunol* 50: 1560-1570.

Figures were created with BioRender.com.

Acknowledgements

I would like to express my sincere gratitude to my advisor Prof. Dr. Ulrich Rothbauer for his continuous support, motivation and dedication during my PhD study. Thanks to Prof. Dr. Rothbauer, I was given unique opportunities to grow both scientifically and personally. I would like to thank my second advisor Prof. Dr. Bernd Pichler for the great collaboration between the Werner Siemens Imaging Center and the NMI Natural and Medical Sciences Institute at the University of Tübingen, which enabled me to do my PhD thesis.

I would like to thank all cooperation partners, with whom we were able to perform versatile research projects. Especially I want to thank Dr. Nicole Schneiderhan-Marra and her team for the intensive collaboration for all SARS-CoV-2 related projects, which were successfully completed under extreme time pressure. I would like to thank Prof. Dr. Thilo Stehle, Prof. Dr. Michael Schindler, Prof. Dr. Martin Schwemmle, Prof. Dr. Karin Klingel and their teams for the interdisciplinary joint effort to characterize the SARS-CoV-2 specific Nbs. I would like to thank Dr. Anne Zeck and her team for their support concerning HDX-MS and MS analysis. I would like to thank PD Dr. Manfred Kneilling and Dr. Dominik Sonanini and their teams for the fruitful collaboration for the Nb-based PET tracers, a topic that will continue to challenge us.

Special thanks to Dr. Björn Tränkle and Dr. Philipp Kaiser, who supported me with their many years of experience throughout the entire PhD. I would like to thank all NanoBuddies from the AG Rothbauer, especially Ursula Härle, Funmilayo Fagbadebo, Desiree Frecot, Dr. Sandra Burgstaller, Theresa Fröhlich and Inga Leske for their support, stimulating discussions, motivation, and friendly working environment.

Finally, I would like to thank my family for their unlimited support and encouragement.

Declaration

Ich erkläre hiermit, dass ich die zur Promotion eingereichte Arbeit mit dem Titel: *„Two Birds with One Stone: Theranostic Applications of Nanobodies“* selbständig verfasst, nur die angegebenen Quellen und Hilfsmittel benutzt und wörtlich oder inhaltlich übernommene Stellen als solche gekennzeichnet habe. Ich erkläre, dass die Richtlinien zur Sicherung guter wissenschaftlicher Praxis der Universität Tübingen (Beschluss des Senats vom 25.5.2000) beachtet wurden. Ich versichere an Eides statt, dass diese Angaben wahr sind und dass ich nichts verschwiegen habe. Mir ist bekannt, dass die falsche Abgabe einer Versicherung an Eides statt mit Freiheitsstrafe bis zu drei Jahren oder mit Geldstrafe bestraft wird.

Teresa R. Wagner

Appendix

Appendix I:

Wagner TR§, Ostertag E§, Kaiser PD, Gramlich M, Ruetalo N, Junker D, Haering J, Traenkle B, Becker M, Dulovic A, Schweizer H, Nueske S, Scholz A, Zeck A, Schenke-Layland K, Nelde A, Strengert M, Walz JS, Zocher G, Stehle T, Schindler M, Schneiderhan-Marra N, Rothbauer U (2021) **NeutrobodyPlex-monitoring SARS-CoV-2 neutralizing immune responses using nanobodies**. EMBO Rep 22: e52325.

Article

TRANSPARENT PROCESS OPEN ACCESS

EMBO reports

NeutrobodyPlex—monitoring SARS-CoV-2 neutralizing immune responses using nanobodies

Teresa R Wagner[1,2,†], Elena Ostertag[3,†], Philipp D Kaiser[2], Marius Gramlich[2], Natalia Ruetalo[4], Daniel Junker[2], Julia Haering[2], Bjoern Traenkle[2], Matthias Becker[2], Alex Dulovic[2], Helen Schweizer[5], Stefan Nueske[5], Armin Scholz[5], Anne Zeck[2], Katja Schenke-Layland[2,6,7,8], Annika Nelde[6,9,10], Monika Strengert[11,12], Juliane S Walz[6,9,10,13], Georg Zocher[3], Thilo Stehle[3,14], Michael Schindler[4], Nicole Schneiderhan-Marra[2] & Ulrich Rothbauer[1,2,6,*]

Abstract

In light of the COVID-19 pandemic, there is an ongoing need for diagnostic tools to monitor the immune status of large patient cohorts and the effectiveness of vaccination campaigns. Here, we present 11 unique nanobodies (Nbs) specific for the SARS-CoV-2 spike receptor-binding domain (RBD), of which 8 Nbs potently inhibit the interaction of RBD with angiotensin-converting enzyme 2 (ACE2) as the major viral docking site. Following detailed epitope mapping and structural analysis, we select two inhibitory Nbs, one of which binds an epitope inside and one of which binds an epitope outside the RBD:ACE2 interface. Based on these, we generate a biparatopic nanobody (bipNb) with viral neutralization efficacy in the picomolar range. Using bipNb as a surrogate, we establish a competitive multiplex binding assay ("NeutrobodyPlex") for detailed analysis of the presence and performance of neutralizing RBD-binding antibodies in serum of convalescent or vaccinated patients. We demonstrate that NeutrobodyPlex enables high-throughput screening and detailed analysis of neutralizing immune responses in infected or vaccinated individuals, to monitor immune status or to guide vaccine design.

Keywords immune response; nanobodies; neutralizing antibodies; SARS-CoV-2; serological assay

Subject Categories Immunology; Microbiology, Virology & Host Pathogen Interaction; Structural Biology

DOI 10.15252/embr.202052325 | Received 21 December 2020 | Revised 23 March 2021 | Accepted 25 March 2021 | Published online 27 April 2021

EMBO Reports (2021) 22: e52325

Introduction

As of March 2021, the COVID-19 pandemic has led to the deaths of more than 2.8 million people worldwide and continues to cause severe lockdowns and dramatic economic losses. The emergence and spread of new mutants pose additional risk to current vaccination campaigns (Wang *et al*, 2021). The severe acute respiratory syndrome coronavirus 2 (SARS-CoV-2) as causative agent of the disease expresses a surface spike glycoprotein (spike), which consists of two subunits S1 and S2 (Wrapp *et al*, 2020b; Zhu *et al*, 2020). For viral infection, the receptor-binding domain (RBD), located within S1 interacts with the angiotensin-converting enzyme 2 (ACE2) expressed on human epithelial cells of the respiratory tract (Tai *et al*, 2020; Wrapp *et al*, 2020b; Yan *et al*, 2020). In-depth analysis revealed the presence of spike-specific neutralizing antibodies (NAbs) in convalescent individuals, which were shown to inhibit viral uptake by various mechanisms (Rogers *et al*, 2020; Tortorici *et al*, 2020). In this context, a constantly growing number of NAbs specifically targeting the RBD have been described, underlining the importance of blocking the RBD:ACE2 interaction site for the

1 Pharmaceutical Biotechnology, Eberhard Karls University, Tuebingen, Germany
2 Natural and Medical Sciences Institute, University of Tuebingen, Reutlingen, Germany
3 Interfaculty Institute of Biochemistry, Eberhard Karls University, Tuebingen, Germany
4 Institute for Medical Virology and Epidemiology of Viral Diseases, University Hospital Tuebingen, Tuebingen, Germany
5 Livestock Center of the Faculty of Veterinary Medicine, Ludwig Maximilians University, Oberschleissheim, Germany
6 Cluster of Excellence iFIT (EXC2180) "Image-Guided and Functionally Instructed Tumor Therapies", Eberhard Karls University, Tuebingen, Germany
7 Department of Women's Health, Research Institute for Women's Health, Eberhard Karls University, Tuebingen, Germany
8 Department of Medicine/Cardiology, Cardiovascular Research Laboratories, David Geffen School of Medicine at UCLA, Los Angeles, CA, USA
9 Clinical Collaboration Unit Translational Immunology, German Cancer Consortium (DKTK), Department of Internal Medicine, University Hospital Tuebingen, Tuebingen, Germany
10 Institute for Cell Biology, Department of Immunology, Eberhard Karls University, Tuebingen, Germany
11 Department of Epidemiology. Helmholtz Centre for Infection Research. Braunschweig. Germany
12 TWINCORE GmbH, Centre for Experimental and Clinical Infection Research, A Joint venture of the Hannover Medical School and the Helmholtz Centre for Infection Research, Hannover, Germany
13 Dr. Margarete Fischer-Bosch Institute of Clinical Pharmacology and Robert Bosch Center for Tumor Disease, RBCT, Stuttgart, Germany
14 Vanderbilt University School of Medicine, Nashville, TN, USA
*Corresponding author. Tel: +49 7121 51530-415; Fax: +49 7121 51530-816; E-mail: ulrich.rothbauer@uni-tuebingen.de
†These authors contributed equally to this work

development of a protective immune response (Brouwer *et al,* 2020; Cao *et al,* 2020; Ju *et al,* 2020; Robbiani *et al,* 2020; Shi *et al,* 2020; Tai *et al,* 2020; Yu *et al,* 2020). To date, numerous NAbs are in preclinical or clinical development for prophylactic and therapeutic options, providing immediate protection against SARS-CoV-2 infection (reviewed in Jiang *et al,* 2020; Zohar & Alter, 2020).

Promising alternatives to conventional antibodies (IgGs) are single-domain antibodies (nanobodies, Nbs) derived from the heavy-chain antibodies of camelids (Fig 1) (Muyldermans, 2013). Due to their small size and compact fold, Nbs show high chemical stability, solubility, and fast tissue penetration. Nbs can be efficiently selected against different epitopes on the same antigen and converted into multivalent formats (Muyldermans, 2013). The potential of Nbs to address SARS-CoV-2 has been impressively demonstrated by the recent identification of several RBD-specific Nbs from naïve/ synthetic libraries (Chi *et al,* 2020a; Custodio *et al,* 2020; Huo *et al,* 2020; preprint: Schoof *et al,* 2020; preprint: Walter *et al,* 2020; preprint: Ahmad *et al,* 2021) or immunized animals (Chi *et al,* 2020a; preprint: Esparza *et al,* 2020; preprint: Gai *et al,* 2020; Hanke *et al,* 2020; preprint: Nieto *et al,* 2020; Wrapp *et al,* 2020a; Xiang *et al,* 2020; Koenig *et al,* 2021). Some of the identified Nbs show a high viral neutralizing potency proposed by blocking the RBD:ACE2 interface (Custodio *et al,* 2020; Hanke *et al,* 2020; Koenig *et al,* 2021), activation of the SARS-CoV-2 fusion machinery (Koenig *et al,* 2021), or induction of an inactive spike conformation (preprint: Schoof *et al,* 2020).

Since the pandemic outbreak, multiple serological SARS-CoV-2 assays have been established to monitor seroconversion in individuals and estimate the level of endemic infection in the general population. However, most available serological tests measure the full immune response and can therefore not differentiate between total binding and neutralizing antibodies (Amanat *et al,* 2020; preprint: Lassaunière *et al,* 2020; Robbiani *et al,* 2020; preprint: Roxhed *et al,* 2020; Stadlbauer *et al,* 2020; Tang *et al,* 2020; Becker *et al,* 2021). Detection of the latter is still mostly performed by conventional virus neutralization tests (VNTs), which are both time consuming (2–4 days) and require work with infectious SARS-CoV-2 virions in a specialized biosafety level 3 (BSL3) facility (Muruato *et al,* 2020; Scholer *et al,* 2020).

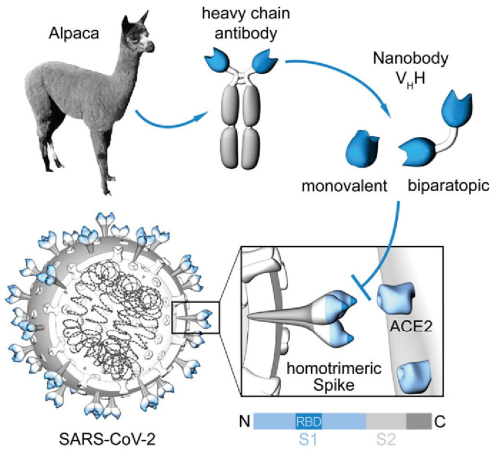

Figure 1. Generation of nanobodies blocking the SARS-CoV-2 RBD:ACE2 interface.

Nanobodies (Nbs) are genetically engineered from heavy-chain only antibodies of alpacas. The interaction between the SARS-CoV-2 homotrimeric spike protein and angiotensin-converting enzyme (ACE) 2 can be blocked by receptor-binding domain (RBD)-specific Nbs in the monovalent or biparatopic format.

To overcome these limitations, we aimed to employ Nbs as antibody surrogates and developed a competitive binding approach to screen for neutralizing antibodies on a high-throughput basis in samples from patients or vaccinated individuals. Here, we describe the selection of 11 unique Nbs derived from an alpaca immunized with glycosylated SARS-CoV-2 RBD. Employing a multiplex *in vitro* binding assay, we identified 8 Nbs that effectively block the interaction between RBD, S1, and homotrimeric spike protein (spike) with ACE2 and neutralize SARS-CoV-2 infection in a human cell line. Based on a detailed epitope mapping and structural analysis of RBD:Nb complexes, we selected two of the most potent Nbs simultaneously targeting different epitopes within the RBD and generated a biparatopic Nb (bipNb). The bipNb represents a potent antibody surrogate with IC_{50} values in the low picomolar range and exhibits substantially improved binding affinities. Notably, by addressing at least one conserved epitope outside the RBD:ACE2 interface, the bipNb is still capable to bind recently described RBD mutants derived from strains B.1.1.7 (UK) and B.1.351 (South Africa). To monitor the presence and performance of neutralizing antibodies addressing the RBD:ACE2 interface in convalescent patient samples, we implemented the bipNb in a competitive multiplex binding assay, termed NeutrobodyPlex. Based on the data presented, the NeutrobodyPlex provides a versatile high-throughput approach to screen for a neutralizing immune response in infected or vaccinated individuals, helping to monitor immune status of large populations, to determine the success of vaccination campaigns and to guide vaccine design.

Results

Selection of SARS-CoV-2-specific Nbs

To generate Nbs directed against the RBD of SARS-CoV-2, we immunized an alpaca (*Vicugna pacos*) with purified RBD (Amanat *et al,* 2020) and established a Nb phagemid library comprising ~ 4×10^7 clones representing the full repertoire of variable heavy chains of heavy-chain antibodies (V_HHs or Nbs). After two rounds of phage display on passively adsorbed or biotinylated RBD immobilized on streptavidin plates, we analyzed 492 individual clones in a solid-phase phage ELISA and identified 325 positive binders. Sequence analysis of 72 clones revealed 11 unique Nbs, which cluster into eight families with highly diverse complementarity determining regions (CDR) 3 (Fig 2A, Appendix Table S1). Individual Nbs were produced and purified from *Escherichia coli* (*E. coli*) (Fig 2B), and affinity measurements revealed K_D values ranging from ~ 1.4 to ~ 53 nM indicating the selection of 10 high-affinity monovalent binders. NM1225, that displayed a binding affinity in the micromolar range, was not

considered for further analysis (Fig 2C, Appendix Fig S1). Next, we analyzed whether selected Nbs can block the interaction between RBD, S1, or spike of SARS-CoV-2 to human ACE2. To this end, we utilized a multiplex ACE2 competition assay employing the respective SARS-CoV-2 antigens coupled to paramagnetic beads (MagPlex Microspheres) (Becker *et al*, 2021) and incubated them with biotinylated ACE2 and dilutions of purified Nbs, before measuring residual binding of ACE2 via streptavidin-PE conjugate. As controls, we included a non-specific Nb (GFP-Nb, negative control) and two inhibiting mouse antibodies (Gorshkov *et al*, 2020) as positive controls. Data obtained through this multiplex binding assay showed that 8 out of 10 analyzed Nbs inhibit ACE2 binding to all tested SARS-CoV-2 antigens (Fig EV1). Notably, IC_{50} values obtained for the most potent inhibitory Nbs NM1228 (0.5 nM), NM1226 (0.82 nM) and NM1230 (2.12 nM) are highly comparable to IC_{50} values measured for the mouse IgGs (MM43: 0.38 nM; MM57: 3.22 nM).

Nanobodies show a high potency in neutralizing SARS-CoV-2

Next, a set of Nbs representing the full diversity according to the CDR3 region and highest affinities were examined for their potential to inhibit viral infection. For a viral neutralization test (VNT), human Caco-2 cells were co-incubated with the SARS-CoV-2-mNG infectious clone and serial dilutions of NM1223, NM1224, NM1226, NM1228, NM1230 or GFP-Nb as negative control. 48 h post-infection neutralization potency was determined via automated fluorescence-microscopy of fixed and nuclear-stained cells. The infection rate, normalized to a non-treated control was plotted and IC_{50} values were determined via sigmoidal inhibition curve fits. NM1226 and NM1228 showed a strong neutralization potency with IC_{50} values of ~ 15 and ~ 7 nM followed by NM1230 (~ 37 nM) and NM1224 (~ 256 nM) (Appendix Fig S2). As expected from our biochemical analysis, NM1223 was not found to neutralize SARS-CoV-2 (Appendix Fig S2). Overall, these findings are highly consistent with the results obtained from the multiplex ACE2 competition assay, thus demonstrating high potencies of ACE2-blocking Nbs to neutralize viral infection.

Epitope identification

To identify the relative location of Nb epitopes within the RBD, we firstly performed epitope binning experiments using biolayer interferometry (BLI). For this, sensors, pre-coated with biotinylated RBD, were loaded with a first Nb followed by a short dissociation step and subsequent loading of a second Nb (Appendix Fig S3A). As expected, Nbs displaying similar CDR3 sequences (NM1221, NM1222, and NM1230, Nb-Set2) were unable to bind

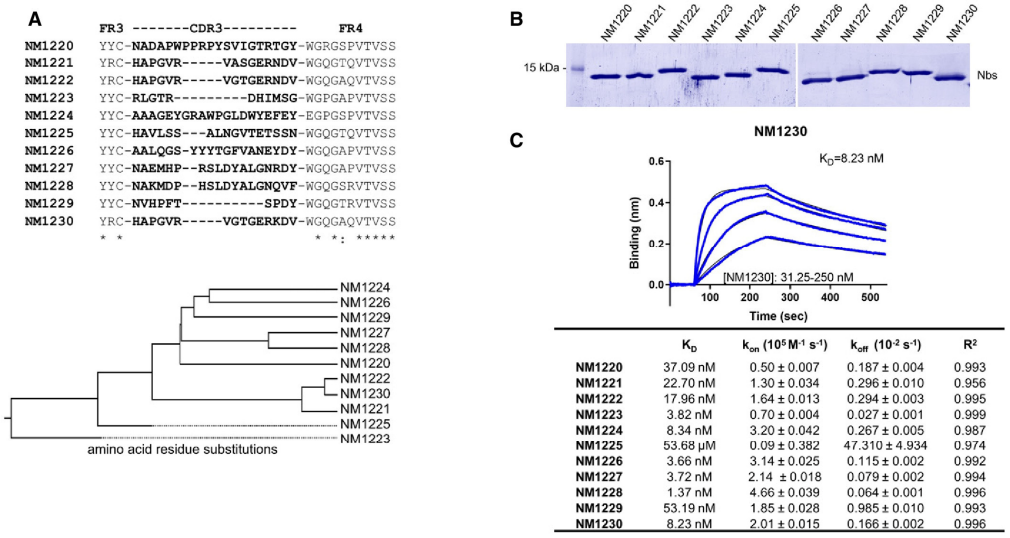

	K_D	k_{on} (10^5 M^{-1} s^{-1})	k_{off} (10^{-2} s^{-1})	R^2
NM1220	37.09 nM	0.50 ± 0.007	0.187 ± 0.004	0.993
NM1221	22.70 nM	1.30 ± 0.034	0.296 ± 0.010	0.956
NM1222	17.96 nM	1.64 ± 0.013	0.294 ± 0.003	0.995
NM1223	3.82 nM	0.70 ± 0.004	0.027 ± 0.001	0.999
NM1224	8.34 nM	3.20 ± 0.042	0.267 ± 0.005	0.987
NM1225	53.68 µM	0.09 ± 0.382	47.310 ± 4.934	0.974
NM1226	3.66 nM	3.14 ± 0.025	0.115 ± 0.002	0.992
NM1227	3.72 nM	2.14 ± 0.018	0.079 ± 0.002	0.994
NM1228	1.37 nM	4.66 ± 0.039	0.064 ± 0.001	0.996
NM1229	53.19 nM	1.85 ± 0.028	0.985 ± 0.010	0.993
NM1230	8.23 nM	2.01 ± 0.015	0.166 ± 0.002	0.996

Figure 2. Biochemical characterization of RBD-specific Nbs.

A Amino acid sequences of the complementarity determining region (CDR) 3 from unique Nbs selected after two rounds of biopanning are listed (upper panel). Phylogenetic tree based on a ClustalW alignment of the Nb sequences is shown (lower panel).

B Recombinant expression and purification of Nbs using immobilized metal affinity chromatography (IMAC) and size exclusion chromatography (SEC). Coomassie staining of 2 µg of purified Nbs is shown.

C For biolayer interferometry (BLI)-based affinity measurements, biotinylated RBD was immobilized on streptavidin biosensors. Kinetic measurements were performed by using four concentrations of purified Nbs ranging from 15.6 nM to 2 µM. As an example, the sensogram of NM1230 at indicated concentrations is shown (upper panel). The table summarizes affinities (K_D), association (k_{on}), and dissociation constants (k_{off}) determined for individual Nbs (lower panel).

simultaneously as they recognize identical or highly similar epitopes. Interestingly, we noticed that Nbs with highly diverse CDR3s such as NM1228, NM1226, NM1227, and NM1229 could not bind simultaneously, suggesting that these Nbs also recognize similar or overlapping epitopes. Consequently, we clustered these diverse Nbs into Nb-Set1. In total, we identified five distinct Nbs-Sets, comprising at least one candidate targeting a different epitope within the RBD compared with any member of a different Nb-Set (Appendix Fig S3B).

For detailed epitope mapping, we performed Hydrogen-Deuterium Exchange Mass Spectrometry (HDX-MS) using the most potent inhibitory Nbs selected from the different Nb-Sets and determined their binding regions within the RBD in relation to previously described ACE2 interaction sites (Fig EV2A, Appendix Fig S4) (Lan *et al,* 2020; Yan *et al,* 2020). Both members of Nb-Set1, NM1226 and NM1228, interacted with the RBD at the back/ lower right site (Back View, Fig EV2B and C). The highest exchange protection for NM1226 was found in the amino acid (aa) region $N_{RBD}370$ – $L_{RBD}387$ (Fig EV2B). This region is also covered by NM1228, which displayed additional binding to $Y_{RBD}489$ - $S_{RBD}514$, being part of the RBD:ACE2 interface (Fig EV2C). NM1230 (Nb-Set2) shows the highest protection in the region of $C_{RBD}432$ - $L_{RBD}452$ covering two amino acids involved in ACE2 binding ($G_{RBD}446$, $Y_{RBD}449$). A second protected region was found covering $N_{RBD}487$ - $G_{RBD}496$, which overlaps with the RBD:ACE2 interface (Fig EV2D). In accordance with our binning studies, the main epitope regions differ considerably from both Nb-Sets. As expected, NM1221 and NM1222 (both Nb-Set2) addressed similar RBD regions compared with NM1230 (Fig EV2E and F) while NM1224 (Nb-Set4) showed an interaction distinct from all other Nbs, covering both its main binding region located at the lower right side (Fig EV2G, Front View) and residues in the RBD:ACE2 interface (Fig EV2G, Front View, upper left corner). Notably, the non-inhibitory NM1223 (Nb-Set3) was shown not to contact residues involved in the RBD:ACE2 interface but rather binds to the opposite side (Fig EV2H, Front View).

Crystal structure of RBD:Nb complexes

To obtain a deeper insight into the binding mode of the most potent inhibitory Nbs, we analyzed the crystal structures of NM1226 and NM1230 in complex with RBD (Fig 3A). All Nb amino acid residues listed below follow the numbering according to Kabat (Kabat *et al,* 1991). The RBD:NM1226 complex structure was solved at a resolution of 2.3 Å (Appendix Table S2). NM1226 was found to interact with various RBD regions (aa 369–384 and aa 504–508) as well as $D_{RBD}405$ and $R_{RBD}408$. Major contacts of NM1226 to RBD are established by residues of the CDR3 ($L_{NM1226}95$, $Q_{NM1226}96$, $G_{NM1226}97$, $S_{NM1226}98$, $Y_{NM1226}99$, $Y_{NM1226}100$, $Y_{NM1226}100a$, $V_{NM1226}100e$, $N_{NM1226}100g$, $E_{NM1226}100h$, $Y_{NM1226}100i$, $D_{NM1226}101$) and CDR1 ($Y_{NM1226}30$). Beside a salt-bridge ($D_{NM1226}101$ to $R_{RBD}408$ and $K_{RBD}378$), various hydrogen bonds were found at contact sites (Fig 3B). In total, the interface of NM1226 buries an area of 698 Å^2. The RBD:NM1226 complex superimposes well onto spike protein (pdb code: 7KMS) with a Cα-rmsd derivation of 1.7 Å for all three RBD and shows that binding of NM1226 takes place exclusively in the "up" conformation of the spike protein (Fig EV3A and B) (Zhou *et al,* 2020). Although its epitope does not overlap with the binding site of ACE2, our structural data suggest that binding of NM1226 prohibits ACE2 recruitment by steric collision, which would explain its neutralizing effect (Fig EV3A and B).

For the RBD:NM1230 complex, we determined the structure at a resolution of 2.9 Å (Appendix Table S2). In accordance with our HDX-MS analysis, NM1230 binds a distinct three-dimensional epitope located at the opposite site of RBD (Fig 3A). Major contacts were formed by residues of the CDR3 ($P_{NM1230}95$, $R_{NM1230}98$, $T_{NM1230}100a$, $E_{NM1230}100c$, $R_{NM1230}100d$, $K_{NM1230}100e$, $D_{NM1230}101$, $V_{NM1230}102$, $W_{NM1230}103$). In contrast to NM1226, also residues located in the framework regions (FR) including FR1 ($Q_{NM1230}1$), FR2 ($N_{NM1230}35$, $Y_{NM1230}37$, $Q_{NM1230}39$, $G_{NM1230}42$, $K_{NM1230}43$, $A_{NM1230}44$, $L_{NM1230}45$ and $L_{NM1230}47$, and $A_{NM1230}49$), and FR3 ($E_{NM1230}60$) are involved in binding. Consequently, specific binding of NM1230 is achieved by a combination of the CDR3 and residues of the framework regions as previously observed for other Nbs (Kirchhofer *et al,* 2010). On the RBD site, NM1230 interacts with $Y_{RBD}351$ and the large loop region ranging from aa 437–503 (Fig 3C). The RBD:NM1230 interface is mainly formed by polar contacts and one salt-bridge ($R_{NM1230}98$ to $E_{RBD}484$), but also π-π stackings ($W_{NM1230}103$ to $F490_{RBD}$, $R_{NM1230}100d$ to $Y_{RBD}489$) are present (Fig 3C). In total, it buries a surface area of ~ 830 Å^2. The alignment (Cα-rmsd deviation of 1.2 Å for all three RBD) and comparison to a recently reported structure of the SARS-CoV-2 spike protein bound to neutralizing Nb-Ty1 (pdb code: 6ZXN) (Hanke *et al,* 2020) revealed that NM1230 is able to bind in "up" as well as in "down" conformation (Fig EV3A and B; Appendix Fig S5A).

Next, we compared the RBD:NM1230 structure with the recently reported RBD:ACE2 receptor complex (pdb code:6M17) (Yan *et al,* 2020) to structurally validate the neutralizing potential of NM1230. Closer inspection of the binding site (Appendix Fig S5B and C) showed that NM1230 partially overlaps with the ACE2-binding interface and that the neutralizing effect can be isolated to a limited set of residues within the RBD ($K_{RBD}417$, $Y_{RBD}449$, $F_{RBD}456$, $Y_{RBD}489$, $Q_{RBD}493$, $S_{RBD}494$) (Fig 3C, Appendix Fig S5C). However, NM1230 does not only block binding to ACE2 via its interaction with the RBD on the same protomer (Appendix Fig S5A, clash I), but also impairs ACE2 binding through steric collision on the neighboring RBD (Appendix Fig S5A, clash II). Based upon our structural data, we propose that NM1230-mediated blocking of two out of three RBDs would suffice to abolish ACE2 binding to a trimeric spike molecule.

Considering viral mutagenesis of SARS-CoV-2 within the RBD and associated occurrence of new super spreading strains (preprint: Davies *et al,* 2020; preprint: Tegally *et al,* 2020; Davies *et al,* 2021; Lauring & Hodcroft, 2021; preprint: Walker *et al,* 2021), we analyzed the impact of mutated RBD positions in the recently described SARS-CoV-2 strains B.1.1.7 (UK) and B.1.351 (South Africa) on binding to both neutralizing Nbs NM1226 and NM1230. From our structural data, we assumed that the common amino acid exchange on position 501 (N > Y) has no influence on Nb binding, whereas exchanges on position 417 (K > N) and 484 (E > K), both present in B.1.351, might only affect binding of NM1230 (Appendix Fig S6). In fact, when determining affinities of both Nbs for the RBD mutants derived from B.1.1.7 or B.1.351 by BLI, we obtained similar affinities compared with RBD_{wt} for NM1226 (K_D = ~ 5.4 nM for $RBD_{B.1.1.7}$; K_D = ~ 5.5 nM for $RBD_{B.1.351}$) (Appendix Fig S7A). Interestingly, while affinity of NM1230 to $RBD_{B.1.1.7}$ was not affected (K_D = ~ 10 nM), it decreased for $RBD_{B.1.351}$ (K_D = ~ 26 nM) (Appendix Fig S7B). In accordance with

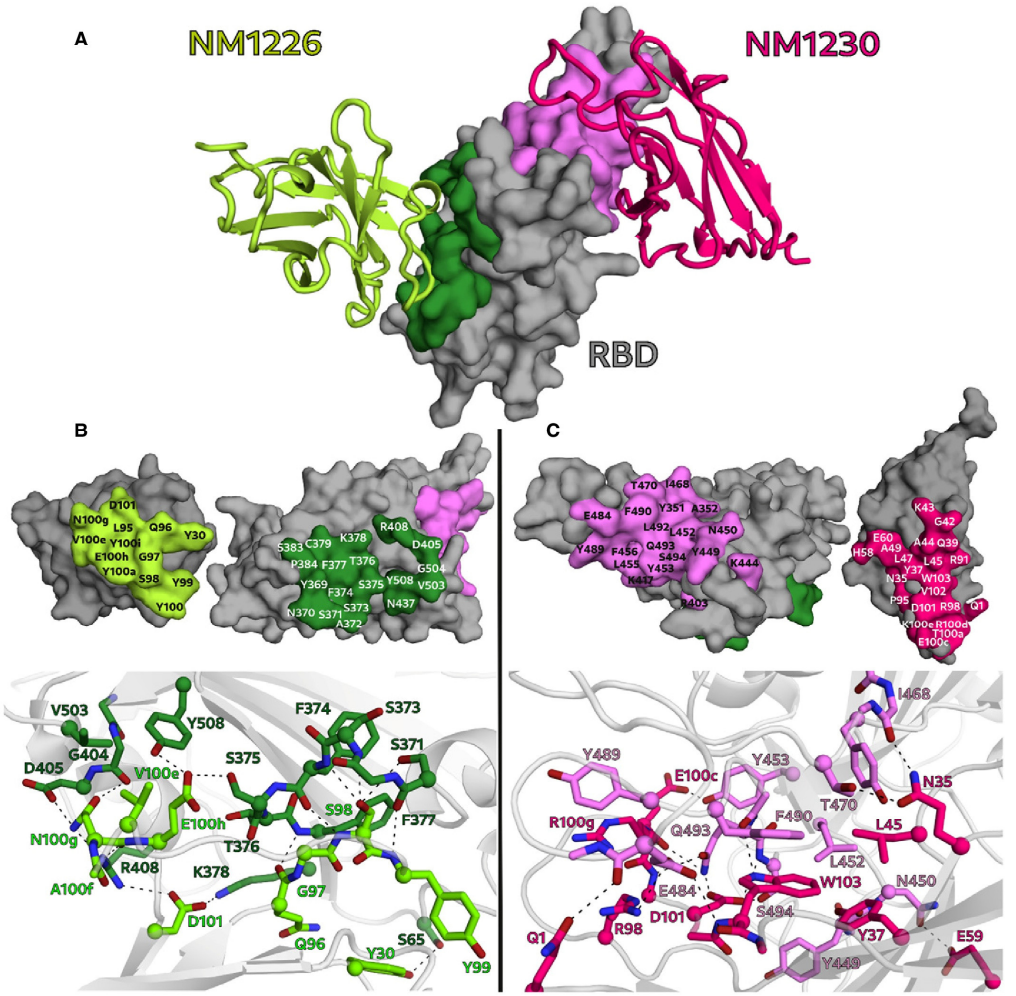

Figure 3. NM1226 and NM1230 binding epitopes on RBD.

A Overview of the binding epitopes of NM1226 (light green) on RBD (dark green) and NM1230 (magenta) on RBD (light pink), respectively.

B, C The binding interfaces of NM1226 (B) and NM1230 (C) with the RBD are shown as surface representation (upper panels) and in a close-up view as balls and sticks with direct hydrogen bonds and salt bridges indicated as dotted lines (lower panels). All residues involved in contact formation at a distance cutoff of < 4 Å are listed and labeled. A close-up view of both interfaces reports a detailed interaction map of both contact areas.

our structural epitope analysis, the reduced affinity is most likely due to the loss of the charged interaction between $R_{NM1230}98$ to $E_{RBD}484$. Also, an additional influence by mutation $K_{RBD}417$>N cannot be excluded, since position 417 is part of the NM1230 binding epitope but does not form direct contact to NM1230.

Generation of a biparatopic Nb with improved efficacies

Having identified potent Nbs with strong neutralizing characteristics, we proposed that candidates derived from Nb-Set1 (NM1226) and Nb-Set2 (NM1230) might act synergistically. To examine this,

we genetically fused the coding sequences of NM1230 and NM1226 head-to-tail thereby inserting a flexible Gly-Ser linker ($(G_4S)_4$) of 20 amino acids and generated a biparatopic Nb (bipNb) named NM1267. Following production and purification from mammalian cells (Fig 4A), we determined the affinity and analyzed its performance in our multiplex ACE2 competition assay and in the VNT. Compared with the monovalent format, the bipNb showed considerably improved affinities not only for RBD_{wt} (K_D = ~ 0.5 nM) but also for RBD mutants (K_D = ~ 0.6 nM for $RBD_{B.1.1.7}$; K_D = ~ 1.15 nM for $RBD_{B.1.351}$) (Fig 4B and C; Appendix Fig S7C). In line with these findings, it revealed an outstanding inhibition of ACE2 binding to RBD, S1, and spike with an IC_{50} in the low picomolar range (Fig 4B and D). Additionally, we observed an increased potency for viral neutralization indicated by an IC_{50} of ~ 0.9 nM (Fig 4B and E), demonstrating that the bipNb NM1267 embodies a substantially refined tool which is beneficial for viral neutralization and competitive binding studies.

NeutrobodyPlex—using Nbs to determine a SARS-CoV-2 neutralizing immune response

Currently available serological assays provide data on the presence and distribution of antibody subtypes against different SARS-CoV-2 antigens within serum samples of infected and recovered SARS-CoV-2 patients (Amanat *et al*, 2020; preprint: Lassaunière *et al*, 2020; Robbiani *et al*, 2020; preprint: Roxhed *et al*, 2020; Stadlbauer *et al*, 2020; Becker *et al*, 2021; Fink *et al*, 2021). However, they do not differentiate between total and neutralizing RBD-binding antibodies, which sterically inhibit viral entry via ACE2 (Ju *et al*, 2020; Rogers *et al*, 2020; Tang *et al*, 2020). To address this important issue, our bipNb NM1267 might be a suitable surrogate to monitor the emergence and presence of neutralizing antibodies in serum samples of patients. We speculated that NM1267 specifically displaces such antibodies from the RBD:ACE2 interface, which can be monitored as a declining IgG signal (Fig 5A). To test this hypothesis, we first co-incubated antigen-coated beads comprising RBD, S1, or spike with a dilution series of NM1267 and a well-characterized NAb (clone REGN10933), targeting an epitope within the RBD:ACE2 interface (Hansen *et al*, 2020; Jiang *et al*, 2020). As control, we applied the IgG 4A8 (anti-Spike NTD) which was shown to bind an epitope outside the RBD (Chi *et al*, 2020b). Antigen-bound IgGs in the presence of bipNb were detected via an anti-human IgG-PE as mean fluorescent intensities (MFI). Upon addition of increasing concentrations of NM1267, a distinct displacement of REGN10933 was observed (Appendix Fig S8A and B). In contrast, binding of 4A8 was not affected in the presence of NM1267 (Appendix Fig S8C and D), thus proofing the suitability of the bipNb as potent surrogate to displace NAbs targeting the RBD:ACE2 interface. In a next step, we generated a high-throughput competitive binding assay, termed NeutrobodyPlex, by implementing the NM1267 in a recently

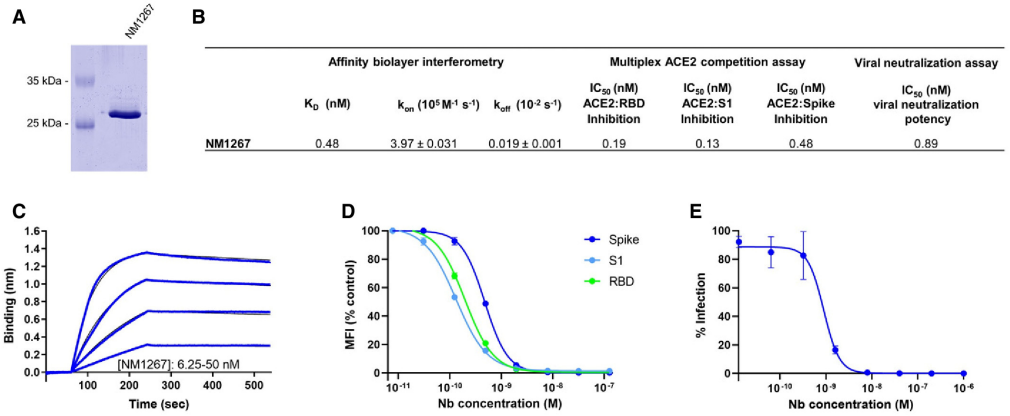

Figure 4. Biparatopic NM1267 competes with ACE2 and neutralizes SARS-CoV-2 infection.

A Coomassie staining of 1 μg of purified biparatopic Nb NM1267.

B Table summarizing the affinity (K_D), association (k_{on}), and dissociation constants (k_{off}) determined by BLI and IC_{50} values of the multiplex ACE2 competition assay and virus neutralization assay obtained for NM1267.

C Sensogram of affinity measurements via BLI using four concentrations (6.25–50 nM) of NM1267.

D Results from multiplex ACE2 competition assay are shown for the three spike-derived antigens: RBD, S1-domain (S1), and homotrimeric spike (Spike). Color-coded beads coated with the respective antigens were co-incubated with biotinylated ACE2 and dilution series of NM1267 (8 pM to 126 nM) followed by measuring residual binding of ACE2. MFI signals were normalized to the maximum detectable signal per antigen given by the ACE2-only control. IC_{50} values were calculated from a four-parametric sigmoidal model. Data are presented as mean ± s.d. of three technical replicates.

E Neutralization potency of NM1267 was analyzed in Caco-2 cells using the SARS-CoV-2-mNG infectious clones. Infection rate normalized to virus-only infection control is illustrated as percent of infection (% Infection). IC_{50} value was calculated from a four-parametric sigmoidal model, and data are presented as mean ± s.e.m. of three biological replicates (n = 3).

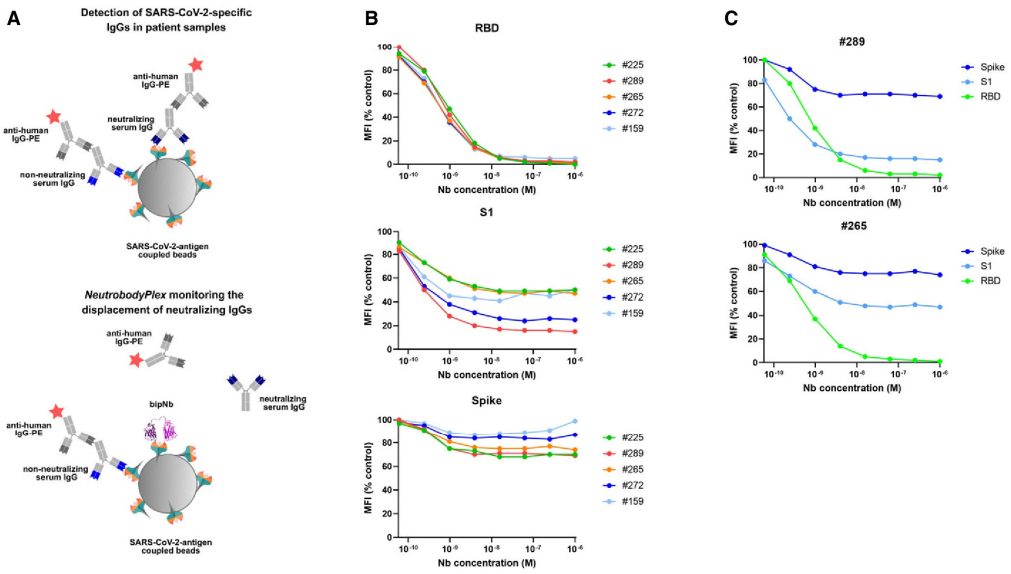

Figure 5. NeutrobodyPlex: multiplex competitive binding assay to monitor a neutralizing immune response in patients.

A Schematic illustration of the NeutrobodyPlex. The displacement of serum-derived neutralizing IgGs binding to SARS-CoV-2 antigens upon addition of bipNb is measured. In presence of neutralizing IgGs, the fluorescent signal from anti-human-IgG-PE is inversely proportional to the applied bipNb concentration.

B For the NeutrobodyPlex, antigen-coated beads comprising RBD, S1, or spike were co-incubated with serum samples from five patients and a dilution series of NM1267 (1 μM to 6 pM) (n = 1). Mean fluorescent intensities (MFI) derived from antigen-bound IgGs in the presence of bipNb normalized to the MFI values of IgGs in the serum-only samples, illustrated as MFI (% control), are shown.

C For two patient-derived serum samples (#289, #265), differences in the NM1267-mediated displacement of IgGs binding the three spike-derived antigens (RBD, S1, spike) are shown.

developed, multiplexed serological assay (Becker *et al*, 2021). Initially, serum samples from five patients were screened. When analyzing IgG binding to RBD, we detected a complete displacement in the presence of ~ 63 nM NM1267. Similarly, a distinct signal reduction for S1 binding IgGs became observable reaching a plateau upon addition of ~ 63 nM NM1267 (Fig 5B, Appendix Table S3). Notably, we observed only minor signal reduction when analyzing spike-binding IgGs (Fig 5B) indicating that the majority of serum IgGs bound this large antigen at epitopes beyond the RBD:ACE2 interaction site (preprint: Heffron *et al*, 2020). From these data, we concluded that all five tested individuals comprise a substantial proportion of neutralizing IgGs that could be detected by competitive bipNb binding using RBD or S1 as antigens. To demonstrate that the NeutrobodyPlex can determine the presence of neutralizing IgGs at detailed resolution, we highlight the results of monitoring the displacement of S1-binding IgGs in two selected patient samples #289 and #265. Upon addition of increasing concentrations of NM1267, we observed a prominent signal reduction of ~ 85% in patient #289, whereas samples of patient #265 only revealed ~ 53% displacement of S1-binding IgGs (Fig 5C).

Next, we compared the NeutrobodyPlex on RBD with the cell-based VNT by analyzing a set of 18 serum samples from convalescent SARS-CoV-2 patients, collected on days 19–57 following a positive PCR test result, and four control samples from healthy donors. To detect differences within the overall immune response and to qualify the neutralizing capacity of the serum samples, we performed the NeutrobodyPlex using two concentrations of NM1267 previously shown to completely (1 μM) or partly (1 nM) displace IgGs binding the RBD:ACE2 interface (Fig 5B). Both assays demonstrated the presence of neutralizing antibodies in all serum samples from convalescent individuals, when using the 1:40 serum dilution in the VNT or when adding 1 μM NM1267 in the NeutrobodyPlex (Fig 6A and B). Notably, neutralizing IgGs were not detected in any of the control serum samples (Appendix Table S4). Further analysis of the displacement of RBD-binding IgGs using the lower NM1267 concentration (1 nM) revealed significant differences in individual neutralization capacities. Whereas some patient samples contained potent neutralizing IgGs that could displace NM1267 upon binding to the RBD:ACE2 interface (Fig 6A, high MFI (% control), light squares), continuous bipNb-mediated displacement of IgGs was detectable in other samples (Fig 6A, low MFI (% control), dark squares), indicating the presence of IgGs with lower neutralizing potency. In parallel, VNT considering the full range of serum dilutions also showed significant differences in individual neutralizing

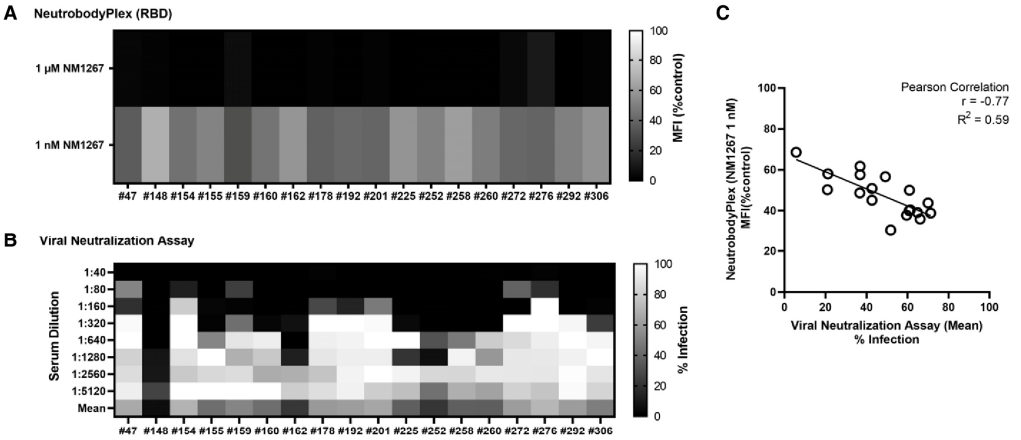

Figure 6. Specificity of the NeutrobodyPlex in determining individual neutralizing immune responses.

Serum samples of 18 convalescent SARS-CoV-2-infected individuals were analyzed using the NeutrobodyPlex and the virus neutralization assay.

A For the NeutrobodyPlex on RBD, two concentrations of NM1267 (1 µM and 1 nM) were applied (n = 1). Light colored squares (high MFI (%control)) are indicative for IgGs outcompeting NM1267 from the RBD:ACE2 interface; dark colored squares (low MFI (%control)) show a continuous displacement of IgGs from serum samples in the presence of NM1267.

B For the virus neutralization assay, serial dilutions of the serum samples (1:40 – 1:5,120) were applied (n = 1). Dark colored squares are indicative for a low infection level (low % Infection); light colored squares show a high infection rate (high % Infection).

C The mean percent of infection (% Infection) derived from all individual serum dilutions obtained by the virus neutralization assay was calculated and plotted against the respective MFI (% control) obtained from the NeutrobodyPlex on RBD in the presence of NM1267 (1 nM). The Pearson correlation determined a negative correlation with $r = -0.77$ and $R^2 = 0.59$ ($P < 0.05$).

potency (Fig 6B). To confirm the validity of the NeutrobodyPlex, we calculated the mean percent of infection (% Infection) of all individual serum dilutions and plotted these values against the respective MFI (% control) obtained from the NeutrobodyPlex (Fig 6C). The observed negative correlation (high MFI (% control) vs. low mean % Infection) strongly suggests that the NeutrobodyPlex allows the detection of individual neutralizing immune responses and assessment of their potency.

For final validation, we screened a serum sample set of 112 convalescent SARS-CoV-2-infected and eight uninfected individuals in the NeutrobodyPlex. In addition to RBD, S1, and spike, we included the S2 domain (S2) and the nucleocapsid (N) of SARS-CoV-2 to monitor total immune response. Incubation with the higher amount of NM1267 (1 µM) revealed the presence of neutralizing IgGs in all serum samples from convalescent patients as shown by an effective replacement of IgGs from RBD, S1, and partially from spike, but not from S2 or N (Fig EV4A). In line with findings from the initial patient sample set, differences in the potencies of neutralizing IgGs present in the individual serum samples became detectable upon addition of the lower concentration of NM1267 (1 nM) (Fig EV4B). As observed previously, non-infected individuals did not display any detectable antibody signal for the presented antigens. We further analyzed, if total level of SARS-CoV-2-specific IgGs correlates with the amount of neutralizing IgGs. As a marker for total IgGs we defined MFI values measured for spike-binding IgGs (Fig 7A and B) and N-binding IgGs (Fig 7C and D) and plotted them against normalized MFI values from IgGs binding to RBD in the presence of both concentrations of NM1267 (1 µM, 1 nM (MFI RBD (%control)) (Fig 7A–D). Overall, we found high variability of total IgGs (MFI: ~ 3,500 – ~ 50,000) in tested serum samples. Upon addition of the higher concentration of NM1267 (1 µM), we observed a complete displacement of IgGs binding the RBD:ACE2 interface independent of the amount of total IgG (Fig 7A and C), whereas upon addition of the lower amount of bipNb, substantial differences of the neutralizing capacity of individual patient samples became detectable (Fig 7B and D). Specifically, using the NeutrobodyPlex, we identified several individuals who have low levels of SARS-CoV-2-specific antibodies overall but have strong neutralizing IgGs (Fig 7B and D highlighted with light-blue background). From these data, it can be concluded that the appearance of neutralizing IgGs after infection with SARS-CoV-2 does not correlate with an overall high SARS-CoV-2-specific antibody titer. However, an increased likelihood for a higher neutralizing capacity in patients showing an overall high SARS-CoV-2-specific IgG level also cannot be excluded. In summary, these results demonstrate how the NeutrobodyPlex can not only provide detailed information on the presence of neutralizing antibodies in patient samples, but also allow qualitative and quantitative assessment of the individual immune response.

Discussion

In this study, we identified a set of 11 high-affinity RBD-specific Nbs derived from an immunized animal. The high success rate in

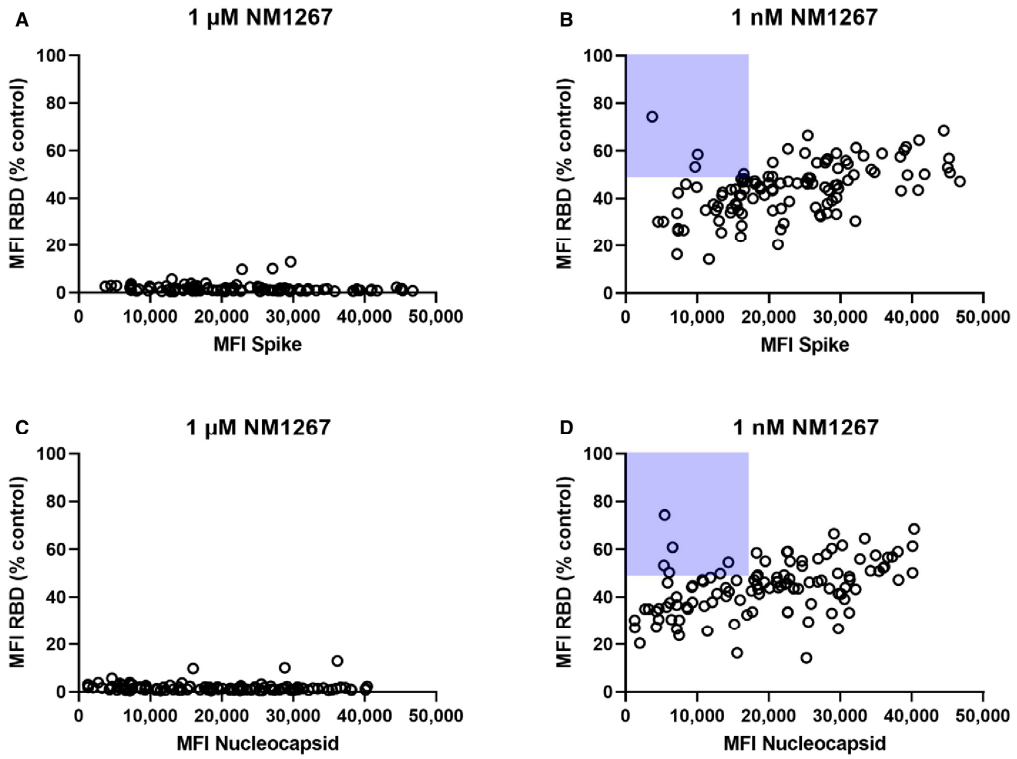

Figure 7. NeutrobodyPlex enables a differentiated analysis on neutralizing IgGs compared with total SARS-CoV-2 binding IgGs in individuals.

To investigate neutralizing capacities in relation to total levels of SARS-CoV-2-specific IgGs in individuals, serum samples of 112 convalescent SARS-CoV-2 infected individuals were analyzed using the NeutrobodyPlex (n = 1). Individuals displaying strong neutralizing IgGs but showed an overall low level of SARS-CoV-2-specific antibodies are highlighted with light-blue background.

A, B Total IgGs derived from spike-binding IgGs were plotted against normalized MFI values from IgGs binding to RBD (MFI RBD (%control)) in the presence of both concentrations of NM1267 (1 µM; 1 nM).

C, D Total IgGs derived from N-binding IgGs were plotted against normalized MFI values from IgGs binding to RBD (MFI RBD (%control)) in the presence of both concentrations of NM1267 (1 µM; 1 nM).

identifying well-functioning Nbs is consistent with recently reported findings describing an ever-growing list of such binders derived from either immunized (Chi *et al,* 2020a; preprint: Esparza *et al,* 2020; preprint: Gai *et al,* 2020; Hanke *et al,* 2020; preprint: Nieto *et al,* 2020; Wrapp *et al,* 2020a; Xiang *et al,* 2020; Koenig *et al,* 2021) or naïve/ synthetic Nb gene libraries (Chi *et al,* 2020a; Custodio *et al,* 2020; Huo *et al,* 2020; preprint: Schoof *et al,* 2020; preprint: Walter *et al,* 2020; preprint: Ahmad *et al,* 2021). By establishing a workflow involving a multiplexed ACE2 competition assay followed by a cell-based VNT, we were able to select high-affinity binding candidates that blocked the interaction between RBD and ACE2 in the context of various SARS-CoV-2 spike-derived antigens and additionally exhibited high viral neutralizing potency. Detailed epitope analysis based on HDX-MS and structural analysis of RBD:Nb complexes for two of the most potent binders further revealed the molecular basis of the observed neutralizing effect. Both structurally characterized Nbs (NM1226 and NM1230) bind to opposite sides of the RBD. Similar to the recently reported strong neutralizing Nb-Ty1, which displays a partially overlapping binding epitope (Hanke *et al,* 2020), NM1230 can bind to the "down" and "up" form of the spike protomer, thereby inhibiting ACE2 interaction either by steric collisions or due to the overlapping interface (Appendix Fig S5). In contrast, NM1226 binds only the "up" conformation on RBD. As the RBD:ACE2 interface is not addressed by NM1226, its neutralizing effect can most likely be explained due to steric collision. Moreover, NM1226 seems to be more robust against mutations within the RBD:ACE2 interface. Indeed, our comprehensive analyses showed that both Nbs are able to bind the

RBD variant of B.1.1.7 (UK) with similar affinities to RBD_{wt}. In comparison, binding of NM1226 to RBD of the more virulent SARS-CoV-2 variant B.1.351 (South Africa) was unaffected, whereas NM1230 showed reduced affinity. To combine the advantages of both single Nbs, add avidity to the construct, and reduce the possibility of viral escape by targeting two independent epitopes, we generated the biparatopic Nb NM1267, which performed excellently in our multiplexed ACE2 competition assay and VNT with IC_{50} values in the picomolar range. In addition, NM1267 revealed high binding affinities to RBDs either derived from B.1.1.7 (UK) or B.1.351 (South Africa) from which we postulated that NM1267 represents a substantially refined tool with highly versatile binding properties.

The ongoing pandemic and the emergence of new mutations leading to more infectious viral strains make the development of improved diagnostic tools and therapies essential. In this context, several studies have shown that humoral immune responses resulting in antibodies directed against the interaction site of RBD and the ACE2 receptor exposed on epithelial cells of the human respiratory tract lead to a strong viral neutralizing effect (Brouwer *et al,* 2020; Cao *et al,* 2020; Chi *et al,* 2020b; Jiang *et al,* 2020; Ju *et al,* 2020; Robbiani *et al,* 2020; Shi *et al,* 2020; Tai *et al,* 2020; Yu *et al,* 2020; Zohar & Alter, 2020). Consequently, there is a keen demand to expand currently applied serological diagnostics toward a more differentiated analysis to specifically monitor and classify immune responses. Therefore, we extended our previously described multiplex serological assay (Becker *et al,* 2021) and implemented NM1267 as a potent surrogate, which specifically displaces IgGs from binding to the RBD:ACE2 interface to monitor the presence and emergence of NAbs in serum samples from convalescent and vaccinated individuals. The NeutrobodyPlex was not only able to successfully detect the overall presence of NAbs targeting the RBD:ACE2 interface, but also to categorize them according to their potency. In addition, it allows comparison between neutralizing IgGs and the total level of SARS-CoV-2 antibodies, which is an important parameter, e.g., for determining the success of a vaccine. However, the NeutrobodyPlex approach is limited in that only NAbs that preferably bind the RBD:ACE2 interaction site can be detected. While such NAbs have been proposed as a milestone for the development of a protective immune response against SARS-CoV-2 (Brouwer *et al,* 2020; Cao *et al,* 2020; Ju *et al,* 2020; Robbiani *et al,* 2020; Shi *et al,* 2020; Tai *et al,* 2020; Yu *et al,* 2020), several NAbs have also been identified that bind outside the RBD:ACE2 interface (Chi *et al,* 2020b; Liu *et al,* 2020), which would be missed by the NeutrobodyPlex.

Compared with recently described assays that directly measure antibody-mediated displacement of ACE2 to determine a neutralizing immune response (preprint: Byrnes *et al,* 2020; Tan *et al,* 2020; Walker *et al,* 2020), a much lower binding affinity of ~ 15–30 nM of RBD to ACE2 must be considered. Consequently, neutralizing immune responses may be detected even in the presence of weak RBD-binding antibodies, which could lead to a false statement of immune protection. Additionally, the usage of small-sized, Nb-derived surrogates further lowers the possibility of a non-targeted and non-reproducible displacement of ACE2, e.g., mediated by steric inhibition and dimerization effects derived from non-specifically binding IgGs. Finally, the multiplex design of the NeutrobodyPlex allows rapid expansion to different antibody isotypes and additional antigens to include, e.g., new relevant RBD mutants that are of importance for advanced vaccination strategies.

To our knowledge, the NeutrobodyPlex demonstrates for the first time a multiplex, antigen-resolved analysis of the presence of neutralizing human IgGs in convalescent individuals suffering from SARS-CoV-2 infection. Compared with other assays, the NeutrobodyPlex can be performed in a fully automated, high-throughput manner and can be readily used for large cohort screening. Since it requires only non-living and non-infectious viral material, costs and safety conditions can be significantly reduced (Muruato *et al,* 2020; Scholer *et al,* 2020; Tan *et al,* 2020). In addition, the NeutrobodyPlex is highly sensitive, as low dilutions of serum (tested dilution: 1:400) are sufficient for analysis, significantly reducing patient material compared with standard assays. However, in its current state, important parameters such as specificity and linearity remain to be defined and more detailed information about the binding properties of neutralizing IgGs are needed. Thus, we have initiated a collaboration with the University Hospital Tuebingen to test large cohorts of convalescent and vaccinated individuals with the NeutrobodyPlex in comparison with RBD ELISA assays and VNTs.

In summary, we envision that the NeutrobodyPlex will provide unique opportunities for detailed classification of individual immune status with respect to the development of protective antibodies. In addition, the NeutrobodyPlex could represent a valuable approach to monitor the efficiency of currently starting vaccination campaigns and their long-term efficacy.

Materials and Methods

Expression constructs

For bacterial expression of Nbs, sequences were cloned into the pHEN6 vector (Arbabi Ghahroudi *et al,* 1997), thereby adding a C-terminal His_6-Tag for IMAC purification as described previously (Rothbauer *et al,* 2008; Kirchhofer *et al,* 2010). To generate the biparatopic Nb NM1267 from NM1230 and NM1226, cDNAs were amplified by PCR using forward primer 1230Nfor 5′- GGA CGT CTC AAC TCT CAA GTG CAG CTG GTG GAG TC - 3′ and reverse primer 1230Nrev 5′- CAC CAC CGC CAG ATC CAC CGC CAC CTG ATC CTC CGC CTC CTG AGG ACA CGG TGA CCT GGG CCC - 3′ for NM1230 Nb, and forward primer 1226Cfor 5′- GGT GGA TCT GGC GGT GGT GGA AGT GGT GGC GGA GGT AGT CAG GTG CAG CTG GTG GAA T - 3′ and reverse primer 1226Crev 5′- GGG GAA TTC AGT GAT GGT GAT GGT GGT GTG AGG ACA CGG TGA CCG GGG CC - 3′ for NM1226 Nb. Next PCR products from Nbs NM1230 and NM1226 were genetically fused via an internal $(G_4S)_4$–linker by fusion PCR using forward primer 1230Nfor and reverse primer 1226Crev. Full-length cDNA was cloned into Esp3I and EcoRI site of pCDNA3.4 expression vector with N-terminal signal peptide (MGWTLVFLFLLSVTAGVHS) for secretory pathway that comprises Esp3I site.

The pCAGGS plasmids encoding the stabilized homotrimeric spike protein and the receptor-binding domain (RBD) of SARS-CoV-2 were kindly provided by F. Krammer (Amanat *et al,* 2020). The cDNA encoding the S1 domain (aa 1 - 681) of the SARS-CoV-2 spike protein was obtained by PCR amplification using the forward primer S1_CoV2-for 5′- CTT CTG GCG TGT GAC CGG - 3′ and reverse

primer S1_CoV2-rev 5′ - GTT GCG GCC GCT TAG TGG TGG TGG TCG TGG TGG CTG TTT GTC TGT GTC TG - 3′ and the full-length SARS-CoV-2 spike cDNA as template and cloned into the XbaI/ NotI-digested backbone of the pCAGGS vector, thereby adding a C-terminal His_6-tag. The optimized sequence of the full-length nucleocapsid protein of SARS-CoV-2 with an N-terminal hexahistidine (His_6)-tag was obtained by DNA synthesis (Thermo Fisher Scientific) (GenBank accession numbers QHD43423.2) and cloned into the bacterial expression vector pRSET2b (Thermo Fisher Scientific) via NdeI/HindIII restriction sites. RBDs of virus mutants were generated by PCR amplification of fragments from wild-type DNA template followed by fusion PCRs to introduce described mutation N501Y for B.1.1.7 ($RBD_{B.1.1.7}$) and additional mutations K417N and E484K for B.1.351 ($RBD_{B.1.351}$) (https://covariants.org/shared-mutations). Forward primer RBDfor 5′- ATA TCT AGA GCC ACC ATG TTC GTG TTT CTG G - 3′ and reverse primer N501Yrev 5′- CCA CGC CAT ATG TGG GCT GAA AGC CGT AG - 3′ were used for amplification of fragment 1, forward primer N501Yfor 5′- GGC TTT CAG CCC ACA TAT GGC GTG GGC TAT CAG C - 3′ and reverse primer RBDrev 5′- AAG ATC TGC TAG CTC GAG TCG C - 3′ were used for amplification of fragment 2. Both fragments containing an overlap sequence at the 3` and 5` end were fused by an additional PCR using forward primer RBDfor and RBDrev. Based on cDNA for $RBD_{B.1.1.7}$, additional mutations of B.1.351 were introduced by PCR amplification of three fragments using forward primer RBDfor and reverse primer K417Nrev 5′- GTT GTA GTC GGC GAT GTT GCC TGT CTG TCC AGG G - 3′, forward primer K417Nfor 5′- GAC AGA CAG GCA ACA TCG CCG ACT ACA ACT ACA AGC - 3′ and reverse primer E484Krev 5′- GCA GTT GAA GCC TTT CAC GCC GTT ACA AGG GGT - 3′, forward primer E484Kfor 5′- GTA ACG GCG TGA AAG GCT TCA ACT GCT ACT TCC C - 3′ and reverse primer RBDrev. Amplified fragments were assembled by subsequent fusion PCR using forward primer RBDfor and RBDrev. DNA coding for mutant RBDs (amino acids 319–541 of respective spike proteins) was cloned into Esp3I and EcoRI site of pCDNA3.4 expression vector as described for NM1267. All expression constructs were verified by sequence analysis.

Nb libraries

Alpaca immunizations with purified RBD and Nb library construction were carried out as described previously (Rothbauer *et al*, 2006). Animal immunization was approved by the government of Upper Bavaria (Permit number: 55.2-1-54-2532.0-80-14). In brief, nine weeks after immunization of an animal (*Vicugna pacos*) with C-terminal histidine-tagged RBD (RBD-His_6), ~ 100 ml blood was collected and lymphocytes were isolated by Ficoll gradient centrifugation using the Lymphocyte Separation Medium (PAA Laboratories GmbH). Total RNA was extracted using TRIzol (Life Technologies) and mRNA was reverse transcribed to cDNA using a First-Strand cDNA Synthesis Kit (GE Healthcare). The Nb repertoire was isolated in three subsequent PCRs using the following primer combinations (i) CALL001 (5′-GTC CTG GCT GCT CTT CTA CA A GG-3′) and CALL002 (5′-GGT ACG TGC TGT TGA ACT GTT CC-3′); (ii) forward primer set FR1-1, FR1-2, FR1-3, FR1-4 (5′-CAT GGC NSA NGT GCA GCT GGT GGA NTC NGG NGG-3′, 5′-CAT GGC NSA NGT GCA GCT GCA GGA NTC NGG NGG-3′, 5′-CAT GGC NSA NGT GCA GCT GGT GGA NAG YGG NGG-3′, 5′-CAT GGC NSA NGT GCA GCT GCA GGA NAG YGG NGG-3′) and reverse primer CALL002 and (3) forward primer FR1-ext1 and FR1-ext2 (5′-GTA GGC CCA GCC GGC CAT GGC NSA NGT GCA GCT GGT GG-3`, 5`-GTA GGC CCA GCC GGC CAT GGC NSA NGT GCA GCT GCA GGA-3′ A-) and reverse primer set FR4-1, FR4-2, FR4-3, FR4-4, FR4-5 and FR4-6 (5`-GAT GCG GCC GCN GAN GAN ACG GTG ACC NGN RYN CC-3′. 5`-GAT GCG GCC GCN GAN GAN ACG GTG ACC NGN GAN CC-3′. 5`-GAT GCG GCC GCN GAN GAN ACG GTG ACC NGR CTN CC-3′. 5`-GAT GCG GCC GCR CTN GAN ACG GTG ACC NGN RYN CC-3′. 5`-GAT GCG GCC GCR CTN GAN ACG GTG ACC NGN GAN CC-3′. 5`-GAT GCG GCC GCR CTN GAN ACG GTG ACC NGR CTN CC-3′) introducing SfiI and NotI restriction sites. The Nb library was subcloned into the SfiI/ NotI sites of the pHEN4 phagemid vector (Arbabi Ghahroudi *et al*, 1997).

Nb screening

For the selection of RBD-specific Nbs, two consecutive phage enrichment rounds were performed. TG1 cells containing the "immune"-library in pHEN4 were infected with the M13K07 helper phage, hence the V_HH domains were presented superficially on phages. For each round, 1×10^{11} phages of the "immune"-library were applied on RBD either directly coated on immunotubes (10 µg/ml) or biotinylated RBD (5 µg/ml) immobilized on 96-well plates precoated with Streptavidin. In each selection round, extensive blocking of antigen and phages was performed by using 5% milk or BSA in PBS-T and with increasing panning round, PBS-T washing stringency was intensified. Bound phages were eluted in 100 mM triethylamin, TEA (pH 10.0), followed by immediate neutralization with 1 M Tris/HCl (pH 7.4). For phage preparation for following rounds, exponentially growing TG1 cells were infected and spread on selection plates. Antigen-specific enrichment for each round was monitored by comparing colony number of antigen vs. no antigen selection. Following panning 492 individual clones of the second selection round were screened by standard Phage-ELISA procedures using a horseradish peroxidase-labeled anti-M13 monoclonal antibody (GE Healthcare).

Protein expression and purification

RBD-specific Nbs were expressed and purified as previously described (Rothbauer *et al*, 2008; Kirchhofer *et al*, 2010). For the expression of SARS-CoV-2 proteins (RBD, stabilized homotrimeric spike, and S1 domain), Expi293 cells were used (Stadlbauer *et al*. 2020) and the biparatopic Nb NM1267 was expressed using the ExpiCHO system. The full-length nucleocapsid protein (N) was expressed using E.coli BL21 (DE3) cells and purification was performed as described previously (Becker *et al*, 2021). The S2 ectodomain of the SARS-CoV-2 spike protein (aa 686–1213) was purchased from Sino Biological (cat # 40590, lot # LC14MC3007). For quality control, all purified proteins were analyzed via SDS–PAGE according to standard procedures. For immunoblotting, proteins were transferred on nitrocellulose membranes (Bio-Rad Laboratories) and detection was performed using anti-His antibody (Penta-His Antibody, #34660, Qiagen) followed by donkey-anti-mouse antibody labeled with AlexaFluor647 (Invitrogen) using a Typhoon Trio scanner (GE Healthcare, Freiburg, Germany; excitation 633 nm, emission filter settings 670 nm BP 30).

Biophysical biolayer interferometry (BLI)

To analyze the binding affinity of purified Nbs toward RBD, biolayer interferometry (BLItz, ForteBio) was performed as per the manufacturer's protocols. Briefly, biotinylated RBD was immobilized on single-use high-precision streptavidin biosensors (SAX). Depending on the affinity of the RBD-Nb interaction, an appropriate concentration range (15.6 nM to 2 μM) of Nbs was used. For each run, four different Nb concentrations were measured as well as a reference run using PBS instead of Nb in the association step. As negative control, GFP-Nb (500 nM) was applied in the binding studies. Global fits were determined using the BLItzPro software and the global dissociation constant (K_D) was calculated.

Bead-based multiplex ACE2 competition assay

Purified RBD, S1 domain, and homotrimeric spike of SARS-CoV-2 were covalently immobilized on spectrally distinct populations of carboxylated paramagnetic beads (MagPlex Microspheres, Luminex Corporation, Austin, TX) using 1-ethyl-3-(3-dimethylaminopropyl)-carbodiimide (EDC)/ sulfo-N-hydroxysuccinimide (sNHS) chemistry as described by Becker *et al* (2021). Briefly, beads were activated in activation buffer containing 5 mg/ml EDC and 5 mg/ml sNHS. For immobilization, activated beads and respective antigens were incubated in coupling buffer (500 mM MES, pH 5.0, 0.005% (v/v) Triton X-100) for 2 h at 21°C and individual bead populations were combined into a bead mix. For the bead-based ACE2 competition assay, Nbs were incubated with the bead mix (containing beads coupled with SARS-CoV-2 homotrimeric spike, RBD, and S1 proteins) and biotinylated ACE2 (Sino Biological), which competes for the binding of SARS-CoV-2 spike-derived antigens. Single Nbs or bipNbs were pre-diluted to a concentration of 6.3 μmol/L per Nb in assay buffer. Afterward, a fourfold dilution series was made over eight steps in assay buffer containing 160 ng/ml biotinylated ACE2. Subsequently, every dilution was transferred the same volume of bead mix in a 96-well half-area plate. The plate was incubated for 2 h at 21°C, shaking at 750 rpm. Beads were washed using a microplate washer (Biotek 405TS, Biotek Instruments GmbH) to remove unbound ACE2 or Nbs. R-phycoerythrin (PE)-labeled streptavidin was used to detect biotinylated ACE2. Measurements were performed with a FLEXMAP 3D instrument using the xPONENT Software version 4.3 (settings: sample size: 80 μl, 50 events, Gate: 7,500 – 15,000, Reporter Gain: Standard PMT).

NeutrobodyPlex: Bead-based multiplex neutralizing antibody detection assay

Based on the recently described automatable multiplex immunoassay (Becker *et al*, 2021), the NeutrobodyPlex was developed and similar assay conditions were applied. For the detection of neutralizing serum antibodies, the bead mix containing beads coupled with purified RBD (receptor-binding domain), S1 (S1 domain), spike (homotrimeric spike), S2 (S2 domain), or N (nucleocapsid) of SARS-CoV-2 was incubated with bipNb NM1267 (concentrations ranging from 1 μM to 6 pM) and purified NAbs (0.08 nM, REGN10933 Cell Sciences; 4A8 ProteoGenix) or serum samples of convalescent SARS-CoV-2 patients and healthy donors at a 1:400 dilution. As positive control and maximal signal detection per sample, serum only was included. Bound serum IgGs were detected via PE-labeled anti-human-IF(ab')$_2$ Fragment (#109-116-098 Jackson ImmunoResearch) as previously described (Becker *et al*, 2021).

Hydrogen-Deuterium exchange

RBD deuteration kinetics and epitope elucidation

RBD (5 μl, 73 μM) was either incubated with PBS or RBD-specific Nbs (2.5 μl, 2.5 mg/ml in PBS) at 25°C for 10 min. Deuterium exchange of the pre-incubated nanobody-antigen complex was initiated by dilution with 67.5 μl PBS (150 mM NaCl, pH 7.4) prepared with D_2O and incubation for 5 and 50 min, respectively, at 25°C. To ensure a minimum of 90% of complex formation, the molar ratio of antigen to Nbs was calculated as previously described(Kochert *et al*, 2018), using the affinity constants of 1.37 nM (NM1228), 3.66 nM (NM1226), 3.82 nM (NM1223), 8.23 nM (NM1230), and 8.34 nM (NM1224) (pre-determined by BLI analysis). The final D_2O concentration was 90%. After 5 and 50 min at 25°C, aliquots of 15 μl were taken and quenched by adding 15 μl ice-cold quenching solution (0.2 M TCEP with 1.5% formic acid and 4 M guanidine HCl in 100 mM ammonium formate solution pH 2.2) resulting in a final pH of 2.5. Quenched samples were immediately snap-frozen. The immobilized pepsin was prepared by adding 60 μl of 50% slurry (in ammonium formate solution pH 2.5) to a tube and dried by centrifugation at 1,000 *g* for 3 min at 0°C and discarding the supernatant. Before injection, aliquots were thawed and added to the dried pepsin beads. Proteolysis was performed for 2 min in a water ice bath followed by filtration using a 22 μm filter and centrifugation at 1,000 *g* for 30 s at 0°C. Samples were immediately injected into a LC-MS system. Undeuterated control samples were prepared under the same conditions using H_2O instead of D_2O. The same protocol was applied for the Nbs without addition of RBD as well to create a list of peptic peptides. The HDX experiments of the RBD-Nb-complex were performed in triplicates. The back-exchange of the method as estimated using a standard peptide mixture of 14 synthetic peptides was 24%.

Chromatography and mass spectrometry

HDX samples were analyzed on a LC-MS system comprised of RSLC pumps (UltiMate 3000 RSLCnano, Thermo Fisher Scientific, Dreieich, Germany), a chilling device for chromatography (MéCour Temperature Control, Groveland, MA, USA), and a mass spectrometer Q Exactive (Thermo Fisher Scientific, Dreieich, Germany). The chilling device contained the LC column (ACQUITY BEH C18, 1.7 μm, 300 Å, 1 mm × 50 mm (Waters GmbH, Eschborn, Germany)), a cooling loop for HPLC solvents, a sample loop, and the injection valve and kept all components at 0°C. Samples were analyzed using a two-step 20 min linear gradient with a flow rate of 50 μl/min. Solvent A was 0.1% (v/v) formic acid, and solvent B was 80% acetonitrile (v/v) with 0.1% formic acid (v/v). After 3 min desalting at 10% B, a 9 min linear gradient from 10 to 25% B was applied followed by an 8 min linear gradient from 25 to 68.8%. Experiments were performed using a Q Exactive (Thermo Fisher Scientific, Dreieich, Germany) with 70,000 resolutions instrument configurations as follows: sheath gas flow rate of 25; aux gas flow rate of 5; S-lens RF level of 50, spray voltage of 3.5 kV, and a capillary temperature of 300°C.

HDX data analysis

A peptic peptide list containing peptide sequence, retention time, and charge state was generated in a preliminary LC-MS/MS experiment. The peptides were identified by exact mass and their fragment ion spectrum using protein database searches by Proteome Discoverer v2.1.0.81 (Thermo Fisher Scientific, Dreieich, Germany) and implemented SEQUEST HT search engine. The protein database contained the RBD and the pepsin sequences. Precursor and fragments mass tolerance were set to 6 ppm and 0.05 Da, respectively. No enzyme selectivity was applied; however, identified peptides were manually evaluated to exclude peptides originated through cleavage after arginine, histidine, lysine, proline, and the residue after proline (Hamuro & Coales, 2018). FDR was estimated using q-values calculated by Perculator and only peptides with high-confidence identification (q-value $\leq$ 0.01) were included to the list. Peptides with overlapping mass, retention time, and charge in Nb and antigen digest, were manually removed. The deuterated samples were recorded in MS mode only, and the generated peptide list was imported into HDExaminer v2.5.0 (Sierra Analytics, Modesto, CA, USA). Deuterium uptake was calculated using the increase in the centroid mass of the deuterated peptides. HDX could be followed for 79% of the RBD amino acid sequence. The calculated percentage deuterium uptake of each peptide between RBD-Nb and RBD-only were compared. Any peptide with uptake reduction of 5% or greater upon Nb binding was considered as protected.

Crystallization and structural analysis

Production of the RBD domain and complex formation with Nbs for crystallization

The RBD domain was produced and purified as described previously (Stadlbauer *et al,* 2020). As a variation to the established protocol, the production of the RBD (residues 319–541) was performed in the Expi293F™ GntI- expression system (Thermo Fisher Scientific, Dreieich, Germany). Expi293F™ GntI- cells were cultivated (37°C, 125 rpm, 8% (v/v) CO_2) to a density of 5.5×10^6 cells/ml. The cells were diluted with Expi293F expression medium to a density of 3.0×10^6 cells/ml, followed by transfection of RBD plasmid (1 µg/ml cell culture) with Expifectamine (Thermo Fisher Scientific) dissolved in Opti-MEM medium (Thermo Fisher Scientific), according the manufacturer's instructions. 20 h post-transfection, the transfection enhancers were added as documented in the Expi293F™ GntI- cells manufacturer's instructions. The cell suspension was cultivated for 5 days (37°C, 125 rpm, 8% (v/v) CO_2) and centrifuged (4°C, 23.900 *g*, 20 min) to clarify the supernatant. The supernatant was supplemented with His-A buffer stock solution (final concentration in the medium: 20 mM Na_2HPO_4, 300 mM NaCl, 20 mM imidazole, pH 7.4), before the solution was applied to a HisTrap FF crude column (GE Healthcare). The column was extensively washed with His-buffer-A (20 mM Na_2HPO_4, 300 mM NaCl, 20 mM imidazole, pH 7.4) and 50 mM imidazole before the RBD was eluted with 280 mM imidazole from the column. The RBD was dialyzed against PBS and concentrated to 2 mg/ml. The nanobody complex was formed by mixing the RBD with the purified NM1226 or NM1230 in a molar ratio of 1:1.1, followed by incubation for 3 h at 4°C.

For crystallization, the complexes were treated with Endo H_f (New England Biolabs) to truncate the oligosaccharide chain on the RBD. Therefore, Endo H_f (300 U per mg RBD) was added to the RBD:Nb complex and incubated for 2 days at 8°C. Endo H_f was removed by passing the sample through a MBP-Trap column (GE Healthcare). Finally, a size exclusion chromatography using a SD200 16/60 column (GE Healthcare) exchanged the buffer (20 mM HEPES, 150 mM NaCl, pH 7.4) and separated the RBD:Nb complexes from aggregates and nanobody excess.

Crystallization

The RBD:NM1230 and RBD:NM1226 complexes were concentrated to 23.2 mg/ml and 29.6 mg/ml, respectively, prior to crystallization. Initial crystallization screening was performed on an ART Robbins Gryphon crystallization robot with placing 400 nL drop RBD:Nb and mixed in a 1:1 ratio with the reservoir solution. For RBD:NM1230, initial crystals appeared overnight in crystallization buffer (200 mM $MgCl_2$, 20% (w/v) PEG 3350, pH 5.9) at 20°C and grew to a final size of $30 \times 30 \times 120$ µm^3 within 4 days. After 8 weeks, RBD:NM1226 complex crystallized in a precipitation solution (50 mM K_2HPO_4, 20% (w/v) PEG 8000, pH 5.0) at 4°C. The crystals were harvested and frozen in liquid nitrogen until data collection.

Structure determination and refinement

Data collection was performed on beamline X06SA at the Swiss Light Source (Villigen, Switzerland). For data reduction, the XDS package was used (Kabsch, 2010) and the resulting dataset was analyzed by XDSSTAT (Diederichs, 2006) to check for radiation damage. For RBD:1226 crystals, a dataset with 2.3 Å resolution was obtained and processed in space group $I4_1$ containing one complex in the asymmetric unit. The tetragonal crystals of RBD:NM1230 diffracted to 2.9 Å and were processed in space group $P4_32_12$ containing two copies of the complex. The structures were solved by molecular replacement using PHASER (McCoy, 2007) and CHAINSAW (Stein, 2008) modified templates of the RBD domain (pdb code: 6Z1Z) and a structure homologue of the nanobody (pdb code: 6XC4). Initial refinement involved simulated annealing as implemented in PHENIX (Adams *et al,* 2010) to reduce model bias. Further refinement was done in a cyclic procedure of reciprocal space refinement as implemented in REFMAC5 (Vagin *et al,* 2004) and real space corrections using COOT (Emsley *et al,* 2010). Several cycles of refinement yielded to a model with good stereochemistry and acceptable R-factors with R_{work}/ R_{free} of 26.7% / 30.7% and 19.0% / 22.2% for RBD:NM1230 and RBD:NM1226 complex, respectively (Appendix Table S2). The structure was validated with MOLPROBITY (Williams *et al,* 2018) prior deposition to the protein data bank (pdb code: 7NKT and 7B27 for RBD:NM1226 and RBD:NM1230, respectively). Figures were generated with PYMOL (SCHRODINGER, L. L. C. The PyMOL molecular graphics system. Version, 2010, 1. Jg., Nr. 5, S. 0.) and structure comparison was performed with DALI (Holm, 2019).

Cell culture

Caco-2 (Human Colorectal adenocarcinoma, ATCC HTB-37) cells were cultured at 37°C with 5% CO_2 in DMEM containing 10% FCS, 2 mM l-glutamine, 100 µg/ml penicillin-streptomycin, and 1% NEAA. The cell line was tested negative for mycoplasma using the

PCR mycoplasma kit Venor GeM Classic (Minerva Biolabs) and the Taq DNA Polymerase (Minerva Biolabs).

Viruses

All experiments associated with the SARS-CoV-2 virus were conducted in Biosafety Level 3 laboratory. The recombinant infectious SARS-CoV-2 clone expressing mNeonGreen (icSARS-CoV-2-mNG) (PMID: 32289263) was obtained from the World Reference Center for Emerging Viruses and Arboviruses (WRCEVA) at the UTMB (University of Texas Medical Branch). To generate icSARS-CoV-2-mNG stocks, 200.000 Caco-2 cells were infected with 50 µl of virus in a 6-well plate; the supernatant was harvested 48 hpi, centrifuged, and stored at −80°C. For MOI determination, a titration using serial dilutions of the mNeonGreen (icSARS-CoV-2-mNG) was conducted. The number of infectious virus particles per ml was calculated as the (MOI × cell number)/ (infection volume), where MOI = −ln(1 − infection rate).

Virus neutralization assay

For neutralization experiments, 1×10^4 Caco-2 cells/well were seeded in 96-well plates the day before infection in media containing 5% FCS. Caco-2 cells were co-incubated with the SARS-CoV-2 strain icSARS-CoV-2-mNG at a MOI = 1.1 and Nbs or serum samples in serial dilutions in the indicated concentrations. 48 hpi cells were fixed with 2% PFA and stained with Hoechst33342 (1 µg/ml final concentration) for 10 min at 37°C. The staining solution was removed and exchanged for PBS. For quantification of infection rates, images were taken with the Cytation3 (Biotek) and Hoechst+ and mNG+ cells were automatically counted by the Gen5 Software (Biotek). Infection rate was determined by dividing the number of infected cells through total cell count per condition. Data were normalized to respective virus-only infection control. Inhibitory concentration 50 (IC_{50}) was calculated as the half-maximal inhibitory dose using 4-parameter nonlinear regression (GraphPad Prism).

Patient samples

112 Serum samples of convalescent SARS-CoV-2-infected and eight uninfected individuals were analyzed in the course of this study. All samples used were de-identified and pre-existing. Ethical consent was granted from the Ethics Commission of the University of Tuebingen under the votum 179/2020/BO2. Samples were classified as SARS-CoV-2 infected, based upon a self-reported positive SARS-CoV-2 RT–PCR result.

Analyses and statistics

Graph preparation and statistical analysis were performed using the GraphPad Prism Software (Version 9.0.0).

Data availability

Atomic coordinates and structure factors have been deposited in the Protein Data Bank (PDB) under accession code 7NKT (RBD:NM1226 complex, www.rcsb.org/structure/unreleased/7NKT) and 7B27 (RBD:NM1230 complex, www.rcsb.org/structure/unreleased/7B27). Protein sequences of all nanobodies are listed in Appendix Table S1. All data that support the findings of this study are available from the corresponding authors upon reasonable request.

Expanded View for this article is available online.

Acknowledgements
This work was supported by the Initiative and Networking Fund of the Helmholtz Association of German Research Centers (grant number SO-96), the European Union's Horizon 2020 research and innovation program under grant agreement No 101003480—CORESMA. This work has further received funding from State Ministry of Baden-Württemberg for Economic Affairs, Labour and Housing Construction (FKZ 3-4332.62-NMI/68). We thank Florian Krammer for providing expression constructs for SARS-CoV-2 homotrimeric Spike and RBD. Open Access funding enabled and organized by Projekt DEAL.

Author contributions
Study design: NSM, TRW, MB, UR; Nb selection and biochemical characterization: PDK, BT, TRW; Immunization of the animal: HS, SN, AS; Multiplex binding assay: JH, DJ, MB; HDX-MS experiments: MG, AZ; Organization and providing patient samples: MoS, AN, JSW, KSL; Designing and performing crystallization studies: EO, GZ, TS; Virus neutralization assays: NR, MiS; Data analysis and statistical analysis: TRW, MB, JH, MG, AZ, NR, MiS, UR; Manuscript drafting: TRW, AD, UR; Study supervision: NSM, UR; Manuscript reading: All authors.

Conflict of interest
T.R.W., P.K., N.S.M., and U.R. are named as inventors on a patent application (EP 20 197 031.6) claiming the use of the described Nanobodies for diagnosis and therapeutics filed by the Natural and Medical Sciences Institute. The other authors declare no competing interest.

References

Adams PD, Afonine PV, Bunkoczi G, Chen VB, Davis IW, Echols N, Headd JJ, Hung LW, Kapral GJ, Grosse-Kunstleve RW *et al* (2010) PHENIX: a comprehensive Python-based system for macromolecular structure solution. *Acta Crystallogr D Biol Crystallogr* 66: 213 – 221

Ahmad J, Jiang J, Boyd LF, Natarajan K, Margulies DH (2021) Synthetic nanobody–SARS-CoV-2 receptor-binding domain structures identify distinct epitopes. *bioRxiv* https://doi.org/10.1101/2021.01.27.428466 [PREPRINT]

Amanat F, Stadlbauer D, Strohmeier S, Nguyen THO, Chromikova V, McMahon M. Jiang K. Arunkumar GA. Jurczyszak D. Polanco J *et al* (2020) A serological assay to detect SARS-CoV-2 seroconversion in humans. *Nat Med* 26: 1033 – 1036

Arbabi Ghahroudi M, Desmyter A, Wyns L, Hamers R, Muyldermans S (1997) Selection and identification of single domain antibody fragments from camel heavy-chain antibodies. *FEBS Lett* 414: 521 – 526

Becker M, Strengert M, Junker D, Kaiser PD, Kerrinnes T, Traenkle B, Dinter H, Häring J, Ghozzi S, Zeck A *et al* (2021) Exploring beyond clinical routine SARS-CoV-2 serology using MultiCoV-Ab to evaluate endemic coronavirus cross-reactivity. *Nat Commun* 12: 1152

Brouwer PJM, Caniels TG, van der Straten K, Snitselaar JL, Aldon Y, Bangaru S, Torres JL, Okba NMA, Claireaux M, Kerster G *et al* (2020) Potent neutralizing antibodies from COVID-19 patients define multiple targets of vulnerability. *Science* 369: 643 – 650

Byrnes JR, Zhou XX, Lui I, Elledge SK, Glasgow JE, Lim SA, Loudermilk R, Chiu CY, Wilson MR, Leung KK (2020) A SARS-CoV-2 serological assay to determine the presence of blocking antibodies that compete for human ACE2 binding. *medRxiv* https://doi.org/10.1101/2020.05.27.20114652 [PREPRINT]

Cao Y, Su B, Guo X, Sun W, Deng Y, Bao L, Zhu Q, Zhang X, Zheng Y, Geng C *et al* (2020) Potent neutralizing antibodies against SARS-CoV-2 identified by high-throughput single-cell sequencing of convalescent patients' B cells. *Cell* 182: 73 – 84 e16

Chi X, Liu X, Wang C, Zhang X, Li X, Hou J, Ren L, Jin Q, Wang J, Yang W (2020a) Humanized single domain antibodies neutralize SARS-CoV-2 by targeting the spike receptor binding domain. *Nat Commun* 11: 4528

Chi X, Yan R, Zhang J, Zhang G, Zhang Y, Hao M, Zhang Z, Fan P, Dong Y, Yang Y *et al* (2020b) A neutralizing human antibody binds to the N-terminal domain of the Spike protein of SARS-CoV-2. *Science* 369: 650 – 655

Custódio TF, Das H, Sheward DJ, Hanke L, Pazicky S, Pieprzyk J, Sorgenfrei M, Schroer MA, Gruzinov AY, Jeffries CM *et al* (2020) Selection, biophysical and structural analysis of synthetic nanobodies that effectively neutralize SARS-CoV-2. *Nat Commun* 11: 5588

Davies NG, Barnard RC, Jarvis CI, Kucharski AJ, Munday J, Pearson CAB, Russell TW, Tully DC, Abbott S, Gimma A *et al* (2020) Estimated transmissibility and severity of novel SARS-CoV-2 Variant of Concern 202012/01 in England. *medRxiv* https://doi.org/10.1101/2020.12.24.20248822 [PREPRINT]

Davies NG, Jarvis CI, Edmunds WJ, Jewell NP, Diaz-Ordaz K, Keogh RH (2021) Increased hazard of death in community-tested cases of SARS-CoV-2 variant of concern 202012/01. *medRxiv* https://doi.org/10.1101/2021.02.01.21250959 [PREPRINT]

Diederichs K (2006) Some aspects of quantitative analysis and correction of radiation damage. *Acta Crystallogr D Biol Crystallogr* 62: 96 – 101

Emsley P, Lohkamp B, Scott WG, Cowtan K (2010) Features and development of Coot. *Acta Crystallogr D Biol Crystallogr* 66: 486 – 501

Esparza TJ, Martin NP, Anderson GP, Goldman ER, Brody DL (2020) High affinity nanobodies block SARS-CoV-2 spike receptor binding domain interaction with human angiotensin converting enzyme. *bioRxiv* https://doi.org/10.1101/2020.07.24.219857 [PREPRINT]

Fink S, Ruoff F, Stahl A, Becker M, Kaiser P, Traenkle B, Junker D, Weise F, Ruetalo N, Horber S *et al* (2021) Multiplexed serum antibody screening platform using virus extracts from endemic coronaviridae and SARS-CoV-2. *ACS Infect Dis* https://doi.org/10.1021/acsinfecdis.0c00725

Gai J, Ma L, Li G, Zhu M, Qiao P, Li X, Zhang H, Zhang Y, Chen Y, Gong R *et al* (2020) A potent neutralizing nanobody against SARS-CoV-2 with inhaled delivery potential. *bioRxiv* https://doi.org/10.1101/2020.08.09.242867 [PREPRINT]

Gorshkov K, Susumu K, Chen J, Xu M, Pradhan M, Zhu W, Hu X, Breger JC, Wolak M. Oh E (2020) Quantum dot-conjugated SARS-CoV-2 spike pseudo-virions enable tracking of angiotensin converting enzyme 2 binding and endocytosis. *ACS Nano* 14: 12234 – 12247

Hamuro Y, Coales SJ (2018) Optimization of feasibility stage for hydrogen/deuterium exchange mass spectrometry. *J Am Soc Mass Spectrom* 29: 623 – 629

Hanke L, Vidakovics Perez L, Sheward DJ, Das H, Schulte T, Moliner-Morro A, Corcoran M, Achour A, Karlsson Hedestam GB, Hällberg BM *et al* (2020) An alpaca nanobody neutralizes SARS-CoV-2 by blocking receptor interaction. *Nat Commun* 11: 4420

Hansen J, Baum A, Pascal KE, Russo V, Giordano S, Wloga E, Fulton BO, Yan Y, Koon K, Patel K *et al* (2020) Studies in humanized mice and convalescent humans yield a SARS-CoV-2 antibody cocktail. *Science* 369: 1010 – 1014

Heffron AS, McIlwain SJ, Baker DA, Amjadi MF, Khullar S, Sethi AK, Shelef MA, O'Connor DH, Ong IM (2020) The landscape of antibody binding to SARS-CoV-2. *bioRxiv* https://doi.org/10.1101/2020.10.10.334292 [PREPRINT]

Holm L (2019) Benchmarking fold detection by DaliLite vol 5. *Bioinformatics* 35: 5326 – 5327

Huo J, Le Bas A, Ruza RR, Duyvesteyn HME, Mikolajek H, Malinauskas T, Tan TK, Rijal P, Dumoux M, Ward PN *et al* (2020) Neutralizing nanobodies bind SARS-CoV-2 spike RBD and block interaction with ACE2. *Nat Struct Mol Biol* 9: 846 – 854

Jiang S, Zhang X, Yang Y, Hotez PJ, Du L (2020) Neutralizing antibodies for the treatment of COVID-19. *Nat Biomed Eng* 4: 1134 – 1139

Ju B, Zhang Qi, Ge J, Wang R, Sun J, Ge X, Yu J, Shan S, Zhou B, Song S *et al* (2020) Human neutralizing antibodies elicited by SARS-CoV-2 infection. *Nature* 584: 115 – 119

Kabat E, Wu T, Perry H, Gottesman K, Foeller C (1991) *Sequences of proteins of immunological interest (Fifth)*, Washington, DC: US Department of Public Health Service, National Institutes of Health

Kabsch W (2010) Integration, scaling, space-group assignment and post-refinement. *Acta Crystallogr D Biol Crystallogr* 66: 133 – 144

Kirchhofer A, Helma J, Schmidthals K, Frauer C, Cui S, Karcher A, Pellis M, Muyldermans S, Casas-Delucchi CS, Cardoso MC *et al* (2010) Modulation of protein properties in living cells using nanobodies. *Nat Struct Mol Biol* 17: 133 – 138

Kochert BA, Iacob RE, Wales TE, Makriyannis A, Engen JR (2018) Hydrogen-deuterium exchange mass spectrometry to study protein complexes. *Methods Mol Biol* 1764: 153 – 171

Koenig PA, Das H, Liu H, Kummerer BM, Gohr FN, Jenster LM, Schiffelers LDJ, Tesfamariam YM, Uchima M, Wuerth JD *et al* (2021) Structure-guided multivalent nanobodies block SARS-CoV-2 infection and suppress mutational escape. *Science* 371: eabe6230

Lan J, Ge J, Yu J, Shan S, Zhou H, Fan S, Zhang Qi, Shi X, Wang Q, Zhang L *et al* (2020) Structure of the SARS-CoV-2 spike receptor-binding domain bound to the ACE2 receptor. *Nature* 581: 215 – 220

Lassaunière R, Frische A, Harboe ZB, Nielsen AC, Fomsgaard A, Krogfelt KA, Jørgensen CS (2020) Evaluation of nine commercial SARS-CoV-2 immunoassays. *medRxiv* https://doi.org/10.1101/2020.04.09.20056325 [PREPRINT]

Lauring AS, Hodcroft EB (2021) Genetic variants of SARS-CoV-2-what do they mean? *JAMA* 325: 529 – 531

Liu L, Wang P, Nair MS, Yu J, Rapp M, Wang Q, Luo Y, Chan J-W, Sahi V, Figueroa A *et al* (2020) Potent neutralizing antibodies against multiple epitopes on SARS-CoV-2 spike. *Nature* 584: 450 – 456

McCoy AJ (2007) Solving structures of protein complexes by molecular replacement with Phaser. *Acta Crystallogr D Biol Crystallogr* 63: 32 – 41

Muruato AE, Fontes-Garfias CR, Ren P, Garcia-Blanco MA, Menachery VD, Xie X, Shi PY (2020) A high-throughput neutralizing antibody assay for COVID-19 diagnosis and vaccine evaluation. *Nat Commun* 11: 4059

Muyldermans S (2013) Nanobodies: natural single-domain antibodies. *Annu Rev Biochem* 82: 775 – 797

Nieto GV, Jara R, Himelreichs J, Salinas C, Pinto T, Cheuquemilla Y, Margolles Y, del Rey NLG, Miranda-Chacon Z, Cuevas A *et al* (2020) Fast isolation of sub-nanomolar affinity alpaca nanobody against the Spike RBD of SARS-CoV-2 by combining bacterial display and a simple single-step density gradient selection. *bioRxiv* https://doi.org/10.1101/2020.06.09.137935 [PREPRINT]

Robbiani DF, Gaebler C, Muecksch F, Lorenzi JCC, Wang Z, Cho A, Agudelo M, Barnes CO, Gazumyan A, Finkin S *et al* (2020) Convergent antibody responses to SARS-CoV-2 in convalescent individuals. *Nature* 584: 437 – 442

Rogers TF, Zhao F, Huang D, Beutler N, Burns A, He W-T, Limbo O, Smith C, Song Ge, Woehl J *et al* (2020) Isolation of potent SARS-CoV-2 neutralizing antibodies and protection from disease in a small animal model. *Science* 369: 956 – 963

Rothbauer U, Zolghadr K, Tillib S, Nowak D, Schermelleh L, Gahl A, Backmann N, Conrath K, Muyldermans S, Cardoso MC *et al* (2006) Targeting and tracing antigens in live cells with fluorescent nanobodies. *Nat Methods* 3: 887 – 889

Rothbauer U, Zolghadr K, Muyldermans S, Schepers A, Cardoso MC, Leonhardt H (2008) A versatile nanotrap for biochemical and functional studies with fluorescent fusion proteins. *Mol Cell Proteomics* 7: 282 – 289

Roxhed N, Bendes A, Dale M, Mattsson C, Hanke L, Dodig-Crnkovic T, Christian M, Meineke B, Elsasser S, Andrell J *et al* (2020) A translational multiplex serology approach to profile the prevalence of anti-SARS-CoV-2 antibodies in home-sampled blood. *medRxiv* https://doi.org/10.1101/2020.07.01.20143966 [PREPRINT]

Scholer L, Le-Trilling VTK, Eilbrecht M, Mennerich D, Anastasiou OE, Krawczyk A, Herrmann A, Dittmer U, Trilling M (2020) A novel in-cell ELISA assay allows rapid and automated quantification of SARS-CoV-2 to analyze neutralizing antibodies and antiviral compounds. *Front Immunol* 11: 573526

Schoof M, Faust B, Saunders RA, Sangwan S, Rezelj V, Hoppe N, Boone M, Billesbolle CB, Zimanyi M, Deshpande I *et al* (2020) An ultra-high affinity synthetic nanobody blocks SARS-CoV-2 infection by locking Spike into an inactive conformation. *bioRxiv* https://doi.org/10.1101/2020.08.08.238469 [PREPRINT]

Shi R, Shan C, Duan X, Chen Z, Liu P, Song J, Song T, Bi X, Han C, Wu L *et al* (2020) A human neutralizing antibody targets the receptor-binding site of SARS-CoV-2. *Nature* 584: 120 – 124

Stadlbauer D, Amanat F, Chromikova V, Jiang K, Strohmeier S, Arunkumar GA, Tan J, Bhavsar D, Capuano C, Kirkpatrick E *et al* (2020) SARS-CoV-2 seroconversion in humans: a detailed protocol for a serological assay, antigen production, and test setup. *Curr Protoc Microbiol* 57: e100

Stein N (2008) CHAINSAW: a program for mutating pdb files used as templates in molecular replacement. *J Appl Crystallogr* 41: 641 – 643

Tai W, He L, Zhang X, Pu J, Voronin D, Jiang S, Zhou Y, Du L (2020) Characterization of the receptor-binding domain (RBD) of 2019 novel coronavirus: implication for development of RBD protein as a viral attachment inhibitor and vaccine. *Cell Mol Immunol* 17: 613 – 620

Tan CW, Chia WN, Qin X, Liu P, Chen M-C, Tiu C, Hu Z, Chen V-W, Young BE, Sia WR *et al* (2020) A SARS-CoV-2 surrogate virus neutralization test based on antibody-mediated blockage of ACE2-spike protein-protein interaction. *Nat Biotechnol* 38: 1073 – 1078

Tang MS, Case JB, Franks CE, Chen RE, Anderson NW, Henderson JP, Diamond MS, Gronowski AM, Farnsworth CW (2020) Association between SARS-CoV-2 neutralizing antibodies and commercial serological assays. *Clin Chem* 66: 1538 – 1547

Tegally H, Wilkinson E, Giovanetti M, Iranzadeh A, Fonseca V, Giandhari J, Doolabh D, Pillay S, San EJ, Msomi N *et al* (2020) Emergence and rapid spread of a new severe acute respiratory syndrome-related coronavirus 2 (SARS-CoV-2) lineage with multiple spike mutations in South Africa. *medRxiv* https://doi.org/10.1101/2020.12.21.20248640 [PREPRINT]

Tortorici MA, Beltramello M, Lempp FA, Pinto D, Dang HV, Rosen LE, McCallum M, Bowen J, Minola A, Jaconi S *et al* (2020) Ultrapotent human antibodies protect against SARS-CoV-2 challenge via multiple mechanisms. *Science* 370: 950 – 957

Vagin AA, Steiner RA, Lebedev AA, Potterton L, McNicholas S, Long F, Murshudov GN (2004) REFMAC5 dictionary: organization of prior chemical knowledge and guidelines for its use. *Acta Crystallogr D Biol Crystallogr* 60: 2184 – 2195

Walker SN, Chokkalingam N, Reuschel EL, Purwar M, Xu Z, Gary EN, Kim KY, Helble M, Schultheis K, Walters J *et al* (2020) SARS-CoV-2 assays to detect functional antibody responses that block ACE2 recognition in vaccinated animals and infected patients. *J Clin Microbiol* 58: e01533-20

Walker AS, Vihta K-D, Gethings O, Pritchard E, Jones J, House T, Bell I, Bell JI, Newton JN, Farrar J *et al* (2021) Increased infections, but not viral burden, with a new SARS-CoV-2 variant. *medRxiv* https://doi.org/10.1101/2021.01.13.21249721 [PREPRINT]

Walter JD, Hutter CAJ, Zimmermann I, Wyss M, Egloff P, Sorgenfrei M, Hürlimann LM, Gonda I, Meier G, Remm S *et al* (2020) Sybodies targeting the SARS-CoV-2 receptor-binding domain. *bioRxiv* https://doi.org/10.1101/2020.04.16.045419 [PREPRINT]

Wang Z, Schmidt F, Weisblum Y, Muecksch F, Barnes CO, Finkin S, Schaefer-Babajew D, Cipolla M, Gaebler C, Lieberman JA *et al* (2021) mRNA vaccine-elicited antibodies to SARS-CoV-2 and circulating variants. *Nature* https://doi.org/10.1038/s41586-021-03324-6

Williams CJ, Headd JJ, Moriarty NW, Prisant MG, Videau LL, Deis LN, Verma V, Keedy DA, Hintze BJ, Chen VB *et al* (2018) MolProbity: more and better reference data for improved all-atom structure validation. *Protein Sci* 27: 293 – 315

Wrapp D, De Vlieger D, Corbett KS, Torres GM, Wang N, Van Breedam W, Roose K, van Schie L, VIB-CMB COVID-19 Response Team, Hoffmann M *et al* (2020a) Structural basis for potent neutralization of betacoronaviruses by single-domain camelid antibodies. *Cell* 181: 1004 – 1015

Wrapp D, Wang N, Corbett KS, Goldsmith JA, Hsieh CL, Abiona O, Graham BS, McLellan JS (2020b) Cryo-EM structure of the 2019-nCoV spike in the prefusion conformation. *Science* 367: 1260 – 1263

Xiang Y, Nambulli S, Xiao Z, Liu H, Sang Z, Duprex WP, Schneidman-Duhovny D, Zhang C, Shi Y (2020) Versatile and multivalent nanobodies efficiently neutralize SARS-CoV-2. *Science* 370: 1479 – 1484

Yan R, Zhang Y, Li Y, Xia L, Guo Y, Zhou Q (2020) Structural basis for the recognition of SARS-CoV-2 by full-length human ACE2. *Science* 367: 1444 – 1448

Yu F, Xiang R, Deng X, Wang L, Yu Z, Tian S, Liang R, Li Y, Ying T, Jiang S (2020) Receptor-binding domain-specific human neutralizing monoclonal antibodies against SARS-CoV and SARS-CoV-2. *Signal Transduct Target Ther* 5: 212

Zhou T, Tsybovsky Y, Gorman J, Rapp M, Cerutti G, Chuang GY, Katsamba PS, Sampson JM, Schon A, Bimela J *et al* (2020) Cryo-EM structures of SARS-CoV-2 spike without and with ACE2 reveal a pH-dependent switch to mediate endosomal positioning of receptor-binding domains. *Cell Host Microbe* 28: 867 – 879

Zhu Na, Zhang D, Wang W, Li X, Yang Bo, Song J, Zhao X, Huang B, Shi W, Lu R *et al* (2020) A novel coronavirus from patients with pneumonia in China, 2019. *N Engl J Med* 382: 727 – 733

Zohar T, Alter G (2020) Dissecting antibody-mediated protection against SARS-CoV-2. *Nat Rev Immunol* 20: 392 – 394

Expanded View Figures

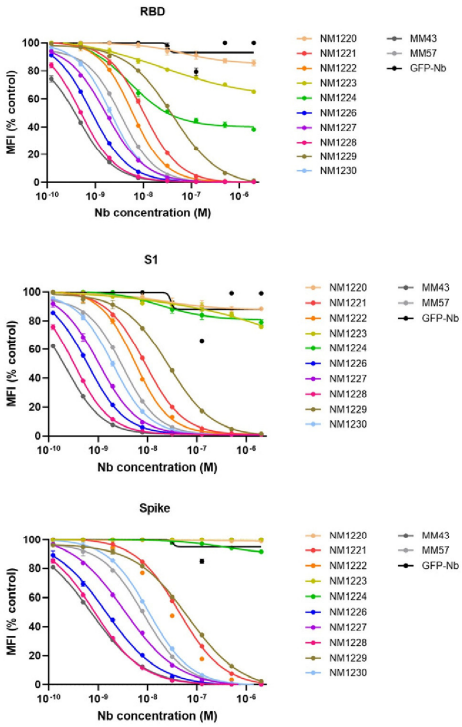

	IC_{50} (nM) ACE2:RBD Inhibition	IC_{50} (nM) ACE2:S1 Inhibition	IC_{50} (nM) ACE2:Spike Inhibition
NM1220	NA	NA	NA
NM1221	10.14	43.28	8.95
NM1222	5.80	27.28	5.50
NM1223	NA	NA	NA
NM1224	36.58	NA	NA
NM1226	0.82	1.44	0.63
NM1227	1.65	3.51	1.06
NM1228	0.50	0.85	0.32
NM1229	37.83	56.07	24.95
NM1230	2.12	10.57	1.96
GFP-Nb	NA	NA	NA
MM43	0.38	0.71	0.20
MM57	3.22	7.83	2.93

Figure EV1. ACE2-competing Nbs identified by multiplex binding assay.

Results from multiplex ACE2 competition assay are shown for the three spike-derived antigens: RBD, S1-domain (S1) and homotrimeric spike (Spike). Nbs were diluted from 2.1 μM to 0.12 nM in the presence ACE2 and antigen-bound ACE2 was measured. MFI signals were normalized to the maximum detectable signal per antigen given by the ACE2-only control. IC_{50} values were calculated from a four-parametric sigmoidal model. Data are presented as mean ± s.d. of three technical replicates.

Figure EV2. Epitope mapping of Nbs by HDX mass spectrometry.

Surface structure model of RBD showing the ACE2 interface and the HDX-MS epitope mapping results of RBD epitopes protected upon Nb binding are highlighted in different colors indicating the strength of protection. Accordingly, amino acid residues, which are part of the Nb recognized epitopes, are highlighted in the RBD sequence.

A Numbered amino acid residues of RBD (pdb code: 6M17 (Yan *et al*, 2020)) involved in the RBD:ACE2 interaction site (Lan *et al*, 2020; Yan *et al*, 2020) are shown in red.
B NM1226 (Nb-Set1)
C NM1228 (Nb-Set1)
D NM1230 (Nb-Set2)
E NM1221 (Nb-Set2)
F NM1222 (Nb-Set2)
G NM1224 (Nb-Set4)
H NM1223 (Nb-Set3)

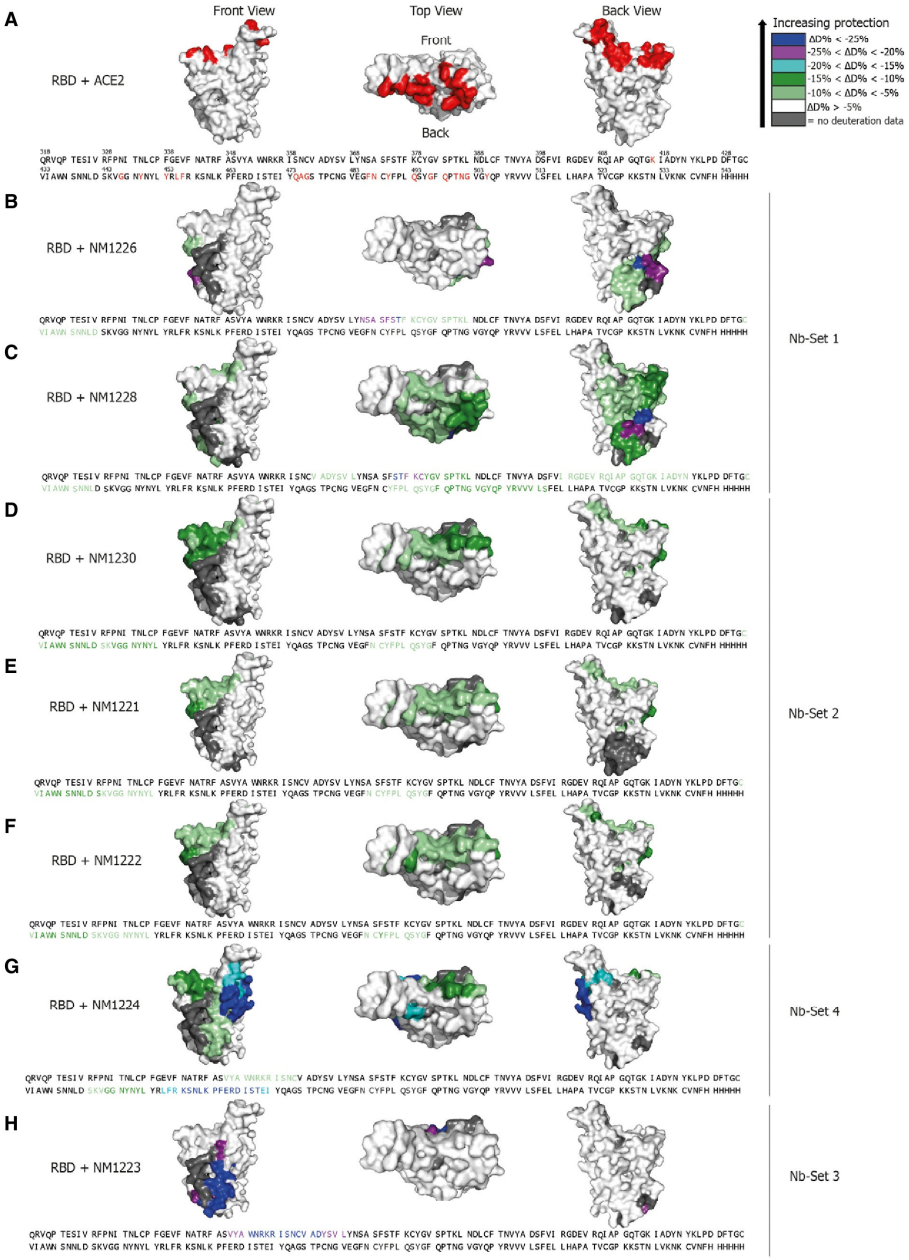

Figure EV2.

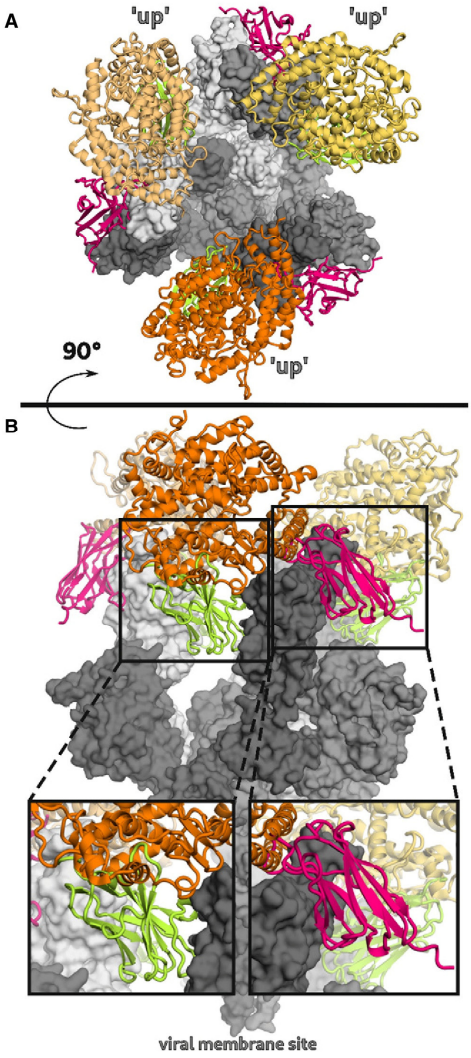

Figure EV3. Mechanism of ACE2 attachment inhibition by NM1226 and NM1230.

A, B (A) Top and (B) side view of the SARS-CoV-2 spike protein (gray) in complex with the ACE2 receptor (yellow, orange, dark orange) (pdb code: 7KMS) superposed on the RBD:Nb complexes NM1226 (light green) and NM1230 (magenta). A close-up view shown in black boxes elucidates how both Nbs block ACE2 receptor attachment.

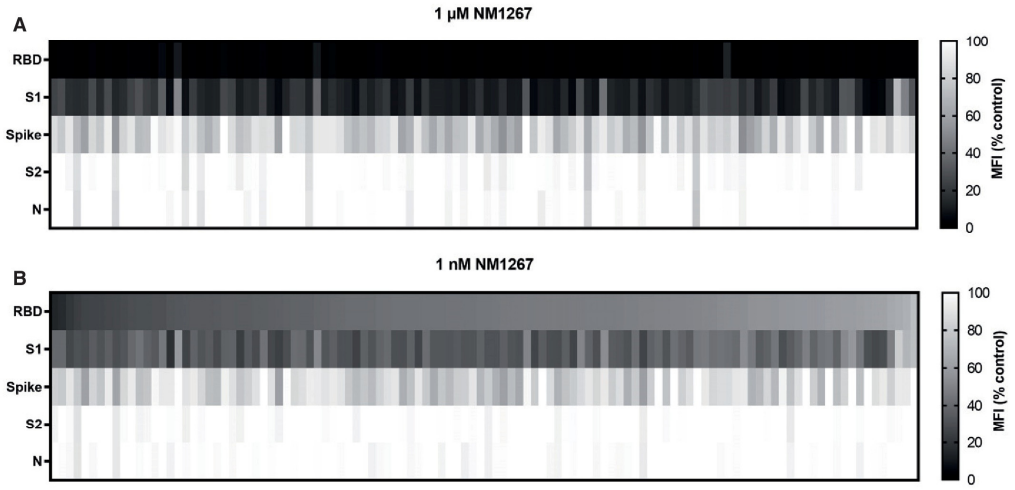

Figure EV4. NeutrobodyPlex enables a differentiated analysis on neutralizing IgGs.

Serum samples of 112 convalescent SARS-CoV-2-infected individuals were analyzed using the NeutrobodyPlex with antigen-coated beads comprising RBD, S1, spike, S2-domain (S2), and nucleocapsid (N) and two concentrations of NM1267 ($n = 1$). Light colored squares (high MFI (%control)) are indicative for IgGs outcompeting NM1267 from the RBD:ACE2 interface; dark colored squares (low MFI (% control)) show a continuous displacement of IgGs from serum samples in the presence of NM1267.

A NeutrobodyPlex NM1267 1 µM.
B NeutrobodyPlex NM1267 1 nM.

Appendix:

NeutrobodyPlex - monitoring SARS-CoV-2 neutralizing immune responses using nanobodies

Teresa R. Wagner[1,2], Elena Ostertag[3*]; Philipp D. Kaiser[2], Marius Gramlich[2], Natalia Ruetalo[4], Daniel Junker[2], Julia Haering[2], Bjoern Traenkle[2], Matthias Becker[2], Alex Dulovic[2], Helen Schweizer[5], Stefan Nueske[5], Armin Scholz[5], Anne Zeck[2], Katja Schenke-Layland[2,6,7,8], Annika Nelde[6,9,10], Monika Strengert[12,13], Juliane S. Walz[6,9,10,11], Georg Zocher[3], Thilo Stehle[3,14], Michael Schindler[4], Nicole Schneiderhan-Marra[2] and Ulrich Rothbauer[1,2,6#]*

Addresses

[1] Pharmaceutical Biotechnology, Eberhard Karls University, Tuebingen, Germany

[2] Natural and Medical Sciences Institute at the University of Tuebingen, Reutlingen, Germany

[3] Interfaculty Institute of Biochemistry, Eberhard Karls University, Tuebingen, Germany

[4] Institute for Medical Virology and Epidemiology of Viral Diseases, University Hospital Tuebingen, Tuebingen, Germany

[5] Livestock Center of the Faculty of Veterinary Medicine, Ludwig Maximilians University, Oberschleissheim, Germany

[6] Cluster of Excellence iFIT (EXC2180) "Image-Guided and Functionally Instructed Tumor Therapies", Eberhard Karls University, Tuebingen, Germany

[7] Department of Women's Health, Research Institute for Women's Health, Eberhard Karls University, Tuebingen, Germany

[8] Department of Medicine/Cardiology, Cardiovascular Research Laboratories, David Geffen School of Medicine at UCLA, Los Angeles, CA, USA

[9] Clinical Collaboration Unit Translational Immunology, German Cancer Consortium (DKTK), Department of Internal Medicine, University Hospital Tuebingen, Tuebingen, Germany

[10] Institute for Cell Biology, Department of Immunology, Eberhard Karls University, Tuebingen, Germany

[11] Dr. Margarete Fischer-Bosch Institute of Clinical Pharmacology and Robert Bosch Center for Tumor Disease, RBCT, Stuttgart, Germany

[12] Department of Epidemiology, Helmholtz Centre for Infection Research, Braunschweig, Germany

[13] TWINCORE GmbH, Centre for Experimental and Clinical Infection Research, a joint venture of the Hannover Medical School and the Helmholtz Centre for Infection Research, Hannover, Germany

[14] Vanderbilt University School of Medicine, Nashville, TN, USA

* both authors contributed equally to this work

corresponding author

Correspondence:

Prof. Dr. Ulrich Rothbauer, Natural and Medical Sciences Institute at the University of Tuebingen

Markwiesenstr. 55, 72770 Reutlingen, Germany.

E-mail: ulrich.rothbauer@uni-tuebingen.de

Phone: +49 7121 51530-415

Fax: +49 7121 51530-816

Orcid ID: 0000-0001-5923-8986

Table of Content

Appendix Figures

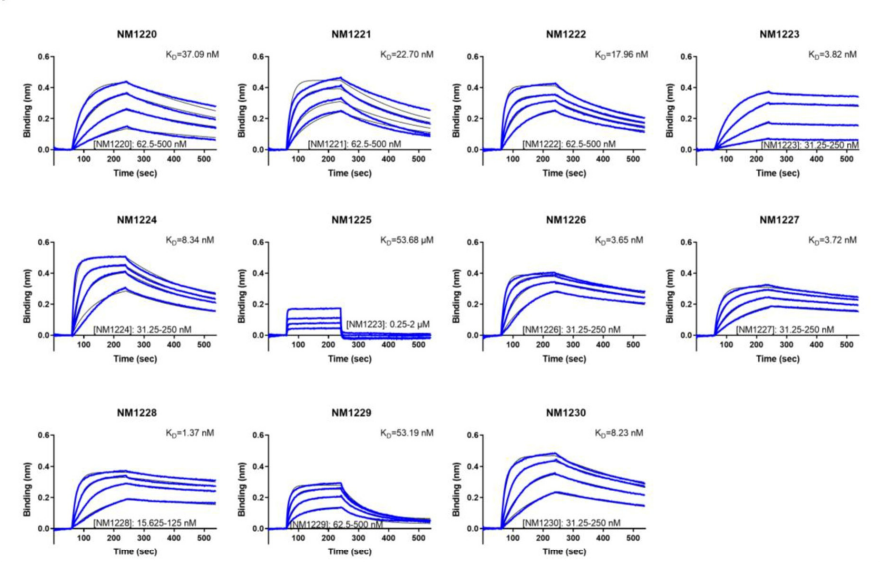

Appendix Figure S1 - Affinities of Nbs determined by biolayer interferometry.

Sensograms of BLI-based affinity measurements of 11 identified RBD-specific Nbs are shown. Biotinylated RBD was immobilized on streptavidin biosensors and kinetic measurements were performed by using four concentrations of purified Nbs ranging from 15.6 nM - 2 µM.

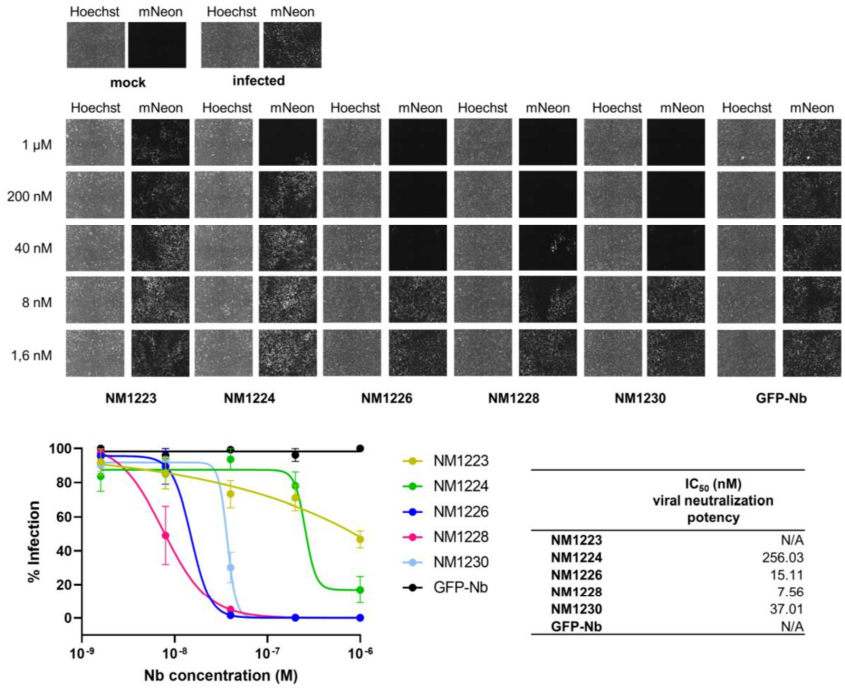

	IC_{50} (nM) viral neutralization potency
NM1223	N/A
NM1224	256.03
NM1226	15.11
NM1228	7.56
NM1230	37.01
GFP-Nb	N/A

Appendix Figure S2 - Selected Nbs neutralize SARS-CoV-2 infection.

Neutralization potency of NM1223, NM1224, NM1226, NM1228 and NM1230 was analyzed in Caco-2 cells using the SARS-CoV-2-mNG strain. As negative control, the GFP-Nb was used. Representative images of human Caco-2 cells upon infection with SARS-CoV-2 expressing mNeonGreen either in presence or absence of serial dilutions of RBD Nbs are shown. Infection rate normalized to virus-only infection control is illustrated as percent of infection (% Infection). IC_{50} value was calculated from a four-parametric sigmoidal model and data are presented as mean ± s.e.m. of three biological replicates (n = 3).

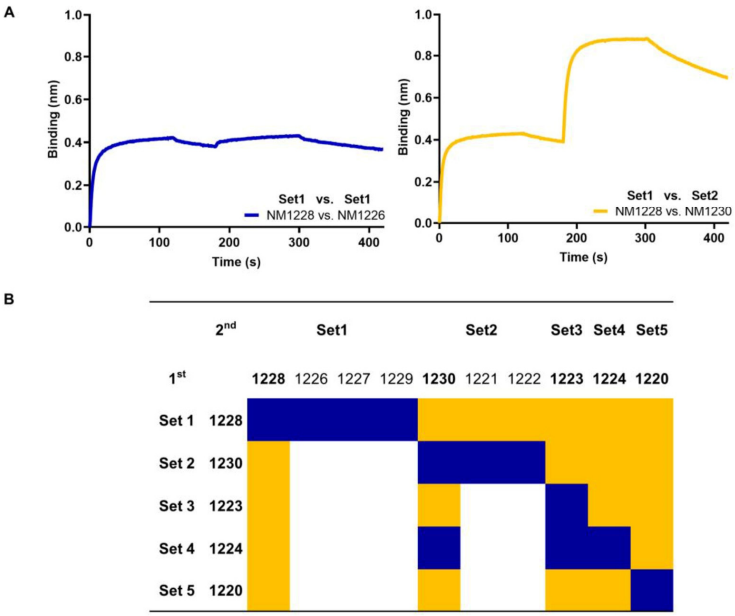

Appendix Figure S3 - Epitope binning of Nbs by biolayer interferometry.

A Representative sensograms of single measurements of Nbs affiliated to the same Nb-Set (NM1228/ NM1226, blue) and two different Nb-Sets (NM1228/ NM1230, orange) are shown. **B** Heat map illustration of competitive Nb epitope binning on RBD using BLI. Rows and columns represent the loading of the first and second Nb, respectively. Blue colored squares illustrate no additional binding of the second Nb meaning both Nbs belong to the same Nb-Set. Orange colored squares represent additional binding of the second Nb, hence these Nbs belong to different Nb-Sets.

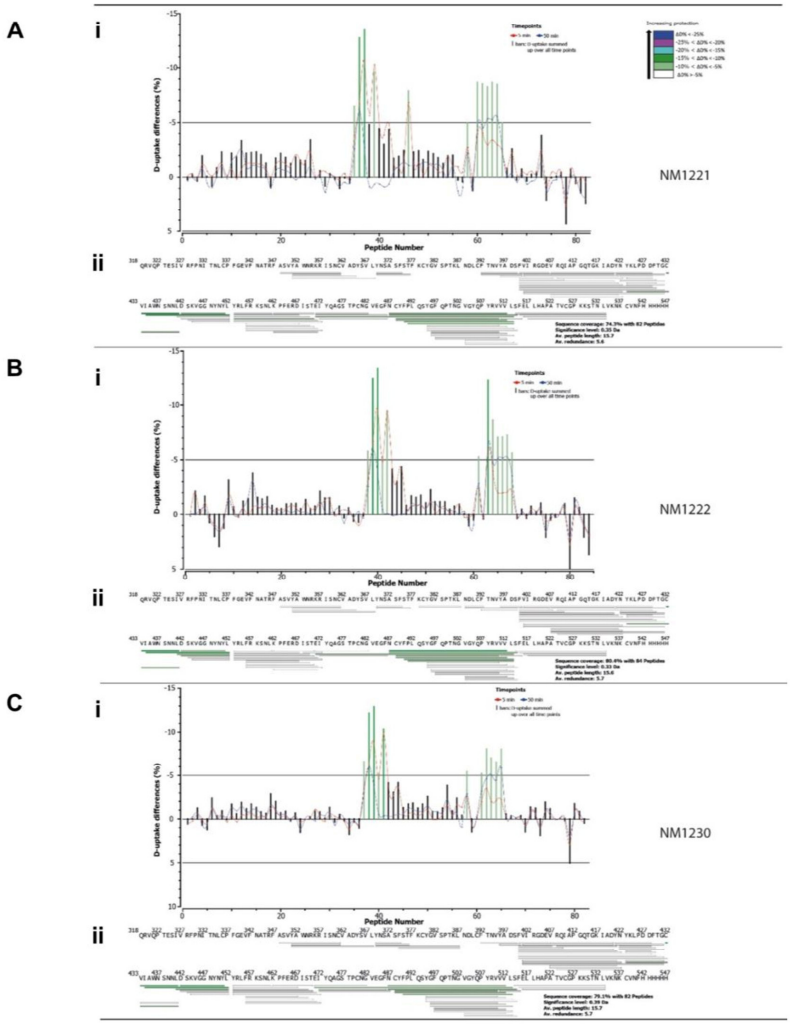
A
i
ii
B
i
ii
C
i
ii
NM1221
NM1222
NM1230
D-uptake differences (%)
Peptide Number

104

7

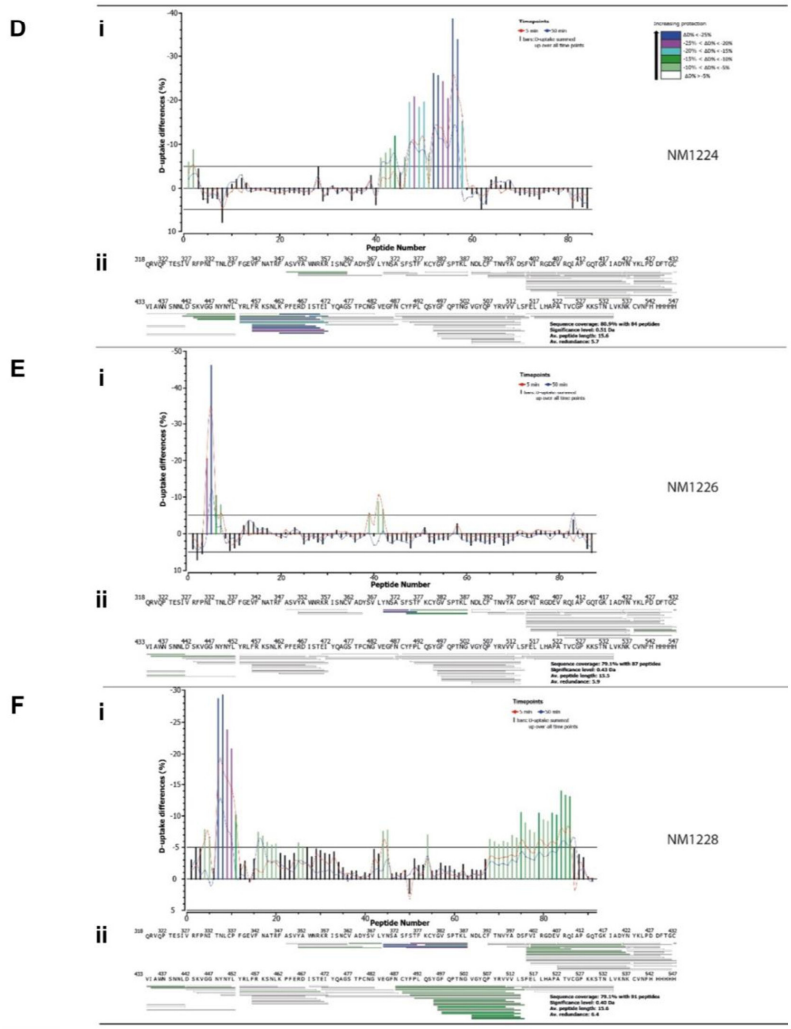
D
i
NM1224
D-uptake differences (%)
Peptide Number
ii
E
i
NM1226
D-uptake differences (%)
Peptide Number
ii
F
i
NM1228
D-uptake differences (%)
Peptide Number
ii

105

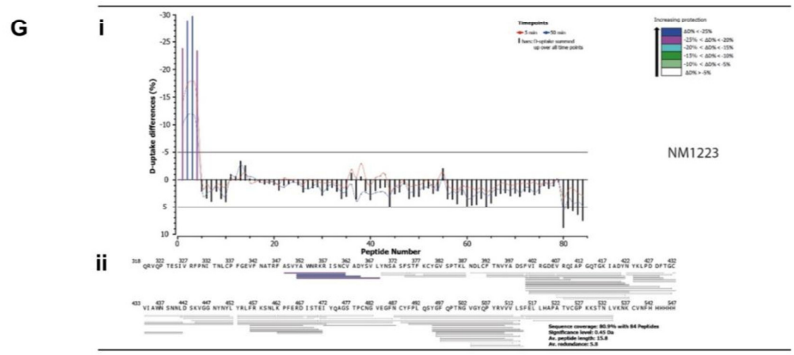

Appendix Figure S4 - Differential HDX and sequence coverage of RBD upon Nb binding.

A NM1221

B NM1222

C NM1230

D NM1224

E NM1226

F NM1228

G NM1223

i Residual differential HDX of partially overlapping peptic peptides numbered from the N- to the C-terminus and from short to long peptides. The minimum significant deuterium uptake difference (significance level) was calculated by HDExaminer from the variance of triplicate runs. On this basis, a minimum threshold of 3% deuterium difference was used to define regions as unprotected upon Nb binding. Peptides showing higher protection than 5% were considered as protected and corresponding bars were color-coded according to the legend.

ii Sequence coverage map of peptides validated for HDX data analysis for each nanobody-RBD pair. Peptides above the 5% protection threshold were color-coded using the colors from (i).

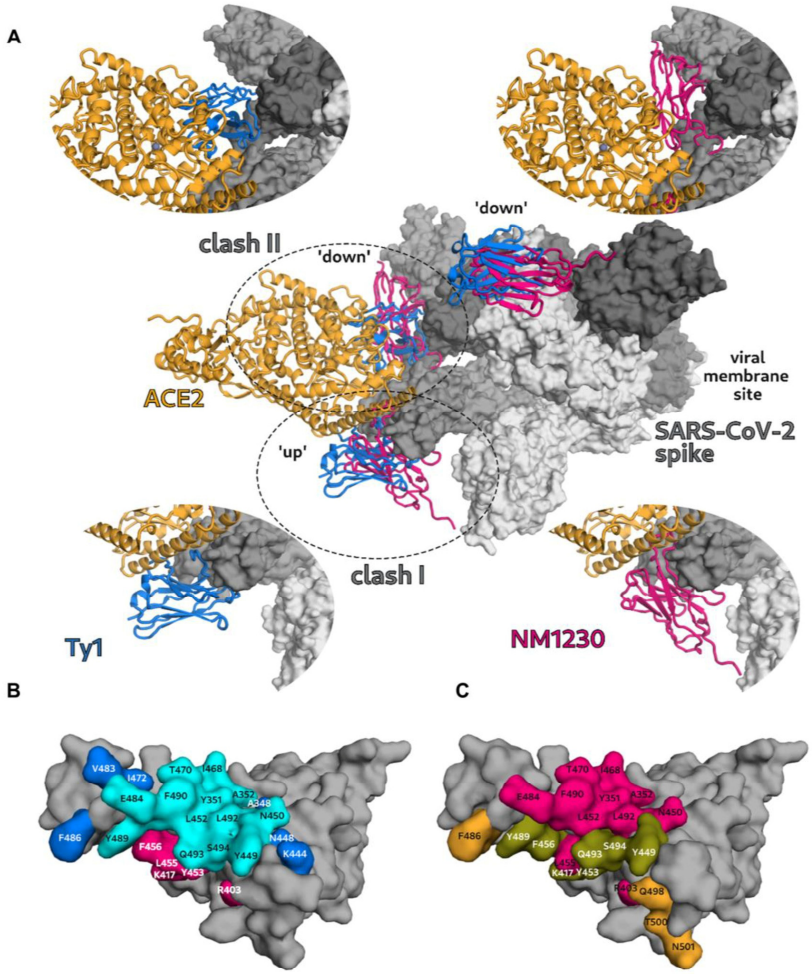

Appendix Figure S5 - NM1230 binding onto a spike in 'up/down/down' conformation and mapping of RBD:NM1230 interaction sites.

A Alignment of the SARS-CoV-2 spike:Ty1-Nb (blue) cryoEM structure (pdb code: 6ZXN) (Hanke *et al*, 2020) with the RBD:NM1230 complex. The ACE2 (orange) (pdb code: 6M17) and the NM1230 (pink) and Ty1-Nb (blue) are depicted as cartoons, whereas the spike trimer is shown in surface representation (grey). The neutralizing effect of NM1230 and Ty1-Nb is shown by expected collisions (clash I and clash II) with ACE2 in the alignment. Additional

close-up views of the individual Nb positions are shown to highlight the differences in Nb binding and ACE2 blocking.

B Individual binding sites of NM1230 (pink) and the Ty1-Nb (blue) (Hanke *et al.*, 2020) as well as common interaction residues (cyan) are highlighted on the surface representation of RBD.

C Comparison of the ACE2 interaction site and NM1230 epitope on RBD. Common residues are shown in olive, whereas residues exclusively in contact with ACE2 and NM1230 are colored in orange and pink, respectively. All interactions of NM1230, Ty1-Nb and ACE2 are depicted using a distance cut-off of < 4 Å to the surface of RBD.

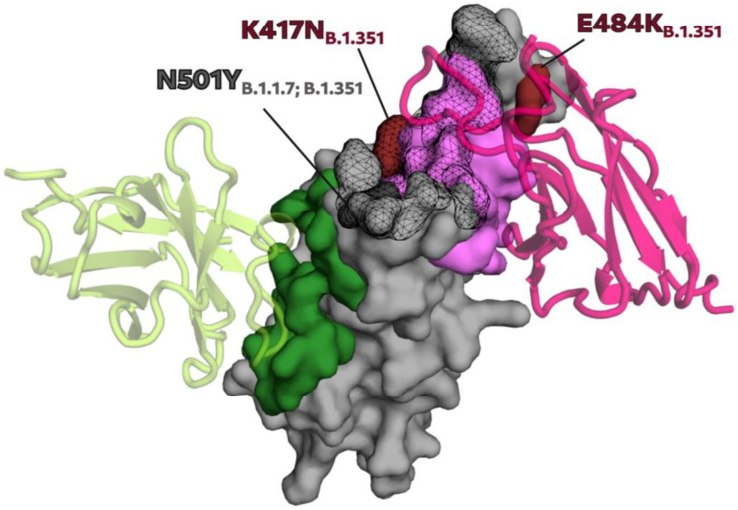

Virus Strain	RBD Mutation
B.1.1.7 (UK)	N501Y
B.1.351 (South Africa)	N501Y, E484K, K417N

Appendix Figure S6- Influence of RBD mutations on NM1226 and NM1230 binding.

NM1226 (light green) and NM1230 (magenta) are shown as cartoon with their corresponding binding epitopes on the RBD (surface representation) surface in dark green and light pink, respectively. Mutations on the RBD and in the binding epitope of NM1230, discovered in B.1.1.7 (United Kingdom) and B.1.351 (South Africa) SARS-CoV-2 strains, are highlighted in dark grey and dark red, respectively. In addition, the ACE2 interaction site on RBD is indicated as black mesh.

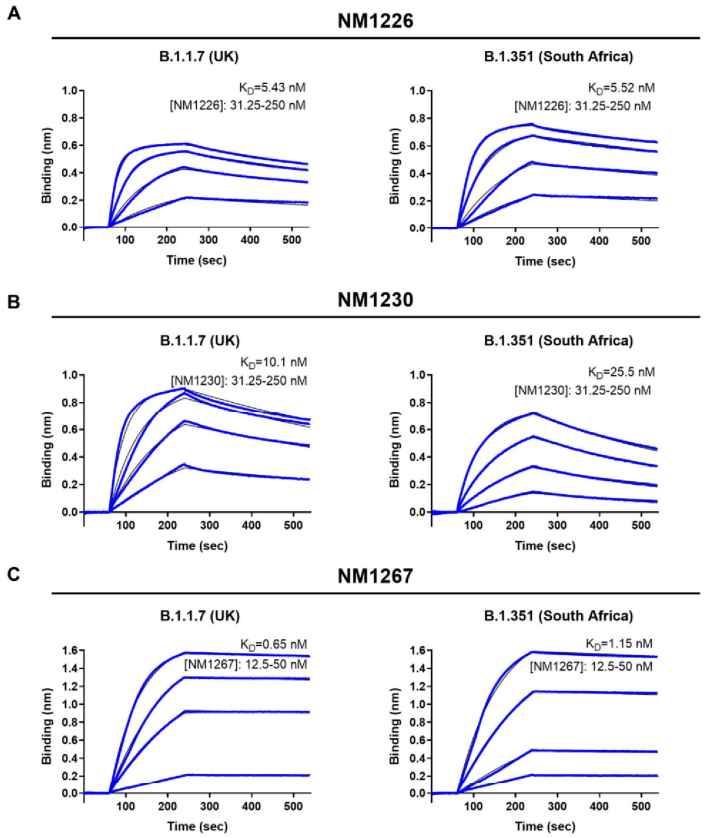

Appendix Figure S7 – Affinities of Nbs against mutated versions of RBD derived from B.1.1.7 and B.1.351.

Sensograms of BLI-based affinity measurements of selected RBD-specific Nbs are shown. Biotinylated RBD mutants derived from B.1.1.7 (UK) or B.1.351 (South Africa) were immobilized on streptavidin biosensors and kinetic measurements were performed by using four concentrations of purified Nbs ranging from 12.5 nM – 250 nM.

A NM1226

B NM1230

C NM1267

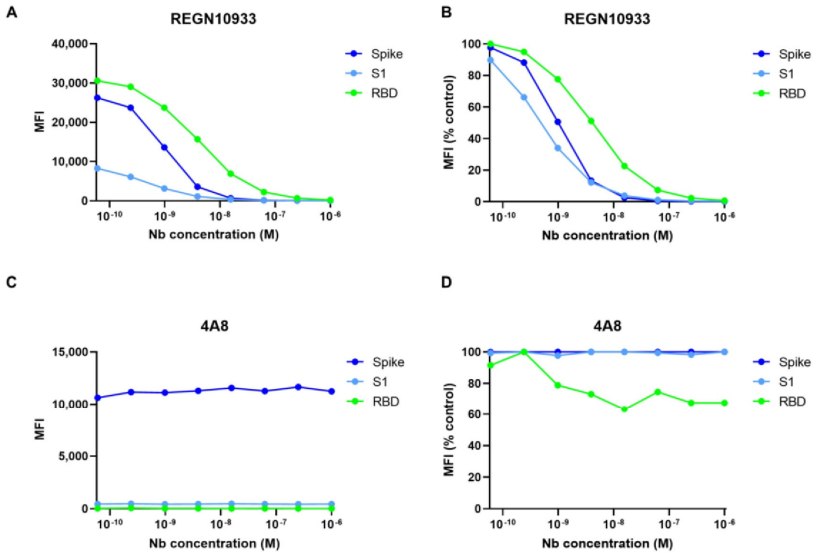

Appendix Figure S8 – Biparatopic NM1267 displaces neutralizing IgG binding the RBD:ACE2 interaction site.

Antigen-coated beads comprising RBD, S1 or spike were co-incubated with purified IgGs and a dilution series of NM1267 (1 µM to 6 pM). Mean fluorescent intensities (MFI) derived from antigen-bound IgGs in the presence of bipNb and MFIs normalized to the MFI values of IgG-only samples ((MFI (% control)) are illustrated.

A, B Anti-Spike RBD IgG clone REGN10933 (Hansen *et al*, 2020).

C, D Anti-Spike NTD IgG clone 4A8 (Chi *et al*, 2020)

177 **Appendix Tables**

178 **Appendix Table S1 – Amino acid sequences of RBD-specific Nbs.**

RBD-specific Nb	Amino Acid Sequence
NM1220	QVQLVESGGGLVQPGESLRLSCVAYGNMLRGYVVGWYRQAPGKQRELVAGIDTSGEKKKYADA VKGRFTISRDNAGNTVYLQMNSLKPEDTAVYYCNADAPWPPRPYSVIGTRTGYWGRGSPVTVSS
NM1221	DVQLVESGGGLVQPGGSLTLSCVGSGFLFSGYAMNWYRQAPGKALELVAGISNAGDITHYEEAM KGRVAISRVNDKNTVYLQMDDLKPEDTAVYRCHAPGVRVASGERNDVWGQGTQVTVSS
NM1222	EVQLVESGGGLVRPGGSLRLSCVGSGFTFSGYAINWYRQAPGKALELVAGISNAGDLTHYEEAM KGRVAISRANDKNTVYLQMDDLKPEDTAVYRCHAPGVRVGTGERNDVWGQGAQVTVSS
NM1223	EVQLVESGGGLVQPGGSLRLSCSASGFAFSSVSMSWVRLLPGKGTEWVAEIDRDGGNGNYEDS VKGRFTISRDNAKNTLFLQMNSLVPEDTALYYCRLGTRDHIMSGWGPGAPVTVSS
NM1224	DVQLVESGGSLVQPGGSLRLSCETSRSSLDAYAIGWFRQAPGKEREGVASISSSSMRTEYADSV KGRFTISRDNAKNTAYLDMNSLKPEDTAVYYCAAAGEYGRAWPGLDWYEFEYEGPGSPVTVSS
NM1225	QVQLVESGGGLVQPGGSLRLSCAASGNILRVHDMGWYRQAPGKQREYVAMITHGGITNYIDSVK GRFTISRDNAKNTVYLQMNSLKPEDTAVYYCHAVLSSALNGVTETSSNWGQGTQVTVSS
NM1226	QVQLVESGGGSVQPGGSLRLSCLGSGSLDYYAIGWFRQAPGKEREGVSCIASSGDRTIYADSVK GRFTISRDYGKNTVYLQMNSLKPEDTAMYYCAALQGSYYYTGFVANEYDYWGQGAPVTVSS
NM1227	EVQLVESGGGLVQPGGSLTLSCETSGRHFDIDDMGWYRQAPGKQRELVACITTESSTTYADAVK GRFTISRDNPDNTVYLQMTNLKPEDTAVYYCNAEMHPRSLDYALGNRDYWGQGAPVTVSS
NM1228	DVQLVESGGGLVRPGGSLRLSCESSGRHFDIDTMGWYRQAPGKQRELVASITSEKSTVYADALK GRFTISRDIPDNNVYLQMNNLKPEDTAVYYCNAKMDPHSLDYALGNQVFWGQGSLVTVSS
NM1229	EVQLQESGGGLVQPGESLRLSCAASGRTHDWYTMGWFRQAPGKEREFVARINWSSGMTYYAD SVKGRFTISRDNPKNTVYLQMNSLTPDDTAVYYCNVHPFTSPDYWGQGTRVTVSS
NM1230	QVQLVESGGGLVRPGGSLRLSCVGSGFTFSGYAMNWYRQAPGKALELVAGISNAGDLTHYEEP MKGRVAISRANDKNTVYLQMDDLKPEDTAVYRCHAPGVRVGTGERKDVWGQGAQVTVSS

179

Appendix Table S2 – Data collection and refinement statistics for the RBD:NM1226 and RBD:NM1230 complex structures.

Values in parentheses are for the highest resolution shell.

	RBD:NM1226 complex (PDB: 7NKT)	RBD:NM1230 complex (PDB: 7B27)
Resolution (Å)	46.1-2.3 (2.44-2.30)	46.5-2.90 (2.98-2.90)
Space group	$I4_1$	$P4_32_12$
Unit cell		
a, c (Å)	128.09, 77.68	63.29, 411.91
No of reflections	255015 (38715)	112109 (8061)
unique reflections	28115 (4500)	18493 (1340)
Redundancy	9.07	6.06
Completeness (%)	99.9 (99.6)	93.5 (95.7)
I/σ (I)	19.5 (1.42)	7.8 (1.15)
CC1/2	99.9 (48.4)	99.8 (66.2)
Wilson B ($Å^2$)	57	61
R_{meas} (%)	9.5 (156.8)	20.7 (186.2)
R_{work} / R_{free} (%)	18.4 / 22.4	26.6 / 30.5
Rmsd		
Bond angle (°)	1.45	1.21
Bond length (Å)	0.011	0.016
Average B-Factor ($Å^2$)		
RBD (chain A/B)	61.7	74.6 / 75.2
NM1230 (chain C/D)		64.5 / 81.2
NM1226(chain B)	70.7	
water	55.5	
Ramachandran		
Favoured (%)	97.0	86.3
Outlier (%)	0.3	3.9

185 **Appendix Table S3 - NeutrobodyPlex data illustrated in Fig 5B, C.**

186 Values as MFI and MFI (% control).

				# 225			
	Conc. NM1267 [nM]	MFI S1	MFI S1 (% control)	MFI Spike	MFI Spike (% control)	MFI RBD	MFI RBD (% control)
NM1267	1000.00	4453	49.58	26793	69.78	103	0.49
	250.00	4425	49.27	26898	70.05	162	0.77
	62.50	4377	48.74	26219	68.28	336	1.60
	15.63	4423	49.24	26126	68.04	1043	4.95
	3.91	4769	53.10	27975	72.85	3717	17.66
	0.98	5304	59.06	28713	74.78	9823	46.66
	0.24	6556	73.00	34834	90.72	16580	78.76
	0.06	8069	89.84	37128	96.69	19723	93.69
Control n=2 (Serum 1:400)	-	9076		38978		21104	
	-	8886		37819		20999	
				# 289			
	Conc. NM1267 [nM]	MFI S1	MFI S1 (% control)	MFI Spike	MFI Spike (% control)	MFI RBD	MFI RBD (% control)
NM1267	1000.00	503.0	15.31	15943	69.07	258	2.29
	250.00	512.0	15.58	16250	70.40	291	2.59
	62.50	527.5	16.05	16316	70.69	349	3.10
	15.63	547.0	16.65	16319	70.70	639	5.68
	3.91	641.0	19.51	16263	70.46	1667	14.82
	0.98	908.0	27.63	17369	75.25	4753	42.26
	0.24	1630.5	49.62	21303	92.29	8985	79.89
	0.06	2713.0	82.56	23808	103.15	11377	100.00
Control n=2 (Serum 1:400)	-	3320.0		23012		11250	
	-	3252.5		23152		11244	
				# 265			
	Conc. NM1267 [nM]	MFI S1	MFI S1 (% control)	MFI Spike	MFI Spike (% control)	MFI RBD	MFI RBD (% control)
NM1267	1000.00	1217	47.00	14574	73.63	93	1.36
	250.00	1264	48.81	15273	77.16	118	1.74
	62.50	1230	47.50	14896	75.26	174	2.56
	15.63	1255	48.48	14788	74.71	351	5.18
	3.91	1310	50.61	14993	75.75	947	13.96
	0.98	1549	59.84	15985	80.76	2535	37.38
	0.24	1881	72.65	17932	90.60	4648	68.52
	0.06	2225	85.96	19524	98.64	6147	90.63
Control n=2 (Serum 1:400)	-	2567		19781		6666	
	-	2610		19805		6899	

187

188

	# 272						
	Conc. NM1267 [nM]	MFI S1	MFI S1 (% control)	MFI Spike	MFI Spike (% control)	MFI RBD	MFI RBD (% control)
NM1267	1000.00	159	25.37	15289	86.71	48	2.05
	250.00	163	25.93	14686	83.29	53	2.24
	62.50	153	24.41	14857	84.26	65	2.77
	15.63	163	26.01	14923	84.63	116	4.95
	3.91	192	30.63	14895	84.47	321	13.70
	0.98	237	37.73	15036	85.27	853	36.40
	0.24	335	53.45	16833	95.47	1647	70.28
	0.06	531	84.72	17305	98.14	2165	92.38
Control n=2 (Serum 1:400)	-	611		17575		2329	
	-	643		17690		2359	

	# 159						
	Conc. NM1267 [nM]	MFI S1	MFI S1 (% control)	MFI Spike	MFI Spike (% control)	MFI RBD	MFI RBD (% control)
NM1267	1000.00	96	49.61	12792	99.38	37	5.07
	250.00	87	45.19	11708	90.96	37	5.00
	62.50	90	46.75	11503	89.36	43	5.83
	15.63	79	41.04	11340	88.10	51	6.99
	3.91	82	42.60	11263	87.50	92	12.54
	0.98	86	44.68	11437	88.85	257	35.23
	0.24	117	60.78	12483	96.98	531	72.79
	0.06	166	85.97	13044	100.00	681	93.28
Control n=2 (Serum 1:400)	-	191		13077		758	
	-	194		12668		702	

189

18

Appendix Table S4 - Data of control samples (C1-C4) from healthy donors tested in the NeutrobodyPlex and viral infection assay.

NeutrobodyPlex								
	C1		C2		C3		C4	
	MFI RBD	MFI RBD (% control)	MFI RBD	MFI RBD (% control)	MFI RBD	MFI RBD (% control)	MFI RBD	MFI RBD (% control)
1 µM NM1267	83	80.58	71	89.87	73	72.28	49	76.56
1 nM NM1267	103	100.00	103	100.00	89	88.12	80	100.00
Serum only	103	100.00	79	100.00	101	100.00	64	100.00

Viral Infection Assay				
Serum Dilution	% Infection			
	C1	C2	C3	C4
1:40	100.00	100.00	55.56	91.54
1:80	98.24	100.00	95.44	94.69
1:160	100.00	100.00	100.00	98.45
1:320	100.00	100.00	100.00	96.90
1:640	84.62	100.00	100.00	100.67
1:1280	95.77	91.11	99.26	70.12
1:2560	93.01	75.81	95.86	85.80
1:5120	83.85	94.74	94.39	100.00

194 **References**

195 Chi X, Yan R, Zhang J, Zhang G, Zhang Y, Hao M, Zhang Z, Fan P, Dong Y, Yang Y *et al*
196 (2020) A neutralizing human antibody binds to the N-terminal domain of the Spike protein of
197 SARS-CoV-2. *Science* 369: 650-655

198 Hanke L, Vidakovics Perez L, Sheward DJ, Das H, Schulte T, Moliner-Morro A, Corcoran M,
199 Achour A, Karlsson Hedestam GB, Hallberg BM *et al* (2020) An alpaca nanobody neutralizes
200 SARS-CoV-2 by blocking receptor interaction. *Nat Commun* 11: 4420

201 Hansen J, Baum A, Pascal KE, Russo V, Giordano S, Wloga E, Fulton BO, Yan Y, Koon K,
202 Patel K *et al* (2020) Studies in humanized mice and convalescent humans yield a SARS-
203 CoV-2 antibody cocktail. *Science* 369: 1010-1014

204

Appendix II:

Wagner TR[§], Schnepf D[§], Beer J[§], Ruetalo N[§], Klingel K, Kaiser PD, Junker D, Sauter M, Traenkle B, Frecot DI, Becker M, Schneiderhan-Marra N, Ohnemus A, Schwemmle M, Schindler M, Rothbauer U (2022) **Biparatopic nanobodies protect mice from lethal challenge with SARS-CoV-2 variants of concern.** EMBO Rep 23: e53865.

Article

TRANSPARENT PROCESS OPEN ACCESS

EMBO reports

Biparatopic nanobodies protect mice from lethal challenge with SARS-CoV-2 variants of concern

Teresa R Wagner[1,2,†], Daniel Schnepf[3,†], Julius Beer[3,†], Natalia Ruetalo[4,†], Karin Klingel[5], Philipp D Kaiser[2], Daniel Junker[2], Martina Sauter[5], Bjoern Traenkle[2], Desiree I Frecot[1,2], Matthias Becker[2], Nicole Schneiderhan-Marra[2], Annette Ohnemus[3], Martin Schwemmle[3,6], Michael Schindler[4] & Ulrich Rothbauer[1,2,7,*]

Abstract

The ongoing COVID-19 pandemic and the emergence of new SARS-CoV-2 variants of concern (VOCs) requires continued development of effective therapeutics. Recently, we identified high-affinity neutralizing nanobodies (Nbs) specific for the receptor-binding domain (RBD) of SARS-CoV-2. Taking advantage of detailed epitope mapping, we generate two biparatopic Nbs (bipNbs) targeting a conserved epitope outside and two different epitopes inside the RBD: ACE2 interface. Both bipNbs bind all currently circulating VOCs with high affinities and are capable to neutralize cellular infection with VOC B.1.351 (Beta) and B.1.617.2 (Delta) *in vitro*. To assess if the bipNbs NM1267 and NM1268 confer protection against SARS-CoV-2 infection *in vivo*, human ACE2 transgenic mice are treated intranasally before infection with a lethal dose of SARS-CoV-2 B.1, B.1.351 (Beta) or B.1.617.2 (Delta). Nb-treated mice show significantly reduced disease progression and increased survival rates. Histopathological analyses further reveal a drastically reduced viral load and inflammatory response in lungs. These data suggest that both bipNbs are broadly active against a variety of emerging SARS-CoV-2 VOCs and represent easily applicable drug candidates.

Keywords human ACE-2 mouse; neutralizing nanobodies; SARS-CoV-2; therapeutics; variants of concern

Subject Categories Immunology; Microbiology, Virology & Host Pathogen Interaction; Molecular Biology of Disease

DOI 10.15252/embr.202153865 | Received 13 October 2021 | Revised 30 November 2021 | Accepted 6 December 2021 | Published online 20 December 2021

EMBO Reports (2022) 23: e53865

Introduction

The ongoing SARS-CoV-2 pandemic continues to be challenging due to limited access to vaccines in certain countries, vaccine fatigue in others, the lack of effective and easy-to-administer antivirals, and the emergence of new variants of concern (VOCs) (Scudellari, 2020). Despite the rapid development of effective vaccines, global immunity or alternatively eradication of SARS-CoV-2 is currently out of reach (Kwok *et al*, 2020; Dagan *et al*, 2021). In addition, vaccination does not confer sterile immunity against SARS-CoV-2 infection and especially in the elderly, immunocompromised individuals, or individuals with severe preexisting conditions, breakthrough infections can still develop into life-threatening disease (Beaudoin-Bussières *et al*, 2020; Long *et al*, 2020; Havlin *et al*, 2021; Kustin *et al*, 2021). In particular, novel variants of concern (VOCs) with increased transmissibility and pathogenicity accompanied by a partial immune escape were reported to cause severe disease progression even in vaccinated individuals (Becker *et al*, 2021; Challen *et al*, 2021; Davies *et al*, 2021a, 2021b; Jewell, 2021; Madhi *et al*, 2021; Volz *et al*, 2021; Zhou *et al*, 2021). Consequently, there is a continuing and urgent need for effective and easily applicable antivirals against emerging VOCs. Neutralizing monoclonal antibodies (Nabs) have been granted emergency use authorization by the U.S. Food and Drug Administration and were shown to efficiently reduce mortality in COVID-19 patients with increased risk for a severe disease progression (Chen *et al*, 2020; Jiang *et al*, 2020; Weinreich *et al*, 2020). Most of these Nabs target the interaction site between receptor-binding domain (RBD) of the SARS-CoV-2 spike protein and angiotensin-converting enzyme (ACE) 2 to prevent viral entry into epithelial cells of the respiratory tract (Brouwer *et al*, 2020; Cao *et al*, 2020; Ju *et al*, 2020). However, viral escape from neutralizing antibodies resulted in several mutations affecting the RBD:ACE2 interface, which impairs binding of established Nabs and thus limits

1 Pharmaceutical Biotechnology, Eberhard Karls University, Tübingen, Germany
2 NMI Natural and Medical Sciences Institute at the University of Tübingen, Reutlingen, Germany
3 Institute of Virology, Medical Center University Freiburg, Freiburg, Germany
4 Institute for Medical Virology and Epidemiology of Viral Diseases, University Hospital Tübingen, Tübingen, Germany
5 Institute for Pathology and Neuropathology, University Hospital Tübingen, Tübingen, Germany
6 Faculty of Medicine, University of Freiburg, Freiburg, Germany
7 Cluster of Excellence iFIT (EXC2180) "Image-Guided and Functionally Instructed Tumor Therapies", Eberhard Karls University, Tübingen, Germany
*Corresponding author. Tel: +49 7121 51530 415; Fax: +49 7121 51530 816; E-mail: ulrich.rothbauer@uni-tuebingen.de
†These authors contributed equally to this work

current direct-acting antiviral treatment options (Dejnirattisai *et al*, 2021; preprint: Diamond *et al*, 2021; Wang *et al*, 2021).

In parallel to conventional antibodies, camelid single-domain antibody fragments, better known as nanobodies (Nbs), have been developed to target the RBD of SARS-CoV-2 (Chi *et al*, 2020; Hanke *et al*, 2020; Huo *et al*, 2020; Wrapp *et al*, 2020; Wagner *et al*, 2021). Due to their unique physicochemical properties such as small size, stable folding, and efficient tissue penetration, Nbs are considered to be ideal for therapeutic application. Indeed, some of these Nbs showed strong neutralizing efficacies against SARS-CoV-2, especially when used in the multivalent or multiparatopic format (Xiang *et al*, 2020; Huo *et al*, 2021; Koenig *et al*, 2021; Nambulli *et al*, 2021; Schepens *et al*, 2021; Wagner *et al*, 2021).

Recently, we generated a biparatopic (bip) Nb (NM1267) that binds two distinct sites, one epitope inside and one outside of the RBD:ACE2 interface and showed a strong neutralizing capacity (Wagner *et al*, 2021). In this study, we expanded our portfolio for potential therapeutic applications by developing a new bipNb NM1268 that additionally targets a different epitope within the RBD:ACE2 interface. To evaluate their protective efficacy *in vivo*, transgenic mice expressing human ACE2 (K18-hACE2 mice) (McCray *et al*, 2007; Winkler *et al*, 2020) were challenged with a lethal dose of the early circulating SARS-CoV-2 B.1, VOC B.1.351 (Beta) or VOC B.1.617.2 (Delta). Consistent with its neutralizing activity *in vitro*, NM1267 efficiently protected mice from weight loss and profound lung tissue damage after infection with SARS-CoV-2 B.1 or VOC B.1.351 (Beta), whereas NM1268 was slightly more protective against the VOC B.1.617.2 (Delta). This demonstrates how well-characterized Nbs targeting different functional epitopes can be combined as bipNbs to serve as promising drug candidates.

Results

Following our recently reported approach in which we combined two SARS-CoV-2 RBD-binding Nbs to generate the strongly neutralizing biparatopic Nb (bipNb) NM1267 (Wagner *et al*, 2021), we designed an additional bipNb by genetically coupling the neutralizing Nbs NM1228 and NM1226 via a flexible Gly-Ser ($(G_4S)_4$) linker (Appendix Table S1). While the bipNb NM1267 combines the two Nbs NM1230 and NM1226, which have been shown to target two distinct epitopes, one inside and one outside the RBD:ACE2 interface, the new bipNb NM1268 includes, in addition to NM1226, Nb NM1228, which binds a different epitope inside the RBD:ACE2 interface (Fig EV1A and B). Like NM1267 (Wagner *et al*, 2021), NM1268 was produced with high yield and good purity in mammalian cells and showed picomolar affinities to RBD derived from SARS-CoV-2 B.1 ($RBD_{B.1}$) as measured by biolayer interferometry (BLI; Fig 1A). The results of a multiplex ACE2 competition assay (Wagner *et al*, 2021) further revealed that both bipNbs block the interaction of SARS-CoV-2 RBD, S1, or homotrimeric Spike and human ACE2 in a low picomolar range (Fig EV2A–D). For further analysis, we next assessed their biophysical properties by measuring thermal unfolding and aggregation with nano differential scanning fluorimetry (nanoDSF; Fig 1B). While both bipNbs showed a slight increase in light scattering, indicating a higher aggregation tendency at higher, non-physiological temperatures, reanalysis after accelerated aging at 37°C for 10 days revealed no considerable differences compared to baseline (Fig 1B). From these data, we concluded that both bipNbs are highly stable and applicable for further *in vivo* analysis.

With the precise epitopes known, we considered that both bipNbs could also be effective against lately described VOCs (Fig EV1A–C). Therefore, we analyzed binding affinities of NM1267 and NM1268 toward RBDs of emerging SARS-CoV-2 variants using BLI (Fig 2A–Q). Compared to RBD of B.1, NM1267 showed similar or even increased affinity to RBDs from B.1.1.7 (Alpha; Fig 2A), B.1.351 (Beta; Fig 2B), P1 (Gamma; Fig 2C), P3 (Theta; Fig 2F) and A.23.1 (Fig 2H). A slight decrease in affinity was observed for RBDs from B.1.617.2 (Delta; Fig 2D), B.1.429 (Epsilon; Fig 2E) and B.1.617.1 (Kappa; Fig 2G), all of which have the exchange of Leu for Arg at position 452 (L452R). In contrast, NM1268 displayed robust binding affinities to all measured VOCs (Fig 2I–Q), with remarkable ~ 100-fold increased binding affinities compared to other VOCs determined for B.1.617.2 (Delta; Fig 2L) and B.1.429 (Epsilon; Fig 2M). In summary, the measured affinities confirmed the high potential of NM1267 and NM1268 to efficiently bind SARS-CoV-2 variants with multiple mutations at different positions of the RBD (Figs 2A–Q and EV1A–C).

The VOCs can evade the immune response after vaccination or treatment with established Nabs (Becker *et al*, 2021; Madhi *et al*, 2021; Mlcochova *et al*, 2021; Wang *et al*, 2021), due to escape mutations within the RBD (Li *et al*, 2021; Zhou *et al*, 2021). To investigate the neutralization capacity of NM1267 and NM1268 against the two escape variants B.1.351 (Beta) and B.1.617.2 (Delta) *in vitro*, we performed virus neutralization assays (VNTs) using a non-specific bivalent Nb (bivNb) NM1251 as negative control. For NM1267, we observed a strong neutralization of SARS-CoV-2 B.1 and B.1.351 (Beta), with IC_{50} values of 0.33 and 0.78 nM, respectively. Still efficient, albeit lower neutralization was determined for the B.1.617.2 (Delta) variant with an IC_{50} value of 52.55 nM, a finding that was consistent with the decreased affinity measured for all VOCs harboring the L452R mutation (Fig 3A–C and G). In contrast, a strong neutralization potency of NM1268 was determined for all variants with IC_{50} values of 2.37 nM for SARS-CoV-2 B.1, 6.06 nM

Figure 1. Affinity and stability of different biparatopic nanobodies.

A Affinity measurements by biolayer interferometry (BLI) of bipNbs NM1267 and NM1268. NM1267 and NM1268 were applied with concentrations ranging from 5 to 0.625 nM and from 20 to 2.5 nM, respectively (illustrated with gradually lighter shades) on immobilized RBD derived from SARS-CoV-2 B.1 ($RBD_{B.1}$). Global 1:1 fits are illustrated as dashed lines and binding affinity (K_D), association (k_{on}), and dissociation constant (k_{off}) determined for the individual bipNbs are summarized.

B Stability analysis of bipNbs NM1267 and NM1268 was performed at time points T_0 and T_{10} after storage at 37°C for 10 days to induce accelerated aging. Protein unfolding was determined by fluorescence emission wavelength shifts illustrated as fluorescence ratios (350 nm/ 330 nm) as first derivative. Protein aggregation status was measured by light intensity loss due to scattering illustrated as first derivative. Melting (T_m) and aggregation (T_{Agg}) temperature are summarized as table for both time points.

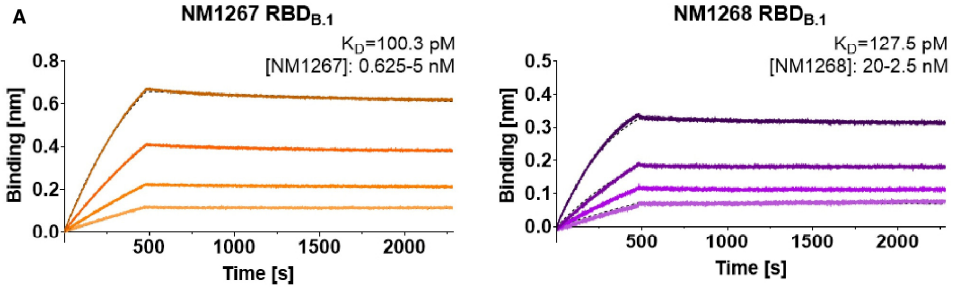

	K_D (pM)	k_{on} (10^5 M^{-1} s^{-1})	k_{off} (10^{-5} s^{-1})
NM1267	100.3	3.88 ± 0.006	3.89 ± 0.010
NM1268	127.5	1.53 ± 0.004	1.94 ± 0.023

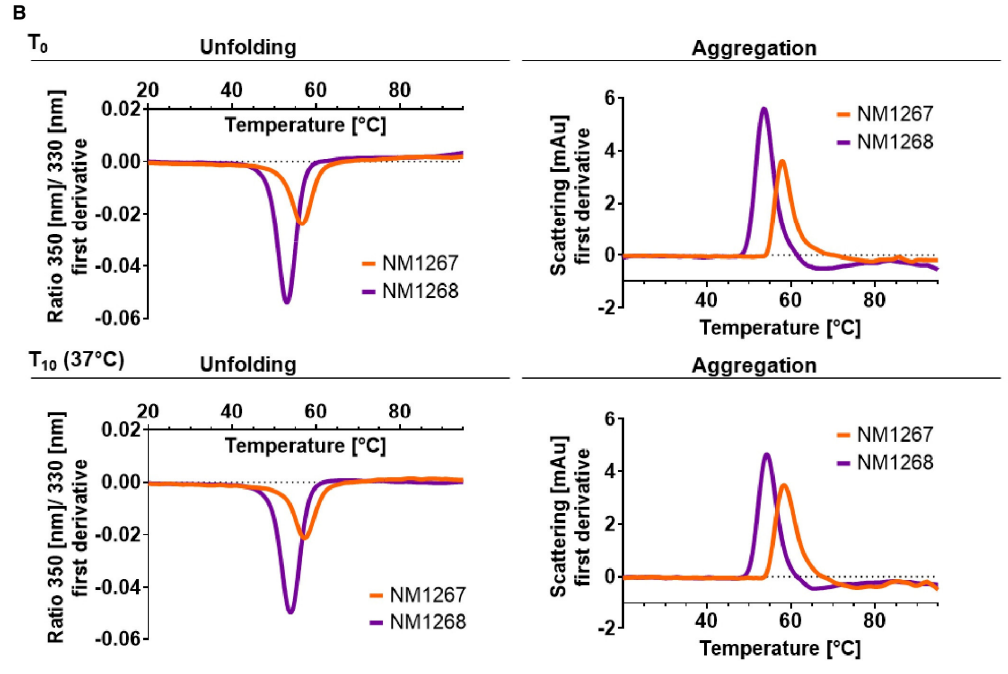

	T_0		T_{10} (37°C)	
	T_M (°C)	T_{Agg} (°C)	T_M (°C)	T_{Agg} (°C)
NM1267	56.5 ± 0.03	55.9 ± 0.09	57.2 ± 0.12	55.7 ± 0.08
NM1268	53.0 ± 0.05	50.2 ± 0.22	53.8 ± 0.01	51.0 ± 0.23

Figure 1.

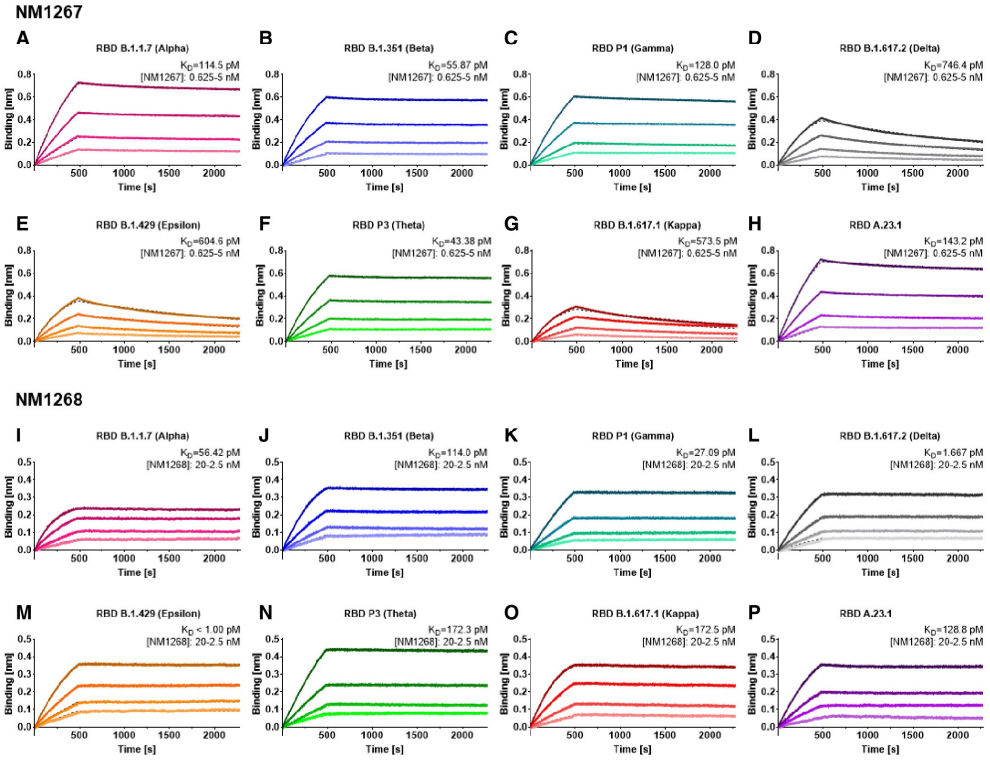

Q

Pangolin (WHO)	NM1267			NM1268		
	K_D [pM]	k_{on} [$10^5 M^{-1} s^{-1}$]	k_{off} [$10^{-5} s^{-1}$]	K_D [pM]	k_{on} [$10^5 M^{-1} s^{-1}$]	k_{off} [$10^{-5} s^{-1}$]
B.1.1.7 (Alpha)	114.5	3.87 ± 0.007	4.43 ± 0.011	56.42	2.32 ± 0.004	1.31 ± 0.021
B.1.351 (Beta)	55.87	3.96 ± 0.007	2.21 ± 0.011	114.0	1.15 ± 0.021	1.31 ± 0.017
P1 (Gamma)	128.0	2.75 ± 0.007	3.53 ± 0.011	27.09	0.53 ± 0.003	0.14 ± 0.016
B.1.617.2 (Delta)	764.4	5.17 ± 0.016	38.6 ± 0.031	1.667	0.55 ± 0.003	< 0.01 ± 0.000
B.1.429 (Epsilon)	604.6	5.68 ± 0.018	34.4 ± 0.032	< 1.00	0.90 ± 0.003	< 0.01 ± 0.000
P3 (Theta)	43.38	3.96 ± 0.006	1.27 ± 0.010	172.3	0.49 ± 0.002	0.85 ± 0.013
B.1.617.1 (Kappa)	573.5	6.46 ± 0.028	37.0 ± 0.048	172.5	1.47 ± 0.003	2.54 ± 0.016
A.23.1	143.2	4.20 ± 0.008	6.01 ± 0.013	128.8	1.05 ± 0.003	1.03 ± 0.018

Figure 2. Biparatopic Nanobodies target several recently identified RBD variants with picomolar affinity.

A–P Affinity measurements by BLI of bipNb NM1267 and NM1268 on recently identified RBD variants B.1.1.7 (Alpha) (A, I), B.1.351 (Beta) (B, J), P1 (Gamma) (C, K), B.1.617.2 (Delta) (D, L), B.1.429 (Epsilon) (E, M), P3 (Theta) (F, N), B.1.617.1 (Kappa) (G, O), and A.23.1 (H, P). NM1267 and NM1268 were applied with concentrations ranging from 5 to 0.625 nM and from 20 to 2.5 nM, respectively (illustrated with gradually lighter shades), on immobilized RBD variants. Global 1:1 fits are illustrated as dashed lines.

Q Tabular summary of binding affinity (K_D), association (k_{on}), and dissociation constant (k_{off}) determined for the individual RBD variants.

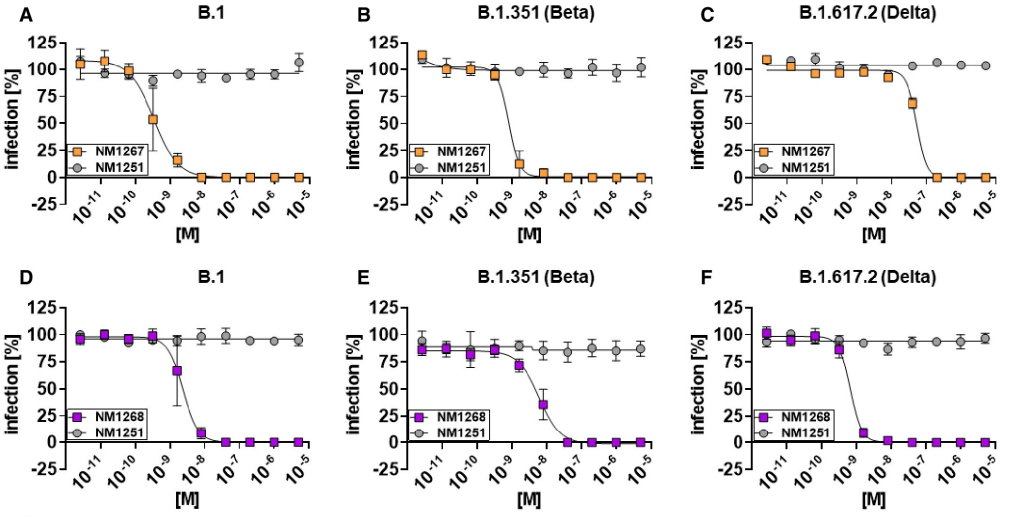

G

	NM1267 IC_{50}	Control NM1251 IC_{50}	NM1268 IC_{50}	Control NM1251 IC_{50}
B.1	0.33 nM	-	2.37 nM	-
B.1.351 (Beta)	0.78 nM	-	6.06 nM	-
B.1.617.2 (Delta)	52.55 nM	-	0.67 nM	-

Figure 3. Biparatopic Nanobodies neutralize B.1, B.1.351, and B.1.617.2 SARS-CoV-2 infection in Caco-2 cells.

A–F Neutralization potency of NM1267 and NM1268 were analyzed in Caco-2 cells using the SARS-CoV-2 B.1 (A, D) SARS-CoV-2 B.1.351 (Beta) (B, E), and SARS-CoV-2 B.1.617.2 (Delta) (C, F). Infection normalized to virus-only infection control is illustrated as percent of infection (infection [%]). Data are presented as mean ± SEM of three (n = 3) biological replicates.

G Tabular summary of IC_{50} values, calculated from a four-parametric sigmoidal model.

for B.1.351 (Beta), and 0.67 nM for B.1.617.2 (Delta; Fig 3D–G), in line with the measured affinities.

Next, we evaluated the efficacy of bipNbs as potential therapeutics to combat infections with SARS-CoV-2 *in vivo*. Therefore, we used K18-hACE2 transgenic mice expressing human ACE2 which are highly permissive for infection with clinical SARS-CoV-2 isolates (Winkler *et al*, 2020). Considering a broad applicability for which noninvasive routes of administration are preferred, we chose to deliver the bipNbs intranasally. In an initial experimental setting, mice were treated prophylactically with 20 μg NM1267 or the non-specific control (NM1251) followed by SARS-CoV-2 B.1 infection 7 h later (Fig 4A). Weight loss and survival of infected mice were monitored for 14 days post-infection (d p.i.). All infected animals treated with the negative control NM1251 became severely sick with obvious clinical signs of disease, lost substantial amounts of body weight, and 14 out of 15 animals had to be euthanized (Fig 4B and C). In contrast, administration of NM1267 significantly reduced signs of disease, weight loss, and 9 out of 12 animals survived the infection. Additionally, virus shedding by NM1267-treated mice, determined by viral load on nasal swabs, was significantly reduced in comparison with control animals on day 1 after infection (Fig 4D). We further performed histopathological analyses of lungs from SARS-CoV-2 B.1-infected mice treated with either NM1251 or NM1267. Hematoxylin and eosin (H&E) staining was performed to evaluate the degree of tissue damage upon infection, and *in situ* hybridization (ISH) was used to visualize the extent and localization of viral RNA. Applying a grading system from 0 (no tissue damage) to 4 (strong tissue damage), it became evident that all SARS-CoV-2-infected mice under control treatment (NM1251) exhibited a pronounced inflammation and loss of functional lung epithelia (Fig 5A–C). In contrast, prophylactic treatment with NM1267 efficiently reduced virus- and inflammation-induced tissue damage within the lungs (scoring 0.5–1.5) of SARS-CoV-2 B.1-infected mice (Fig 5A–C). In line with these findings, distinctly lower levels of SARS-CoV-2 RNA were found in samples taken from NM1267-treated mice, restricted to minimal areas of the lung at sub-pleural position and some fat cells. Analysis of lung sections of control-treated mice showed widespread presence of virus RNA-positive epithelial cells (Fig 5B).

Prophylactic treatment with NM1267 was equally potent in blocking disease progression if VOC B.1.351 (Beta) was used to infect mice. Only one NM1267-treated mouse infected with B.1.351 (Beta) lost substantial amounts of weight and had to be euthanized, whereas five out of six animals did not show any signs of disease

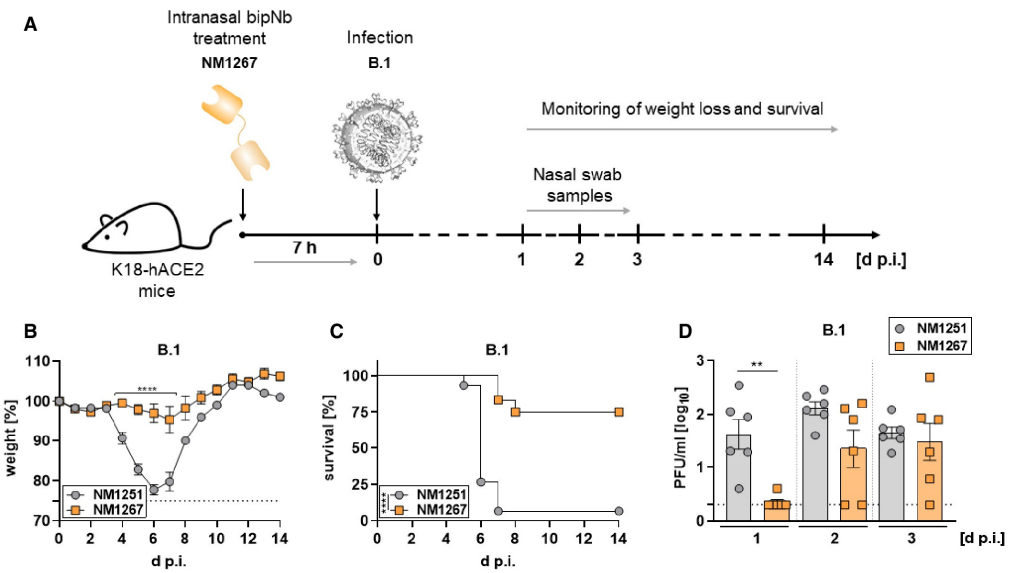

Figure 4. Intranasal application of NM1267 protects K18-hACE2 mice against SARS-CoV-2 B.1-induced disease and reduces mortality and virus shedding.

A Schematic illustration of treatment scheme.

B, C Hemizygous K18-hACE2 mice were treated intranasally with 20 μg of NM1251 (n = 15) or NM1267 (n = 12) 7 h prior to infection with 3×10^3 PFU SARS-CoV-2 B.1. Weight loss (B) and survival (C) were monitored for 14 days.

D Nasal swabs were collected from six mice per group (n = 6) at the indicated time points and viral load was determined by plaque-assay.

Data information: Dashed line indicates humane end point in (B) and symbols represent mean ± SEM in (B) or individual animals in (D). Bars in (D) represent mean ± SEM. ****P < 0.0001, by two-way ANOVA with Sidak's multiple comparison test in (B), ****P < 0.0001, by log-rank test in (C), and **P < 0.01, by unpaired t-test in (D).

and survived the infection (Fig EV3A and B). Similarly, histopathological examinations demonstrated a significant reduction of virus replication and tissue damage by NM1267 treatment (Fig EV3C).

After demonstrating the general applicability of bipNbs for prophylactic treatment, we performed a comparative study of the two bipNbs NM1267 and NM1268 with respect to their potential to block disease progression upon infection with the currently predominant VOC B.1.617.2 (Delta). Hence, mice were treated with 20 μg of either NM1267 or NM1268 followed by infection with the B.1.617.2 (Delta; Fig 6A). Similar to SARS-CoV-2 B.1 and B.1.351 (Beta), all NM1251-treated animals infected with B.1.617.2 became severely ill and reached humane end points between day 6 and day 8 post-infection. In contrast, the majority of animals treated with bipNbs NM1267 and NM1268 survived the infection. In direct comparison and consistent with the VNT data, NM1268 showed a slightly stronger protective effect against B.1.617.2 (Delta) compared with NM1267, as only one out of nine animals treated with NM1268 had to be euthanized in contrast to three out of nine mice in the NM1267-treated group (Fig 6B and C).

In conclusion, the *in vivo* data demonstrate that prophylactic intranasal administration of bipNbs NM1267 and NM1268 can efficiently prevent disease progression and mortality caused by SARS-CoV-2 B.1, B.1.351 (Beta), and B.1.617.2 (Delta). This highlights the potential of both bipNbs as broadly applicable drug candidates to prevent or treat SARS-CoV-2 infections in unvaccinated or immunocompromised individuals at high risk of developing severe disease.

Discussion

In this study, we investigated the potential of two biparatopic Nbs, NM1267 and NM1268, targeting different epitopes within the RBD, to prevent SARS-CoV-2-induced disease and mortality. Biochemical analyses of NM1267 and NM1268 demonstrated vigorous ACE2 displacement, high thermal stabilities, and strong binding to all SARS-CoV-2 RBD variants tested. Importantly, we could show profound neutralizing capacity of both bipNbs against SARS-CoV-2 B.1 and two immune-evading VOCs, B.1.351 (Beta) and B.1.617.2 (Delta).

Prophylactic administration of both NM1267 or NM1268 *in vivo*, strongly diminished disease progression and mortality in SARS-CoV-2 B.1, B.1.351 (Beta)- or B.1.617.2 (Delta)-infected transgenic mice. Overall, these data underscore the potential of both bipNbs to prevent or treat infections with VOCs for which currently available vaccines and therapeutic approaches are suspected to have reduced

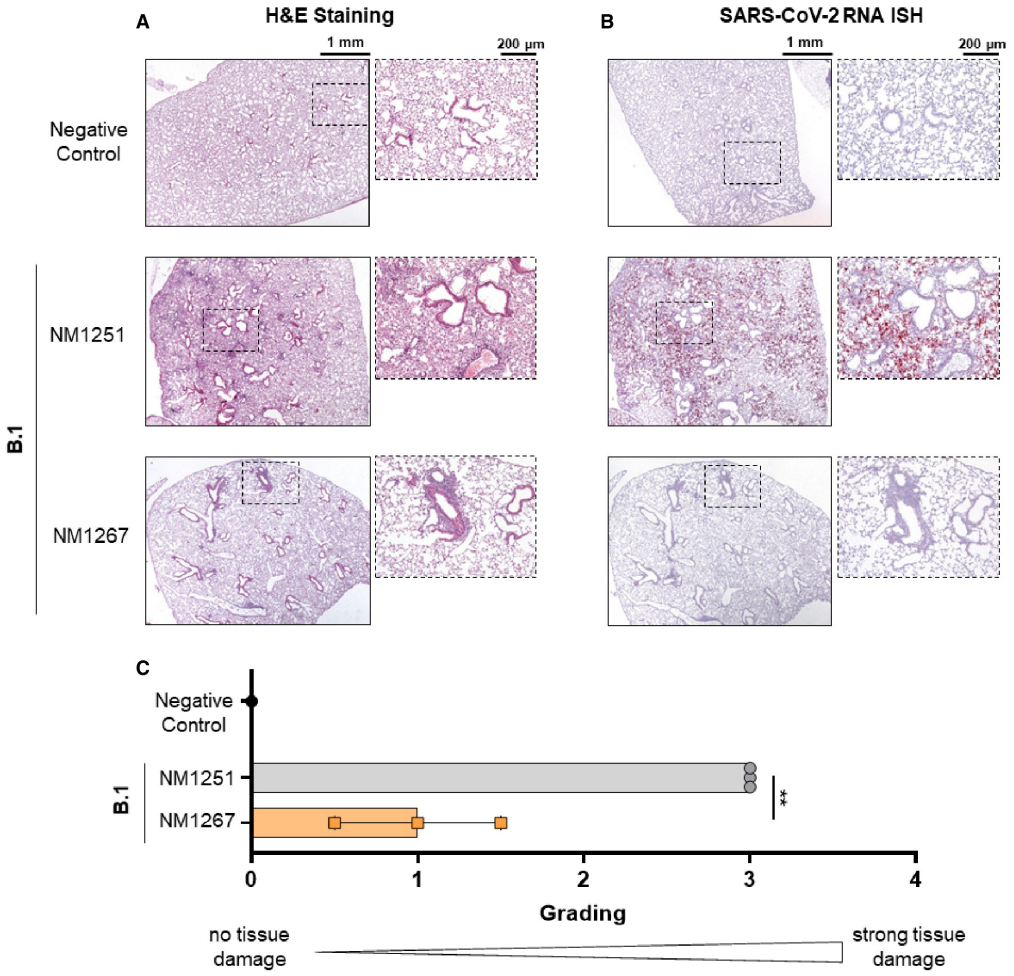

Figure 5. Microscopic analysis of lung tissue from SARS-CoV-2-infected K18-hACE2 mice.

Histopathological analysis of mice, which were intranasally treated with bipNb NM1267 or control Nb NM1251 and subsequently infected with 3×10^3 PFU SARS-CoV-2 B.1.

A, B Serial tissue sections revealed severe inflammation (H&E) and numerous widespread SARS-CoV-2 RNA-positive alveolar epithelia cells and macrophages (*in situ* hybridization [ISH]) in lungs of infected, control-treated mice. In infected and NM1267-treated animals no inflammation or only small focal areas with inflammation and a few SARS-CoV-2 RNA-positive cells were observed. Scale bars represent 1 mm and 200 µm, respectively.

C Quantitation of lung damage was done in $n = 3$ animals per group and grading score of individual animals is presented as mean ± SD with $^{**}P < 0.01$, by unpaired *t*-test.

efficacy (Becker *et al*, 2021; Kustin *et al*, 2021; Madhi *et al*, 2021; Planas *et al*, 2021; Zhou *et al*, 2021). Histopathological analyses and *in situ* hybridization detecting viral RNA in lung tissue samples further revealed significantly reduced tissue damage and virus replication, suggesting that bipNb treatment may also reduce long-term effects of SARS-CoV-2 infections (Han *et al*, 2021; Yong, 2021).

Notably, most strategies for engineering neutralizing Nbs currently rely on increasing avidity by generating multivalent

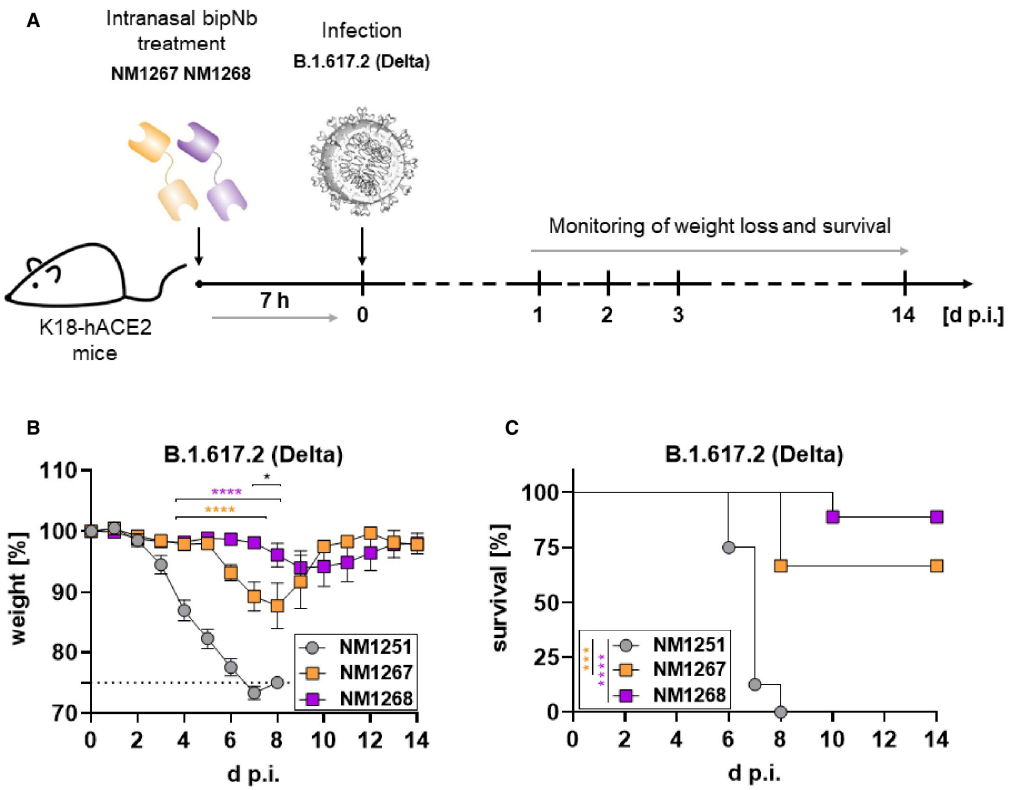

Figure 6. Intranasal application of NM1267 and NM1268 protects K18-hACE2 mice against VOC B.1.617.2-induced disease and reduces mortality.

A Schematic illustration of treatment scheme.

B, C Hemizygous K18-hACE2 mice were treated intranasally with 20 μg of NM1251 (n = 8), NM1267 (n = 9) or NM1268 (n = 9) 7 h prior to infection with 3×10^3 PFU SARS-CoV-2 B.1.617.2 (Delta). Weight loss (B) and survival (C) were monitored for 14 days.

Data information: Dashed line indicates humane end point and symbols represent mean ± SEM in (B). ****$P < 0.0001$ in orange between NM1251 and NM1267 and in purple between NM1251 and NM1268, *$P < 0.1$ in black between NM1267 and NM1268, by two-way ANOVA with Sidak's multiple comparison test in (B). ***$P < 0.001$ in orange between NM1251 and NM1267 and ****$P < 0.0001$ in purple between NM1251 and NM1268, by log-rank test in (C).

constructs binding the same epitope (Nambulli *et al*, 2021; Schepens *et al*, 2021; Wu *et al*, 2021), whereas only very few reports are available in which two Nbs targeting different epitopes on RBD were combined to prevent virus escape (preprint: Hanke *et al*, 2021; Koenig *et al*, 2021). Administration of NM1267 and NM1268 showed strong short-term efficacy *in vivo*. Additional modifications like fusion to an Fc-moiety, addition of an albumin-binding motif or direct linkage to carrier proteins like albumin may be beneficial to improve duration of effectiveness (preprint: Hanke *et al*, 2021; Huo *et al*, 2021; Nambulli *et al*, 2021; Schepens *et al*, 2021; Wu *et al*, 2021). Moreover, the extraordinary susceptibility of transgenic hACE2 mice to SARS-CoV-2-induced disease due to the artificial overexpression of hACE2 in a variety of tissues and organs, may even result in an underestimated therapeutic potential of both bipNbs. To address this issue and to investigate the potential of NM1267 and NM1268 to prevent virus transmission, further studies in more physiological models, such as Syrian hamsters or non-human primates, will be required (Haga *et al*, 2021; Nambulli *et al*, 2021; Schepens *et al*, 2021). Additionally, in terms of clinical translation the immunogenicity profile of both bipNbs needs to be evaluated. Notably, it has recently been shown that clinically applied Nbs are only weakly immunogenic (Ackaert *et al*, 2021). Furthermore, strategies for humanization at selected positions are available (Muyldermans *et al*, 2009; Vincke *et al*, 2009).

In summary, this study demonstrates how rational design based on detailed knowledge of binding properties, recognized epitopes, and *in vitro* determination of neutralization capacities can be combined to develop drug candidates that blocks SARS-CoV-2-induced disease and mortality *in vivo*. Given the restricted access to vaccines in various countries, vaccination fatigue, and the frequent emergence of new variants of concern, we believe that the development of such easily applicable therapeutic approaches to protect and treat predisposed individuals are highly promising strategies and urgently warranted.

Materials and Methods

Expression constructs

To generate described expression constructs, all used primer sequences are listed in Appendix Table S2. Nb NM1267 was generated as described previously (Wagner *et al*, 2021). BipNb NM1268 composed of Nb NM1228 and Nb NM1226 (Wagner *et al*, 2021) was similarly generated using primers NM1228Nfor, NM1228Nrev and NM1226Cfor, NM1226Crev. DNA coding for bipNbs were cloned into pCDNA3.4 expression vector seamlessly downstream of comprising N-terminal signal peptide (MGWTLVFLFLLSVTAGVHS) for secretory pathway using type IIS restriction enzyme Esp3I and EcoRI site. Coding sequence of bivNb NM1251 (Traenkle *et al*, 2020) was produced by gene synthesis (Thermo Fisher Scientific) and similarly cloned into pCDNA3.4 expression vector. Receptor-binding domain (RBD) variants of SARS-CoV-2 were generated as earlier published (Wagner *et al*, 2021). The expression plasmid pCAGGS encoding the RBD of SARS-CoV-2 spike protein (amino acids 319–541) was kindly provided by F. Krammer. RBDs of SARS-CoV-2 variants of concern (VOCs) B.1.1.7 (Alpha), B.1.351 (Beta), P1 (Gamma), B.1.617.2 (Delta), B.1.429 (Epsilon), P3 (Theta), B.1.617.1 (Kappa), and A.23.1 were generated by PCR amplification of fragments from B.1 or cognate DNA template and subsequent fusion PCR by overlap extension to introduce described mutations. Based on $RBD_{B.1}$ sequence primer pairs RBDfor N501Yrev and N501Yfor RBDrev were used for the amplification of B.1.1.7 (Alpha) sequence; primer pairs RBDfor L452Rrev and L452Rfor RBDrev for B.1.429 (Epsilon); RBDfor V367Frev and V367F for RBDrev for A.23.1. B.1.617.2 (Delta) was generated based on B.1.429 (Epsilon) using primer pairs RBDfor T478Krev and T478Kfor RBDrev. Based on B.1.1.7 (Alpha) sequence P3 (Theta) was generated using primer pairs RBDfor E484Krev and E484Kfor RBDrev. B.1.617.1 (Kappa) was generated using primer pairs RBDfor E484Krev and E484Kfor RBDrev as well as RBDfor L452Rrev and L452Rfor RBDrev. B.1.351 (Beta) and P1 (Gamma) were generated based on P3 (Theta) sequence using primer pairs RBDfor K417Nrev and K417Nfor RBDrev; and RBDfor K417Trev and K417Tfor RBDrev, respectively. Amplicons were inserted using XbaI and NotI site into the pCDNA3.4 expression vector. The integrity of all expression constructs was confirmed by standard sequencing analysis.

Protein expression and purification

Confirmed constructs were expressed in Expi293 or ExpiCHO cells and transfection was performed as per the manufacturer's instructions (Thermo Fisher Scientific). Cell suspensions were then cultivated for 2–5 days (37°C, 125 rpm, 8% (v/v) CO_2) and then centrifuged (4°C, 23,900 *g*, 20 min) to clarify the supernatant. Supernatants were then filtered with a 0.22-µm membrane (Millipore) and supplemented with His-A buffer stock solution (20 mM Na_2HPO_4, 30 mM NaCl, 20 mM imidazole, pH 7.4). The solution was then applied to a HisTrap FF crude column on an Aekta pure system (GE Healthcare), extensively washed with His-A buffer, and eluted with an imidazole gradient (50–400 mM). Buffer exchange to PBS and concentration of eluted proteins were carried out using Amicon 10 K centrifugal filter units (Millipore). Protein quality was analyzed by standard SDS–PAGE and via the NanoDrop protein concentration was determined.

Affinity measurements

Binding affinity of bipNbs toward variants of RBD was determined via biolayer interferometry (BLI) using the Octet RED96e system according to standard protocol. Therefore, RBD variants were biotinylated and immobilized on streptavidin biosensors (SA, Sartorius). Dilution series ranging from 20 to 0.625 nM of bipNbs were applied and one reference was included per run. For affinity determination, the 1:1 global fit of the Data Analysis HT 12.0 software was used.

Bead-based multiplex ACE2 competition assay

To analyze binding competition of human ACE2 versus generated bipNbs the bead-based multiplex ACE2 competition assay was performed as previously described (Wagner *et al*, 2021).

Stability analysis

Stability analysis was performed by the Prometheus NT.48 (Nanotemper). Therefore, freshly thawed bipNbs were diluted to 0.25 mg/ml and measurements were carried out at time point T_0 and after incubation for 10 days at 37°C (T_{10}) using high-sensitivity capillaries. Thermal unfolding and aggregation of the bipNbs were induced by the application of a thermal ramp of 20–95°C, while measuring fluorescence ratios (F350/F330) and light scattering. Via the PR. ThermControl v2.0.4 the melting (T_m) and aggregation ($T_{Agg}/T_{turbidity}$) temperature was determined.

Viruses

All experiments with SARS-CoV-2 viruses were conducted in Biosafety Level 3 laboratories and approved by the Regierungspräsidium Tübingen (UNI.FRK.05.22-101; UNI.TÜK.44.03). SARS-CoV-2 B.1 (SARS-CoV-2 Tü1 or SARS-CoV-2 Muc-IMB-1) and SARS-CoV-2 B.1.351 (Beta) were isolated from patient samples and variant identity was confirmed by next-generation sequencing of the entire viral genome as described in (Ruetalo *et al*, 2021) and (Becker *et al*, 2021), respectively. SARS-CoV-2 B.1.617.2 (Delta) was isolated from a throat swab collected in May 2021 at the Institute for Medical Virology and Epidemiology of Viral Diseases, University Hospital Tübingen, from a PCR-positive patient. Forty microliters of patient material was diluted in medium and used directly to inoculate 150,000 Caco-2 cells in a six-well plate. Seventy-two hours post-infection, the supernatant was collected, centrifuged, and stored at

−80°C. After two consecutive passages, an RNA sample from the supernatant was prepared, and NGS confirmed that the clinical isolate belongs to the lineage B.1.617.2. Caco-2 cell infection with and SARS-CoV-2 B.1.617.2 (Delta) was detected by Western blotting, using sera from a convalescent patient. Multiplicity of infection determination (MOI) was conducted by titration using serial dilutions of both virus stocks. The number of infectious virus particles per millimeter was calculated as (MOI × cell number)/(infection volume), where MOI = −ln (1 − infection rate).

Virus neutralization assay

Caco-2 (Human Colorectal adenocarcinoma, ATCC HTB-37) cells were cultured at 37°C with 5% CO_2 in DMEM containing 10% FCS, 2 mM L-glutamine, 100 µg/ ml penicillin-streptomycin and 1% NEAA.

Neutralization assays using clinical isolates (Fig 3A–C) were performed as described in (Becker *et al*, 2021; Ruetalo *et al*, 2021). Briefly, cells were co-incubated with the respective clinical isolate SARS-CoV-2 B.1, SARS-CoV-2 B.1.351 (Beta), or SARS-CoV-2 B.1.617.2 (Delta) at MOI of ~1.0 and serial dilutions of the bipNb from 5 µM to 0.064 nM. Forty-eight hours post-infection, cells were fixed with 80% acetone, and immune fluorescence (IF) staining was performed using an anti-SARS-CoV-2 nucleocapsid antibody (GeneTex, Cat No. GTX135357) and goat anti-rabbit Alexa594-conjugated secondary antibody. Cells were counterstained with DAPI solution and images were taken with the Cytation3 (BioTek). Infection rates were calculated as the ratio of DAPI-positive over Alexa594-positive cells, which were automatically counted by the Gen5 software (BioTek). Inhibitory concentration 50 (IC_{50}) was calculated as the half-maximal inhibitory dose using four-parameter nonlinear regression (GraphPad Prism).

In vivo infection experiments

Transgenic (K18-hACE2)2Prlmn mice were purchased from The Jackson Laboratory and bred and kept under specific pathogen-free conditions in the animal facilities of the University Medical Center Freiburg. Hemizygous 8–14-week-old animals of both sexes were used in accordance with the guidelines of the Federation for Laboratory Animal Science Associations and the National Animal Welfare Body. All experiments were in compliance with the German animal protection law and approved by the animal welfare committee of the Regierungspraesidium Freiburg (permit G-20/91). Mice were anesthetized using isoflurane and treated intranasally (i.n.) with 20 µg of NM1251, NM1267, or NM1268 7 h prior to infection with 3×10^3 PFU of the respective SARS-CoV-2 isolate (SARS-CoV-2 B.1, SARS-CoV-2 B.1.351 [Beta], and SARS-CoV-2 B.1.617.2 [Delta]) in 40 µl PBS containing 0.1% BSA. Infected mice were monitored for weight loss and clinical signs of disease for 14 days and sacrificed if severe symptoms were observed or body weight loss exceeded 25% of the initial weight. Superficial nasal swabs were taken on days 1, 2, and 3 post-infection. Swabs were collected in OptiMEM containing 0.3% BSA and titers determined by plaque assay using Vero E6 cells. Infected ketamine/xylazine-anesthetized mice were prepared for histological analyses by transcardial perfusion with 15 ml of 4% formaldehyde solution and stored in 4% formaldehyde at 4°C until organs were processed further. All experiments were performed under BSL3 conditions.

Hematoxylin and eosin (H&E) staining and *in situ* hybridization (ISH)

Lung tissue was routinely embedded in paraffin and H&E staining was performed from 4-µm-thick lung tissue sections by using the Tissue-Tek® Prisma (Sakura). To detect SARS-CoV-2 RNA (plus-strand RNA), 4-µm-thick lung tissue sections, including negative and positive controls, were hybridized using specific probes for SARS-CoV-2 (Advanced Cell Diagnostics ACD) followed by the RNAscope 2.5 HD Detection Kit Red from ACD according to the manufacturer's protocol. Quantitation of tissue damage including inflammation was defined as grade 0: no damage, grade 1: 1–10%, grade 2: 10–20%, grade 3: 20–50%, grade 4: 50–80% of lung tissue was involved.

Analyses and statistics

Graph preparation and statistical analysis was performed using the GraphPad Prism Software (Version 9.0.0 or higher).

Data availability

No data that require deposition in a public database have been generated.

Expanded View for this article is available online.

Acknowledgements
This work was supported by the Initiative and Networking Fund of the Helmholtz Association of German Research Centers (grant number SO-96), the European Union's Horizon 2020 research and innovation program under grant agreement No 101003480—CORESMA. Further funding was received from the State Ministry of Baden-Württemberg for Economic Affairs, Labour and Tourism (FKZ 3-4332.62-NMI/68), from the Ministry of Science, Research and Arts of the State of Baden-Württemberg (COVID-19 funding) and from the Deutsche Herzstiftung. Additional support was received from the Bundesministerium fuer Bildung und Forschung (BMBF) through the Deutsches Zentrum fuer Luft- und Raumfahrt, Germany, (DLR, grant number 01KI2077) and by the Federal State of Baden-Wuerttemberg, Germany, MWK-Sonderfoerdermaßnahme COVID-19/AZ.:33-7533.-6-21/7/2 to MS. We thank Florian Krammer for providing expression constructs for SARS-CoV-2 homotrimeric Spike and RBD. Open access funding enabled and organized by Projekt DEAL.

Author contributions
Study design: TRW, DS, MiS, MaS, and UR; Nb biochemical characterization: TRW, PDK, BT, and DIF; Multiplex binding assay: DJ, MB, NSM; Virus neutralization assays: NR, MiS; mouse infection experiments: DS, JB, and AO; histopathological analysis and *in situ* hybridization: KK and MSa; Data analysis and statistical analysis: TRW, DS, JB, NR, MiS, KK, MaS, and UR; Manuscript drafting: TRW and UR; Study supervision: MaS, MiS, and UR; Manuscript reviewing and editing: All authors.

Conflict of interest
TRW, PDK, NSM, and UR are named as inventors on a patent application (EP 20 197 031.6) claiming the use of the described Nanobodies for diagnosis and therapeutics filed by the Natural and Medical Sciences Institute. The other authors declare no competing interest.

References

Ackaert C, Smiejkowska N, Xavier C, Sterckx YGJ, Denies S, Stijlemans B, Elkrim Y, Devoogdt N, Caveliers V, Lahoutte T *et al* (2021) Immunogenicity risk profile of nanobodies. *Front Immunol* 12: 578

Beaudoin-Bussières G, Laumaea A, Anand SP, Prévost J, Gasser R, Goyette G, Medjahed H, Perreault J, Tremblay T, Lewin A *et al* (2020) Decline of humoral responses against SARS-CoV-2 spike in convalescent individuals. *MBio* 11: e02590-20

Becker M, Dulovic A, Junker D, Ruetalo N, Kaiser PD, Pinilla YT, Heinzel C, Haering J, Traenkle B, Wagner TR *et al* (2021) Immune response to SARS-CoV-2 variants of concern in vaccinated individuals. *Nat Commun* 12: 3109

Brouwer PJM, Caniels TG, van der Straten K, Snitselaar JL, Aldon Y, Bangaru S, Torres JL, Okba NMA, Claireaux M, Kerster G *et al* (2020) Potent neutralizing antibodies from COVID-19 patients define multiple targets of vulnerability. *Science* 369: 643 – 650

Cao Y, Su B, Guo X, Sun W, Deng Y, Bao L, Zhu Q, Zhang XU, Zheng Y, Geng C *et al* (2020) Potent neutralizing antibodies against SARS-CoV-2 identified by high-throughput single-cell sequencing of convalescent patients' B cells. *Cell* 182: 73 – 84.e16

Challen R, Brooks-Pollock E, Read JM, Dyson L, Tsaneva-Atanasova K, Danon L 2021) Risk of mortality in patients infected with SARS-CoV-2 variant of concern 202012/1: matched cohort study. *BMJ* 372: n579

Chen P, Nirula A, Heller B, Gottlieb RL, Boscia J, Morris J, Huhn G, Cardona J, Mocherla B, Stosor V *et al* (2020) SARS-CoV-2 neutralizing antibody LY-CoV555 in outpatients with Covid-19. *N Engl J Med* 384: 229 – 237

Chi X, Liu X, Wang C, Zhang X, Li X, Hou J, Ren L, Jin Q, Wang J, Yang W (2020) Humanized single domain antibodies neutralize SARS-CoV-2 by targeting the spike receptor binding domain. *Nat Commun* 11: 1 – 7

Dagan N, Barda N, Kepten E, Miron O, Perchik S, Katz MA, Hernán MA, Lipsitch M, Reis B, Balicer RD (2021) BNT162b2 mRNA Covid-19 vaccine in a nationwide mass vaccination setting. *N Engl J Med* 384: 1412 – 1423

Davies NG, Abbott S, Barnard RC, Jarvis CI, Kucharski AJ, Munday JD, Pearson CAB, Russell TW, Tully DC, Washburne AD *et al* (2021a) Estimated transmissibility and impact of SARS-CoV-2 lineage B.1.1.7 in England. *Science* 372: eabg3055

Davies NG, Jarvis CI, van Zandvoort K, Clifford S, Sun FY, Funk S, Medley G, Jafari Y, Meakin SR, Lowe R *et al* (2021b) Increased mortality in community-tested cases of SARS-CoV-2 lineage B.1.1.7. *Nature* 593: 270 – 274

Dejnirattisai W, Zhou D, Supasa P, Liu C, Mentzer AJ, Ginn HM, Zhao Y, Duyvesteyn HM, Tuekprakhon A, Nutalai R (2021) Antibody evasion by the P. 1 strain of SARS-CoV-2. *Cell* 184: 2939 – 2954.e2939

Diamond M, Chen R, Xie X, Case J, Zhang X, VanBlargan L, Liu Y, Liu J, Errico J, Winkler E (2021) SARS-CoV-2 variants show resistance to neutralization by many monoclonal and serum-derived polyclonal antibodies. *Res Sq* https://doi.org/10.21203/rs.3.rs-228079/v1 [PREPRINT]

Haga K, Takai-Todaka R, Matsumura Y, Song C, Takano T, Tojo T, Nagami A, Ishida Y, Masaki H, Tsuchiya M *et al* (2021) Nasal delivery of single-domain antibody improves symptoms of SARS-CoV-2 infection in an animal model. *PLoS Pathog* 17: e1009542

Han X, Fan Y, Alwalid O, Li NA, Jia XI, Yuan M, Li Y, Cao Y, Gu J, Wu H *et al* (2021) Six-month follow-up chest CT findings after severe COVID-19 pneumonia. *Radiology* 299: E177 – E186

Hanke L, Vidakovics Perez L, Sheward DJ, Das H, Schulte T, Moliner-Morro A, Corcoran M, Achour A, Karlsson Hedestam GB, Hällberg BM *et al* (2020) An alpaca nanobody neutralizes SARS-CoV-2 by blocking receptor interaction. *Nat Commun* 11: 1 – 9

Hanke L, Das H, Sheward DJ, Vidakovics LP, Urgard E, Moliner-Morro A, Karl V, Pankow A, Kim C, Smith NL *et al* (2021) A bispecific monomeric nanobody induces SARS-COV-2 Spike trimer dimers. *bioRxiv* https://doi.org/10.1101/2021.03.20.436243 [PREPRINT]

Havlin J, Svorcova M, Dvorackova E, Lastovicka J, Lischke R, Kalina T, Hubacek P (2021) Immunogenicity of BNT162b2 mRNA COVID-19 vaccine and SARS-CoV-2 infection in lung transplant recipients. *J Heart Lung Transplant* 40: 754 – 758

Huo J, Le Bas A, Ruza RR, Duyvesteyn HME, Mikolajek H, Malinauskas T, Tan TK, Rijal P, Dumoux M, Ward PN *et al* (2020) Neutralizing nanobodies bind SARS-CoV-2 spike RBD and block interaction with ACE2. *Nat Struct Mol Biol* 27: 846 – 854

Huo J, Mikolajek H, Le Bas A, Clark JJ, Sharma P, Kipar A, Dormon J, Norman C, Weckener M, Clare DK *et al* (2021) A potent SARS-CoV-2 neutralising nanobody shows therapeutic efficacy in the Syrian golden hamster model of COVID-19. *Nat Commun* 12: 1 – 18

Jewell BL (2021) Monitoring differences between the SARS-CoV-2 B.1.1.7 variant and other lineages. *Lancet Public Health* 6: e267 – e268

Jiang S, Hillyer C, Du L (2020) Neutralizing antibodies against SARS-CoV-2 and other human coronaviruses. *Trends Immunol* 41: 355 – 359

Ju B, Zhang QI, Ge J, Wang R, Sun J, Ge X, Yu J, Shan S, Zhou B, Song S *et al* (2020) Human neutralizing antibodies elicited by SARS-CoV-2 infection. *Nature* 584: 115 – 119

Koenig P-A, Das H, Liu H, Kümmerer BM, Gohr FN, Jenster L-M, Schiffelers LD, Tesfamariam YM, Uchima M, Wuerth JD (2021) Structure-guided multivalent nanobodies block SARS-CoV-2 infection and suppress mutational escape. *Science* 371: eabe6230

Kustin T, Harel N, Finkel U, Perchik S, Harari S, Tahor M, Caspi I, Levy R, Leshchinsky M, Ken Dror S *et al* (2021) Evidence for increased breakthrough rates of SARS-CoV-2 variants of concern in BNT162b2-mRNA-vaccinated individuals. *Nat Med* 27: 1379 – 1384

Kwok KO, Lai F, Wei WI, Wong SYS, Tang JW (2020) Herd immunity–estimating the level required to halt the COVID-19 epidemics in affected countries. *J Infect* 80: e32 – e33

Li Q, Nie J, Wu J, Zhang L, Ding R, Wang H, Zhang Y, Li T, Liu S, Zhang M (2021) SARS-CoV-2 501Y. V2 variants lack higher infectivity but do have immune escape. *Cell* 184: 2362 – 2371.e2369

Long Q-X, Tang X-J, Shi Q-L, Li Q, Deng H-J, Yuan J, Hu J-L, Xu W, Zhang Y, Lv F-J *et al* (2020) Clinical and immunological assessment of asymptomatic SARS-CoV-2 infections. *Nat Med* 26: 1200 – 1204

Madhi SA, Baillie V, Cutland CL, Voysey M, Koen AL, Fairlie L, Padayachee SD, Dheda K, Barnabas SL, Bhorat QE *et al* (2021) Efficacy of the ChAdOx1 nCoV-19 Covid-19 vaccine against the B.1.351 variant. *N Engl J Med* 384: 1885 – 1898

McCray Jr PB, Pewe L, Wohlford-Lenane C, Hickey M, Manzel L, Shi L, Netland J, Jia HP, Halabi C, Sigmund CD (2007) Lethal infection of K18-hACE2 mice infected with severe acute respiratory syndrome coronavirus. *J Virol* 81: 813 – 821

Mlcochova P, Kemp S, Dhar MS, Papa G, Meng B, Ferreira IA, Datir R, Collier DA, Albecka A, Singh S (2021) SARS-CoV-2 B.1.617.2 Delta variant replication and immune evasion. *Nature* 599: 114 – 119

Muyldermans S, Baral TN, Retamozzo VC, De Baetselier P, De Genst E, Kinne J, Leonhardt H, Magez S, Nguyen VK, Revets H *et al* (2009) Camelid immunoglobulins and nanobody technology. *Vet Immunol Immunopathol* 128: 178 – 183

Nambulli S, Xiang Y, Tilston-Lunel NL, Rennick LJ, Sang Z, Klimstra WB, Reed DS, Crossland NA, Shi Y, Duprex WP (2021) Inhalable Nanobody (PiN-21)

prevents and treats SARS-CoV-2 infections in Syrian hamsters at ultra-low doses. *Sci Adv* 7: eabh0319

Planas D, Bruel T, Grzelak L, Guivel-Benhassine F, Staropoli I, Porrot F, Planchais C, Buchrieser J, Rajah MM, Bishop E (2021) Sensitivity of infectious SARS-CoV-2 B. 1.1. 7 and B. 1.351 variants to neutralizing antibodies. *Nat Med* 27: 917 – 924

Ruetalo N, Businger R, Althaus K, Fink S, Ruoff F, Pogoda M, Iftner A, Ganzenmüller T, Hamprecht K, Flehmig B (2021) Antibody response against SARS-CoV-2 and seasonal coronaviruses in nonhospitalized COVID-19 patients. *Msphere* 6: e01145 – e01120

Schepens B, van Schie L, Nerinckx W, Roose K, Van Breedam W, Fijalkowska D, Devos S, Weyts W, De Cae S, Vanmarcke S *et al* (2021) An affinity-enhanced, broadly neutralizing heavy chain-only antibody protects against SARS-CoV-2 infection in animal models. *Sci Transl Med* 13: eabi7826

Scudellari M (2020) How the pandemic might play out in 2021 and beyond. *Nature* 584: 22 – 25

Traenkle B, Segan S, Fagbadebo FO, Kaiser PD, Rothbauer U (2020) A novel epitope tagging system to visualize and monitor antigens in live cells with chromobodies. *Sci Rep* 10: 1 – 13

Vincke C, Loris R, Saerens D, Martinez-Rodriguez S, Muyldermans S, Conrath K (2009) General strategy to humanize a camelid single-domain antibody and identification of a universal humanized nanobody scaffold. *J Biol Chem* 284: 3273 – 3284

Volz E, Mishra S, Chand M, Barrett JC, Johnson R, Geidelberg L, Hinsley WR, Laydon DJ, Dabrera G, O'Toole Á *et al* (2021) Assessing transmissibility of SARS-CoV-2 lineage B.1.1.7 in England. *Nature* 593: 266 – 269

Wagner TR, Ostertag E, Kaiser PD, Gramlich M, Ruetalo N, Junker D, Haering J, Traenkle B, Becker M, Dulovic A *et al* (2021) NeutrobodyPlex-monitoring SARS-CoV-2 neutralizing immune responses using nanobodies. *EMBO Rep* 22: e52325

Wang P, Nair MS, Liu L, Iketani S, Luo Y, Guo Y, Wang M, Yu J, Zhang B, Kwong PD *et al* (2021) Antibody resistance of SARS-CoV-2 variants B. 1.351 and B. 1.1. 7. *Nature* 593: 130 – 135

Weinreich DM, Sivapalasingam S, Norton T, Ali S, Gao H, Bhore R, Musser BJ, Soo Y, Rofail D, Im J *et al* (2020) REGN-COV2, a neutralizing antibody cocktail, in outpatients with covid-19. *N Engl J Med* 384: 238 – 251

Winkler ES, Bailey AL, Kafai NM, Nair S, McCune BT, Yu J, Fox JM, Chen RE, Earnest JT, Keeler SP *et al* (2020) SARS-CoV-2 infection of human ACE2-transgenic mice causes severe lung inflammation and impaired function. *Nat Immunol* 21: 1327 – 1335

Wrapp D, De Vlieger D, Corbett KS, Torres GM, Wang N, Van Breedam W, Roose K, van Schie L; VIB-CMB COVID-19 Response Team (2020) Structural basis for potent neutralization of betacoronaviruses by single-domain camelid antibodies. *Cell* 181: 1004 – 1015.e1015

Wu X, Cheng L, Fu M, Huang B, Zhu L, Xu S, Shi H, Zhang D, Yuan H, Nawaz W *et al* (2021) A potent bispecific nanobody protects hACE2 mice against SARS-CoV-2 infection via intranasal administration. *Cell Rep* 37: 109869

Xiang Y, Nambulli S, Xiao Z, Liu H, Sang Z, Duprex WP, Schneidman-Duhovny D, Zhang C, Shi Y (2020) Versatile and multivalent nanobodies efficiently neutralize SARS-CoV-2. *Science* 370: 1479 – 1484

Yong SJ (2021) Long COVID or post-COVID-19 syndrome: putative pathophysiology, risk factors, and treatments. *Infect Dis* 53: 737 – 754

Zhou D, Dejnirattisai W, Supasa P, Liu C, Mentzer AJ, Ginn HM, Zhao Y, Duyvesteyn HM, Tuekprakhon A, Nutalai R (2021) Evidence of escape of SARS-CoV-2 variant B. 1.351 from natural and vaccine-induced sera. *Cell* 184: 2348 – 2361.e2346

Expanded View Figures

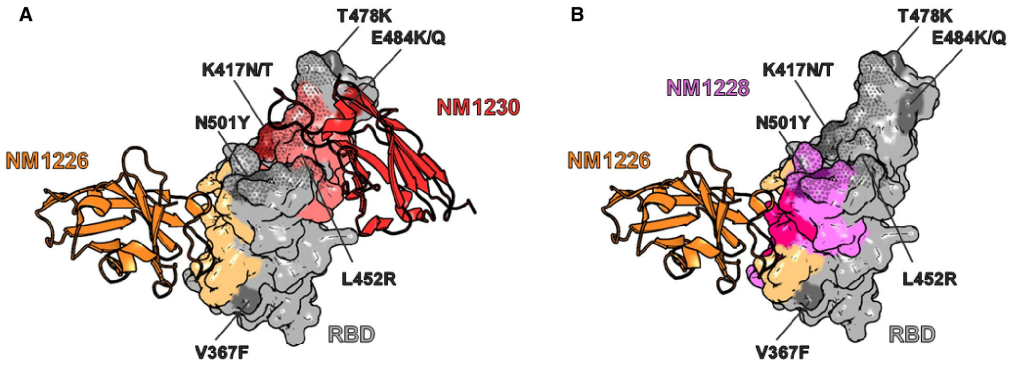

C

Pangolin (WHO)	RBD Mutation
B.1.1.7 (Alpha)	N501Y
B.1.351 (Beta)	K417N E484K N501Y
P1 (Gamma)	K417T E484K N501Y
B.1.617.2 (Delta)	L452R T478K
B.1.429 (Epsilon)	L452R
P3 (Theta)	E484K N501Y
B.1.617.1 (Kappa)	L452R E484Q
A.23.1	V367F

Figure EV1. Influence of RBD mutations on bipNb binding.

A NM1267-binding epitope on RBD derived from crystal structure of single RBD:Nb complexes NM1226 (orange, PDB 7NKT) and NM1230 (red, PDB 7B27) (Wagner *et al*, 2021). NM1267-forming single Nbs are shown as cartoon with their corresponding binding epitopes on the RBD surface in light orange and light red, respectively. In addition, the ACE2 interaction site on RBD is illustrated as dotted surface. Mutations on RBD of identified SARS-CoV-2 variants, including B.1.1.7 (Alpha), B.1.351 (Beta), P1 (Gamma), B.1.617.2 (Delta), B.1.429 (Epsilon), P3 (Theta), B.1.617.1 (Kappa), and A.23.1 are highlighted in dark gray or dark red and labeled, respectively.

B NM1268-binding epitope on RBD derived from crystal structure of the RBD:Nb complex for NM1226 (orange, PDB 7NKT) and HDX-MS analysis for NM1228 (purple) (Wagner *et al*, 2021). NM1268-forming single Nb NM1226 is shown as cartoon with its corresponding binding epitope on the RBD surface in light orange. Binding epitope of NM1228 is illustrated in purple, while shared binding sites of NM1226 and NM1228 are illustrated in pink. In addition, the ACE2 interaction site on RBD is illustrated as a dotted surface. Mutations on RBD of identified VOCs, including B.1.1.7 (Alpha), B.1.351 (Beta), P1 (Gamma), B.1.617.2 (Delta), B.1.429 (Epsilon), P3 (Theta), B.1.617.1 (Kappa), and A.23.1 are highlighted in dark gray or dark purple and labeled, respectively.

C Table summarizing mutations on RBD of different SARS-CoV-2 VOCs.

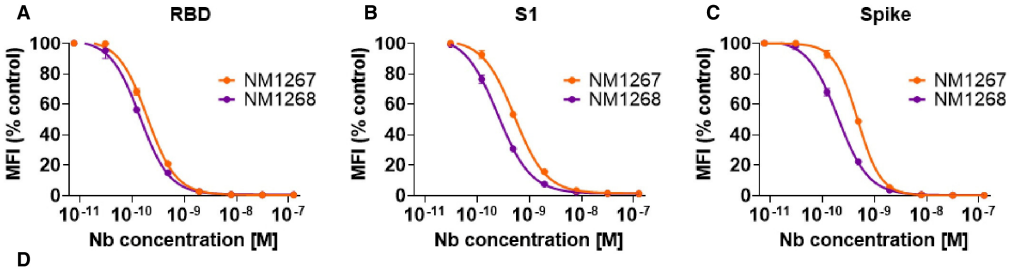

D

	IC_{50} [nM] ACE2:RBD Inhibition	IC_{50} [nM] ACE2:S1 Inhibition	IC_{50} [nM] ACE2:Spike Inhibition
NM1267	0.19	0.13	0.48
NM1268	0.14	0.06	0.20

Figure EV2. Biparatopic NM1267 and NM1268 compete with ACE2.

A–C Results from multiplex ACE2 competition assay are shown for the three spike-derived antigens: RBD (A), S1-domain (S1) (B), and homotrimeric spike (Spike) (C). Color-coded beads coated with the respective antigens were co-incubated with biotinylated ACE2 and dilution series of NM1267 and NM1268 (8 pM to 126 nM) followed by measuring residual binding of ACE2. MFI signals were normalized to the maximum detectable signal per antigen given by the ACE2-only control. IC_{50} values were calculated from a four-parametric sigmoidal model. Data are presented as mean ± SD of three technical replicates.

D Table summarizing IC_{50} values of the multiplex ACE2 competition assay obtained for NM1267 and NM1268.

Figure EV3. Intranasal application of NM1267 protects K18-hACE2 mice against B.1.351 (Beta)-induced disease, reduces mortality, and lung tissue damage.

A Schematic illustration of treatment scheme.

B Hemizygous K18-hACE2 mice were treated intranasally with 20 μg of NM1251 (n = 9) or NM1267 (n = 6) 7 h prior to infection with 3×10^3 PFU SARS-CoV-2 B.1.351 (Beta). Weight loss (left) and survival (right) were monitored for 14 days. Dashed line indicates humane end point and symbols for weight loss (left) represent mean ± SEM. ****$P < 0.0001$, by two-way ANOVA with Sidak's multiple comparison test (left) and *$P < 0.05$, by log-rank test for survival (right).

C Serial tissue sections revealed severe inflammation (H&E) and numerous widespread SARS-CoV-2 RNA-positive alveolar epithelia cells and macrophages (*in situ* hybridization [ISH]) in lungs of infected, control-treated mice. In infected and NM1267 bipNb-treated animals no inflammation or only small focal areas with inflammation and a few SARS-CoV-2 RNA-positive cells were observed. A negative control is displayed in Fig 5A and B. Scale bars represent 1 mm and 200 μm, respectively. Quantitation of lung damage was done in n = 3 animals per group and grading score of individual animals is presented as mean ± SD with **$P < 0.01$, by unpaired t-test.

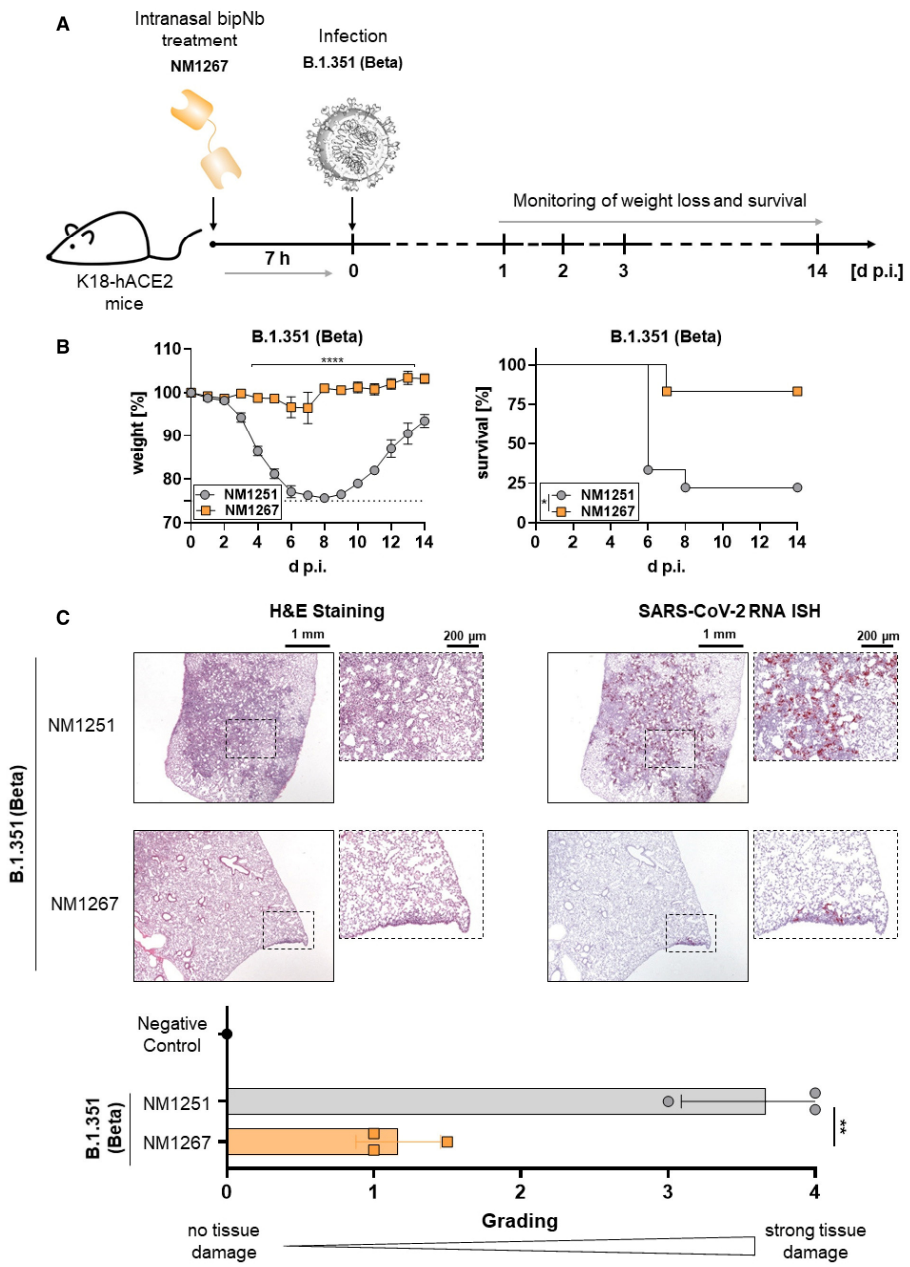

Figure EV3.

Appendix:

Biparatopic Nanobodies protect mice from lethal challenge with SARS-CoV-2 variants of concern

Teresa R. Wagner[1,2*], Daniel Schnepf[3*], Julius Beer[3*], Natalia Ruetalo[4*], Karin Klingel[5], Philipp D. Kaiser[2], Daniel Junker[2], Martina Sauter[5], Bjoern Traenkle[2], Desiree I. Frecot[1,2], Matthias Becker[2], Nicole Schneiderhan-Marra[2], Annette Ohnemus[3], Martin Schwemmle[3,6], Michael Schindler[4], Ulrich Rothbauer[1,2,7#]

Addresses

[1] Pharmaceutical Biotechnology, Eberhard Karls University, Tübingen, Germany

[2] NMI Natural and Medical Sciences Institute at the University of Tübingen, Reutlingen, Germany

[3] Institute of Virology, Medical Center University Freiburg, Freiburg, Germany

[4] Institute for Medical Virology and Epidemiology of Viral Diseases, University Hospital Tübingen, Tübingen, Germany

[5] Institute for Pathology and Neuropathology, University Hospital Tübingen, Tübingen, Germany

[6] Faculty of Medicine, University of Freiburg, Freiburg, Germany

[7] Cluster of Excellence iFIT (EXC2180) "Image-Guided and Functionally Instructed Tumor Therapies", Eberhard Karls University, Tübingen, Germany

* authors contributed equally to this work

corresponding author

Correspondence:

Prof. Dr. Ulrich Rothbauer, NMI Natural and Medical Sciences Institute at the University of Tübingen

27 Markwiesenstr. 55, 72770 Reutlingen, Germany.
28 E-mail: ulrich.rothbauer@uni-tuebingen.de
29 Phone: +49 7121 51530-415
30 Fax: +49 7121 51530-816
31 Orcid ID: 0000-0001-5923-8986
32
33

Table of Content

Appendix Tables

Appendix Table S1. Nb combinations for bipNbs

Biparatopic (Bip)/ bivalent Nb	**Single Nb combination**
NM1267	NM1230-$(G_4S)_4$-NM1226
NM1268	NM1228-$(G_4S)_4$-NM1226
NM1251 (Control)	Pep-Nb-$(G_4S)_4$-Pep-Nb

Appendix Table S2. Primer Sequences

Primer	Sequence 5'-3'
NM1228Nfor	GGACGTCTCAACTCTGACGTGCAGCTGGTGGAAT
NM1228Nrev	CACCACCGCCAGATCCACCGCCACCTGATCCTCCGCCTCCTGAGGACACGGTGACCAGGGACCC
NM1226Cfor	GGTGGATCTGGCGGTGGTGGAAGTGGTGGCGGAGGTAGTCAGGTGCAGCTGGTGGAAT
NM1226Crev	GGGGAATTCAGTGATGGTGATGGTGGTGTGAGGACACGGTGACCGGGGCC
RBDfor	ATATCTAGAGCCACCATGTTCGTGTTTCTGG
RBDrev	AAGATCTGCTAGCTCGAGTCGC
N501Yfor	GGCTTTCAGCCCACATATGGCGTGGGCTATCAGC
N501Yrev	CCACGCCATATGTGGGCTGAAAGCCGTAG
L452Rfor	GGCAACTACAATTACCGGTACCGGCTGTTCCGGAAG
L452Rrev	CGGTACCGGTAATTGTAGTTGCCGCCG
V367Ffor	CGACTACTCCTTCCTGTACAACTCCGCCAGCTTC
V367Frev	CGGAGTTGTACAGGAAGGAGTAGTCGGCCACGCA
T478Kfor	CCGGCAGCAAGCCTTGTAACGGCGTGGAAG
T478Krev	CGTTACAAGGCTTGCTGCCGGCCTGATAGA
E484Kfor	GTAACGGCGTGAAAGGCTTCAACTGCTACTTCCC
E484Krev	GCAGTTGAAGCCTTTCACGCCGTTACAAGGGGT
K417Nfor	GACAGACAGGCAACATCGCCGACTACAACTACAAGC
K417Nrev	GTTGTAGTCGGCGATGTTGCCTGTCTGTCCAGGG
K417Tfor	GACAGACAGGCACCATCGCCGACTACAACTACAAG
K417Trev	GTTGTAGTCGGCGATGGTGCCTGTCTGTCCAGGGG

Appendix III:

Wagner TR, Blaess S, Leske IB, Frecot DI, Gramlich M, Traenkle B, Kaiser PD, Seyfried D, Maier S, Rezza A, Sonego F, Thiam K, Pezzana S, Zeck A, Gouttefangeas C, Scholz A, Nueske S, Maurer A, Kneilling M, Pichler BJ, Sonanini D, Rothbauer U (2023) **Two birds with one stone: human SIRPα nanobodies for functional modulation and in vivo imaging of myeloid cells**. Front Immunol 14: 1264179.

frontiers | Frontiers in Immunology

TYPE Original Research
PUBLISHED 18 December 2023
DOI 10.3389/fimmu.2023.1264179

OPEN ACCESS

EDITED BY
Jan Gettemans,
Ghent University, Belgium

REVIEWED BY
Evangelia Bolli,
University of Geneva, Switzerland
Fang Zheng,
Xi'an Jiaotong University, China

*CORRESPONDENCE
Ulrich Rothbauer
ulrich.rothbauer@uni-tuebingen.de

RECEIVED 20 July 2023
ACCEPTED 20 November 2023
PUBLISHED 18 December 2023

CITATION
Wagner TR, Blaess S, Leske IB, Frecot DI, Gramlich M, Traenkle B, Kaiser PD, Seyfried D, Maier S, Rezza A, Sônego F, Thiam K, Pezzana S, Zeck A, Gouttefangeas C, Scholz AM, Nueske S, Maurer A, Kneilling M, Pichler BJ, Sonanini D and Rothbauer U (2023) Two birds with one stone: human SIRPα nanobodies for functional modulation and *in vivo* imaging of myeloid cells. *Front. Immunol.* 14:1264179. doi: 10.3389/fimmu.2023.1264179

Two birds with one stone: human SIRPα nanobodies for functional modulation and *in vivo* imaging of myeloid cells

Teresa R. Wagner [1,2], Simone Blaess [3], Inga B. Leske [2], Desiree I. Frecot [1,2], Marius Gramlich [1], Bjoern Traenkle [1], Philipp D. Kaiser [1], Dominik Seyfried [3,4], Sandra Maier [1], Amélie Rezza [5], Fabiane Sônego [5], Kader Thiam [5], Stefania Pezzana [3], Anne Zeck [1], Cécile Gouttefangeas [4,6,7], Armin M. Scholz [8], Stefan Nueske [8], Andreas Maurer [3,7], Manfred Kneilling [3,7,9], Bernd J. Pichler [3,4,7], Dominik Sonanini [3,10] and Ulrich Rothbauer [2,7]*

[1]NMI Natural and Medical Sciences Institute at the University of Tübingen, Reutlingen, Germany, [2]Pharmaceutical Biotechnology, Eberhard Karls University Tübingen, Tübingen, Germany, [3]Werner Siemens Imaging Center, Department of Preclinical Imaging and Radiopharmacy, University of Tübingen, Tübingen, Germany, [4]German Cancer Consortium (DKTK) and German Cancer Research Center (DKFZ) partner site Tübingen, Tübingen, Germany, [5]Preclinical Models & Services, genOway, Lyon, France, [6]Department of Immunology, Institute of Cell Biology, University of Tübingen, Tübingen, Germany, [7]Cluster of Excellence iFIT (EXC2180) "Image-Guided and Functionally Instructed Tumor Therapies", University of Tübingen, Tübingen, Germany, [8]Livestock Center of the Faculty of Veterinary Medicine, Ludwig Maximilians University Munich, Oberschleissheim, Germany, [9]Department of Dermatology, University of Tübingen, Tübingen, Germany, [10]Department of Medical Oncology and Pneumology, University of Tübingen, Tübingen, Germany

Signal-regulatory protein α (SIRPα) expressed by myeloid cells is of particular interest for therapeutic strategies targeting the interaction between SIRPα and the "don't eat me" ligand CD47 and as a marker to monitor macrophage infiltration into tumor lesions. To address both approaches, we developed a set of novel human SIRPα (hSIRPα)–specific nanobodies (Nbs). We identified high-affinity Nbs targeting the hSIRPα/hCD47 interface, thereby enhancing antibody-dependent cellular phagocytosis. For non-invasive *in vivo* imaging, we chose S36 Nb as a non-modulating binder. By quantitative positron emission tomography in novel hSIRPα/hCD47 knock-in mice, we demonstrated the applicability of ^{64}Cu-hSIRPα-S36 Nb to visualize tumor infiltration of myeloid cells. We envision that the hSIRPα-Nbs presented in this study have potential as versatile theranostic probes, including novel myeloid-specific checkpoint inhibitors for combinatorial treatment approaches and for *in vivo* stratification and monitoring of individual responses during cancer immunotherapies.

KEYWORDS

nanobodies (Nbs), SIRPalpha, myeloid cells, PET imaging tracer, immune checkpoint inhibitor (ICI), theranostics

10.3389/fimmu.2023.1264179

Introduction

During tumor development, there is a continuous exchange between malignant cells, neighboring parenchymal cells, stromal cells, and immune cells. Together with the extracellular matrix and soluble mediators, these cells constitute the tumor microenvironment (TME). The composition of the immune infiltrate within the TME largely determines cancer progression and sensitivity to immunotherapies (1). Myeloid cells are known to regulate T-cell responses, thereby bridging innate and adaptive immunity (2–4). Tumor cells further utilize myeloid cells to create a pro-tumorigenic milieu by exploiting their ability to produce immune-regulating mediators (e.g., interleukin-6 and tumor necrosis factor), growth factors influencing tumor proliferation and vascularization (e.g., transforming growth factor–β and vascular endothelial growth factor), as well as matrix-degrading enzymes (e.g., matrix metalloproteinases) (5). Within the myeloid cell population, tumor-associated macrophages (TAMs) are highly abundant, and widely varying densities of up to 50% of the tumor mass are observed (6). At the same time, depending on their polarization state, TAMs exhibit partially opposing effects either as key drivers for tumor progression or by exerting potent antitumor activity (7, 8). Consequently, monitoring tumor infiltration of TAMs is of great importance for patient stratification and companion diagnostic (9–11), and targeted recruitment or activation of anti-tumor TAMs opens new strategies to achieve persisting anti-tumor immune responses (12).

In this context, the myeloid-specific immune checkpoint signal-regulatory protein α (SIRPα), expressed by monocytes, macrophages, dendritic cells, and neutrophils (13, 14), represents an interesting theranostic target. Interaction with its ligand CD47, a "marker of self" virtually expressed by all cells of the body, mediates a "don't eat me" signal that inhibits phagocytosis, and prevents subsequent autoimmune responses. Exploiting this physiological checkpoint, tumor cells often upregulate CD47 and thereby escape recognition and removal by macrophages (15, 16). Similarly, enhanced expression of SIRPα by intratumoral monocytes/macrophages has recently been shown to be associated with poorer survival in follicular lymphoma, colorectal cancer, intrahepatic cholangiocarcinoma, and esophageal cancer (17–19).

To address the potential as a biomarker and immune modulating target, we generated human SIRPα (hSIRPα)–specific nanobodies (Nbs) for diagnostic and potential therapeutic applications. Nbs are single-domain antibodies derived from heavy-chain antibodies of camelids (20, 21) and have emerged as versatile biologicals for therapeutic as well as diagnostic purposes (22–24). Compared with conventional antibodies, Nbs exhibit superior characteristics concerning chemical stability, solubility, and tissue penetration due to their small size and compact folding (20). Following a binary screening strategy, in-depth biochemical characterization, epitope mapping, and functional studies, we identified two hSIRPα-Nb subsets that either block the hSIRPα/hCD47 interface or serve as inert probes for molecular imaging.

Results

Selection of high-affinity anti-human SIRPα nanobodies

To generate Nbs against hSIRPα that can be used either as probes for diagnostic imaging or to modulate interaction with human CD47, we immunized an alpaca (*Vicugna pacos*) with the recombinant extracellular portion of hSIRPα and established an Nb phagemid library (2×10^7 clones). This Nb library was subjected to phage display–based selection campaigns targeting either the entire extracellular portion or exclusively domain 1 (D1) of hSIRPα (hSIRPαD1) to guide the selection of Nbs that specifically block the hSIRPα/hCD47 interaction. Sequencing of individual clones resulted in 14 unique hSIRPα Nbs with high diversity in the complementarity-determining region 3 (CDR3) (Figure 1A; Supplementary Table 1). Nbs S7 to S36 were derived from the full-length hSIRPα screening, whereas Nbs S41 to S45 were identified as hSIRPαD1 binders. Individual Nbs were produced in *Escherichia coli* (*E. coli*) and isolated with high purity (Figure 1B). Folding stability of all Nbs was analyzed by differential scanning fluorimetry. For 12 out of the 14 Nb candidates, melting temperatures ranging from ~55°C to ~75°C without aggregation (Figures 1C, D; Supplementary Figure 1A) were determined, whereas affinity measurements against recombinant hSIRPα by biolayer interferometry (BLI) revealed K_D values between ~0.12 nM and ~27 nM for 11 out of the 12 Nbs (Figures 1C, D; Supplementary Figure 1B). In addition, live-cell immunofluorescence staining of U2OS - Human Bone Osteosarcoma Epithelial Cells stably expressing full-length hSIRPα showed that all selected Nbs recognize hSIRPα localized at the plasma membrane (Figure 1E; Supplementary Figure 2A).

Domain mapping of hSIRPα Nbs

Whereas Nbs targeting hSIRPαD1 have a higher chance to block interaction with CD47, Nbs targeting domain D2 or D3 (hSIRPαD2 and hSIRPαD3) might be functionally inert, which is preferable for diagnostic approaches. Thus, we assessed domain specificity using U2OS cells expressing the individual domains of hSIRPα by immunofluorescence staining (Figure 2A, Supplementary Figure 2B). Eight Nbs (S12, S14, S17, S41, S42, S43, S44, and S45) stained hSIRPαD1, whereas Nbs S14 and S17 additionally stained hSIRPαD2. Five Nbs (S8, S21, S29, S33, and S36) revealed specific binding to hSIRPαD2, whereas only Nb S7 stained cells expressing hSIRPαD3. On the basis of their respective production yield, stability, affinity, domain specificity, and developability, we selected Nbs S7, S8, S12, S33, S36, S41, S44, and S45 for further characterization. To determine the diversity of epitopes recognized by this subset in more detail, we performed an epitope binning analysis using BLI (Figure 2B; Supplementary Figures 3A, B). On the basis of the results, we grouped the Nbs according to shared or overlapping epitopes and found two groups each for hSIRPαD1-targeting (Nbs S12 and S41 and Nbs S44

Wagner et al.

10.3389/fimmu.2023.1264179

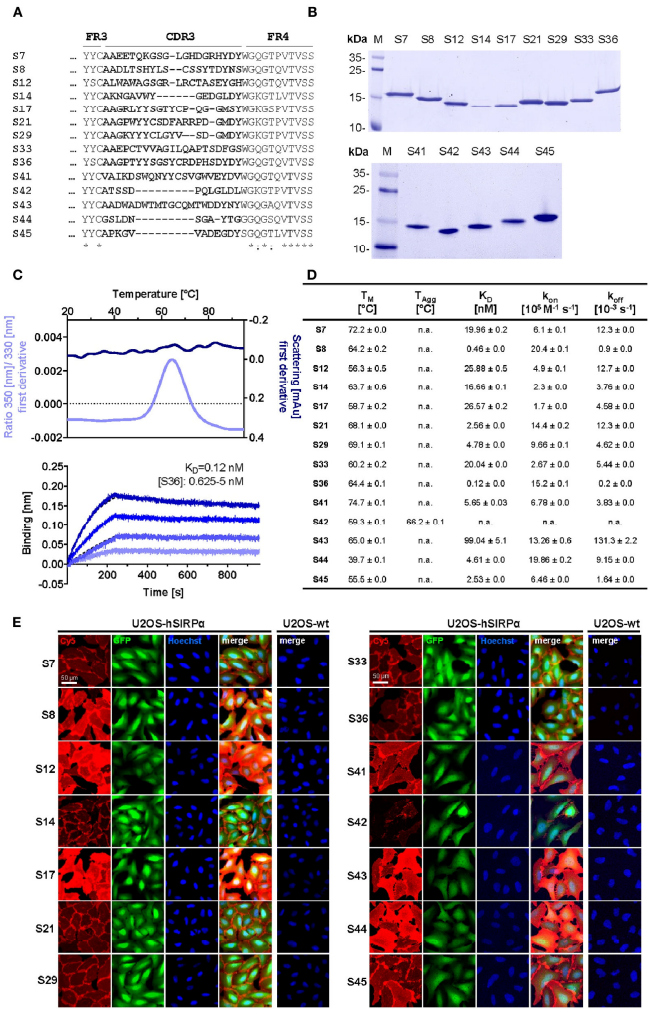

	T_M [°C]	T_{Agg} [°C]	K_D [nM]	k_{on} [10^5 M^{-1} s^{-1}]	k_{off} [10^{-3} s^{-1}]
S7	72.2 ± 0.0	n.a.	19.96 ± 0.2	6.1 ± 0.1	12.3 ± 0.0
S8	64.2 ± 0.2	n.a.	0.46 ± 0.0	20.4 ± 0.1	0.9 ± 0.0
S12	56.3 ± 0.5	n.a.	25.88 ± 0.5	4.9 ± 0.1	12.7 ± 0.0
S14	63.7 ± 0.6	n.a.	16.66 ± 0.1	2.3 ± 0.0	3.76 ± 0.0
S17	58.7 ± 0.2	n.a.	26.57 ± 0.2	1.7 ± 0.0	4.59 ± 0.0
S21	68.1 ± 0.0	n.a.	2.56 ± 0.0	14.4 ± 0.2	12.3 ± 0.0
S29	69.1 ± 0.1	n.a.	4.78 ± 0.0	9.66 ± 0.1	4.62 ± 0.0
S33	60.2 ± 0.2	n.a.	20.04 ± 0.0	2.67 ± 0.0	5.44 ± 0.0
S36	64.4 ± 0.1	n.a.	0.12 ± 0.0	15.2 ± 0.1	0.2 ± 0.0
S41	74.7 ± 0.1	n.a.	5.65 ± 0.03	6.78 ± 0.0	3.83 ± 0.0
S42	69.3 ± 0.1	66.2 ± 0.1	n.a.	n.a.	n.a.
S43	65.0 ± 0.1	n.a.	99.04 ± 5.1	13.26 ± 0.6	131.3 ± 2.2
S44	39.7 ± 0.1	n.a.	4.61 ± 0.0	19.86 ± 0.2	9.15 ± 0.0
S45	55.5 ± 0.0	n.a.	2.53 ± 0.0	6.46 ± 0.0	1.64 ± 0.0

FIGURE 1
Biochemical characterization of hSIRPα Nbs. **(A)** Amino acid (aa) sequences of the complementarity-determining region (CDR) 3 from 14 unique hSIRPα Nbs (complete sequences shown in Supplementary Table 1) identified by a bidirectional screening strategy. Nbs S7 to S36 were selected against full-length hSIRPα and Nbs S41 to 45 against domain 1 of hSIRPα (hSIRPαD1). **(B)** Recombinant expression and purification of hSIRPα Nbs using immobilized metal affinity chromatography (IMAC) and size exclusion chromatography (SEC). Coomassie staining of purified Nbs is shown. **(C)** Stability analysis using nano–differential scanning fluorimetry (nanoDSF) displaying fluorescence ratio (350 nm/330 nm) and light intensity loss due to scattering shown as first derivative exemplarily shown for Nb S36 (upper panel). Data are shown as mean value of three technical replicates. BLI-based affinity measurements exemplarily shown for Nb S36 (bottom panel). Biotinylated hSIRPα was immobilized on streptavidin biosensors. Kinetic measurements were performed using four concentrations of purified Nbs ranging from 0.625 nM to 5 nM (displayed with gradually darker shades of color). The binding affinity (K_D) was calculated from global 1:1 fits shown as dashed lines. **(D)** Summary table of stability and affinity analysis of selected hSIRPα Nbs. Melting temperature (T_M) and aggregation temperature (T_{Agg}) determined by nanoDSF shown as mean ± SD of three technical replicates. Affinities (K_D), association constants (k_{on}), and dissociation constants (k_{off}) determined by BLI using four concentrations of purified Nbs shown as mean ± SD. **(E)** Representative images of hSIRPα and GFP-coexpressing U2OS cells stained with hSIRPα Nbs of three technical replicates. Images show individual Nb staining detected with anti-VHH-Cy5 (red), intracellular IRES-derived GFP signal (green), nuclei staining (Hoechst, blue), and merged signals; scale bar, 50 µm.

10.3389/fimmu.2023.1264179

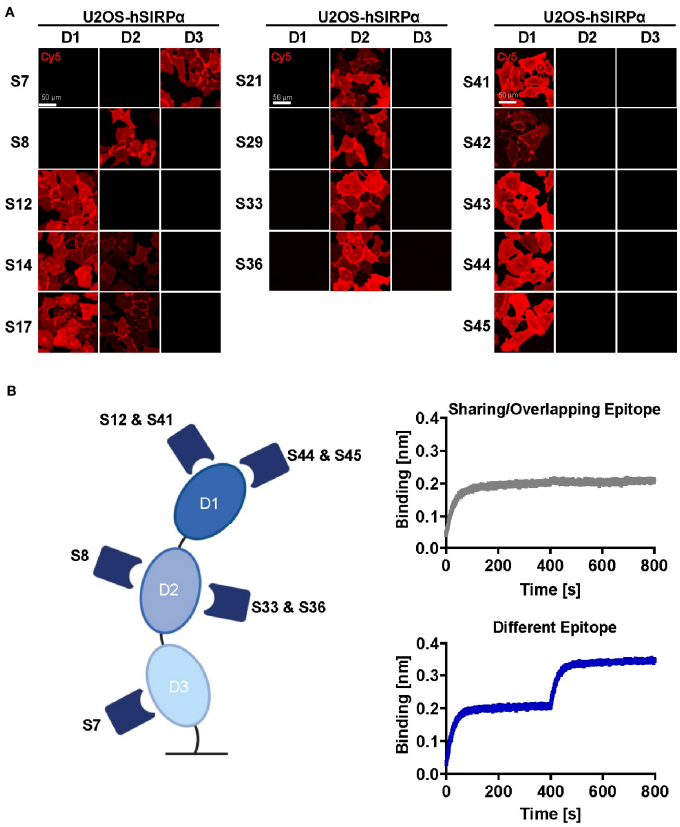

FIGURE 2
Epitope characterization of hSIRPα Nbs. **(A)** Domain mapping analysis by immunofluorescence staining with hSIRPα Nbs on U2OS cells displaying human hSIRPα domain 1 (D1), domain 2 (D2), or domain 3 (D3) at their surface. Representative images of live cells stained with individual Nbs in combination with Cy5-labeled anti-VHH of three technical replicates are shown; scale bar, 50 µm. **(B)** Epitope binning analysis of hSIRPα Nbs by BLI. Graphical summary of epitope binning analysis on the different hSIRPα domains (left panel). Representative sensograms (n = 1) of combinatorial Nb binding to recombinant hSIRPα on sharing/overlapping epitopes or on different epitopes (right panel).

and S45) and hSIRPαD2-targeting (Nb S8 and Nbs S33 and S36) Nbs (Supplementary Figures 3A, B).

Specificity of hSIRPα Nbs for allelic variants and closely related SIRP family members

hSIRPα belongs to the hSIRP family of immune receptors, which also includes the highly homologous activating receptor hSIRPβ1 present on macrophages, and the decoy receptor hSIRPγ, which is expressed mainly on T cells (14). Moreover, hSIRPα allelic variants, hSIRPαV1 and hSIRPαV2, are expressed either homozygously (v1/v1 or v2/v2) or heterozygously (v1/v2) (25). To address potential cross-reactivity, binding of selected hSIRPα Nbs to hSIRPβ1, hSIRPγ, the hSIRPα variants hSIRPα-V1 and hSIRPα-V2, and murine SIRPα was visualized using immunofluorescence staining (Figure 3A; Supplementary Figure 2C). Cellular imaging revealed that all Nbs recognized the homologous hSIRPβ1, whereas hSIRPγ was detected with Nbs S12 and S44 (both hSIRPαD1-targeting Nbs) as well as Nbs S8 and S36 (both hSIRPαD2-targeting Nbs). Furthermore, all hSIRPαD2- and D3-targeting Nbs recognized hSIRPα-V1 and hSIRPα-V2, whereas S45 was the only hSIRPαD1-targeting Nb to show binding to both variants. Notably, none of the selected Nbs revealed any cross-reactivity towards murine SIRPα.

10.3389/fimmu.2023.1264179

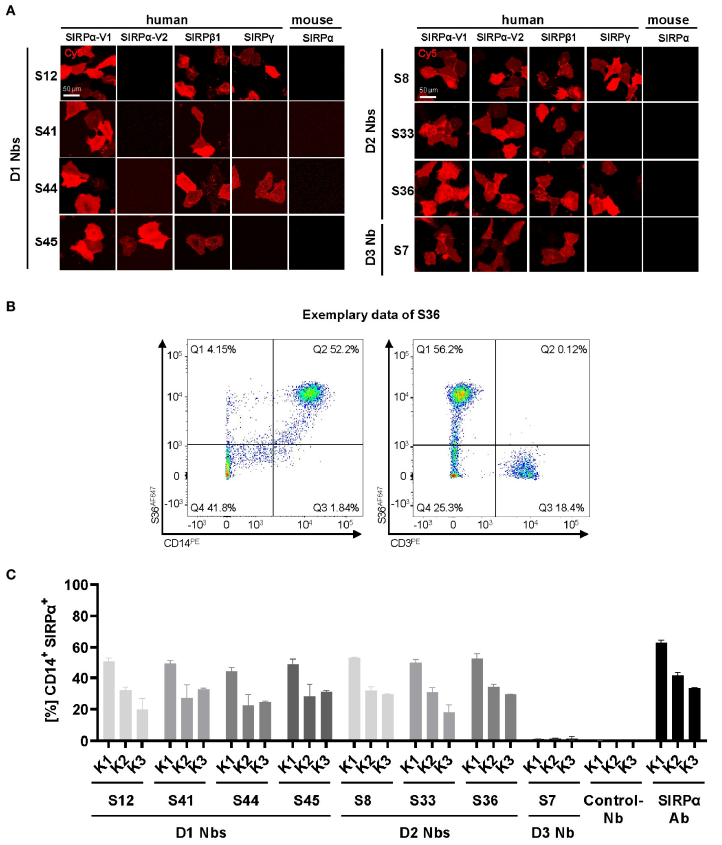

FIGURE 3
Cross-reactivity and binding specificity of hSIRPα Nbs. **(A)** Cross-reactivity analysis of hSIRPα Nbs by immunofluorescence staining on U2OS cells displaying hSIRPα-V1, hSIRPα-V2, hSIRPβ1, hSIRPγ, or mouse SIRPα at their surface. Representative images of live cells stained with individual Nbs in combination with Cy5-labeled anti-VHH are shown of three technical replicates; scale bar, 50 µm. **(B)** Flow cytometry analysis of human peripheral blood mononuclear cells (PBMCs) stained with fluorescently labeled hSIRPα Nbs (AlexaFluor 647, AF647). Flow cytometry plots of Nb S36 staining on $CD14^+$ and $CD3^+$ PBMC populations derived from human donor K1 are shown as an example. **(C)** Flow cytometry analysis of hSIRPα Nbs staining $CD14^+$ PBMCs of three different human donors (K1, K2, and K3). As control, PBMCs were stained with a Pep Nb (Control-Nb) and a SIRPα-antibody (positive control). Data are presented as mean ± SD of three technical replicates.

Binding of hSIRPα Nbs to primary human monocyte/macrophage cells

To evaluate whether our hSIRPα Nbs recognize endogenously expressed hSIRPα, we performed flow cytometry analysis of peripheral blood mononuclear cells (PBMCs) from three different donors (K1–K3). In addition to the monocyte/macrophage marker CD14, we also included the T-cell marker CD3 to evaluate potential recognition of T cells by hSIRPγ–cross-reactive Nbs (Figure 3B). All hSIRPα Nbs, except S7, stained comparably on $CD14^+$ PBMCs from all tested donors, whereas none of the Nbs stained $CD3^+$ T cells (Figures 3B, C).

Considering our binary strategy to select hSIRPα Nbs (i) that are eligible to inhibit the hSIRPα/hCD47 interaction and (ii) as probes for positron emission tomography (PET)–based *in vivo* imaging of myeloid cells, we divided the identified Nbs into two subgroups. In the following, hSIRPαD1-targeting Nbs S12, S41, S44, and S45 were further investigated with respect to their inhibitory properties, and hSIRPαD2-targeting Nbs S8, S33, and S36 for their applicability as *in vivo* imaging probes.

10.3389/fimmu.2023.1264179

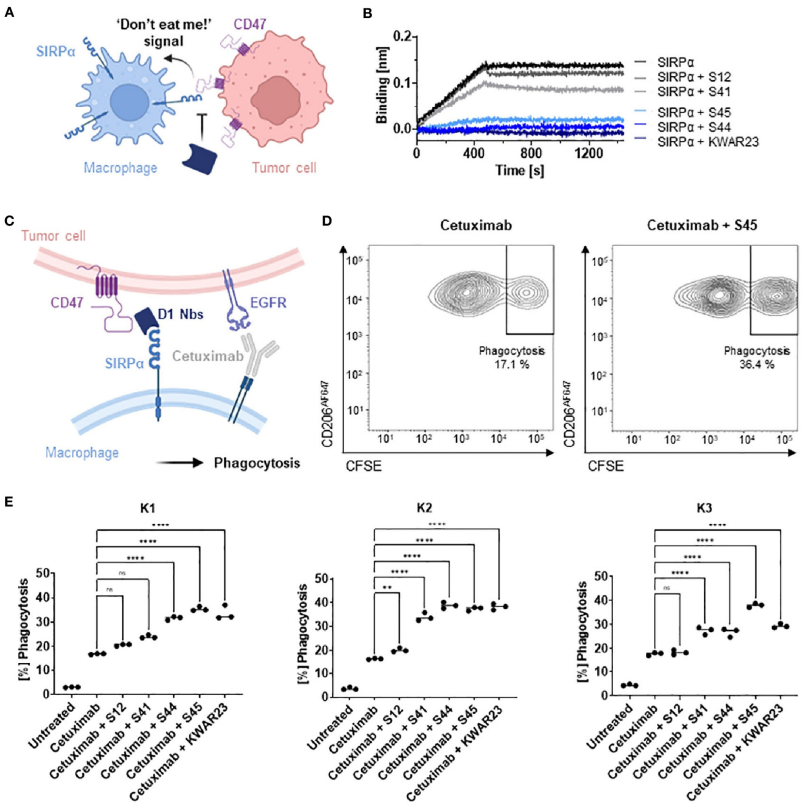

FIGURE 4
Potential of hSIRPαD1 Nbs to augment phagocytosis of tumor cells. **(A)** Graphical illustration of hSIRPα/hCD47 interaction leading to suppression of macrophage-mediated phagocytosis of tumor cells. **(B)** Competition analysis of hSIRPα-binding to hCD47 in the presence of hSIRPαD1 Nbs (S12, S41, S44, and S45) by BLI (n = 1). Biotinylated hCD47 was immobilized on streptavidin biosensors, and a mixture of 20 nM hSIRPα and 250 nM of hSIRPαD1 Nbs or 5 nM of KWAR23 was applied to elucidate potential inhibition of hSIRPα binding to hCD47. **(C)** Schematic illustration of macrophage-mediated phagocytosis of tumor cells by hSIRPαD1 Nbs and tumor-opsonizing antibodies (e.g., the anti-EGFR antibody cetuximab). **(D)** Phagocytosis of CFSE–labeled DLD-1 cells by human monocyte-derived macrophages. A representative flow cytometry plot of the phagocytosis assay of cetuximab only and combinatorial treatment of cetuximab and hSIRPα Nb S45 with donor K1–derived macrophages is shown. **(E)** Quantitative analysis of the phagocytosis assay. Percent of phagocytosis of CFSE-labeled DLD-1 cells analyzed for macrophages derived from three different donors (K1, left; K2, center; K3, right) in different conditions is shown. Data are shown as individual and mean value of three technical replicates. $p < 0.05$ was considered statistically significant (*) and marked as ** for $p < 0.01$, *** for $p < 0.001$, and **** for $p < 0.0001$; non-significant results were marked with ns.

hSIRPαD1 Nbs functionally block the interaction with hCD47

To evaluate potential inhibition of the interaction between hSIRPα and hCD47 (Figure 4A), we first performed a competitive BLI-based binding assay. As control, we used the anti–hSIRPα-blocking antibody KWAR23 (26). After incubation with Nb S44 or S45, binding of hSIRPα to CD47 was inhibited to a similar extent as upon addition of KWAR23; whereas only partial blocking was observed for S41, S12 showed no effect (Figure 4B). For functional analysis, we next tested the ability of hSIRPαD1-targeting Nbs to potentiate macrophage-mediated antibody-dependent cellular phagocytosis (ADCP) (Figure 4C). To this end, human monocyte-derived macrophages (MDMs) isolated from three different donors (K1–K3) were incubated with Epidermal Growth Factor Receptor ($EGFR^+$) expressing human colorectal adenocarcinoma DLD-1 cells preloaded with carboxyfluorescein diacetate succinimidyl ester (CFSE) alone or in the presence of the opsonizing EGFR-specific antibody cetuximab and hSIRPαD1-targeting Nbs or the KWAR23 antibody as positive control. The degree of ADCP was determined on the basis of the detection of $CD206^+CFSE^+$ cells by flow cytometry analysis (Figure 4D). For all tested donors, macrophages exhibited minimal phagocytosis of DLD-1

10.3389/fimmu.2023.1264179

cells without treatment, whereas phagocytic activity was significantly increased upon addition of cetuximab. In the presence of the hSIRPα-blocking antibody KWAR23, phagocytosis was further induced, which is in line with previous findings (26). Similarly, the hSIRPα-blocking Nbs S44 and S45 augmented ADCP in all three tested donors, whereas Nb S12 and S41 only revealed limited effect on macrophage-mediated phagocytosis (Figure 4E). From these results, we concluded that Nbs S44 and S45 represent promising candidates for further development as novel hSIRPα/CD47-inhibitory biologicals for potential therapeutic applications.

Inert hSIRPα-S36 Nb as lead candidate for non-invasive *in vivo* imaging

For the application as non-invasive PET tracer, immunologically inert hSIRPα Nbs are preferred. Thus, we selected Nbs S8, S33, and S36, which bind to hSIRPαD2, and performed a detailed analysis of the recognized epitopes by hydrogen-deuterium exchange mass spectrometry (HDX-MS). All selected Nbs recognized three-dimensional epitopes within hSIRPαD2, which are spatially distant from the hSIRPα/hCD47 interface (Supplementary Table 2; Supplementary Figures 4A, B). In particular, S36 Nb showed the strongest deuteration protection (<−15%) for amino acid (aa) D163 to L187 and aa H202 to G207 of hSIRPα, whereas an additional slightly lower protection was observed for the region ranging from aa C140 to K153 (Supplementary Figures 4A, B). Considering its detailed epitope mapping. strong binding affinity. and good production yield, we selected S36 Nb as the lead candidate for imaging.

For radiolabeling, we conceived a novel protein engineering approach that enables site-specific chemical conjugation. We first adapted the sequence of the original S36 Nb by replacing all four lysine residues with arginine (hSIRPα-$S36_{K>R}$ Nb) (Supplementary Figure 5A) and conjugated the chelator via isothiocyanate (p-NCS-benzyl-NODA-GA) to the remaining primary NH_2-group at the N-terminus (Supplementary Figure 5A). The hSIRPα-$S36_{K>R}$ Nb was producible with comparable yield and purity to the original version in *E.coli* (Supplementary Figure 5B) and efficient site-specific chelator conjugation (~96%) was confirmed by mass spectrometry. Most importantly, the hSIRPα-$S36_{K>R}$ Nb showed comparable affinities and characteristics to the original S36 Nb (Supplementary Figures 5C–E). Finally, we examined the hSIRPα-$S36_{K>R}$ Nb in the macrophage-dependent phagocytosis assay. Here, we observed a minor induction of macrophage-dependent phagocytosis that is comparable to the effect of the non-blocking Nb S12 (Supplementary Figure 5F; Figure 4E). From these results, we concluded that hSIRPα-$S36_{K>R}$ Nb, represents a lead candidate suitable for non-invasive *in vivo* PET imaging of SIRPα expression.

PET/MR imaging with ^{64}Cu-hSIRPα-$S36_{K>R}$ Nb

For *in vivo* validation, the hSIRPα-$S36_{K>R}$ Nb and the non-specific $GFP_{K>R}$ Nb (6) as control were radiolabeled with ^{64}Cu yielding high radiolabeling efficiencies of ≥95% (Figure 5A) and an *in vitro* immunoreactive fraction of ~82% (B_{max}) of the ^{64}Cu-labeled hSIRPα-$S36_{K>R}$ Nb (^{64}Cu-hSIRPα-$S36_{K>R}$ Nb) to HT1080 hSIRPα knock-in (KI) (HT1080-hSIRPα) cells (Figure 5B).

To visualize the distribution of hSIRPα-positive cells in a tumor-relevant system, we employed a novel immunocompetent hSIRPα/hCD47 KI mouse model (hSIRPα/hCD47 mice), expressing the extracellular domain of hSIRPα, and C57BL/6 wild-type (wt) mice as controls. In both models, tumors were generated by subcutaneous (*s.c.*) injection of hCD47-overexpressing MC38 (MC38-hCD47) colon adenocarcinoma cells. Nine days after tumor inoculation, we intravenously (*i.v.*) injected ^{64}Cu-hSIRPα-$S36_{K>R}$ Nb into both groups. As additional control, the non-specific ^{64}Cu-$GFP_{K>R}$ Nb was injected in tumor-bearing hSIRPα/hCD47 mice. Non-invasive *in vivo* PET/MR imaging revealed a strongly enhanced ^{64}Cu-hSIRPα-$S36_{K>R}$ Nb accumulation in the tumors of hSIRPα/hCD47 mice within the first minutes after injection, which remained stable at a high level for 6 h. In contrast, both control groups, ^{64}Cu-$GFP_{K>R}$ Nb–injected hSIRPα/hCD47 mice and ^{64}Cu-hSIRPα-$S36_{K>R}$ Nb–injected wt mice, showed rapid tracer clearance in the tumors and blood (Figure 5C). Importantly, ^{64}Cu-hSIRPα-$S36_{K>R}$ Nb–injected hSIRPα/hCD47 mice exhibited a constantly higher PET signal in the blood over time, indicating a specific binding to circulating hSIRPα$^+$ myeloid cells (Figure 5C). Quantification of the PET images 3 h after injection revealed a significantly higher uptake in the tumors of hSIRPα/hCD47 mice (1.89 ± 0.09%ID/cc) compared with that of wt mice (0.60 ± 0.05% ID/cc) and to ^{64}Cu-$GFP_{K>R}$ Nb–injected hSIRPα/hCD47 mice (0.57 ± 0.05%ID/cc) (Figures 5C–E). Furthermore, we observed a ~7-fold enhanced uptake in the spleen, a ~2-fold enhanced uptake in the blood and liver, and a ~3-fold enhanced uptake in the salivary glands and bone in hSIRPα/hCD47 mice (Figures 5D, E), whereas no significant differences were identified in the kidney and the muscle tissue between the ^{64}Cu-hSIRPα-$S36_{K>R}$ Nb–injected hSIRPα/hCD47 mice and both control groups (Figures 5D, E). From these results, we concluded that the novel ^{64}Cu-hSIRPα-$S36_{K>R}$ Nb–based PET tracer is applicable to visualize and monitor the distribution of SIRPα$^+$ cells by non-invasive *in vivo* imaging.

Discussion

Myeloid cells, particularly macrophages, frequently infiltrate tumors, modulate tumor angiogenesis, promote metastasis, and have been associated with tumor resistance to chemotherapy and immune checkpoint blockade (27, 28). A characteristic marker for myeloid cells is the immune checkpoint SIRPα. Therapeutic targeting the SIRPα/CD47 signaling axis is considered a promising strategy for the treatment of advanced cancers. Recent *in vivo* data have demonstrated a synergistic anti-tumor effect of SIRPα-specific antibodies in combination with tumor-opsonizing antibodies such as cetuximab (EGFR), rituximab (CD20), and trastuzumab human epidermal growth factor receptor (HER2) (25, 26, 29), and, currently, several anti-hSIRPα monoclonal antibodies including BI 765063 and GS-0189 (FIS-189) are in clinical trials for mono- and combination therapies (30). In addition to serving as therapeutic target, SIRPα also represents a biomarker, which can be used to stratify patients by myeloid cell

10.3389/fimmu.2023.1264179

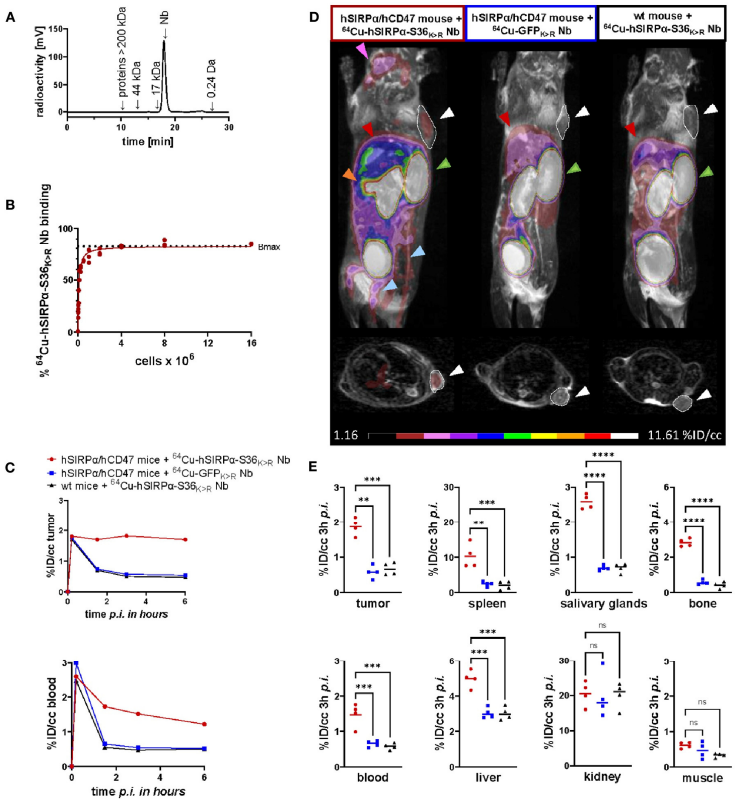

FIGURE 5
PET imaging with ^{64}Cu-hSIRPα-S36$_{K>R}$ Nb. **(A)** Radiochemical purity of ^{64}Cu-hSIRPα-S36$_{K>R}$ Nb was assessed using high-performance liquid chromatography (HPLC). **(B)** Antigen excess binding assay to determine the maximum binding (Bmax) of ^{64}Cu-hSIRPα-S36$_{K>R}$ Nb, referred to as immunoreactive fraction. ^{64}Cu-hSIRPα-S36$_{K>R}$ Nb (1 ng) was applied to an increasing number of HT1080-hSIRPα cells of three technical replicates and binding curves were analyzed using the one-site nonlinear regression model. **(C)** Quantification of ^{64}Cu-hSIRPα-S36$_{K>R}$ Nb tumor and blood uptake of *s.c.* MC38-hCD47 colon carcinoma-bearing hSIRPα/hCD47 mice over 6 h after injection. ^{64}Cu-hSIRPα-S36$_{K>R}$ Nb accumulation is compared to the control groups injected with control Nb or in MC38 wt mice injected with ^{64}Cu-hSIRPα-S36$_{K>R}$ Nb. The resulting values were decay-corrected and presented as percentage of injected dose per cubic centimeter (%ID/cc). Representative data of one animal per group is shown. **(D)** Representative fused MIP (maximum intensity projection) PET/MR images of mice 3 h after ^{64}Cu-hSIRPα-S36$_{K>R}$ (n = 4) or control Nb injection (each n = 4). PET signal in hSIRPα expressing myeloid cell–rich organs is compared to both control groups. Sites with increased ^{64}Cu-hSIRPα-S36$_{K>R}$ Nb uptake are marked by colored arrows indicating the tumor (white and outlined), spleen (orange), bone (blue), salivary glands (purple), kidneys (green), and liver (red). In addition, axial sections of PET/MR images are shown where the tumors are highlighted with white circles and arrows. **(E)** Quantification of ^{64}Cu-hSIRPα-S36$_{K>R}$ Nb in hSIRPα expressing myeloid cell–rich organs. High accumulation was also detected in sites of excretion, namely, the kidney and liver. The resulting values were decay-corrected and presented as percentage of injected dose per cubic centimeter (%ID/cc). Data are shown as individual plots and mean value (n = 4). $p < 0.05$ was considered statistically significant (*) and marked as ** for $p < 0.01$, *** for $p < 0.001$, and **** for $p < 0.0001$; non-significant results were marked with ns.

expression patterns (17–19) and to track the migration and dynamics of myeloid cells in the context of cancer. Recently, murine-specific SIRPα Nbs were successfully employed for non-invasive single-photon emission tomography imaging of myeloid cells in intracranial glioblastoma tumors of experimental mice (31).

Here, we pursued a binary screening strategy to develop the first hSIRPα-specific Nbs as a panel of novel theranostic binding molecules. Our aim was either to identify Nbs as modulating biologics blocking the hSIRPα/hCD47 axis or to monitor TAMs as the most common myeloid cell type in the TME. By choosing Nbs that exclusively bind the D1 domain of hSIRPα, we were able to identify binders that selectively block the interaction with CD47 and enhance ADCP in combination with the tumor-opsonizing antibody cetuximab *in vitro*. In particular, the selectivity of Nb S45 for binding hSIRPα, but not hSIRPγ, might be advantageous, as recent data showed that nonselective hSIRPα/hSIRPγ blockade can

10.3389/fimmu.2023.1264179

impair T-cell activation, proliferation, and endothelial transmigration (32). Notably, as versatile building blocks, Nbs can easily be customized into more effective biologics. Thus, blocking efficacies of the inhibitory hSIRPα-specific Nbs can be further improved, e.g., by establishing bivalent or biparatopic formats as previously shown (24, 33). Alternatively, bispecific binding molecules could be generated, e.g., by fusing the hSIRPα-blocking Nbs with a tumor-opsonizing Nb and Fc moiety (34, 35) or CD40L expressed by activated T cells to bridge innate and adaptive immune responses (36). To address rapid renal clearance, which is a major drawback of small-sized Nbs for therapeutic application, other modifications such as PEGylation, addition of an albumin-binding moiety, or direct linkage to carrier proteins can be considered to extend their systemic half-life (t½) and efficacy (37, 38).

In addition to developing inhibitory hSIRPα Nbs, we also identified binders to elucidate the presence and infiltration of the myeloid cell population using PET-based non-invasive *in vivo* imaging. Current diagnostic methods are based on histology and thus require biopsies through invasive sampling or endpoint analyses. These methods can be associated with severe side effects and limit the predictive value of such diagnostic approaches. In contrast, non-invasive *in vivo* whole-body molecular imaging techniques, particularly PET, represent a powerful method to monitor and quantify specific cell populations and thereby support individual therapy decisions (39–41). Because of their ideal characteristics for PET imaging, including specific binding, fast tissue penetration, and rapid renal clearance, Nbs emerged as next-generation tracer molecules with numerous candidates in preclinical and first candidates in clinical testing (42–44). With the hSIRPα-S36 Nb, we selected a functionally inert but high-affinity binding candidate for which we achieved site-directed chemical chelator labeling based on a unique protein engineering approach that did not compromise the stability or binding properties. Compared with other, more elaborate and less effective labeling strategies such as sortagging (45–47), this approach resulted in rapid chelator conjugation by applying straightforward NCS chemistry.

^{64}Cu-hSIRPα-S36$_{K>R}$ Nb–PET/MR imaging in a novel tumor-bearing hSIRPα/hCD47 KI mouse model revealed rapid recruitment and sustained accumulation of our radiotracer in myeloid-enriched tumors and lymphatic organs with low background signal. We also observed a significantly enhanced ^{64}Cu-hSIRPα-S36$_{K>R}$ Nb uptake in MC38-hCD47 adenocarcinomas of hSIRPα/hCD47 KI mice vs. wt mice, suggesting specific targeting of myeloid cells within the TME. This is also supported by the fact that no enhanced ^{64}Cu-hSIRPα-S36$_{K>R}$ Nb uptake was observed in tumors and lymphatic organs of murine SIRPα and CD47 expressing wt mice. Beyond the crucial role of myeloid cells in tumor progression and cancer immunotherapy resistance, the occurrence of myeloid cells in diseased tissues is a hallmark of several inflammatory diseases like SARS-CoV-2 infection or autoimmune diseases such as systemic sclerosis, rheumatoid arthritis, and inflammatory bowel disease (48, 49). Thus, the non-invasive *in vivo* monitoring of biodistribution, density, and dynamic changes of the myeloid cell compartment presented in this initial study would allow surveillance and early assessment of therapeutic response in a variety of diseases (50). In comparison to established strategies typically targeting TAM subpopulations visualizing the Translocator protein (TSPO) or the macrophage mannose receptor (MMR) using the ^{68}Ga anti-MMR Nb, the ^{64}Cu-hSIRPα-S36$_{K>R}$ Nb enables the monitoring of the entire myeloid cell population (11, 51, 52). Furthermore, given that hSIRPα-S36 Nb detects both hSIRPα allelic variants, its application is not restricted to patient subpopulations.

In summary, this study demonstrates for the first time the generation and detailed characterization of hSIRPα-specific Nbs for potential therapeutic and diagnostic applications. Considering the important role of myeloid cells, particularly TAMs, the herein developed hSIRPα-blocking Nbs have the potential to extend current macrophage-specific therapeutic strategies (30, 53). Moreover, our novel ^{64}Cu-hSIRPα-S36$_{K>R}$ Nb–based PET tracer will broaden the growing pipeline of Nb-based radiotracers to selectively visualize tumor-associated immune cells by non-invasive *in vivo* PET imaging (45, 47, 51, 54). Given the increasing importance of personalized medicine, we anticipate that the presented hSIRPα-specific Nbs might find widespread use as novel theranostics either integrated into or accompanying emerging immunotherapies.

Materials and methods

Nanobody screening

For the selection of hSIRPα-specific Nbs, two consecutive phage enrichment rounds either with immobilized hSIRPα or hSIRPαD1 were performed. To generate Nb-presenting phages, TG1 cells comprising the Nb-library in pHEN4 were infected with the M13K07 helper phage. In each panning round, 1×10^{11} phages were applied to streptavidin or neutravidin plates (Thermo Fisher Scientific) coated with biotinylated antigen (5 µg/mL). For biotinylation, purified antigen (Acrobiosystems) was reacted with Sulfo-NHS-LC-LC-Biotin (Thermo Fisher Scientific) in 5 M excess at ambient temperature for 30 min. Excess of biotin was removed by size exclusion chromatography using Zeba™ Spin Desalting Columns 7K MWCO 0.5 mL (Thermo Fisher Scientific) according to the manufacturer's protocol. Blocking of antigen and phage was performed alternatively with 5% milk or Bovine Serum Albumin (BSA) in Phosphate-Buffered Saline with Tween (PBS-T), and, as the number of panning rounds increased, the wash stringency with PBS-T was intensified. Bound phages were eluted in 100 mM triethylamine (TEA) (pH 10.0), followed by immediate neutralization with 1 M Tris/HCl (pH 7.4). Exponentially growing TG1 cells were infected with eluted phages and spread on selection plates for subsequent selection rounds. In each round, antigen-specific enrichment was monitored by counting colony-forming units.

Whole-cell phage ELISA

For the monoclonal phage enzyme linked immunosorbent assay (ELISA) individual clones were picked, and phage production was

10.3389/fimmu.2023.1264179

induced as described above. Moreover, 96-well cell culture plates (Corning) were coated with poly-L-lysine (Sigma-Aldrich) and washed once with H_2O. U2OS-wt and U2OS overexpressing hSIRPα (U2OS-hSIRPα) or hSIRPαD1 (U2OS-hSIRPαD1) were plated at 2×10^4 cells per well in 100 µL and grown overnight. The next day, 70 µL of phage supernatant was added to each cell type and incubated at 4°C for 3 h. Cells were washed five times with 5% FBS in PBS, followed by adding the Anti-M13 Monoclonal Antibody coulpled Horseradish Peroxidase (M13-HRP)–labeled detection antibody (Progen, 1:2,000 dilution) for 1 h, and washed three times with 5% Fetal Bovine Serum (FBS) in PBS. Finally, Onestep ultra TMB 32048 ELISA substrate (Thermo Fisher Scientific) was added to each well and incubated until color change was visible before stopping the reaction with 100 µL of 1 M H_2SO_4. For detection, the Pherastar plate reader at 450 nm was applied, and phage ELISA-positive clones were defined by a two-fold signal above wt control cells.

Protein expression and purification

hSIRPα Nbs were cloned into the pHEN6 vector (55) and expressed in XL-1 as previously described (22, 56). Sortase A pentamutant (eSrtA) in pET29 was a gift from David Liu (Addgene, plasmid # 75144) and was expressed as published (57). Expressed proteins were purified by immobilized metal affinity chromatography (IMAC) using a HisTrap^{FF} column followed by a size exclusion chromatography (SEC; Superdex 75) on an Aekta pure system (Cytiva). Quality of all purified proteins was analyzed via standard Sodium Dodecyl Sulfate – Polyacrylamid Gel Electrophoresis (SDS-PAGE) under denaturizing conditions [5 min, 95°C in 2× SDS-sample buffer containing 60 mM Tris/HCl (pH 6.8); 2% (w/v) SDS; 5% (v/v) 2-mercaptoethanol, 10% (v/v) glycerol, 0.02% bromphenole blue]. For protein visualization, InstantBlue Coomassie (Expedeon) staining or alternatively immunoblotting as previously published (58) was performed. Protein concentration was determined by NanoDrop ND100 spectrophotometer.

Biolayer interferometry

Analysis of binding kinetics of hSIRPα-specific Nbs was performed using the Octet RED96e system (Sartorius) as per the manufacturer's recommendations. In brief, biotinylated hSIRPα (5 µg/mL) diluted in Octet buffer (PBS, 0.1% BSA, and 0.02% Tween-20) was immobilized on streptavidin coated biosensor tips (SA, Sartorius) for 40 s. In the association step, a dilution series of Nbs ranging from 0.625 nM to 320 nM were reacted for 240 s followed by dissociation in Octet buffer for 720 s. Every run was normalized to a reference run applying Octet buffer for association. Data were analyzed using the Octet Data Analysis HT 12.0 software applying the 1:1 ligand-binding model and global fitting. For epitope binning, two consecutive association steps with different Nbs were performed. By analyzing the binding behavior of the second Nb, conclusions about shared epitopes were drawn. For the hCD47 competition assay, hCD47 was biotinylated and immobilized on SA biosensors followed by the application of pre-mixed solutions containing hSIRPα (20 nM) and Nb (250 nM). hCD47-competing Ab KWAR23 (5 nM) was used as control.

Live-cell immunofluorescence

Stably expressing hSIRPα U2OS cells, U2OS wt or U2OS cells transiently expressing individual hSIRPα domains (D1-3) with SPOT-Tag, or different hSIRP family members (hSIRPα-V1, hSIRPα-V2, hSIRPβ1, hSIRPγ, and murine SIRPα) were plated at ~10,000 cells per well of a µClear 96-well plate (Greiner Bio One, cat. #655090) and cultivated overnight in standard conditions. For imaging, medium was replaced by live-cell visualization medium DMEMgfp-2 (Evrogen, cat. #MC102) supplemented with 10% FBS, 2 mM L-glutamine, Hoechst33258 (2 µg/mL; Sigma-Aldrich) for nuclear staining. Unlabeled hSIRPα Nbs (1 nM to 100 nM) in combination with anti-VHH secondary Cy5 AffiniPure Goat Anti-Alpaca IgG (2.5 µg/mL; Jackson Immuno Research) were added and incubated for 1 h at 37°C. For control staining, hSIRPα Ab Phycoerythrin (PE) (SE5A5, BioLegend) and bivSPOT-Nb labeled with AlexaFluor647 (AF647) were used. Images were acquired with a MetaXpress Micro XL system (Molecular Devices) at ×20 or ×40 magnification.

Stability analysis

Stability analysis was performed by the Prometheus NT.48 (Nanotemper). In brief, freshly thawed hSIRPα Nbs were diluted to 0.25 mg/mL, and measurements were carried out at time point T_0 or after incubation for 10 days at 37°C (T_{10}) using high-sensitivity capillaries. Thermal unfolding and aggregation of the Nbs were induced by the application of a thermal ramp of 20°C to 95°C while measuring fluorescence ratios (F350/F330) and light scattering. Via the PR. ThermControl v2.0.4, the melting temperature (T_M) and aggregation (T_{Agg}) temperature were determined.

Fluorescent labeling

For sortase coupling, 50 µM Nb, 250 µM sortase peptide (H-Gly-Gly-Gly-propyl-azide synthesized by Intavis AG) dissolved in sortase buffer [50 mM Tris (pH 7.5) and 150 mM NaCl], and 10 µM sortase were mixed in coupling buffer (sortase buffer with 10 mM $CaCl_2$) and incubated for 4 h at 4°C. To stop the reaction and remove uncoupled Nb and sortase, an IMAC was performed, followed by protein concentration, and unreacted sortase peptide depletion using the Amicon Ultra-Centrifugal Filter 3-kDa MWCO. For fluorescent labeling, the SPAAC (strain-promoted azide-alkyne cycloaddition) click chemistry reaction was employed by incubating azide-coupled Nbs with two-fold molar excess of DBCO-AF647 (Jena Bioscience) for 2 h at 25°C. Excess DBCO-AF647 was subsequently removed by dialysis (GeBAflex-tube, 6–8 kDa, Scienova). Finally, a hydrophobic interaction chromatography (HiTrap Butyl-S FF, Cytiva) was performed to deplete unlabeled Nb.

PBMC isolation, cell freezing, and thawing

Fresh blood, buffy coats, or mononuclear blood cell concentrates were obtained from healthy volunteers at the Department of Immunology or from the ZKT Tübingen gGmbH. Participants gave informed written consent, and the studies were approved by the ethical review committee of the University of Tübingen, projects 156/2012B01 and 713/2018BO2. Blood products were diluted with PBS 1× (homemade from 10× stock solution, Lonza, Switzerland), and PBMCs were isolated by density gradient centrifugation with Biocoll separation solution (Biochrom, Germany). PBMCs were washed twice with PBS 1×, counted with a NC-250 cell counter (Chemometec, Denmark), and resuspended in heat-inactivated (h.i.) fetal bovine serum (Capricorn Scientific, Germany) containing 10% Dimethylsulfoxide (DMSO) (Merck). Cells were immediately transferred into a −80°C freezer in a freezing container (Mr. Frosty; Thermo Fisher Scientific). After at least 24 h, frozen cells were transferred into a liquid nitrogen tank and were kept frozen until use. For the experiments, cells were thawed in Iscove's Modified Dulbecco's Medium (IMDM) (+L-Glutamin + 25 mM (4-(2-hydroxyethyl)-1-piperazineethanesulfonic acid) HEPES; Life Technologies) supplemented with 2.5% h.i. human serum (HS; PanBiotech, Germany), 1× Penicillin-Streptomycin (P/S) (Sigma-Aldrich), and 50 µm β-Mercaptoethanol (Merck), washed once, counted, and used for downstream assays.

Flow cytometry

For flow cytometry analysis, ~200,000 cells per staining condition were used in flow cytometry buffer: PBS containing 0.02% sodium azide, 2 mM EDTA, and 2% (v/v) FBS (Thermo Fisher Scientific). Extracellular staining was performed with hSIRPα Nbs conjugated to AF647 (200 nM), CD3 Ab Allophycocyanin- Cyanine 7 (APC/Cy7) (HIT3a, BioLegend), CD14 Ab PE (HCD14, BioLegend), dead cell marker Zombie Violet (BioLegend) or the respective unspecific fluorescently labeled Pep Nb (PEP-Nb_{AF647}) (58), the positive control hSIRPα Ab PE (SE5A5, BioLegend), and isotype control Abs (BioLegend), by incubation for 45 min at 4°C. Cells were washed three times with Fluorescence Activated Cell Sorting/ Flow Cytometry (FACS) buffer, and data were acquired on the same day using an LSRFortessa™ flow cytometer (Becton Dickinson) equipped with the DIVA Software (Becton Dickinson). Final data analysis was performed using the FlowJo10® software (Becton Dickinson).

Macrophage-mediated antibody-dependent cellular phagocytosis assay

$CD14^+$ cells were purified from frozen PBMCs and CD14-positive selection (Miltenyi Biotec) according to the manufacturer's protocols. MDMs were generated by seeding three million $CD14^+$ cells into one six-well plate (Nunc™, Thermo Fisher Scientific) in IMDM (Thermo Fisher Scientific) supplemented with 10% (v/v) fetal bovine serum (Thermo Fisher Scientific) and M-CSF (50 ng/mL; Miltenyi Biotec) and cultured for 7 to 9 days. Cells were detached from culture plates with Accutase® (Sigma-Aldrich). DLD-1 cells were labeled with the CFSE Cell Division Tracker Kit (BioLegend) according to manufacturer's instructions. A total of 100,000 DLD-1 cells and 50,000 MDMs were incubated in U-bottom 96-well plates (Corning) with hSIRPα Nbs (1 µM) or KWAR23 (100 nM) and cetuximab (0.66 nM) (MedChemExpress) for 2 h at 37° C, followed by detachment of adherent cells from culture plates with Accutase® (Sigma-Aldrich). For flow cytometry, cells were incubated with CD206 Ab AF647 (clone 15–2, BioLegend) and dead cell marker Zombie Violet (BioLegend). Percent of phagocytosis indicates the percentage of viable $CD206^+CFSE^+$ macrophages.

Chelator conjugation and radiolabeling

For chelator conjugation and radiolabeling with ^{64}Cu, metal-free equipment and buffers pretreated with Chelex 100 (Sigma-Aldrich) were used. Nbs (100 µg) were reacted with 100 M equivalents of p-NCS-benzyl-NODA-GA (CheMatech) in 0.2 M sodium bicarbonate (pH 8.7) for 24 h at room temperature (RT). Excess of chelator was removed by ultrafiltration (Amicon Ultra 0.5 mL, 3-kDa MWCO, Merck Millipore) using the same buffer conditions. For neutralization of $[^{64}Cu]CuCl_2$ (300 MBq in 0.1 M HCl), 1.5 volumes of 0.5 M ammonium acetate solution (pH 4.1) were added, resulting in a pH of 4. Conjugate (150 µg) was added to the solution and incubated at 35°C for 30 min. A 0.2% diethylenetriaminepentaacetic acid (3 µL) solution was added to quench the labeling reaction. Complete incorporation of the radioisotope was confirmed after each radiosynthesis by thin-layer chromatography [Agilent Technologies; mobile phase, 0.1 M sodium citrate buffer (pH 5)] and high-performance size exclusion chromatography (Superdex 75 Increase, 300 × 10 mm, Cytiva; mobile phase, DPBS with 0.5 mM EDTA, adjusted to pH 6.9).

In vitro radioimmunoassay

To determine the immunoreactive fraction (maximum binding, B_{max}), an increasing number of HT1080-hSIRPα cells were incubated in triplicates with 1 ng (2 MBq/µg) of ^{64}Cu-hSIRPα-$S36_{K>R}$ Nb for 1 h at 37°C and washed twice with PBS/1% FBS. The remaining cell-bound radioactivity was measured using a Wizard² 2480 gamma counter (PerkinElmer Inc.) and quantified as percentage of the total added activity.

Tumor-bearing mouse models and PET imaging

Six-week-old female C57BL/6N wt mice were purchased from Charles River. C57BL/6 hSIRPα/hCD47 KI ($C57BL/6N^{CD47tm1.1(CD47)Geno;Sirpatm2.1(SIRPA)Geno}$) mice (hSIRPα/hCD47) were developed by genOway (manuscript in preparation). For tumor cell inoculation, 1×10^6 MC38-hPD-L1-hCD47-luciferase-Zsgreen (MC38-hCD47) KI

colon adenocarcinoma cells (developed by genOway) were resuspended in 100 µL of PBS and subcutaneously injected into hSIRPα/hCD47or wt mice.

hSIRPα/hCD47 and wt mice were injected intravenously (*i.v.*) with 5 µg (~10 MBq) of ^{64}Cu-hSIRPα-S36$_{K>R}$ Nb or ^{64}Cu-GFP$_{K>R}$ Nb 9 days after tumor cell inoculation. Mice were anesthetized with 1.5% isoflurane in 100% oxygen during the scans. Ten-minute static PET scans were performed after 5 min, 90 min, 3 h, and 6 h in a dedicated small-animal Inveon microPET scanner (Siemens Healthineers) with temperature-controlled heating mats. For anatomical colocalization, sequential T2 TurboRARE MR images were acquired immediately after the PET scans on a small animal 7 T ClinScan magnetic resonance scanner (Bruker BioSpin GmbH). PET images were reconstructed using an ordered subset expectation maximization (OSEM3D) algorithm and analyzed with Inveon Research Workplace (Siemens Preclinical Solutions). The volumes of interest of each organ were defined on the basis of anatomical MRI to acquire the corresponding PET tracer uptake within the tumor and organs of interest. The resulting radioactive concentration was measured per tissue volume (Becquerel/cubic centimeter) decay-corrected and presented as percentage of injected dose per cubic centimeter (%ID/cc).

Analyses, statistics, and graphical illustrations

Graph preparation and statistical analysis were performed using the GraphPad Prism Software (version 9.0.0 or higher). One-way ANOVA was performed for multiple comparisons using Tukey as a *post-hoc* test (mean and SEM). A value of $p < 0.05$ was considered statistically significant and marked as * for $p < 0.05$, ** for $p < 0.01$, *** for $p < 0.001$, and **** for $p < 0.0001$; non-significant results were marked with ns. Graphical illustrations were created with BioRender.com.

Data availability statement

The original contributions presented in the study are included in the article/Supplementary Material. Further inquiries can be directed to the corresponding author.

Ethics statement

The studies involving humans were approved by the ethical review committee of the University of Tübingen, projects 156/2012B01 and 713/2018BO2. The studies were conducted in accordance with the local legislation and institutional requirements. The participants provided their written informed consent to participate in this study.

Author contributions

TW: Investigation, Methodology, Writing – original draft, Writing – review & editing. SB: Investigation, Methodology, Writing – original draft. IL: Investigation, Writing – original draft. DF: Investigation, Writing – original draft. MG: Investigation, Methodology, Writing – original draft. BT: Investigation, Methodology, Writing – original draft. PK: Investigation, Methodology, Writing – original draft. DSe: Investigation, Writing – original draft. SM: Methodology, Writing – original draft. AR: Resources, Writing – original draft. FS: Resources, Writing – original draft. KT: Resources, Writing – original draft. SP: Investigation, Methodology, Writing – original draft. AZ: Resources, Writing – original draft. CG: Resources, Writing – original draft. AS: Resources, Writing – original draft. SN: Resources, Writing – original draft. AM: Investigation, Writing – original draft. MK: Conceptualization, Writing – original draft. BP: Conceptualization, Formal analysis, Resources, Writing – original draft. DSo: Investigation, Writing – original draft, Writing – review & editing. UR: Conceptualization, Funding acquisition, Investigation, Supervision, Writing – original draft, Writing – review & editing.

Funding

The author(s) declare financial support was received for the research, authorship, and/or publication of this article. This work received financial support from the State Ministry of Baden-Wuerttemberg for Economic Affairs, Labour and Tourism (Grant: Predictive diagnostics of immune-associated diseases for personalized medicine. FKZ: 35-4223.10/8). This work was supported by the Deutsche Forschungsgemeinschaft (DFG, German Research Foundation, Germany´s Excellence Strategy-EXC2180-390900677) and the Werner Siemens-Foundation. The RSLC U3000 HPLC system and the maXis HD UHR-TOF mass spectrometer used for intact mass analysis were funded by the State Ministry of Baden-Wuerttemberg for Economic Affairs, Labor and Tourism (#7-4332.62-NMI/55). The Orbitrap Eclipse Tribrid Mass Spectrometer used for HDX-MS analysis were financed by the European Regional Development Fund (ERDF) and the State Ministry of Baden-Wuerttemberg for Economic Affairs, Labor and Tourism (#3-4332.62-NMI/69).

Acknowledgments

The authors thank Johannes Kinzler for support in radiolabeling and all genOway SA employees who participated in the generation of the models used in this work. We acknowledge support by Open Access Publishing Fund of University of Tuebingen.

Conflict of interest

DSo, MK, BP, TW, BT, PK, and UR are named as inventors on a patent application claiming the use of the described nanobodies for diagnosis and therapeutics filed by the NMI Natural and Medical Sciences Institute and the University of Tübingen. AR, FS, and KT are employees of the company genOway.

The remaining authors declare that the research was conducted in the absence of any commercial or financial relationships that could be construed as a potential conflict of interest.

Publisher's note

All claims expressed in this article are solely those of the authors and do not necessarily represent those of their affiliated organizations, or those of the publisher, the editors and the reviewers. Any product that may be evaluated in this article, or claim that may be made by its manufacturer, is not guaranteed or endorsed by the publisher.

Supplementary material

The Supplementary Material for this article can be found online at: https://www.frontiersin.org/articles/10.3389/fimmu.2023.1264179/full#supplementary-material

References

1. Binnewies M, Roberts EW, Kersten K, Chan V, Fearon DF, Merad M, et al. Understanding the tumor immune microenvironment (TIME) for effective therapy. *Nat Med* (2018) 24(5):541–50. doi: 10.1038/s41591-018-0014-x

2. DeNardo DG, Ruffell B. Macrophages as regulators of tumour immunity and immunotherapy. *Nat Rev Immunol* (2019) 19(6):369–82. doi: 10.1038/s41577-019-0127-6

3. Jin M-Z, Jin W-L. The updated landscape of tumor microenvironment and drug repurposing. *Signal transduction targeted Ther* (2020) 5(1):1–16. doi: 10.1038/s41392-020-00280-x

4. Labani-Motlagh A, Ashja-Mahdavi M, Loskog A. The tumor microenvironment: a milieu hindering and obstructing antitumor immune responses. *Front Immunol* (2020) 11:940. doi: 10.3389/fimmu.2020.00940

5. Mantovani A, Allavena P, Sica A, Balkwill F. Cancer-related inflammation. *Nature* (2008) 454(7203):436–44. doi: 10.1038/nature07205

6. Vinogradov S, Warren G, Wei X. Macrophages associated with tumors as potential targets and therapeutic intermediates. *Nanomedicine* (2014) 9(5):695–707. doi: 10.2217/nnm.14.13

7. Mantovani A, Marchesi F, Malesci A, Laghi L, Allavena P. Tumour-associated macrophages as treatment targets in oncology. *Nat Rev Clin Oncol* (2017) 14(7):399–416. doi: 10.1038/nrclinonc.2016.217

8. Lin Y, Xu J, Lan H. Tumor-associated macrophages in tumor metastasis: biological roles and clinical therapeutic applications. *J Hematol Oncol* (2019) 12 (1):76. doi: 10.1186/s13045-019-0760-3

9. Tang X. Tumor-associated macrophages as potential diagnostic and prognostic biomarkers in breast cancer. *Cancer Lett* (2013) 332(1):3–10. doi: 10.1016/j.canlet.2013.01.024

10. Räihä MR, Puolakkainen PA. Tumor-associated macrophages (TAMs) as biomarkers for gastric cancer: A review. *Chronic Dis Transl Med* (2018) 4(3):156–63. doi: 10.1016/j.cdtm.2018.07.001

11. Mukherjee S, Sonanini D, Maurer A, Daldrup-Link HE. The yin and yang of imaging tumor associated macrophages with PET and MRI. *Theranostics* (2019) 9 (25):7730–48. doi: 10.7150/thno.37306

12. Mantovani A, Allavena P, Marchesi F, Garlanda C. Macrophages as tools and targets in cancer therapy. *Nat Rev Drug Discovery* (2022) 21(11):799–820. doi: 10.1038/s41573-022-00520-5

13. Adams S, van der Laan LJ, Vernon-Wilson E, de Lavalette CR, Döpp EA, Dijkstra CD, et al. Signal-regulatory protein is selectively expressed by myeloid and neuronal cells. *J Immunol* (1998) 161(4):1853–9. doi: 10.4049/jimmunol.161.4.1853

14. Matlung HL, Szilagyi K, Barclay NA, van den Berg TK. The CD47-SIRPα signaling axis as an innate immune checkpoint in cancer. *Immunol Rev* (2017) 276 (1):145–64. doi: 10.1111/imr.12527

15. Brown EJ, Frazier WA. Integrin-associated protein (CD47) and its ligands. *Trends Cell Biol* (2001) 11(3):130–5. doi: 10.1016/S0962-8924(00)01906-1

16. Jaiswal S, Jamieson CH, Pang WW, Park CY, Chao MP, Majeti R, et al. CD47 is upregulated on circulating hematopoietic stem cells and leukemia cells to avoid phagocytosis. *Cell* (2009) 138(2):271–85. doi: 10.1016/j.cell.2009.05.046

17. Chen Y-P, Kim HJ, Wu H, Price-Troska T, Villasboas JC, Jalali S, et al. SIRPα expression delineates subsets of intratumoral monocyte/macrophages with different functional and prognostic impact in follicular lymphoma. *Blood Cancer J* (2019) 9 (10):1–14. doi: 10.1038/s41408-019-0246-0

18. Sugimura-Nagata A, Koshino A, Inoue S, Matsuo-Nagano A, Komura M, Riku M, et al. Expression and prognostic significance of CD47–SIRPA macrophage checkpoint molecules in colorectal cancer. *Int J Mol Sci* (2021) 22(5):2690. doi: 10.3390/ijms22052690

19. Yang H, Yan M, Li W, Xu L. SIRPα and PD1 expression on tumor-associated macrophage predict prognosis of intrahepatic cholangiocarcinoma. *J Trans Med* (2022) 20(1):1–16. doi: 10.1186/s12967-022-03342-6

20. Muyldermans S. Nanobodies: natural single-domain antibodies. *Annu Rev Biochem* (2013) 82(1):775–97. doi: 10.1146/annurev-biochem-063011-092449

21. Hamers-Casterman C, Atarhouch T, Muyldermans S, Robinson G, Hamers C, Songa EB, et al. Naturally occurring antibodies devoid of light chains. *Nature* (1993) 363(6428):446–8. doi: 10.1038/363446a0

22. Wagner TR, Ostertag E, Kaiser PD, Gramlich M, Ruetalo N, Junker D, et al. NeutrobodyPlex—monitoring SARS-CoV-2 neutralizing immune responses using nanobodies. *EMBO Rep* (2021) 22(5):e52325. doi: 10.15252/embr.202052325

23. Wagner TR, Rothbauer U. Nanobodies–Little helpers unravelling intracellular signaling. *Free Radical Biol Med* (2021) 176(20):46–61. doi: 10.1016/j.freeradbiomed.2021.09.005

24. Wagner TR, Schnepf D, Beer J, Ruetalo N, Klingel K, Kaiser PD, et al. Biparatopic nanobodies protect mice from lethal challenge with SARS-CoV-2 variants of concern. *EMBO Rep* (2022) 23(2):e53865. doi: 10.15252/embr.202153865

25. Sim J, Sockolosky JT, Sangalang E, Izquierdo S, Pedersen D, Harriman W, et al. Discovery of high affinity, pan-allelic, and pan-mammalian reactive antibodies against the myeloid checkpoint receptor SIRPα. *MAbs* (2019) 11(6):1036–52. doi: 10.1080/19420862.2019.1624123

26. Ring NG, Herndler-Brandstetter D, Weiskopf K, Shan L, Volkmer J-P, George BM, et al. Anti-SIRPα antibody immunotherapy enhances neutrophil and macrophage antitumor activity. *Proc Natl Acad Sci* (2017) 114(49):E10578–E85. doi: 10.1073/pnas.1710877114

27. Ugel S, De Sanctis F, Mandruzzato S, Bronte V. Tumor-induced myeloid deviation: when myeloid-derived suppressor cells meet tumor-associated macrophages. *J Clin Invest* (2015) 125(9):3365–76. doi: 10.1172/JCI80006

28. Condamine T, Ramachandran I, Youn JI, Gabrilovich DI. Regulation of tumor metastasis by myeloid-derived suppressor cells. *Annu Rev Med* (2015) 66:97–110. doi: 10.1146/annurev-med-051013-052304

29. Voets E, Paradé M, Lutje Hulsik D, Spijkers S, Janssen W, Rens J, et al. Functional characterization of the selective pan-allele anti-SIRPα antibody ADU-1805 that blocks the SIRPα–CD47 innate immune checkpoint. *J immunother cancer* (2019) 7(1):1–15. doi: 10.1186/s40425-019-0772-0

30. Dizman N, Buchbinder EI. Cancer therapy targeting CD47/SIRPα. *Cancers (Basel)* (2021) 13(24):6229. doi: 10.3390/cancers13246229

31. De Vlaminck K, Romão E, Puttemans J, Pombo Antunes AR, Kancheva D, Scheyltjens I, et al. Imaging of glioblastoma tumor-associated myeloid cells using nanobodies targeting signal regulatory protein alpha. *Front Immunol* (2021) 12:5090. doi: 10.3389/fimmu.2021.777524

32. Gauttier V, Pengam S, Durand J, Biteau K, Mary C, Morello A, et al. Selective SIRPα blockade reverses tumor T cell exclusion and overcomes cancer immunotherapy resistance. *J Clin Invest* (2020) 130(11):6109–23. doi: 10.1172/JCI135528

33. Virant D, Traenkle B, Maier J, Kaiser PD, Bodenhöfer M, Schmees C, et al. A peptide tag-specific nanobody enables high-quality labeling for dSTORM imaging. *Nat Commun* (2018) 9(1):930. doi: 10.1038/s41467-018-03191-2

34. Ma L, Zhu M, Gai J, Li G, Chang Q, Qiao P, et al. Preclinical development of a novel CD47 nanobody with less toxicity and enhanced anti-cancer therapeutic potential. *J Nanobiotechnol* (2020) 18(1):12. doi: 10.1186/s12951-020-0571-2

35. Hatterer E, Barba L, Noraz N, Daubeuf B, Aubry-Lachainaye JP, von der Weid B, et al. Co-engaging CD47 and CD19 with a bispecific antibody abrogates B-cell receptor/CD19 association leading to impaired B-cell proliferation. *MAbs* (2019) 11(2):322–34. doi: 10.1080/19420862.2018.1558698

36. Lakhani N, Richardson D, Kristedja T, Rangwala F, McKay H, Gonzalez L, et al. 429 Phase 1 dose escalation study of the agonist redirected checkpoint, SL-172154 (SIRPα-Fc-CD40L) in subjects with platinum-resistant ovarian cancer. *J ImmunoTher Cancer* (2021) 9(Suppl 2):A459–A. doi: 10.1136/jitc-2021-SITC2021.429

37. Griffiths K, Binder U, McDowell W, Tommasi R, Frigerio M, Darby WG, et al. Half-life extension and non-human primate pharmacokinetic safety studies of i-body

AD-114 targeting human CXCR4. *MAbs* (2019) 11(7):1331–40. doi: 10.1080/19420862.2019.1626652

38. Hanke L, Das H, Sheward DJ, Perez Vidakovics L, Urgard E, Moliner-Morro A, et al. A bispecific monomeric nanobody induces spike trimer dimers and neutralizes SARS-CoV-2 in vivo. *Nat Commun* (2022) 13(1):1–11. doi: 10.1038/s41467-021-27610-z

39. Farwell MD, Gamache RF, Babazada H, Hellmann MD, Harding JJ, Korn R, et al. CD8-targeted PET imaging of tumor-infiltrating T cells in patients with cancer: A phase I first-in-humans study of 89Zr-Df-IAB22M2C, a radiolabeled anti-CD8 minibody. *J Nucl Med* (2022) 63(5):720–6. doi: 10.2967/jnumed.121.262485

40. Edwards KJ, Chang B, Babazada H, Lohith K, Park DH, Farwell MD, et al. Using CD69 PET imaging to monitor immunotherapy-induced immune activation. *Cancer Immunol Res* (2022) 10(9):1084–94. doi: 10.1158/2326-6066.CIR-21-0874

41. Schwenck J, Sonanini D, Cotton JM, Rammensee H-G, la Fougère C, Zender L, et al. Advances in PET imaging of cancer. *Nat Rev Cancer* (2023) 23(7):474–90. doi: 10.1038/s41568-023-00576-4

42. Keyaerts M, Xavier C, Heemskerk J, Devoogdt N, Everaert H, Ackaert C, et al. Phase I study of 68Ga-HER2-nanobody for PET/CT assessment of HER2 expression in breast carcinoma. *J Nucl Med* (2016) 57(1):27–33. doi: 10.2967/jnumed.115.162024

43. Xavier C, Vaneycken I, D'huyvetter M, Heemskerk J, Keyaerts M, Vincke C, et al. Synthesis, preclinical validation, dosimetry, and toxicity of 68Ga-NOTA-anti-HER2 Nanobodies for iPET imaging of HER2 receptor expression in cancer. *J Nucl Med* (2013) 54(5):776–84. doi: 10.2967/jnumed.112.111021

44. Harmand TJ, Islam A, Pishesha N, Ploegh HL. Nanobodies as in *vivo*, non-invasive, imaging agents. *RSC Chem Biol* (2021) 2(3):685–701. doi: 10.1039/D1CB00023C

45. Traenkle B, Emele F, Anton R, Poetz O, Haeussler RS, Maier J, et al. Monitoring interactions and dynamics of endogenous beta-catenin with intracellular nanobodies in living cells*[S]. *Mol Cell Proteomics* (2015) 14(3):707–23. doi: 10.1074/mcp.M114.044016

46. Massa S, Vikani N, Betti C, Ballet S, Vanderhaegen S, Steyaert J, et al. Sortase A-mediated site-specific labeling of camelid single-domain antibody-fragments: a versatile strategy for multiple molecular imaging modalities. *Contrast Media Mol Imaging* (2016) 11(5):328–39. doi: 10.1002/cmmi.1696

47. Rashidian M, Ingram JR, Dougan M, Dongre A, Whang KA, LeGall C, et al. Predicting the response to CTLA-4 blockade by longitudinal noninvasive monitoring of CD8 T cells. *J Exp Med* (2017) 214(8):2243–55. doi: 10.1084/jem.20161950

48. Sefik E, Qu R, Junqueira C, Kaffe E, Mirza H, Zhao J, et al. Inflammasome activation in infected macrophages drives COVID-19 pathology. *Nature* (2022) 606 (7914):585–93. doi: 10.1038/s41586-022-04802-1

49. Ma WT, Gao F, Gu K, Chen DK. The role of monocytes and macrophages in autoimmune diseases: A comprehensive review. *Front Immunol* (2019) 10:1140. doi: 10.3389/fimmu.2019.01140

50. Nakamura K, Smyth MJ. Myeloid immunosuppression and immune checkpoints in the tumor microenvironment. *Cell Mol Immunol* (2020) 17(1):1–12. doi: 10.1038/s41423-019-0306-1

51. Movahedi K, Schoonooghe S, Laoui D, Houbracken I, Waelput W, Breckpot K, et al. Nanobody-based targeting of the macrophage mannose receptor for effective *in vivo* imaging of tumor-associated macrophages. *Cancer Res* (2012) 72(16):4165–77. doi: 10.1158/0008-5472.CAN-11-2994

52. Narayan N, Mandhair H, Smyth E, Dakin SG, Kiriakidis S, Wells L, et al. The macrophage marker translocator protein (TSPO) is down-regulated on pro-inflammatory 'M1' human macrophages. *PLoS One* (2017) 12(10):e0185767. doi: 10.1371/journal.pone.0185767

53. Anfray C, Ummarino A, Andón FT, Allavena P. Current strategies to target tumor-associated-macrophages to improve anti-tumor immune responses. *Cells* (2019) 9(1):46. doi: 10.3390/cells9010046

54. Rashidian M, Keliher EJ, Bilate AM, Duarte JN, Wojtkiewicz GR, Jacobsen JT, et al. Noninvasive imaging of immune responses. *Proc Natl Acad Sci U S A* (2015) 112 (19):6146–51. doi: 10.1073/pnas.1502609112

55. Arbabi Ghahroudi M, Desmyter A, Wyns L, Hamers R, Muyldermans S. Selection and identification of single domain antibody fragments from camel heavy-chain antibodies. *FEBS letters* (1997) 414(3):521–6. doi: 10.1016/S0014-5793(97)01062-4

56. Maier J, Traenkle B, Rothbauer U. Real-time analysis of epithelial-mesenchymal transition using fluorescent single-domain antibodies. *Sci Rep* (2015) 5(1):1–13. doi: 10.1038/srep13402

57. Chen I, Dorr BM, Liu DR. A general strategy for the evolution of bond-forming enzymes using yeast display. *Proc Natl Acad Sci* (2011) 108(28):11399–404. doi: 10.1073/pnas.1101046108

58. Traenkle B, Kaiser PD, Pezzana S, Richardson J, Gramlich M, Wagner TR, et al. Single-domain antibodies for targeting, detection, and *in vivo* imaging of human CD4+ Cells. *Front Immunol* (2021) 12. doi: 10.3389/fimmu.2021.799910

Supplementary Information

Two birds with one stone: human SIRPα nanobodies for functional modulation and in vivo imaging of myeloid cells

Teresa R. Wagner[1,2], Simone Blaess[3], Inga B. Leske[2], Desiree I. Frecot[1,2], Marius Gramlich[1], Bjoern Traenkle[1], Philipp D. Kaiser[1], Dominik Seyfried[3,4], Sandra Maier[1], Amélie Rezza[5], Fabiane Sônego[5], Kader Thiam[5], Stefania Pezzana[3], Anne Zeck[1], Cécile Gouttefangeas[4,6,7], Armin M. Scholz[8], Stefan Nueske[8], Andreas Maurer[3,7], Manfred Kneilling[3,7,9], Bernd J. Pichle[3,4,7], Dominik Sonanini[3,10], Ulrich Rothbauer[2,7#]

Affiliations

[1] NMI Natural and Medical Sciences Institute at the University of Tübingen, Reutlingen, Germany

[2] Pharmaceutical Biotechnology, Eberhard Karls University Tübingen, Germany

[3] Werner Siemens Imaging Center, Department of Preclinical Imaging and Radiopharmacy, University of Tübingen, Tübingen, Germany

[4] German Cancer Consortium (DKTK) and German Cancer Research Center (DKFZ) partner site Tübingen, Tübingen, Germany

[5] Preclinical Models & Services, genOway, Lyon, France

[6] Department of Immunology, Institute of Cell Biology, University of Tübingen, Tübingen, Germany

[7] Cluster of Excellence iFIT (EXC2180) "Image-Guided and Functionally Instructed Tumor Therapies", University of Tübingen, Germany

[8] Livestock Center of the Faculty of Veterinary Medicine, Ludwig Maximilians University Munich, Oberschleissheim, Germany

[9] Department of Dermatology, University of Tübingen, Tübingen, Germany

[10] Department of Medical Oncology and Pneumology, University of Tübingen, Tübingen, Germany

corresponding author

Prof. Dr. Ulrich Rothbauer, Pharmaceutical Biotechnology, Eberhard Karls University Tübingen, Auf der Morgenstelle 8, 72076 Tübingen, Germany.

E-mail: ulrich.rothbauer@uni-tuebingen.de

Phone: +49 7071 29 72469

Fax: +49 7071 29-2476

Orcid ID: 0000-0001-5923-8986

Supplementary Materials & Methods

Expression constructs

DNA coding for hSIRPαV1 (GenBank accession: NM_001040022.1) and hSIRPαV2 (GenBank accession: D86043.1) were synthesized and cloned into NheI and EcoRI site of pcDNA3.1(+) (GenScript Biotech). The vector backbone was adapted by cutting with EcoRI and BstBI and insertion of DNA comprising an internal ribosomal entry site (IRES) and genes for GFP and Blasticidin S deaminase from the expression construct described in (1). For the generation of hSIRPα expression constructs comprising Ig-like V-type domain (D1, aa 31-146), Ig-like C1-type 1 (D2, aa147-252) and Ig-like C1-type 2 (D3, aa253-348), of UniProtKB P13987 were genetically fused N-terminally to aa1-26 of huCD59 (UniProtKB P13987) and SPOT-Tag (2) and C-terminally to aa91-128 of huCD59 and cloned into BglII and NotI sites of pEGFPN2 expression vector. huCD59 sequences of the expressed fusion protein causes both translocation to the endoplasmatic reticulum and GPI anchoring of the protein at the plasma membrane. DNA encoding for hSIRPβ and hSIRPγ were purchased from addgene (Plasmid #116790) (3) and Sino Biological (Catalog Number HG16111-NH) and subcloned into NheI and EcoRI sites of expression vector used for hSIRPα variants. Expression vector for murine SIRPα was generated based on reference sequence NM_007547.4 and includes SPOT-Tag subsequent to signal peptide (aa 1-31) (2). To generate the respective expression construct, cDNA was cloned into KpnI and XbaI restriction sites of pCMV3-C-FLAG vector.

Cell culture, transfection, stable cell line generation

U2OS, DLD-1, and HT-1080 cells (ATCC) were cultivated according to standard protocols in media containing DMEM (Thermo Fisher Scientific) or RPMI (Thermo Fisher Scientific), respectively supplemented with 10% (v/v) FBS (Thermo Fisher Scientific) and penicillin/streptomycin (Thermo Fisher Scientific) at 37°C and 5% CO_2 atmosphere in a humidified chamber and passaged using 0.05% trypsin-EDTA (Thermo Fisher Scientific). For transfection, Lipofectamine 2000 (Thermo Fisher Scientific) was used according to the manufacturer's protocol. To generate cells stably expressing hSIRPα, selection pressure was applied 24 h after transfection with 5 µg/ml Blasticidin S (Sigma Aldrich) for a period of two

weeks, followed by single cell separation. Finally, individual clones were analyzed for hSIRPα expression.

Cell Isolation

PBMCs were isolated as described previously (1). In brief, fresh blood was obtained from healthy volunteers and PBMCs were isolated by density gradient centrifugation with Biocoll separation solution (Biochrom) and frozen in heat-inactivated FBS (Capricorn Scientific, Germany) containing 10% dimethyl sulfoxide (DMSO; Merck).

Nanobody library generation

For alpaca immunization and Nb library generation, a similar protocol as previously described was performed (4, 5). Briefly, two alpacas (*Vicugna pacos*) were immunized with the extracellular portion of hSIRPα (aa31-370) produced in HEK293 cells (Acrobiosystems) with the approval of the Government of Upper Bavaria (approval number: 55.2-1-54-2532.0-80-14). After an initial vaccination with 560 µg, animals received five boost injections of 280 µg hSIRPα every two weeks. Finally, 91 days after initial immunization, ~100 ml of blood was collected, and lymphocytes were isolated by Ficoll gradient centrifugation with lymphocyte separation medium (PAA Laboratories GmbH). To obtain cDNA, total RNA was extracted using TRIzol (Life Technologies), followed by mRNA transcription using the First-Strand cDNA Synthesis Kit (GE Healthcare). The Nb repertoire was isolated and amplified in three subsequent PCR reactions using the following primer combinations: (1) CALL001 and CALL002, (2) forward primers FR1-1, FR1-2, FR1-3, FR1-4, and reverse primer CALL002, and (3) forward primers FR1-ext1 and FR1-ext2 and reverse primers FR4-1, FR4-2, FR4-3, FR4-4, FR4-5, and FR4-6 introducing SfiI and NotI restriction sites (1). Finally, the amplified Nb library was cloned into the pHEN4 phagemid vector (6) using the SfiI/NotI sites.

Hydrogen-deuterium exchange

HDX-MS epitope mapping was performed as recently described (7). In brief, 5 µL hSIRPα (42 µM) was incubated with either 2.5 µL PBS or a specific hSIRPα Nb S8 (103 µM), S33 (145 µM) or S36 (78 µM). After a 10 min pre-incubation at 25 °C, HDX was initiated by a 1:10 dilution in PBS (pH 7.4) prepared with D_2O (final labeling D_2O concentration = 90%). Aliquots of 15 µL

were quenched after deuteration for 5 and 30 min by adding 15 µL ice-cold quenching solution (200 mM TCEP, 1.5% formic acid and 4 M guanidine HCl in 100 mM ammonium formate solution, pH 2.2), resulting in a final pH of 2.5. Samples were immediately snap frozen and stored at -80 °C until analysis. Non-deuterated control samples were processed using PBS prepared with H_2O. Each sample was prepared in independent technical replicates (n=3). Settled gel of immobilized pepsin (Thermo Fisher Scientific) was prepared by centrifugation of 60 µL 50% slurry (in ammonium formate solution pH 2.5) at 1,000 x g and 0 °C for 3 min. The supernatant was discarded, sample aliquots were thawed and added to the settled pepsin gel. The proteolysis was performed for 2 min in an ice-water bath. To improve sequence coverage near the N-glycosylation sites of hSIRPα, a post-proteolysis deglycosylation was performed using PNGase Rc (7). 5 µL PNGase Rc (4 µM) was added under a filter inlet (0.65 µm, Merck Millipore) and the proteolyzed sample was placed on the filter. Centrifugation at 1000 x g for 30 s at 0 °C removed the beads and initiated the deglycosylation of the peptides in the flow-through. Deglycosylation was carried out in an ice-water bath for an additional 2 min, and samples were analyzed by LC-MS as described in (8).

Data analysis was performed as previously described in (8). HDX data were obtained for ≥83% of the hSIRPα sequence. The deuterium uptake of each peptide was normalized to the maximal exchangeable protons of the backbone. The deuteration was compared between hSIRPα alone and in complex. A peptide was considered protected from HDX if the summed difference was ≥5%. A peptide was considered not protected if the summed HDX difference was ≤3%.

Mass spectrometry

To confirm correct expression, integrity and purity, chelator conjugated hSIRPα-$S36_{K>R}$ was analyzed by mass spectrometry. Protein sample (5 µg) was diluted 1:3 with HisNaCl buffer (20 mM His, 140 mM NaCl, pH 6.0) and analyzed by liquid chromatography (HPLC) coupled to electrospray ionization (ESI) quadrupole time-of-flight (QTOF) MS. Sample (0.4 µg per injection) was desalted using reversed phase chromatography on a Dionex U3000 RSLC system (Thermo Scientific, Dreieich, Germany) using a Acquity BEH300 C4 column (1mm x

5

50mm, Waters, Eschborn, Germany) at 75°C and 150 µl/min flow rate applying a 11-min linear gradient with varying slopes. In detail, the gradient steps were applied as follows (min/% Eluent B): 0/5, 0.4/5, 2.55/30, 7/50, 7.5/99, 8/5, 8.75/99, 9.5/5, 10/99, 10.25/5 and 11/5. Eluent B was acetonitrile with 0.1% formic acid, and solvent A was water with 0.1% formic acid. To avoid contamination of the mass spectrometer with buffer salts, the HPLC eluate was directed into waste for the first 2 min. Continuous MS analysis was performed using a QTOF mass spectrometer (Maxis UHR-TOF; Bruker, Bremen, Germany) with an ESI source operating in positive ion mode. Spectra were taken in the mass range of 600–2000 m/z. External calibration was applied by infusion of tune mix via a syringe pump during a short time segment at the beginning of the run. Raw MS data were lock-mass corrected (at m/z 1221.9906) and further processed using Data Analysis 5.3 and MaxEnt Deconvolution software tools (Bruker).

6

Supplementary Tables

Supplementary Table 1. Amino acid sequences of hSIRPα Nbs.

hSIRPα Nb	Amino acid sequence
	HVQLVESGGGLVQVGDSLRLSCAPSGRTFRAYAMAWFRQAPGKEREFVAAIRWIGGTPSYK
S7	DSVKGRFTISRDNARNTFYLQMNSLEPQDTGVYYCAAEETQKGSGLGHDGRHYDYWGQGT
	PVTVSS
	QVQLVESGGGLVQPGGSLRLSCADSEFRLDEYATGWFRQAPGKEREGVACISRSGSNTKYT
S8	DSVKGRFTISRDNAKKTVYLQMNSLKPEDTAVYYCAADLTSHYLSCSSYTDYNSWGQGTQVT
	VSS
	QVQLVESGGGLVQPGGSLRLSCLVSGFSSSYYAIGWFRQAPGKEREGVSCITRSGDTTNYAD
S12	SVKGRFTISRDDARNTVYLQMNSLKTEDTAVYSCALWAWAGSGRLRCTASEYGHWGQGTQ
	VTVSS
	EVQLVESGGGLVQPGGSLRLSCAASGFTANSYRMTWVRQAPGKGLEWVADIGTGNEWKYY
S14	PDSVKGRFTISRDAAKNTVYLQMNSLKPEDTAVYYCAKNGAVWYGEDGLDYWGKGTLVTVS
	S
	QVQLVESGGGLVQPGGSLRLSCAASGFTLDSYVIGWFRQAPGKEREGVSCISQRIGSTDYAD
S17	SVKGRFTISKDNAKNTAYLQMNALKPEDTAVYYCAAGRLYYSGTYCPQGGMSYWGKGSPVT
	VSS
	DVQLVESGGGLVQPGGSLTLSCAASGFTSGTYALAYFRQAPGKEREGVSCISNDGGSRNYA
S21	DSVKGRFTISRDNAKNTMYLQMNSLKPEDTAVYYCAAGPWYYCSDFARRPDGMDYWGKGT
	PVTVSS
	EVQLVESGGGLVQPGGSLRLSCAASGFTSETYAIGWFRQAPGKEREGVSCISNDGGSRNYA
S29	DSVKGRFTISRDNAKNTSYLQMNSLKPEDTAVYYCAAGKYYYCLGYVSDGMDYWGKGTPVT
	VSS
	EVQLVESGGGLVQPGGSLRLSCTTSGFTLDYYSVGWFRQAPGKEREGVSCITASGSSTNYA
S33	NSVKGRFTISRDKVKNTVYLQMSSLKPEDTAVYYCAAEPCTVVAGILQAPTSDFGSWGQGTQ
	VTVSS
	EVQLVESGGGLVQPGGSLRLSCAASGFTLDYYAIGWFRQVPGKEREGVSCISSDGGGNTYY
S36	ADSVKGRFTISRDNAKNTVYLQMNSLKPEDSAVYSCAAGPTYYSGSYCRDPHSDYDYWGQG
	TQVTVSS
	HVQLVESGGGLVQPGGSLRLSCAASGETLDYYAIGYVRQAPGKEREGVSCISSRGDNTNYAD
S41	SVKGRFTISRDNANNTVYLQMNSLKPEDTAVYYCVAIKDSWQNYYCSVGWVEYDVWGQGTQ
	VTVSS

S42	HVQLVESGGGLVQPGGSLRLSCAASGFIFSGYAMSWVRQAPGKGLEWVSDISSDGVRLYYA DSVKGRFTISRDNAKNTVYLEMTSLKPDDTALYYCATSSDPQLGLDLWGKGTPVTVSS
S43	HVQLVESGGGLVQPGGSARLSCAASGFDLDYFAIGWFRQAPGKEREGVSCISTRSETTNYVD SVKGRFTISRDNAISTVYLQMNNLKPEDTAVYYCAADWADWTMTGCQMTWDDYNYWGQGA QVTVSS
S44	QVQLQESGGGLVQPGGSLRLACAASGFTFSSYDMSWVRQAPGKGLEWVSDIKSGGGRTYY ADSVKGRFTISRDNAKNTVYLQMNSLKPEDTAVYYCGSLDNSGAYTGGGQGSQVTVSS
S45	HVQLVESGGGLVQPGGSLRLSCAARGFSFRDSAMSWARQAPGKGLEWVGAIYSDGSTVYE KSVKGRFTISRDNAKNTMYLQMHSLKPEDSARYYCAPKGVVADEGDYSGQGTLVTVSS

Supplementary Table 2. Summary of HDX-MS parameters of epitope mapping of anti-SIRPα-Nbs as per consensus guidelines (9).

HDX parameters			
States	SIRPα & SIRPα bound by **Nb S8**	SIRPα & SIRPα bound by **Nb S33**	SIRPα & SIRPα bound by **Nb S36**
HDX reaction detail	1x PBS pH 7.4, 25 °C, 90% D_2O	1x PBS pH 7.4, 25 °C, 90% D_2O	1x PBS pH 7.4, 25 °C, 90% D_2O
Deuteration time points	5 & 30 min	5 & 30 min	5 & 30 min
Average peptide length (AA)	14.2 (s_d = 6.6)	14.5 (s_d = 7.1)	14.3 (s_d = 6.7)
Average redundancy (AA)	4.4	4.4	4.3
Number of used peptides	108	106	105
Sequence coverage	86%	86%	86%
$\Delta\overline{HX}$ threshold for each time point (p≤0.05)	0.27 Da	0.21 Da	0.23 Da
$\Delta\overline{HX}$ threshold for each time point (p≤0.01)	0.44 Da	0.34 Da	0.38 Da
Complexed SIRPα during labelling	99.9%	99.0%	97.1%

Supplementary Figures

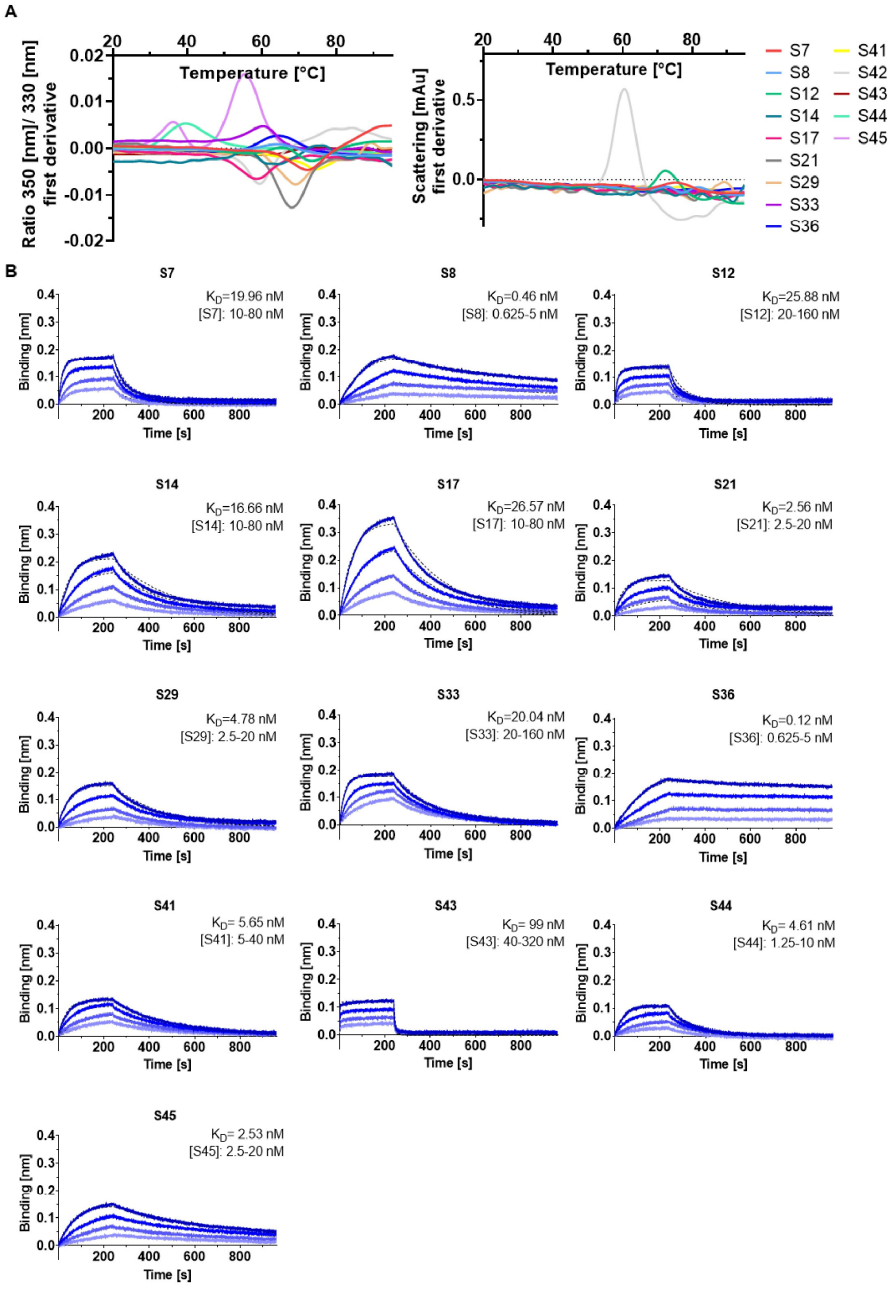

Supplementary Figure 1. Detailed stability analysis and kinetic measurements of hSIRPα Nbs.

A Stability of hSIRPα Nbs was analyzed by nano-differential scanning fluorimetry (nanoDSF). Fluorescence ratios (350 nm/330 nm) and light intensity loss due to scattering illustrated as first derivative are shown. Data are shown as mean value of three technical replicates.

B Sensograms of biolayer interferometry- (BLI-) based affinity measurements of 13 identified hSIRPα Nbs. Biotinylated hSIRPα was immobilized on streptavidin biosensors and kinetic measurements were performed by using four concentrations of purified Nbs ranging from 0.625 to 320 nM (displayed with gradually lighter shades of color). Binding affinity (K_D) was calculated from global 1:1 fits illustrated as dashed lines.

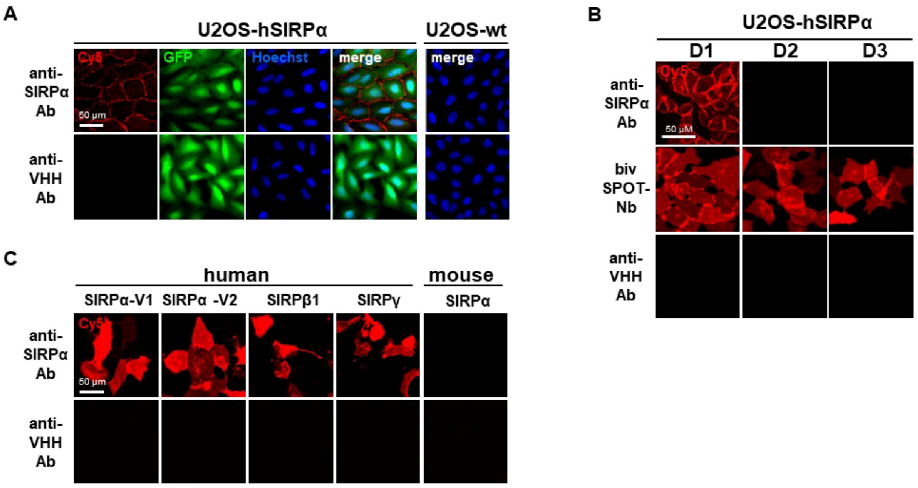

Supplementary Figure 2. Immunofluorescence staining controls.

A Immunofluorescence staining controls of U2OS cells displaying hSIRPα on their surface. Representative images of three technical replicates show hSIRPα Ab (SE5A5) and secondary only Ab control (anti-VHH-Cy5) (red), intracellular IRES derived GFP signal (green), nuclei staining (Hoechst, blue) and merged signals; scale bar: 50 µm.

B Immunofluorescence staining controls of U2OS cells displaying SPOT-tagged hSIRPα domain 1 (D1), domain 2 (D2) or domain 3 (D3) on their surface. Representative images of three technical replicates of live cells stained with hSIRPα Ab (SE5A5), bivSPOT-Nb (2) and secondary only Ab control (anti-VHH-Cy5) are shown; scale bar: 50 µm.

C Immunofluorescence control staining of U2OS cells expressing human hSIRPα-V1, -V2, hSIRPβ1, hSIRPγ or mouse hSIRPα on their surface. Representative images of three technical replicates of live cells stained with hSIRPα Ab (SE5A5) and secondary only Ab control (anti-VHH) are shown; scale bar: 50 µm.

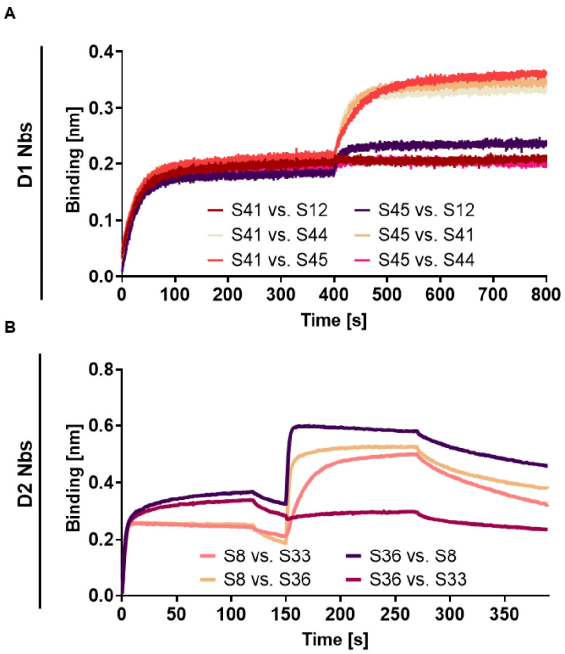

Supplementary Figure 3. Epitope binning analysis of hSIRPα Nbs by BLI.

A Sensograms of BLI-based epitope binning analysis of hSIRPαD1 Nbs are shown (n=1). Biotinylated hSIRPα was immobilized on streptavidin biosensors followed by two consecutive association steps of hSIRPαD1 Nbs S12, S41, S44, S45 (100 nM).

B Sensograms of BLI-based epitope binning analysis of hSIRPαD2 Nbs are shown (n=1). Biotinylated hSIRPα was immobilized on streptavidin biosensors followed by two consecutive association steps of hSIRPαD2 Nbs S8, S33, S36 (100 nM).

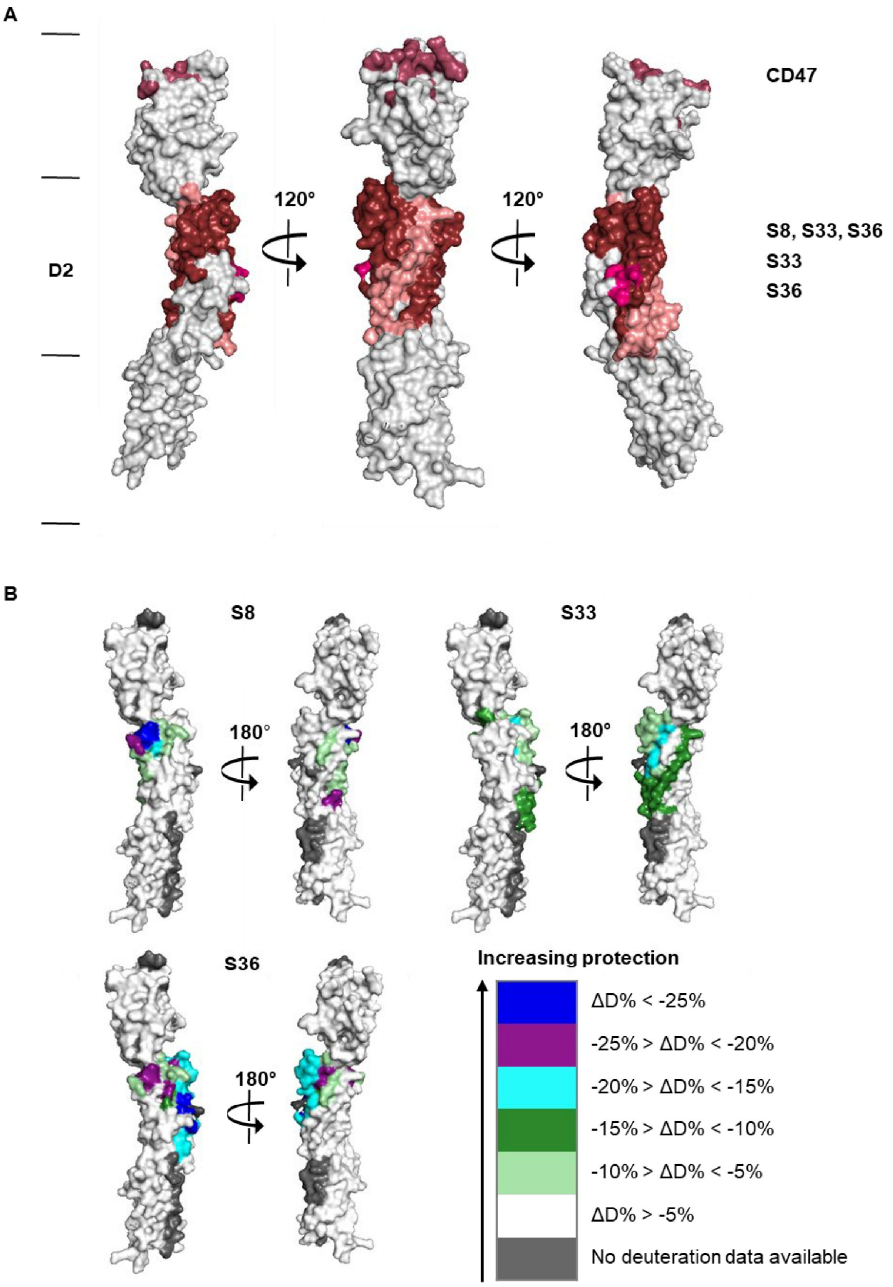
A
D2
120°
120°
CD47
S8, S33, S36
S33
S36
B
S8
180°
S33
180°
S36
180°
Increasing protection
ΔD% < -25%
-25% > ΔD% < -20%
-20% > ΔD% < -15%
-15% > ΔD% < -10%
-10% > ΔD% < -5%
ΔD% > -5%
No deuteration data available

13

Supplementary Figure 4. Detailed epitope mapping analysis of hSIRPαD2 Nbs by HDX-MS.

Localization of hSIRPαD2 Nbs binding epitopes by hydrogen-deuterium exchange mass spectrometry (HDX-MS).

A Surface structure model of hSIRPα (PDB 2wng) showing overlayed epitope mapping results of Nbs S8, S33 and S36.

B Surface structure model of hSIRPα (PDB 2wng) showing individual results of epitopes protected upon binding of hSIRPαD2 Nbs S8, S33 and S36 and different colors indicate the strength of protection (%ΔD).

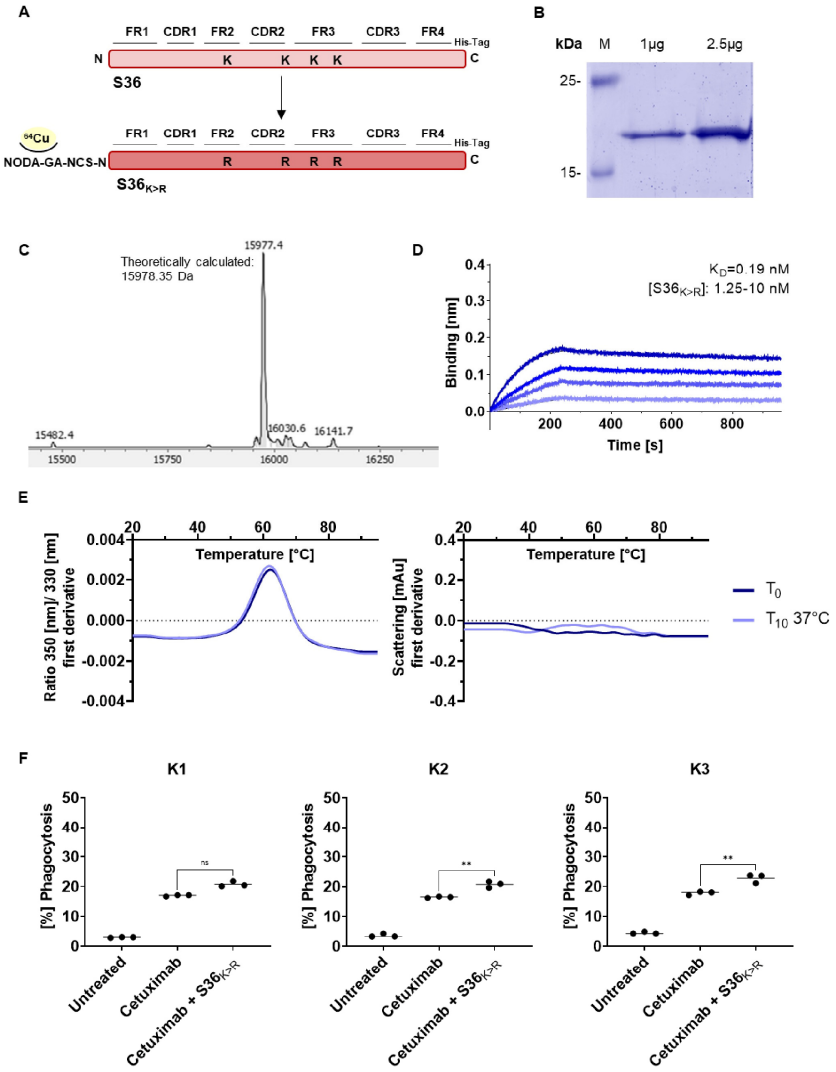

Supplementary Figure 5. Detailed characterization of the sequence optimized hSIRPα-S36$_{K>R}$ Nb for site-specific chelator conjugation.

A Graphical illustration of sequence optimization of hSIRPα-S36 Nb (S36$_{K>R}$) by changing lysine (K) to arginine (R) residues for site-specific chelator (p-NCS-benzyl-NODA-GA) conjugation.

B Expression and purification of hSIRPα-S36$_{K>R}$ Nb using immobilized metal affinity chromatography (IMAC) and size exclusion chromatography (SEC). Coomassie staining of 1 µg and 2.5 µg of purified and chelator-conjugated hSIRPα-S36$_{K>R}$ Nb is shown.

C Confirmation of identity and integrity by mass spectrometric (MS) analysis of chelator conjugated hSIRPα-S36$_{K>R}$ Nb (theoretically calculated molecular weight of 15978.35 Da).

D BLI-based affinity measurements of chelator conjugated hSIRPα-S36$_{K>R}$ Nb. Biotinylated hSIRPα was immobilized on streptavidin biosensors. Kinetic measurements were performed by using four concentrations of purified Nbs ranging from 1.25 nM to 10 nM.

E Stability analysis of chelator conjugated hSIRPα-S36$_{K>R}$ Nb by nanoDSF as fluorescence ratios (350 nm/330 nm) and light intensity loss due to scattering illustrated as first derivative before (T_0) and after 10 days of accelerated aging at 37°C (T_{10}). Data are shown as mean value of three technical replicates.

F Phagocytosis of DLD-1 cells by human monocyte-derived macrophages treated with anti-EGFR cetuximab and chelator conjugated hSIRPα-S36$_{K>R}$ Nb. Analysis of phagocytosis of hSIRPα-S36$_{K>R}$ Nb in combination with cetuximab of three different donors (K1, K2, K3). Data are shown as individual and mean value of three technical replicates. $p < 0.05$ was considered statistically significant (*) and marked as ** for $p < 0.01$, *** for $p < 0.001$, **** for $p < 0.0001$, non-significant results were marked with ns.

16

References

1. Traenkle B, Kaiser PD, Pezzana S, Richardson J, Gramlich M, Wagner TR, et al. Single-Domain Antibodies for Targeting, Detection, and In Vivo Imaging of Human CD4+ Cells. Frontiers in Immunology. 2021;12.

2. Virant D, Traenkle B, Maier J, Kaiser PD, Bodenhöfer M, Schmees C, et al. A peptide tag-specific nanobody enables high-quality labeling for dSTORM imaging. Nature Communications. 2018;9(1):930.

3. Ng PK, Li J, Jeong KJ, Shao S, Chen H, Tsang YH, et al. Systematic Functional Annotation of Somatic Mutations in Cancer. Cancer Cell. 2018;33(3):450-62.e10.

4. Maier J, Traenkle B, Rothbauer U. Real-time analysis of epithelial-mesenchymal transition using fluorescent single-domain antibodies. Scientific reports. 2015;5(1):1-13.

5. Traenkle B, Emele F, Anton R, Poetz O, Haeussler RS, Maier J, et al. Monitoring Interactions and Dynamics of Endogenous Beta-catenin With Intracellular Nanobodies in Living Cells*[S]. Molecular & Cellular Proteomics. 2015;14(3):707-23.

6. Arbabi Ghahroudi M, Desmyter A, Wyns L, Hamers R, Muyldermans S. Selection and identification of single domain antibody fragments from camel heavy-chain antibodies. FEBS letters. 1997;414(3):521-6.

7. Gramlich M, Maier S, Kaiser PD, Traenkle B, Wagner TR, Voglmeir J, et al. A Novel PNGase Rc for Improved Protein N-Deglycosylation in Bioanalytics and Hydrogen–Deuterium Exchange Coupled With Mass Spectrometry Epitope Mapping under Challenging Conditions. Analytical Chemistry. 2022;94(27):9863-71.

8. Wagner TR, Ostertag E, Kaiser PD, Gramlich M, Ruetalo N, Junker D, et al. NeutrobodyPlex—monitoring SARS-CoV-2 neutralizing immune responses using nanobodies. EMBO reports. 2021;22(5):e52325.

9. Masson GR, Burke JE, Ahn NG, Anand GS, Borchers C, Brier S, et al. Recommendations for performing, interpreting and reporting hydrogen deuterium exchange mass spectrometry (HDX-MS) experiments. Nature Methods. 2019;16(7):595-602.